Turbulence in Saturn's Magnetosphere and Forward Modeling of Reduced Spectra from Three-Dimensional Wave Vector Space

Inaugural-Dissertation

zur

Erlangung des Doktorgrades

der Mathematisch-Naturwissenschaftlichen Fakultät

der Universität zu Köln

vorgelegt von

Michael von Papen

aus Frechen

Köln 2014

Berichterstatter: Prof. Dr. J. Saur
Prof. Dr. S. Simon

Tag der mündlichen Prüfung: 13. Oktober 2014

Half of the people can be part right all of the time
Some of the people can be all right part of the time
But all of the people can't be all right all of the time
I think Abraham Lincoln said that
I'll let you be in my dreams if I can be in yours
I said that

Bob Dylan, Talkin' World War III Blues

Abstract

In the first part of this thesis, we analyze the statistical properties of magnetic field fluctuations measured by the Cassini spacecraft inside Saturn's magnetosphere. We introduce Saturn's magnetosphere as a new laboratory for plasma turbulence, where the background magnetic field is strong ($5\,\mathrm{nT} \leq B_0 \leq 75\,\mathrm{nT}$), fluctuations are weak ($\langle \delta B/B \rangle = 0.07$) and the ion plasma β_i is smaller than one. We conduct a case study of the second orbit of Cassini and find the statistics of the fluctuations on MHD scales to be characterized by large scale non-stationary processes. The spectral index on these scales varies between 0.8 and 1.7. At higher frequencies, we observe a steeper spectrum with nearly constant power-law exponent. A spectral break on ion scales separates the two frequency ranges.

We carry out a statistical study of the high frequency, kinetic range, fluctuations using the first seven orbits of Cassini. To account for the changing plasma conditions in the magnetosphere, we use power spectral densities transformed to wave number space normalized to ion scales. At radial distances greater than $9\,R_\mathrm{s}$, we observe an average slope of 2.6 on kinetic scales, but closer to Saturn the spectral indices tend to get shallower. Within error limits, these results are in accordance with a critically balanced cascade of kinetic Alfvén waves. Probability density functions of the fluctuations have increasingly non-Gaussian tails with increasing frequency. The flatness grows with frequency like a power-law indicating intermittency and formation of coherent structures.

We show that the dissipation of magnetic field fluctuations has important implications for Saturn's magnetosphere. We estimate the total energy flux along the turbulent cascade as $140-160\,\mathrm{GW}$, which is ultimately dissipated as heat. For Saturn's magnetosphere, this turbulent heating mechanism is introduced for the first time. It provides energy on the same order of magnitude as needed to explain the large plasma temperatures measured at Saturn. In an extended data set of 42 orbits, we further analyze the local time and longitude asymmetries. We observe significantly stronger fluctuations in the pre-noon sector of the outer magnetosphere and the midnight sector close to the planet. The spectral energy and the turbulent heating rate are enhanced in a longitude range that coincides with regions of denser plasma.

In the second part of this thesis, we present a numerical model to evaluate one-dimensional reduced power spectral densities from arbitrary energy distributions in wave vector space. We assume axisymmetry and approximate the poloidal fluctuations to be passively cascaded by Alfvénic fluctuations. The diagonal elements of the spectral tensor can be calculated separately and we are able to analyze the implications of the measurement geometry. Based on a critically balanced turbulent cascade, we construct an energy distribution in three dimensional **k**-space from MHD to electron scales.

We investigate the power spectra in detail and focus on the spectral slope as a function of field-to-flow angle θ and of outer scale. We show for the first time that critically balanced turbulence develops toward a θ-independent cascade with a quasi-perpendicular spectral slope. This occurs at a frequency $f_{\max}$, which is analytically estimated and is controlled by the outer scale, the critical balance exponent and the field-to-flow angle. We also discuss anisotropic damping terms acting on the **k**-space distribution of energy and their effects on the PSD. Here, the dominating parameter is the electron temperature, which controls the onset of damping.

We calculate synthetic spectra for given measurement geometries and plasma parameters in the solar wind and compare them to recent observations that are interpreted in terms of a critically balanced turbulent cascade. A qualitatively successful reproduction of the observations indicates that the results are indeed in agreement with a critically balanced cascade of (kinetic) Alfvén waves. However, we find that the addition of a damping term is substantial to obtain a smooth transition of spectral slopes from small to large field-to-flow angles.

In order to corroborate our interpretation of turbulence at Saturn, we model magnetospheric power spectral densities using data presented in the first part of this thesis. We qualitatively reproduce the location of the spectral break and the spectral slopes on MHD and kinetic scales for a selected spectrum discussed in the case study. Further, we model the observed radial distribution of spectral indices and find that damping on scales of the hot electrons might explain the shallower spectral slopes inside $9\,R_{\mathrm{S}}$. These results indicate that the energy transferred along the turbulent cascade is predominantly deposited into the hot electron population.

Zusammenfassung

Der erste Teil dieser Dissertation befasst sich mit der Analyse statistischer Eigenschaften von Magnetfeldfluktuationen in der Magnetosphäre des Planeten Saturn. Dabei zeigen wir zum ersten Mal, dass sich auf kinetischen Skalen eine turbulente Kaskade ausbildet, welche innerhalb der mittleren Magnetosphäre einen konsistenten spektralen Index aufweist. Wir stellen damit die Magnetosphäre als ein - zusätzlich zum Sonnenwind - neues Labor für die Turbulenzanalyse vor, welches sich durch ein starkes Hintergrundmagnetfeld ($5\,\mathrm{nT} \leq B_0 \leq 75\,\mathrm{nT}$), schwache Fluktuationen ($\langle \delta B/B_0 \rangle = 0.07$) und ein Ionen-Plasma β_i kleiner Eins auszeichnet. Mittels einer Fallstudie des zweiten Orbits von Cassini zeigen wir, dass die statistischen Eigenschaften von Fluktuationen auf MHD Skalen hauptsächlich durch großskalige magnetopshärische Prozesse bestimmt werden. Der spektrale Index auf diesen Skalen variiert zwischen 0.8 und 1.7. In einem höheren Frequenzbereich, der durch einen spektralen Bruch auf Ionenskalen eingeleitet wird, beobachten wir einen steileren Verlauf mit geringerer Variation des spektralen Indexes.

Wir führen eine statistische Studie der spektralen Dichten auf kinetischen Skalen durch, wofür die ersten sieben Orbits von Cassini verwendet werden. Der mittlere spektrale Index beträgt 2.6 und verringert sich innerhalb von $9\,R_\mathrm{s}$ zu $\sim$2.3. Innerhalb der Fehlergrenzen lassen sich diese Ergebnisse durch eine turbulente Kaskade von kinetischen Alfvénwellen im kritischen Gleichgewicht erklären. Im Verhältnis zu einer Gaußverteilung sind extreme Fluktuationen häufiger anzutreffen. Dieser Effekt verstärkt sich mit ansteigender Frequenz und die Flatness steigt als Funktion der Frequenz einem Potenzgesetz gleich an. Letzteres ist ein deutliches Zeichen von Intermittenz.

Die Dissipation der magnetischen Fluktuationen hat starke Auswirkung auf die Energiebilanz der Magnetosphäre und der gesamte Energiefluss entlang der Kaskade wird auf etwa $140 - 160\,\mathrm{GW}$ abgeschätzt. Unter der Annahme, dass diese Energie in Form von Wärme dissipiert wird, ließen sich die hohen Plasmatemperaturen in der Magnetosphäre erklären. Es ist das erste Mal, dass eine solche turbulente Heizungsrate für das Saturnsystem aufgestellt wird. Mit einem erweiterten Datensatz von 42 Orbits untersuchen wir weiterhin die Abhängigkeit der gewonnenen Parameter von der Lokalzeit

und der planetaren Länge. Es zeigt sich, dass stärkere Fluktuationen insbesondere im Vormittagssektor der äußeren Magnetosphäre und im Mitternachtssektor auf kurzer Distanz zum Planeten auftreten. Außerdem stellen wir erhöhte spektrale Dichten und Heizungsraten auf planetaren Längen fest, auf denen ebenfalls eine erhöhte Plasmadichte beobachtet wurde.

Im zweiten Teil dieser Dissertation stellen wir ein numerisches Modell vor, mit Hilfe dessen sich reduzierte eindimensionale spektrale Dichten aus einer gegebenen Energieverteilung im **k**-Raum berechnen lassen. Diese hängen ebenfalls von der Messgeometrie und den zugrunde liegenden Plasmaparametern ab. Unsere Annahmen zur Herleitung des Modells sind axialsymmetrische Fluktuationen und eine durch toroidale Fluktuationen kontrollierte passive Kaskade von poloidalen Fluktuationen. Damit können wir die diagonalen Elemente des spektralen Tensors einzeln berechnen und untersuchen ausführlich die Eigenschaften einer turbulenten Kaskade von (kinetischen) Alfvénwellen im kritischen Gleichgewicht.

Zum ersten Mal kann gezeigt werden, dass sich der spektrale Index einer solchen Kaskade bei hohen Frequenzen verändert. Die spektralen Dichten werden *quasi-senkrecht* und bei entsprechend hohen Frequenzen letztendlich unabhängig vom Winkel θ zwischen Magnetfeld und Plasmageschwindigkeit. Die Frequenz, bei der dies geschieht, wird analytisch approximiert und wird hauptsächlich durch den Winkel θ, den Exponenten des kritischen Gleichgewichts und die der Energieeinspeisung zugeordnete Länge bestimmt. Wir untersuchen außerdem den Einfluss von anisotropen Dämpfungstermen auf die spektrale Dichte. Hierbei stellt sich heraus, dass insbesondere die Elektronentemperatur maßgeblich für den Einsatz der Dämpfung ist.

Wir verwenden das Modell um zu überprüfen, ob bestimmte Beobachtungen im Sonnenwind in Übereinstimmung mit einer turbulenten Kaskade im kritischen Gleichgewicht sind. Mittels unserer neuartigen Modellierungsmethode reproduzieren wir qualitativ den gemessenen spektralen Index als Funktion des Winkels θ auf MHD und kinetischen Skalen und zeigen damit, dass die Ergebnisse tatsächlich in der verwendeten Form interpretiert werden können. Wir stellen fest, dass der Einfluss der Dämpfung erheblich dazu beiträgt einen langsamen Verlauf der spektralen Anisotropie zu erhalten.

Um unsere im ersten Teil getätigte Interpretation der Magnetfeldfluktuationen in Saturn's Magnetosphäre zu erhärten, modellieren wir eine spektrale Energiedichte, welche im Rahmen der Fallstudie besprochen wurde. Die Form des Spektrums - sowohl spektrale Indizes als auch der spektrale Bruch - kann qualitativ erfolgreich unter Verwendung der im ersten Teil verwendeten Plasmaparameter repro-

duziert werden. Weiterhin modellieren wir die radiale Verteilung der spektralen Indizes, wobei sich herausstellt, dass sich die Veränderung innerhalb von $9\,R_\mathrm{s}$ unter Umständen mittels Dämpfung auf heißen Elektronenskalen erklären lässt. Diese Ergebnisse legen den Verdacht Nahe, dass hauptsächlich die heiße Elektronenpopulation in Saturn's Magnetosphäre durch turbulente Fluktuationen geheizt wird.

Contents

CHAPTER 1

Introduction

Turbulence is an apparently chaotic flow of fluids that transfers energy from large to small scales. It stems from the Latin word for rotate, perturb, or entangle, all of which illustrate the flow patterns in a turbulent flow. Everyone has already seen or experienced the characteristic turbulent whirls or eddies, e.g., in water behind a bridge head, during a horrible transatlantic flight or - to cite the turbulence scientists' most popular example - when you pour milk in your coffee. Because of such common presence in our daily lives, it is surprising that a renowned physicist such as *Richard Feynman* (1918-1988) called turbulence a central unsolved problem of physics (*Feynman et al.*, 2010, Ch. 3). The problem that he is referring to is the inability to exactly describe the particle motions of the fluid when it behaves turbulent, even though we know the underlying equation of motion, namely the Navier-Stokes equation for hydrodynamic flow.

What we can do, however, is describe the motion of the fluid in a *statistical* sense. If we observe fully developed turbulence on the right scales, i.e., in the inertial range, we find that the averaged velocity fluctuation of the particles is constant in time and independent of location. More importantly, the statistical moments at different scales are related to each other in a way that is universal for all hydrodynamic fluids, regardless of how the energy is injected into the system on large scales. This important result was discovered by *A. N. Kolmogorov* (1907-1987) and is in detail explained in the book *Turbulence* by *Frisch*. This universal scale invariance of the statistical moments stems from the self-similar decay of large eddies to smaller ones. Nonlinear interactions between eddies of comparable size transfer energy along a so-called turbulent cascade from large to small scales. In this thesis, it is this turbulent cascade and the energy transfer along it that we are most interested in.

With the beginning of the space era and the ability to conduct in-situ measurements in the solar wind, it became clear that not only fluids on Earth are turbulent, but also the plasmas commonly found in space. Similar to velocity fluctuations in hydrodynamic turbulence, power spectral densities of magnetic fluctuations in the solar wind were found to scale with a power-law of slope 5/3. However, there are important differences in the governing equations describ-

ing plasma and hydrodynamic turbulence. First of all, plasma as an ensemble of quasi-neutral ions and electrons is subject to far reaching electromagnetic forces, which leads to a complex collective behavior and the emergence of wave modes that change the energy transfer substantially. It also has characteristic ion and electron scales. On scales much larger than ion scales, the plasma can be described as a fluid in the framework of magnetohydrodynamics (MHD). However, on smaller scales, so-called kinetic scales, the characteristics of the turbulent cascade change considerably. Lastly, plasma turbulence is inherently anisotropic with regards to a background magnetic field. One approach to explain the observed Kolmogorov-like scaling in the presence of anisotropic plasma waves is the concept of a critically balanced turbulent cascade, which we follow in this thesis. It describes the nonlinear interactions of Alfvén waves and their kinetic counterparts, the kinetic Alfvén waves, as most important for the turbulent cascade of energy. The relevant turbulence theories - starting from hydrodynamic turbulence - are presented in Chapter 2.

The best *laboratory* we have for plasma turbulence so far is the solar wind. Here, the Reynolds number, which quantifies the turbulent flow of a fluid, is orders of magnitudes larger than that of any artificially produced plasma. Solar wind turbulence has been analyzed since more than 30 years and several characteristic features have been found that seem to be universal for plasma turbulence. Here, magnetic field fluctuations have been analyzed most extensively, because they can be determined with high time resolution and accuracy compared to the measurement of other plasma parameters such as the electric field or the plasma velocity. For the same reason, we restrict our analysis to magnetic fluctuations in this thesis. Characteristic features of turbulence in the solar wind include a Kolmogorov-like spectral index of 5/3 on MHD scales and a spectral break around ion scales followed by a steeper slope on kinetic scales. It is believed that turbulent interactions are important to explain the acceleration of energetic particles the solar wind and that the dissipation of turbulent fluctuations substantially heats the plasma. Turbulence is therefore essential to describe the dynamical evolution of the solar wind.

As turbulence is an ubiquitous phenomenon, it is interesting to ask where else, besides in the solar wind, we may encounter turbulent fluctuations. Can planetary magnetospheres be turbulent, as *Saur et al.* (2002) suggest for the case of Jupiter? Is magnetospheric plasma heated by turbulent interactions? And how would that affect the planetary energy budget? In order to answer these questions, we conduct for the first time a turbulence analysis for Saturn's magnetosphere. In contrast to the effectively infinite size of the heliosphere, this planetary system is bounded by the magnetopause and the magnetic field geometry. It is also characterized by a strong planetary magnetic field. Alfvén waves that are launched inside the magnetosphere through large scale instabilities travel along planetary magnetic field lines and are reflected at the density gradients close to the planet. Hence, we may conjecture the magnetosphere as a bath of plasma waves that interact nonlinearly and form a turbulent cascade.

The measurement in this new *laboratory* is facilitated by the spacecraft Cassini, which orbits around Saturn since 2004. Therefore, we have a vast data set publicly available through the Planetary Data System[1]. Despite of this large data set, there are several unanswered questions. One of these questions regards the puzzling high plasma temperatures in the magnetosphere. Although the plasma is produced close to Saturn by the moon Enceladus and expands nearly adiabatically as it is transported radially outward, it does not cool down accordingly. In contrast, the temperature is found to increase with distance to Saturn. This temperature profile can only be explained by a local heating mechanism (*Bagenal and Delamere*, 2011). In this thesis, we elaborate on the idea that the dissipation of turbulent magnetic fluctuations provides the energy that is required to heat the plasma to the observed temperatures.

In Chapter 3, we conduct a spectral analysis of magnetic field data obtained in Saturn's magnetosphere, part of which has already been published in *von Papen et al.* (2014). In Section 3.1, we introduce the second largest magnetosphere of the solar system, which is primarily internally controlled, i.e., the magnetospheric dynamics are mostly fueled by internal sources and by the rapid rotation of the planet. The analysis in the framework of turbulence is thus complicated by large scale plasma processes in Saturn's magnetosphere. After we present the most relevant plasma dynamics of Saturn's magnetosphere in Section 3.2, we analyze in detail the magnetic field data and the power spectral densities in a case study in Section 3.3. We observe a turbulent cascade that is constantly present on kinetic scales and conduct a statistical study in Section 3.4. Here, we estimate the energy that is transferred along the cascade and is ultimately dissipated as heat. The results indicate that turbulent heating is indeed substantial for the magnetospheric energy budget and might help to explain the high plasma temperatures. In Section 3.5, we further analyze the spatial asymmetries in Saturn's magnetosphere with regards to local time and planetary longitude. We show that the turbulent heating rate correlates with planetary longitude and maximizes at longitudes where a higher plasma density is detected.

The results in Saturn's magnetosphere can be interpreted in terms of a critically balanced turbulent cascade formed by kinetic Alfvén waves. This theory of strong turbulence has been proposed to explain the observations in the interstellar medium and the solar wind in the presence of anisotropy (*Goldreich and Sridhar*, 1995). It is based on the conjecture of a critical balance between wave period and nonlinear time and can be defined by the energy distribution in wave vector space. For this theory, power spectra can be calculated analytically only for the extreme cases of a background magnetic field parallel or perpendicular with respect to the plasma flow. However, the field-to-flow angles during in-situ measurements are generally variable and the magnetic field is therefore never perfectly parallel or perpendicular to the flow. Still, it is currently unknown how exactly power spectra scale for such intermediate field-to-flow angles. For

[1] http://ppi.pds.nasa.gov

that matter, we developed a method to numerically calculate spectral densities in frequency space from a given energy distribution in three-dimensional wave vector space for arbitrary measurement geometries. With this method, we can construct for the first time power spectral densities of critically balanced turbulence from MHD to electron scales.

We present this method and the associated analysis in Chapter 4. After we introduce the theoretical framework for this tool in Section 4.1, we test the synthetic models in detail. Interestingly, we find in Section 4.2 that certain assumptions that are implicitly made in the literature, e.g., the constancy of the spectral index with frequency, are not in agreement with a critically balanced cascade. We also show that damping effects are more important than previously thought, which has important consequences for the interpretation of turbulent fluctuations. As the tool proves to be useful for the interpretation of recent solar wind observations in Section 4.3, we also apply it to our results in Saturn's magnetosphere in Section 4.4. This forward modeling method corroborates our former interpretation in terms of critically balanced turbulence in Saturn's magnetosphere and indicates that the energy of the turbulent magnetic field interactions is primarily deposited into the hot electron population at Saturn. In the final Chapter 5, we summarize the results of the analyses and draw our conclusions.

CHAPTER 2

Turbulence Theory

In this chapter, we introduce the main concept of this thesis, namely the energy transfer controlled by nonlinear interactions that form a turbulent cascade. We begin with the description of hydrodynamic (HD) turbulence in Section 2.1 using a dimensional analysis. This analysis leads to a universal scaling law for velocity fluctuations. Then we proceed to plasma turbulence in Section 2.2, in which we introduce magnetohydrodynamics (MHD) and present the most important MHD wave modes. We show that a dimensional analysis for MHD results in non-universal scalings and discuss several MHD turbulence theories, where we focus on critically balanced turbulence after *Goldreich and Sridhar* (1995). On scales smaller than typical MHD scales, kinetic effects change the turbulent cascade and different wave modes emerge. The critically balanced cascade is extended into the kinetic range and we shortly debate the ambiguity of dimensional analysis. Further, we discuss the dissipation range of the turbulent cascade and potential damping mechanisms. The applicability of the introduced turbulence theories is described at the end of this chapter in Section 2.3. Here, we present the solar wind observations that are most relevant for our further analysis of magnetic field fluctuations in Saturn's magnetosphere.

2.1 Hydrodynamic Turbulence

Turbulence is an ubiquitous phenomenon, which is observed in all kinds of fluids. It is characterized by an apparent chaotic flow on a wide range of scales. Observations of turbulent flow patterns date back to Leonardo da Vinci (1452-1519), who not only drew the turbulent flow of water with characteristic eddies, but also described the self-similarity of the vortices (see e.g. *Frisch*, 1995). Around three hundred years later, the now-called Navier-Stokes equation of motion was derived, which allows for a mathematical description of the phenomenon. Indeed,

the equations

$$\partial_t \mathbf{v} + (\mathbf{v} \cdot \nabla)\mathbf{v} = -\frac{1}{\varrho}\nabla p + \nu \Delta \mathbf{v} + \mathbf{f} \tag{2.1}$$

$$\nabla \cdot \mathbf{v} = 0 \tag{2.2}$$

probably describe everything we need to know about incompressible turbulence as long as we are not interested in quantum scales (*Frisch*, 1995). Theoretically, the problem is solved: We could insert the complete set of parameters for the fluid elements as there are velocity $\mathbf{v}$, density ϱ, pressure p, kinematic viscosity ν, and external force density $\mathbf{f}$ that may act on the fluid at an instant t_0 and calculate their dynamical evolution. Practically, however, this is impossible. Therefore, a statistical approach seems more promising to describe the mean properties of an ensemble of particles.

To quantify the turbulence of a flow, one can estimate the ratio of the non-linear term to the dissipation or viscous term in Equation (2.1), which is called the Reynolds number:

$$\mathrm{Re} \sim \frac{(\mathbf{v} \cdot \nabla)\mathbf{v}}{\nu \Delta \mathbf{v}} \sim \frac{vL}{\nu} \, . \tag{2.3}$$

Here, we used a dimensional analysis to derive the last term. In this context and throughout this thesis, '$\sim$' means 'on the same order of magnitude'. The parameter L comes from the gradient of the velocity and is a characteristic length of the system, on which a significant change in velocity is observed. It is usually interpreted as the scale on which energy is injected into the system. In the case of a fluid flowing past an obstacle, this so-called outer scale may be the diameter of the obstacle. For $\mathrm{Re} \ll 1$, we speak of a laminar flow, i.e., there is no turbulent mixing and neighboring stream lines stay next to each other at all times. At slightly higher Reynolds numbers $\mathrm{Re} \sim 10$, the flow begins to develop stationary eddies behind the obstacle and at even higher numbers, $\mathrm{Re} \sim 100$, the so-called Kármán vortex street emerges (*Frisch*, 1995). The Reynolds number that marks the transition from laminar to turbulent flow is called the critical Reynolds number, $\mathrm{Re}_{\mathrm{crit}}$. For Reynolds numbers $\mathrm{Re} \gg \mathrm{Re}_{\mathrm{crit}}$ the flow will evolve to fully developed turbulence, a term coined by Sir William Thomson, Lord Kelvin (*Thomson*, 1887). Figure 2.1 shows an example of such a hydrodynamic turbulent flow behind a grid.

2.1.1 Symmetries and Stationarity

From Figure 2.1 it is fairly clear that the motion of a *single* fluid particle behind the grid is chaotic and asymmetric and also differs at every location. However, if we look at the mean velocity fluctuations $\langle \mathbf{v}(\mathbf{r}, t) \rangle$, averaged over a sufficiently large region around location $\mathbf{r}$ or over a sufficiently large time interval around time t, we will find that the mean velocity of such a group of particles is independent of the location as long as it is far away from the grid and from the

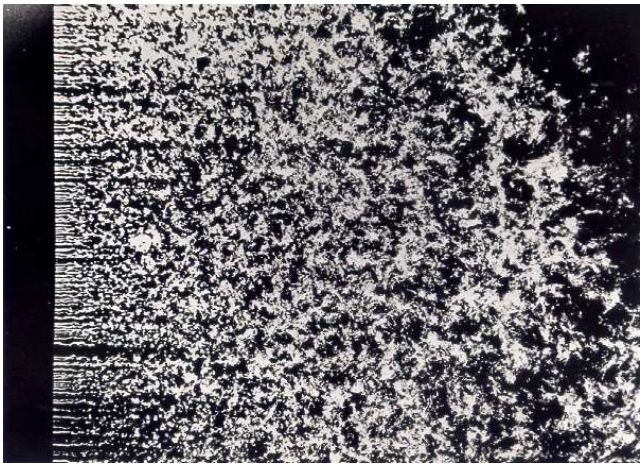

Figure 2.1: *Example of an homogeneous isotropic turbulent flow behind a grid (with permission of H. Nagib, FDRC-IIT).*

system's boundaries. Hence, in a statistical sense, the flow's velocity fluctuations are homogeneous in fully developed turbulence.

As long as we have a non-vanishing mean flow, $\mathbf{V} = \langle \mathbf{v}(\mathbf{r}, t) \rangle$, the flow has a preferred direction and the turbulence seems anisotropic. However, to describe the statistics of a fluid in the framework of turbulence, it is best to look at the fluctuations in the rest frame of the fluid. This perspective can be easily achieved as the governing Navier-Stokes Equation is invariant under Galileo transformations, $(\mathbf{r}', \mathbf{v}') \rightarrow (\mathbf{r}+\mathbf{V}\cdot t, \mathbf{v}+\mathbf{V})$. We can thus subtract any mean flow $\mathbf{V}$ and only consider the centered variable, $\mathbf{v}(\mathbf{r}, t) = \mathbf{v}'(\mathbf{r}, t) - \mathbf{V}$, which we call the fluctuation. Now, there is no preferred direction anymore and it can be shown that the fluctuations are in fact statistically isotropic. Therefore, it suffices to use a scalar value $v(\mathbf{r}, t)$ as random variable to describe the statistics without loss of information. If the rate of energy injected into the system is constant or, in the case of grid turbulence, if the incident fluid flow is constant, we can expect the turbulent motions behind the grid to be quasi-stationary in a statistical sense. This means that the statistical properties are also invariant under time translation and thus are constant in time. In a stationary, homogeneous and isotropic flow, we may therefore measure the velocity fluctuation $v(\mathbf{r}, t)$ at any location, time and in any direction without effect on the resulting statistics. According to *Frisch* (1995), we may write this as

$$v(\mathbf{r}, t) \overset{\text{law}}{=} v(\mathbf{r} + \mathbf{r}', t + t') \ , \tag{2.4}$$

which he calls equality in law. This means that the statistical properties of the variables on both sides of Equation (2.4) are the same.

However, in real measurements we usually obtain finite time series and, thus, we can only estimate the fluctuations' statistical moments. The shorter the time series, the larger is the error of such an estimation. The real statistics of a

random variable v is given by its probability density function (PDF) $p(v)$. The PDF defines the probability to measure a certain velocity v and contains all information on the statistical moments

$$\langle v^n \rangle = \int \mathrm{d}v \, v^n p(v) \tag{2.5}$$

of order n. The ergodicity theorem now states that the estimated time average of the fluctuating quantity v will be equal to the real ensemble average over the PDF if the time interval T is sufficiently large (*Frisch*, 1995)

$$\langle v^n \rangle = \int \mathrm{d}v \, v^n p(v) \approx \frac{1}{T} \int_0^T v^n \mathrm{d}t \ . \tag{2.6}$$

This result is an important basis for our further analysis. It shows that we can make assumptions about the statistics of the system under consideration based on finite time measurements. These measurements can be conducted at any time and location if the turbulence is fully developed, homogeneous, and stationary. It can be shown that the time interval T needed to correctly estimate the statistical moments $\langle v^n \rangle$, grows rapidly with order n (*Frisch*, 1995). The same holds for the corresponding sample size $N = T/\Delta t$ for a given time resolution Δt. This means that we need very long time series to resolve the tails of the PDF, which describe rare extreme events. We therefore restrict our later estimations to the normalized fourth order statistical moment, which is the flatness.

2.1.2 Kolmogorov Spectrum of Hydrodynamic Turbulence

In 1941, *A. N. Kolmogorov* published four papers on hydrodynamic turbulence, which can be seen as the beginning of modern turbulence research (*Kolmogorov*, 1941a,b,c,d). A major contribution of his work was the derivation of the famous four-fifths law (*Kolmogorov*, 1941c), which is a mathematically exact result and describes the dissipation of energy. However, we restrict ourselves to a phenomenological derivation. For a detailed review of *Kolmogorov's* theory, we refer the reader to the book *Turbulence* by *Frisch*.

If energy is injected into a system on a length scale L, eddies of diameter $d \sim L$ will be generated, which have a typical velocity fluctuation v_L. Here, $v_L \sim \sqrt{\langle \delta v^2 \rangle}$ is the root-mean-square (RMS) of the velocity fluctuations' increment,

$$\delta v(r, L) = v(r + L) - v(r) \ , \tag{2.7}$$

and can be thought of as the average velocity difference on the corresponding scale L. The eddies will nonlinearly interact with each other and decay to form smaller eddies on a scale $\ell < L$ with mean velocity difference v_ℓ on scale ℓ. The time, in which an eddy of size ℓ is significantly distorted, is denoted by the

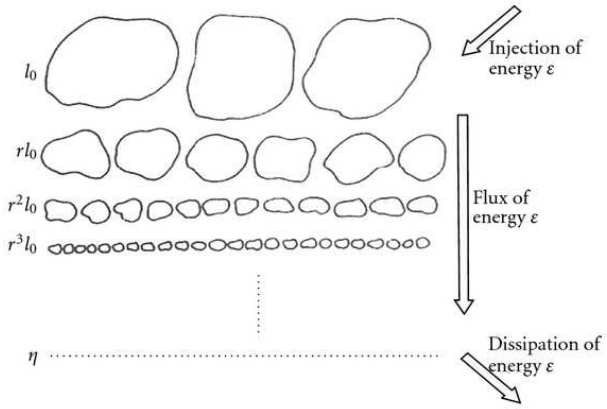

Figure 2.2: *Richardson cascade of hydrodynamic turbulence (Frisch, 1995).*

characteristic nonlinear time

$$\tau_{\mathrm{nl}} \sim \frac{\ell}{v_\ell} \ . \tag{2.8}$$

It is also called eddy-turnover time. The smaller eddies may fill the whole system space, so that despite of less kinetic energy per eddy, v_ℓ^2, the total energy flux is conserved. This decay will go on to smaller scales until a dissipation scale η_d is reached, where the fluctuations' energy is converted into heat. This evolution is pictured in the so-called Richardson cascade, which is schematically shown in Figure 2.2. Here, we separate the cascade into three regions: (1) the energy injection range on scales $\ell \sim L$, (2) the inertial range on scales ℓ, where $L \gg \ell \gg \eta_d$, and (3) the dissipation range on scales $\ell \sim \eta_d$. In hydrodynamic turbulence, the inertial and dissipation ranges, where the energy is nonlinearly transported from large to small scales and finally dissipated as heat, behave in a universal way independent of the type of fluid.

In a stationary turbulent cascade, the energy injection rate is equal to the dissipation rate. As a result, the kinetic energy $E \sim v_L^2$ of the largest eddies on scale L per unit time is also equal to the energy flux through scale ℓ

$$\dot{E} \sim \frac{v_\ell^2}{\tau_{\mathrm{tr}}} \sim \epsilon \ , \tag{2.9}$$

where ϵ denotes the dissipation rate. In the inertial range, the energy is transferred to smaller scales within a characteristic transfer time $\tau_{\mathrm{tr}} = \tau_{\mathrm{tr}}(\ell)$, which is a function of scale ℓ. In hydrodynamics, the transfer time is equal to the nonlinear or eddy-turnover time $\tau_{\mathrm{tr}} \sim \tau_{\mathrm{nl}}$. Inserting this relation in Equation (2.9) leads to

$$\epsilon \sim \frac{v_\ell^3}{\ell} \quad \Leftrightarrow \quad v_\ell \sim (\epsilon\ell)^{1/3} \ , \tag{2.10}$$

which we can use to estimate the one-dimensional energy or power spectrum $E_k = E_k(k)$ as a function of wave number $k \sim \ell^{-1}$. The energy spectrum is related to the total energy by $v_\ell^2 \sim E_k\, k$ and can be written as

$$E_k \sim v_\ell^2\, k^{-1} \sim \epsilon^{2/3} k^{-5/3} \ . \tag{2.11}$$

Equation (2.11) determines the Kolmogorov spectrum and shows that the power spectra $P(k)$ in the inertial range follow a power-law $k^{-\kappa}$ with spectral index $\kappa = 5/3$. This is experimentally verified for various fluids (e.g. *Gibson and Schwarz*, 1963). The inertial range reaches to the so-called Kolmogorov dissipation scale

$$\eta_d \sim \left(\frac{\nu^3}{\epsilon}\right)^{1/4} \ . \tag{2.12}$$

Here, dissipation caused by particle collisions sets in and ultimately leads to heating of the fluid (*Kolmogorov*, 1941a; *Frisch*, 1995). It is interesting to note, that the dissipation scale does not depend on the energy injection mechanism.

2.1.3 Intermittency

The Richardson cascade as shown in Figure 2.2, consists of eddies that decay to smaller self-similar eddies, which fill the whole space. This is also a crucial point in the hypotheses leading to the derivation of Kolmogorov's four-fifths law (*Frisch*, 1995, Ch. 6). Space filling eddies lead to a turbulent signal that shows consistent statistical properties at all times and at all scales according to

$$\delta v(r, \lambda\ell) \overset{\text{law}}{=} \lambda^h \delta v(r, \ell) \ . \tag{2.13}$$

Therefore, the statistics are scale invariant under an associated transformation. Kolmogorov suggested that the scaling exponent $h = 1/3$ is unique and universal for all kinds of fluids. However, *Batchelor and Townsend* (1949) discovered that the signal at wave numbers close to the dissipation scale gets increasingly bursty. These extreme events happen only at a fraction of the time while the flow seemed inactive during the rest of the time. Such a behavior violates Equation (2.13) and a function displaying this characteristic is said to be intermittent (*Frisch*, 1995; *Wan et al.*, 2012).

To measure the intermittency, one often uses so-called structure functions,

$$S_n(\ell) \equiv \langle (v(r+\ell) - v(r))^n \rangle = \langle \delta v(r, \ell)^n \rangle \ , \tag{2.14}$$

which can be estimated with the help of increments. The variable n defines the order of the structure function. In the following, we drop the dependence on location r assuming that the average is taken over a large enough area or time to assume homogeneity. The structure functions are known to follow power-laws in the inertial range, $S_n(\tau) \propto \tau^{\xi(n)}$, where $\xi(n)$ is called scaling exponent (*Frisch*, 1995). For self-similar fluctuations, the scaling exponent varies with

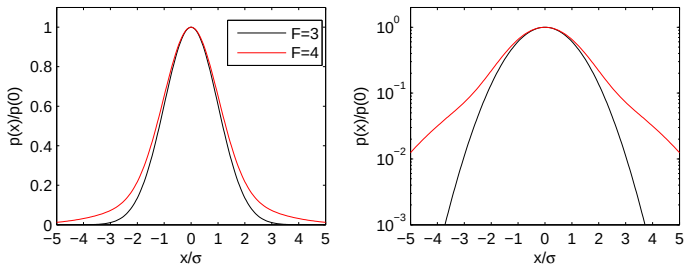

Figure 2.3: *Probability density function $p(x)$ of a normal distributed centered variable x (Gaussian, black line) with flatness $F = 3$ and near-Gaussian PDF with increased tails and flatness $F = 4$ (red line). Both PDF are normed at $x = 0$ and normalized by their standard deviation σ. The left panel shows a linear plot while the right panel shows the same plot with logarithmic y-axis. Here, the increased tails are much clearer.*

order n as $\xi(n) = h \cdot n$, where h is the Hurst exponent (e.g. *Carbone et al.*, 1995; *Kiyani et al.*, 2009; *Salem et al.*, 2009; *Mangeney*, 2012). Deviation from this simple linear law is generally called multifractality. Indeed, a straight forward application of Equation (2.13) with $h = 1/3$ to the structure functions yields $S_n(\ell) \propto \ell^{n/3}$. Yet, measurements have shown that the scaling exponent of the structure functions is not linear in n but rather a nonlinear function ξ_n (see e.g. *Burlaga*, 1992; *Sorriso-Valvo et al.*, 2001; *Kiyani et al.*, 2009; *Salem et al.*, 2009, for measurements in the solar wind). We may therefore write

$$S_n(\ell) \propto \ell^{\xi_n} \ . \tag{2.15}$$

Physically, this may be understood as a correction to the Richardson cascade. Wind tunnel measurements conducted by *Argoul et al.* (1989) indicate that a large scale eddy may decay asymmetrically into two smaller eddies of different energies. If this asymmetric decay is repeated across all scales, energetic fluctuations will concentrate in certain locations forming intermittent or bursty signals. This process might further be scale dependent, which is then equivalent to a multifractal formalism (*Meneveau and Sreenivasan*, 1991; *Burlaga*, 1992; *Muzy et al.*, 1993; *Kiyani et al.*, 2013).

At this point it is instructive to envision the probability density function $p(\delta v)$ of the random variable δv as it is shown in Figure 2.3. If the random variable is normal and centered, its PDF will be a Gaussian as shown by the black line. On the other hand, if extreme events are more likely to happen, which is the case for intermittent signals, the so-called tails of the probability density function will be increased. This is shown by the red line in Figure 2.3. This feature is much easier to detect when the y-axis is scaled logarithmically as shown in the right panel. The increase of the tails can be quantified by the

normalized fourth order statistic moment or flatness of the centered variable δv

$$F = \frac{\langle \delta v^4 \rangle}{\langle \delta v^2 \rangle} \ , \tag{2.16}$$

which is a function of scale ℓ. A normal distribution yields a flatness of $F = 3$. A larger flatness, $F > 3$, means that the tails are enhanced and therefore extreme events are observed more often. The flatness can also be expressed in terms of structure functions

$$F(\ell) = \frac{S_4}{S_2^2} \propto \ell^{\xi_4 - 2\xi_2} \ . \tag{2.17}$$

This shows that the flatness for strictly self-similar decay is constant at all scales, because the exponent vanishes for a function ξ_n that is linear in n. The flatness can thus be used to estimate if the scaling exponent is nonlinear. Indeed, turbulence measurements in the solar wind and planetary magnetospheres have shown that the flatness of magnetic field fluctuations increases as a power-law for decreasing scales, which is in accordance with intermittent fluctuations (*Bruno et al.*, 2003; *Vörös et al.*, 2002; *Alexandrova et al.*, 2008a) and implies the formation of coherent structures (*Mangeney*, 2012). This method has the advantage of measuring only moments of fourth order instead of several higher order structure functions, which would be needed to verify the nonlinearity of $\xi(n)$. However, in order to reliably measure the higher order structure functions, one needs an increasing amount of data. This means, that if we estimate the intermittency with the scale dependent flatness $F(\ell)$, we can use shorter time intervals for our analysis.

2.2 Plasma Turbulence

So far, we have described the principles of hydrodynamic turbulence, where the energy is transferred to smaller scales by interaction of structures such as eddies. But what happens if we consider a plasma? Plasma is a quasi-neutral ensemble of ions and electrons and therefore it is subject to electromagnetic forces

$$\mathbf{F} = q_s(\mathbf{E} + \mathbf{v_s} \times \mathbf{B}) \ , \tag{2.18}$$

where q_s is the charge of particle s, $\mathbf{E}$ the electric field, $\mathbf{v}_s$ the mean velocity of particle s and $\mathbf{B}$ the magnetic field. If we add this force to Equation (2.1), we will get two equations of motion: one for ions with number density n_i and one for electrons with number density n_e. Adding the two equations for an inviscid plasma ($\nu = 0$) and using quasi-neutrality, $n_i \approx n_e$, we can derive the magnetohydrodynamic (MHD) equation of motion

$$\varrho \left(\partial_t \mathbf{v} + (\mathbf{v} \cdot \nabla)\mathbf{v}\right) = -\nabla p + \mathbf{j} \times \mathbf{B} \ . \tag{2.19}$$

In MHD, the plasma is treated as a fluid. This treatment is valid for scales much larger than the ion gyro radius

$$\rho_i = \frac{\sqrt{2 m_i k_B T_{i,\perp}}}{e B_0} \tag{2.20}$$

with ion mass m_i, Boltzmann constant k_B, perpendicular ion temperature $T_{i,\perp}$, elementary charge e and background magnetic field B_0. The frequencies under consideration in MHD must be much lower than the ion cyclotron frequency

$$\Omega_{\mathrm{ic}} = \frac{e B_0}{m_i} \ , \tag{2.21}$$

Using Ampére's law, where displacement currents can be neglected because of the low-frequency approximation, the Lorenz force term can be written as

$$\mathbf{j} \times \mathbf{B} = -\nabla p_B + \frac{1}{\mu_0} (\mathbf{B} \cdot \nabla) \mathbf{B} \ . \tag{2.22}$$

Here, $p_B = B^2/(2\mu_0)$ describes the magnetic pressure and the second term on the right hand side of Equation (2.22) describes the magnetic convection. For a complete description of the fluid motion of the plasma on MHD scales, we further need the induction equation

$$\partial_t \mathbf{B} = -\nabla \times \mathbf{E} \tag{2.23}$$

and the generalized Ohm's law

$$\mathbf{E} + \mathbf{v} \times \mathbf{B} = \eta \mathbf{j} \ , \tag{2.24}$$

where $\eta = (\mu\sigma)^{-1}$ is the magnetic diffusivity that depends on the magnetic permeability μ and the electric conductivity σ of the plasma. For the derivation of Equation (2.24), we have further dropped the terms describing anisotropic electron pressure, electron inertia and the Hall term (*Baumjohann and Treumann*, 1997, Eq. 7.53). For the plasmas considered in this thesis, the conductivities are very high, so that we may simplify Equation (2.24) to $\mathbf{E} = -\mathbf{v} \times \mathbf{B}$. This means that the plasma is frozen-in to the magnetic field lines and if we insert this relation into Equation (2.23), we will see that

$$\partial_t \mathbf{B} = \nabla \times (\mathbf{v} \times \mathbf{B}) \ . \tag{2.25}$$

If the frozen-in theorem applies, we may identify velocity and magnetic field fluctuations: $\delta v \sim \delta b$.

With the help of Elsässer's variables $\mathbf{z}^{\pm} = \mathbf{v} \pm \mathbf{B}/(\mu_0 \varrho)$, one can simplify Equations (2.19) and (2.25) into a form similar to the Navier-Stokes equation (*Elsässer*, 1950). While any mean velocity $\mathbf{V}$ can be subtracted with Galileo transformations, this is not possible for a mean magnetic field $\mathbf{B}_0 = \langle \mathbf{B} \rangle$. There-

fore, we can transform into the rest frame of the plasma and use $\mathbf{z}^{\pm} = \pm\mathbf{V}_{\mathrm{A}} + \delta\mathbf{z}^{\pm}$ with the Alfvén velocity $\mathbf{V}_{\mathrm{A}} = \mathbf{B}_0/(\mu_0\varrho)$ and the fluctuation field $\langle\delta\mathbf{z}^{\pm}\rangle = 0$. Consequently, Equations (2.19) and (2.25) can be written together as

$$\left(\partial_t \pm V_{\mathrm{A}}\partial_{\parallel}\right)\delta\mathbf{z}^{\pm} + \delta\mathbf{z}^{\mp}\nabla\delta\mathbf{z}^{\pm} = -\varrho^{-1}\nabla p_T \ , \tag{2.26}$$

where the differentiation $\partial_{\parallel}$ is parallel to the background magnetic field $\mathbf{B}_0$, $p_T = p + p_B$ is the total pressure and we used both $\nabla\cdot\mathbf{v} = 0$ and $\nabla\cdot\mathbf{B} = 0$. It is illustrative to write the MHD equations with Elsässer's variables because it reduces the MHD equations to a set of equations that look almost identical to the Navier-Stokes equation. This implies that we may use a similar dimensional derivation for plasma turbulence to the one we applied for hydrodynamic turbulence.

2.2.1 MHD Waves

One important difference between HD and MHD turbulence is the influence of waves on the turbulent cascade, which can be neglected for hydrodynamic turbulence. Although HD waves play an important role in weak or wave turbulence (see, e.g., *Nazarenko*, 2011), they are only a minor contributor to the strong HD turbulence described in Section 2.1.2. This is because the energy in strong HD turbulence is cascaded by eddies and not weakly interacting waves. However, waves play an important role for the turbulent cascade in plasmas. We will show in this section, what kind of waves are obtained from the MHD equations, i.e., Equations (2.19) and (2.23), and discuss their importance for the cascading process. For a detailed derivation of the MHD dispersion relation the reader is referred to *Baumjohann and Treumann* (1997, Ch. 9.4).

Alfvén Waves

The linearized MHD equations combined with the continuity equation and the assumption of adiabatic pressure fluctuations can be solved by transverse Alfvén waves, whose dispersion relation is given by

$$\omega = \pm k_{\parallel} V_{\mathrm{A}} \ . \tag{2.27}$$

The group velocity of Alfvén waves is the Alfvén velocity V_{A}, which is strictly parallel or antiparallel to the magnetic field and describes the propagation of a wave packet. The wave fronts, on the other hand, travel in oblique angles to the magnetic field with phase velocity

$$v_{\mathrm{ph,A}} = \omega/k = V_{\mathrm{A}}\cos\theta_{kB} \ . \tag{2.28}$$

Here, θ_{kB} is the angle between wave vector $\mathbf{k}$ and background magnetic field $\mathbf{B}_0$. The Alfvén wave is a purely transverse wave and most of the plasma fluctuations in the solar wind on MHD scales are observed to be of Alfvénic nature (*Belcher*

and Davis, 1971; *Matthaeus and Goldstein*, 1982; *Tu et al.*, 1984). The nonlinearly interacting fluctuations of Alfvén waves are thus the main contributor to the turbulent cascade.

Note, that Equation (2.27) can also be obtained from the linearized Equation (2.26), resulting in Alfvén waves $\delta\mathbf{z}^+$ and $\delta\mathbf{z}^-$ traveling along and antiparallel to the background magnetic field $\mathbf{B}_0$, respectively (see also *Sridhar*, 2011). Here, the structure of the nonlinear term, $\delta\mathbf{z}^{\mp}\nabla\delta\mathbf{z}^{\pm}$, shows an inherent property of Alfvénic turbulence: if there are only Alfvén waves propagating in one direction, e.g., $\delta\mathbf{z}^+ \neq 0$ and $\delta\mathbf{z}^- = 0$, the nonlinear term will vanish. This means, that only Alfvén waves propagating in opposite direction can nonlinearly interact with each other.

Compressible Modes

In the compressible case, two additional MHD waves arise, the fast and slow mode. The fast mode, where velocity and density fluctuations are positively correlated, is supposed to be decoupled from the turbulent cascade (*Lithwick and Goldreich*, 2001; *Cho and Lazarian*, 2005). Measurements in the solar wind suggest that fast modes are only a minor constituent of the fluctuations (*Howes et al.*, 2012; *Klein et al.*, 2012; *TenBarge et al.*, 2012). Further, fast modes are expected to be strongly damped in high β plasmas, where $\beta = p/p_B$ is the ratio of plasma to magnetic pressure, and dissipated after they steepen into shocks (*Schekochihin et al.*, 2009).

The slow mode seems to be more interesting for the turbulent cascade. It is estimated that around 10% of the fluctuations in the solar wind are caused by the pressure-balanced slow mode, i.e., the compressible component in the solar wind is almost entirely generated by the slow mode (*Howes et al.*, 2012; *Klein et al.*, 2012; *TenBarge et al.*, 2012). The slow modes are also decoupled from the Alfvénic cascade, but their damping rate is proportional to $k_\parallel$, which - for wave vectors $k_\perp \gg k_\parallel$ - is slow enough to allow for passive mixing by Alfvénic fluctuations (*Howes et al.*, 2006). Here, $k_\perp$ and $k_\parallel$ are the wave vectors perpendicular and parallel to the background magnetic field $\mathbf{B}_0$. Therefore, although they do not develop a cascade on their own, compressible fluctuations are assumed to have a similar scaling as the purely transverse Alfvénic turbulent cascade (*Lithwick and Goldreich*, 2001; *Schekochihin et al.*, 2009). However, recent observations show that this is not entirely true (*Forman et al.*, 2011; *Wicks et al.*, 2012).

Non-linear Alfvén Wave Collisions

As can be seen from Equation (2.26), only counter-propagating Alfvén waves interact which each other. In a purely linear framework, which we adapted for the derivation of the MHD waves, wave fronts do not interact at all. They may interfere positively or negatively, but there is no energy transfer between the waves. Wave-wave interactions are therefore nonlinear interactions and these

nonlinear interactions are responsible for the energy transfer from large to small scales. Despite of the importance for the turbulent cascade, it is not well known what actually happens during a nonlinear collision of wave fronts.

Howes and Nielson (2013) analyzed the collision of Alfvén waves in weak turbulence and could show that two counter propagating primary waves with the same frequency ω_1 and wave vectors $\mathbf{k}_1^+$ and $\mathbf{k}_1^-$ first undergo a non resonant three wave interaction satisfying

$$\mathbf{k}_1^+ + \mathbf{k}_1^- = \mathbf{k}_2 \qquad \text{and} \qquad \omega_1 + \omega_1 = \omega_2 \ , \tag{2.29}$$

thus forming a secondary wave with wave vector $\mathbf{k}_2$ and frequency ω_2. As the dispersion relation for Alfvén waves is $\omega = |k_\parallel| v_\mathrm{A}$ and as only counter-propagating waves can interact, the Equations (2.29) necessarily lead to $k_{\parallel 2} = 0$. This means that the secondary wave is not an Alfvén wave but a purely nonlinear wave. Figure 2.4 shows schematically, where the involved waves are located in wave vector space. The two primary counter-propagating waves with wave vectors $k_1^\pm$, denoted by the red circles, interact nonlinearly to form the secondary wave with wave vector k_2 (green triangle). After *Howes and Nielson* (2013), this intrinsically nonlinear secondary wave further interacts with each primary wave, which effectively transfers energy to tertiary waves with frequency $\omega_3 = \omega_1$ and wave vectors $k_3^\pm$ (blue squares). During these interactions energy is cascaded in perpendicular direction only, i.e., the tertiary waves have the same parallel wave number as the primary waves $k_{\parallel 1}^\pm = k_{\parallel 3}^\pm$. This result has been numerically validated in *Nielson et al.* (2013) and indicates that the turbulent cascading process is predominantly perpendicular to the background magnetic field.

2.2.2 Weak Isotropic Alfvén Wave Turbulence

The idea that Alfvén waves take the role of the nonlinearly interacting eddies in plasma turbulence led *Iroshnikov* (1964) and *Kraichnan* (1965) (IK) to the derivation of a phenomenological spectrum based on the linear wave period of Alfvén waves. Due to the weak interaction of these linear waves, the theory describes weak or wave turbulence. They defined a new interaction time, the Alfvén time

$$\tau_\mathrm{A} \sim (k V_\mathrm{A})^{-1} \ . \tag{2.30}$$

The fluctuations are expressed as magnetic fluctuations δb and the plasma is frozen-in to the magnetic field. The emergence of another characteristic time necessarily leads to ambiguity in the phenomenological derivation, which we discuss in more detail in Section 2.2.7. It is important to note here, that despite of the presence of a background magnetic field $\mathbf{B}_0$ *Iroshnikov* and *Kraichnan* assumed isotropic interactions - a fact for which this theory is often criticized (*Montgomery and Turner*, 1981; *Sridhar and Goldreich*, 1994).

The Alfvén time can be interpreted as the duration of the interaction of two Alfvén waves of comparable wave length $\ell \sim k^{-1}$, which is much smaller than the nonlinear time $\tau_\mathrm{A} \ll \tau_\mathrm{nl}$. This means that during an interaction of two Alfvén

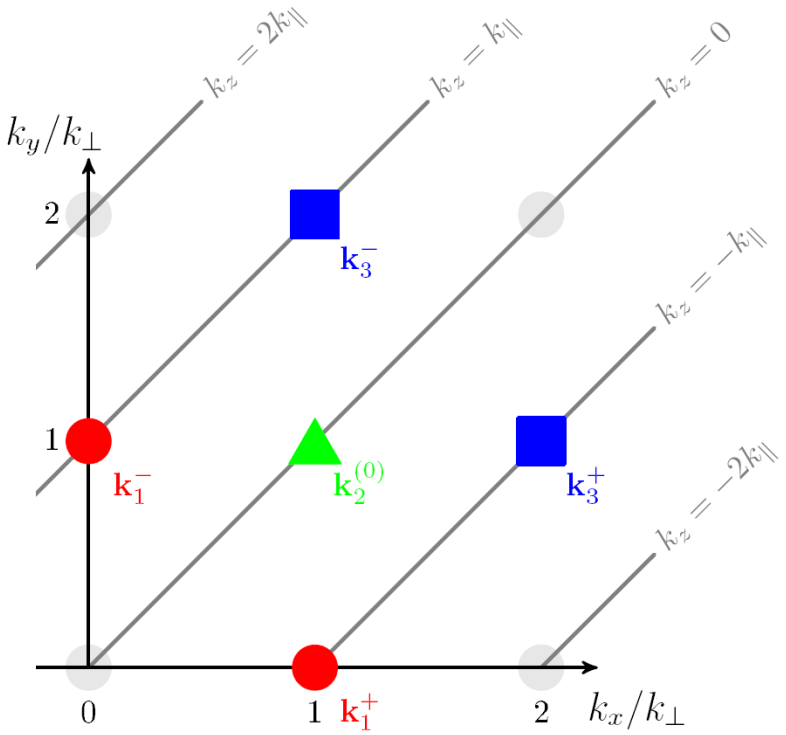

Figure 2.4: *Nonlinear interactions during a collision of two primary Alfvén waves with wave vectors $k_1^\pm$ (red circles) in a plane perpendicular to the background magnetic field. The parallel wave number is given in gray. The two counter-propagating primary waves interact to form a purely nonlinear secondary wave with wave vector k_2 (green triangle). This secondary wave then interacts with the primary waves to form the tertiary waves with wave vectors $k_3^\pm$ (blue squares). Figure from (Howes and Nielson, 2013)*

wave packets only a small amount of energy can be exchanged:

$$\delta E \sim \delta b^2 \frac{\tau_\mathrm{A}}{\tau_\mathrm{nl}} \,. \tag{2.31}$$

Therefore, multiple interactions are needed to exchange energy of order unity. These interactions are randomly phased, so that $N \sim \tau_\mathrm{nl}/\tau_\mathrm{A}$ interactions transfer only an amount of energy $\sqrt{N}\,\delta E$. This means a total amount of N^2 interactions are needed to transfer energy of order unity. This leads to a transfer time given by

$$\tau_\mathrm{tr} \sim N^2 \tau_\mathrm{A} \sim \frac{\tau_\mathrm{nl}^2}{\tau_\mathrm{A}} \,, \tag{2.32}$$

which can be interpreted in the sense that the energy transfer rate controlled by weak Alfvénic interactions is slower than in the hydrodynamic case. Using this

transfer time in Equation (2.9) results in

$$\epsilon \sim \frac{\delta b^2 \tau_\mathrm{A}}{\tau_\mathrm{nl}^2} \quad \Leftrightarrow \quad \delta b \sim V_\mathrm{A} \left(\epsilon \ell\right)^{1/4} \ , \tag{2.33}$$

which further leads to the so-called IK spectrum of isotropic Alfvén turbulence

$$E_k \sim \delta b^2 k^{-1} \sim V_\mathrm{A}^2 \epsilon^{1/2} k^{-3/2} \ . \tag{2.34}$$

The IK spectrum has a spectral index of 3/2 and is thus less steep than the Kolmogorov spectrum. However, it is not always possible to clearly distinguish between Kolmogorov and IK spectral scaling due to measurement uncertainties (*Bruno and Carbone*, 2005; *Podesta*, 2009).

2.2.3 Weak Anisotropic Alfvén Wave Turbulence

There is an apparent contradiction between the isotropic phenomenology of the IK spectrum and the anisotropic nature of plasma turbulence. Due to the preferred direction defined by the background magnetic field and the symmetry of Equation (2.26), the turbulence is expected to be axisymmetric with regards to the magnetic field. This assumption is backed by several observations in the solar wind (*Matthaeus et al.*, 1990; *Bieber et al.*, 1996; *Horbury et al.*, 2008; *Turner et al.*, 2011; *Wicks et al.*, 2012), some of which we also discuss at the end of this chapter in Section 2.3. Therefore, theories for weak Alfvénic turbulence were developed that take into account the probable axisymmetry of the problem (*Montgomery and Turner*, 1981). In this section, we present the anisotropic expansion of the IK theory in the presence of a strong background magnetic field $\mathbf{B}_0$ (*Sridhar and Goldreich*, 1994; *Goldreich and Sridhar*, 1997; *Ng and Bhattacharjee*, 1997). The scalings can be derived by dimensional analysis under assumption of two different scales along ($\ell_\parallel \sim k_\parallel^{-1}$) and perpendicular ($\ell_\perp \sim k_\perp^{-1}$) to the background magnetic field.

Let us assume an anisotropic Alfvén wave packet with characteristic sizes $k_\perp^{-1}$ and $k_\parallel^{-1}$ perpendicular and along the magnetic field, respectively. We may write the linear Alfvén wave period as $\tau_\mathrm{A} \sim (k_\parallel V_\mathrm{A})^{-1}$ and the nonlinear time as $\tau_\mathrm{nl} \sim (k_\perp \delta b)^{-1}$. Here, $\delta b = \delta B / \sqrt{\mu_0 \varrho}$ is the magnetic fluctuation or RMS, δB, in velocity units. Note, that from dimensional considerations the nonlinear time is not unique if we assume different scales $k_\perp^{-1}$ and $k_\parallel^{-1}$ to be present (see also Section 2.2.7). Inserting these times in Equation (2.33) results in

$$\delta b \sim (\epsilon k_\parallel V_\mathrm{A})^{1/4} k_\perp^{-1/2} \ . \tag{2.35}$$

As the turbulence cascades in perpendicular direction we look at the energy given by $E \sim E_\perp k_\perp$ which leads to a spectrum

$$E_\perp \sim \sqrt{\epsilon k_\parallel V_\mathrm{A}}\, k_\perp^{-2} \tag{2.36}$$

with spectral index $\kappa = 2$. *Galtier et al.* (2000) note that there is no energy transfer between planes of different $k_\parallel$ for weak turbulence. Hence, the energy in each plane is preserved and cascades perpendicular to the background field only. This has been shown using a system of kinetic equations, which could be closed under the assumption of randomly phased Alfvén waves (*Galtier et al.*, 2000). A weak anisotropic turbulent cascade according to Equation (2.36) has been observed in Jupiter's magnetosphere by *Saur et al.* (2002), where the condition $\tau_\mathrm{A} \ll \tau_\mathrm{nl}$ was experimentally verified.

2.2.4 Critically Balanced Turbulence

Observations of fluctuations in the interstellar medium indicate a Kolmogorov scaling of 5/3 and fail to comply with the IK spectrum (see *Sridhar and Goldreich*, 1994; *Armstrong and Rickett*, 1995, and references therein). However, due to its hydrodynamic nature the Kolmogorov theory of strong turbulence cannot describe plasma turbulence correctly. As weak turbulence after IK was neither in accordance with observations nor did it respect the inherent anisotropy of plasma turbulence, *Goldreich and Sridhar* (1995) developed a theory of strong plasma turbulence taking into account the background magnetic field. They deduced a critically balanced turbulence based on the thoughts of *Higdon* (1984). Here, the Alfvénic fluctuations δb interact perpendicular to the background magnetic field like eddies with the nonlinear time

$$\tau_\mathrm{nl} \sim (k_\perp \delta b)^{-1} \ . \tag{2.37}$$

Parallel to the magnetic field, the characteristic time scale for interactions between wave packets is assumed to be the linear Alfvén wave period

$$\tau_\mathrm{A} \sim (k_\parallel V_\mathrm{A})^{-1} \ . \tag{2.38}$$

Goldreich and Sridhar (1995) assume that these two characteristic times are critically balanced:

$$\tau_\mathrm{nl} \sim \tau_\mathrm{A} \quad \Leftrightarrow \quad k_\perp \delta b \sim k_\parallel V_\mathrm{A} \ . \tag{2.39}$$

Due to the equality of the nonlinear (eddy turnover) and linear (Alfvén) time scales, the turbulence described by critical balance is strong. The linear term in Equation (2.26) is now of comparable size as the nonlinear term and we may use both characteristic times τ_nl and τ_A as transfer time. This generates two equations for δb, namely

$$\epsilon \sim \delta b^2 (k_\perp \delta b) \qquad \Leftrightarrow \quad \delta b \sim \epsilon^{1/3} k_\perp^{-1/3} \tag{2.40}$$

$$\epsilon \sim \delta b^2 (k_\parallel V_\mathrm{A}) \qquad \Leftrightarrow \quad \delta b \sim \epsilon^{1/2} V_\mathrm{A}^{-1/2} k_\parallel^{-1} \ . \tag{2.41}$$

These equations lead to different scalings if fluctuations are measured along or perpendicular to the magnetic field:

$$E_\perp \sim \frac{\delta b^2}{k_\perp} \sim \epsilon^{2/3} k_\perp^{-5/3} \quad \text{and} \quad E_\parallel \sim \frac{\delta b^2}{k_\parallel} \sim V_\mathrm{A}^{-1} \epsilon k_\parallel^{-2} \ . \tag{2.42}$$

In the perpendicular case, we thus observe a power spectrum with a spectral index of 5/3, similar to the Kolmogorov scaling. In the parallel direction, on the other hand, the energy is cascaded differently. Here, a steeper spectrum with spectral index 2 is expected and the cascade is controlled by the characteristic Alfvén time τ_A. It is generally not possible to determine the orientation of the fluctuations with respect to the background magnetic field because it requires information on the underlying wave vector directions. However, in case Taylor's hypothesis is valid, we may estimate the direction with the field-to-flow angle θ, which is the angle between background magnetic field and the direction of plasma flow (*Mangeney et al.*, 2006; *Bourouaine et al.*, 2012; *Howes et al.*, 2014a). In Section 3.3.4, we further elaborate on this consideration for the case of Saturn's magnetosphere.

In the turbulence theories discussed so far, we have neglected the outer scale L, on which energy is injected into the system. However, for a critically balanced cascade, this outer scale is important because it determines the energy distribution in wave vector space. At the outer scale L, the energy is assumed to be isotropically injected, so that the fluctuation amplitude on this scale can be written as $\delta b \sim V_\mathrm{A}$. Using the right hand side of Equation (2.42) this leads to

$$V_\mathrm{A}^2 \sim \epsilon \frac{L}{V_\mathrm{A}} \quad \Leftrightarrow \quad \epsilon \sim \frac{V_\mathrm{A}^3}{L} \ . \tag{2.43}$$

Inserting this in equations Equation (2.40) and Equation (2.41), we can derive a relation between parallel and perpendicular scales

$$k_\parallel \sim L^{-1/3} k_\perp^{2/3} \ , \tag{2.44}$$

which was also found by *Higdon* (1984). This relation is schematically shown in Figure 2.5 and basically shows that the cascade is preferentially in perpendicular direction: The eddies/waves will decay in such a way, that this relation is fulfilled. In the case of eddies, this leads to an elongation along the magnetic field as $\ell_\parallel \gg \ell_\perp$.

It is a matter of debate if the energy in **k**-space is distributed along the path given by Equation (2.44) or if this relation only gives an upper boundary for $k_\parallel$. In the original paper of *Goldreich and Sridhar* (1995), the latter is not excluded. *Oughton et al.* (2004) describe all modes with $k_\parallel V_\mathrm{A} \leq k_\perp \delta b$ as hydrolike and explicitly allow standing, non-propagating modes with $k_\parallel = 0$ noting that it is not useful to think of these modes as wave-like. In contrast, *Schekochihin et al.* (2009) doubt that a state with $k_\parallel V_\mathrm{A} \ll k_\perp \delta b$ can exist. They argue as

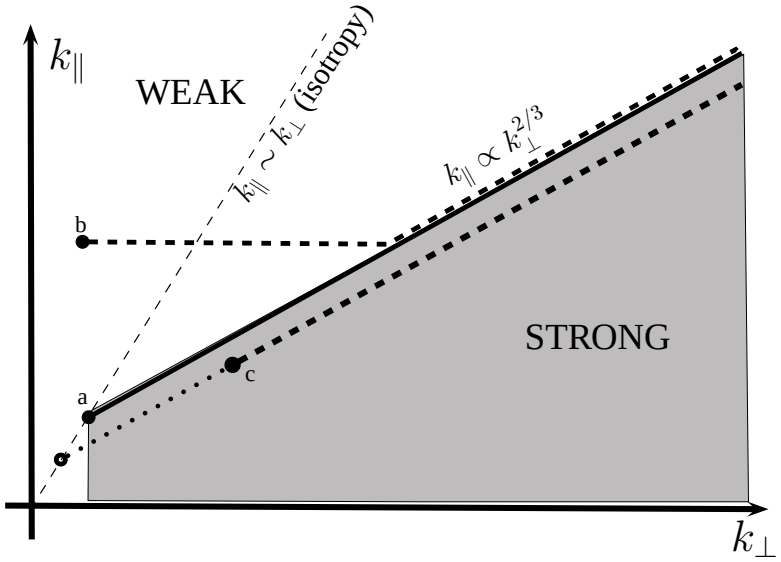

Figure 2.5: *Schematic of different paths of a critically balanced cascade in a double logarithmic plot of k-space with most energy residing in gray shaded area, where turbulence is strong. a) Strong isotropic energy injection, b) Weak energy injection, c) Anisotropic energy injection. The filled circles show location of energy injection. In case of c, the outer scale can be defined at location of empty circle, where critical balance path reaches isotropy.*

follows: Given two planes perpendicular to the background field $\mathbf{B}_0$ separated by a distance $\ell_\parallel$. Fluctuations in these two planes can only stay correlated, if an Alfvén wave can propagate between the two planes in less than the decorrelation time τ_c. This leads to the relation

$$\begin{aligned} \tau_c \sim \frac{\lambda_c}{\delta b} &> \frac{\ell_\parallel}{V_\mathrm{A}} \sim \tau_\mathrm{A} \\ \Leftrightarrow \quad k_\parallel &> \frac{\delta b}{V_\mathrm{A}\lambda_c} \ , \end{aligned} \tag{2.45}$$

where we used the correlation length λ_c. Equation (2.45) gives a minimal boundary to $k_\parallel \sim \ell_\parallel^{-1}$ under the assumption that Alfvén waves control the energy transfer parallel to the background magnetic field. In the schematic of Figure 2.5 we thus pictured the energy containing range in gray with a lower limit.

The outer scale L defined in Equation (2.43) is the scale where isotropic energy injection occurs. If the excitation is initially strong, the critical balance will be reached from the beginning (path a in Figure 2.5). However, even if the energy injection is weak, the cascade will eventually reach the critically balanced state given by Equation (2.44). This is because for weak turbulence, the energy cascades entirely in perpendicular direction, i.e., $k_\perp$ increases while $k_\parallel$ remains constant (*Galtier et al.*, 2000) (path b in Figure 2.5). In case of anisotropic or

weak energy injection, the outer scale L can be defined as the scale, where the path of critical balance reaches an isotropic state $E_\perp \sim E_\parallel$ (*Howes et al.*, 2008). Such a cascade is shown by path c in Figure 2.5, where the energy injection actually happens at the location of the filled circle but the outer scale is defined by the location of the open circle.

Due to the phenomenological nature of the derivation, there are numerous analytical possibilities to formulate the critical balance, some of which include non-vanishing energy at $k_\parallel = 0$ (*Cho et al.*, 2002; *Forman et al.*, 2011). We will present some of these formulations in Section 4.2. However, all of these formulations show the scalings given in Equation (2.42) and ultimately lead to a cascade preferentially perpendicular ($k_\perp \gg k_\parallel$) to the background magnetic field. Several measurements in the solar wind indicate that the turbulent cascade in the solar wind is indeed critically balanced, which we discuss in Section 2.3.

2.2.5 Turbulence on Kinetic Scales

In hydrodynamic turbulence the cascade consists of three regions: the energy injection range, inertial range and dissipation range. For plasma turbulence the situation is more complicated because there are characteristic length scales within the inertial range, where the statistics of the nonlinear interactions change. The phenomenological derivation discussed in Section 2.2.4 is therefore restricted to MHD scales, where the dominant plasma waves are Alfvén waves. As MHD describes the plasma as a fluid, the approach is only valid for scales $\ell \gg \ell_i$. Here, ℓ_i denotes the controlling ion kinetic scale that may be given, e.g., by the ion gyro radius ρ_i. Another important kinetic scale that might control the onset of kinetic turbulence is the ion inertial length

$$\lambda_i = \frac{\omega_{\mathrm{pi}}}{c} = \sqrt{\frac{n_i e^2}{\varepsilon_0 m_i c^2}} \,, \tag{2.46}$$

where c is the speed of light, ω_{pi} is the ion plasma frequency, n_i is the ion number density and ε_0 is the vacuum permittivity or electric constant. The same characteristic length scales ℓ_e can also be defined for electrons instead of ions. To describe the plasma at kinetic scales, the electrons may still be regarded as a fluid but the description of the ions needs a kinetic approach.

On scales $\ell_i \gg \ell \gg \ell_e$ - henceforth denoted as (ion) kinetic scales - the Alfvén, slow and fast wave branches develop new characteristics and split up into kinetic wave modes. These modes can be derived as linear solutions to the Vlasow-Maxwell equations or from the warm and cold plasma dispersion relations (see, e.g., *Lysak and Lotko*, 1996; *Baumjohann and Treumann*, 1997; *Sahraoui et al.*, 2012). The wave vector $\mathbf{k}$ determines which kind of waves develop in the kinetic range. On the one hand, Alfvén waves transition into ion cyclotron waves for $k_\parallel \lambda_i \gtrsim 1$ and into left-hand polarized kinetic Alfvén waves for $k_\perp \rho_i \gg 1$ and $k_\perp \ell_i < 1$ (*Sahraoui et al.*, 2012; *Howes et al.*, 2014a). On the other hand, fast mode waves transition into ion Bernstein waves for $k_\parallel \lambda_i \ll 1$ and

$k_\perp \rho_i \gtrsim 1$ and into right-hand polarized whistler waves for $k_\parallel \lambda_i \gtrsim 1$ (*Stawicki et al.*, 2001; *Sahraoui et al.*, 2012; *Howes et al.*, 2014a). The kinetic slow mode is less well studied because it is believed that the slow mode is strongly damped in collisionless plasmas with $T_i \sim T_e$ (*Klein et al.*, 2012).

Especially two waves that arise on these scales play an important role for turbulent fluctuations at ion kinetic scales: the kinetic Alfvén wave (KAW) and the whistler wave. In Section 2.2.6, we present a phenomenological derivation of the KAW turbulent cascade after *Howes et al.* (2008). We also interpret our results in Saturn's magnetosphere in the framework of KAW turbulence. This has several reasons: first, recent observations and simulations indicate that solar wind fluctuations on kinetic scales are indeed predominantly kinetic Alfvén waves (*Chen et al.*, 2013; *Sahraoui et al.*, 2010; *Podesta and TenBarge*, 2012; *TenBarge et al.*, 2012; *Podesta*, 2013; *TenBarge et al.*, 2013), and second, our observations in Saturn's magnetosphere (Chapter 3) and our synthetic PSD (Chapter 4) cannot be interpreted by whistler turbulence. This is because whistler waves violate Taylor's hypothesis of frozen-in flow, which is a prerequisite for our later analyses (see *Howes et al.*, 2014a, the validity in the solar wind).

2.2.6 Kinetic Alfvén Wave Turbulence

In order to describe the turbulence controlled by kinetic Alfvén waves, we present a phenomenological derivation based on gyrokinetics (*Howes et al.*, 2006, 2008; *Schekochihin et al.*, 2009). The easiest way to write the dispersion relation for kinetic Alfvén waves is

$$\omega^2 \sim k_\perp^2 \rho_i^2 k_\parallel^2 V_\mathrm{A}^2 \tag{2.47}$$

$$\Leftrightarrow \quad \tau_\mathrm{KAW} \sim \left(k_\perp \rho_i k_\parallel V_\mathrm{A}\right)^{-1} \ , \tag{2.48}$$

where we neglected additional functional dependencies on temperature and plasma β, which simplify to a factor close to unity for the plasmas under consideration in this thesis (*Hasegawa*, 1976; *Baumjohann and Treumann*, 1997; *Howes et al.*, 2006). Equation (2.47) is valid under the condition of $k_\perp \rho_i \gg 1$ and results in a phase velocity for kinetic Alfvén waves comparable to that of Alfvén waves, namely $v_\mathrm{ph,KAW} \propto \cos(\theta)$.

On MHD scales, the plasma is frozen-in to the magnetic field, so that we could identify velocity and magnetic fluctuations: $\delta v \sim \delta b$. However, the correlation of magnetic and velocity fluctuations is not perfect on kinetic scales. In fact, the velocity fluctuation δv corresponds to a magnetic fluctuation δb according to (*Howes et al.*, 2006)

$$\delta v \sim k_\perp \rho_i \delta b \ . \tag{2.49}$$

Thus, the nonlinear time becomes

$$\tau_\mathrm{nl} \sim \left(k_\perp^2 \rho_i \delta b\right)^{-1} \ . \tag{2.50}$$

To derive the scalings of the critically balanced KAW cascade, we proceed in the same way as in Section 2.2.4. The only additional information that we put into the derivation are Equations (2.48) and (2.49). The energy flux along the cascade, or dissipation rate ϵ, and the magnetic field fluctuation δb can then be estimated as

$$\epsilon \sim \frac{\delta b^2}{\tau_{\rm nl}} \quad \Leftrightarrow \quad \delta b \sim \epsilon^{1/3} \rho_i^{-1/3} k_\perp^{-2/3} \tag{2.51}$$

for the perpendicular cascade and as

$$\epsilon \sim \frac{\delta b^2}{\tau_{\rm kaw}} \quad \Leftrightarrow \quad \delta b \sim \epsilon \rho_i^{-1} V_{\rm A}^{-2} k_\parallel^{-2} \tag{2.52}$$

for the parallel cascade. For the magnetic field power spectra, those relations result in

$$E_\perp \sim \epsilon^{2/3} \rho_i^{-2/3} k_\perp^{-7/3} \quad \text{and} \quad E_\parallel \sim \epsilon^2 \rho_i^{-2} V_{\rm A}^{-4} k_\parallel^{-5} \ . \tag{2.53}$$

The power spectra of magnetic field fluctuations in the ion kinetic range are therefore steeper than their counterparts in the MHD regime. At the transition between the two regimes, a sharp spectral break is observed, which has been analyzed in various studies (e.g. *Leamon et al.*, 1999; *Smith et al.*, 2006; *Markovskii et al.*, 2008; *Alexandrova et al.*, 2012; *Bourouaine et al.*, 2012). For a purely perpendicular spectrum with field-to-flow angle $\theta_{vB} = 90°$, this spectral break is observed around $k\rho_i \sim 1$ and $k\lambda_i \sim 1$. However, for KAW turbulence the controlling parameter is believed to be the gyro radius (*Howes et al.*, 2008; *Schekochihin et al.*, 2009). A recent observation of a critically balanced KAW cascade in the solar wind by *Chen et al.* (2010a) is presented in Section 2.3.

The associated relation of the wave vectors due to the critical balance can be derived by Equations (2.51), (2.52) and (2.43), which yields

$$k_\parallel \sim L^{-1/3} \rho_i^{-1/3} k_\perp^{1/3} \ . \tag{2.54}$$

A more sophisticated version of Equation (2.54) has been derived by *Howes et al.* (2008), which has an additional factor $(\beta_i + 2/(1 + T_e/T_i))^{1/6}$ on the right hand side. However, this factor is of order unity both in the solar wind and in Saturn's magnetosphere and we therefore neglect it here.

The same derivation for the spectral power can be made under the assumption of weak turbulence with transfer time $\tau_{\rm tr} \sim \tau_{\rm nl}^2/\tau_{\rm kaw}$ (*Howes et al.*, 2011a). Straightforward application according to Section 2.2.3 then leads to a scaling of

$$E_\perp \propto k_\perp^{-5/2} \ . \tag{2.55}$$

Again, there is no spectral transfer of energy along $k_\parallel$ (*Howes et al.*, 2011a).

2.2.7 On the Ambiguity of Dimensional Analyses

The advantage of the dimensional or phenomenological analysis, which has been used so far, lies in its potential to predict scalings of turbulent spectra without having to cope with complicated analytical formulations of the underlying equations or their approximations. However, as we have already noted in Sections 2.2.2 and 2.2.3, a certain ambiguity arises because it is impossible to find an exact solution with dimensional analysis alone. This ambiguity stems from the emergence of characteristic times for plasma waves in addition to the nonlinear time and from the inability to discriminate between anisotropic scales $k_\perp^{-1}$ and $k_\parallel^{-1}$. Therefore, the scalings for plasma turbulence introduced so far represent only some possibilities amongst others.

For the MHD regime governed by Alfvén waves, *Galtier et al.* (2005) presented a more general formulation of the dimensional analysis. Their derivations emanate from an anisotropic spectrum of the form

$$E \propto k_\perp^{-\alpha} k_\parallel^{-\beta} \ , \tag{2.56}$$

where α and β are unknown parameters. Assuming a constant ratio $\tau_\mathrm{A}/\tau_\mathrm{nl}$ along the cascade, they deduced a linear relationship between those parameters, namely

$$3\alpha + 2\beta = 7 \ . \tag{2.57}$$

Based on this relation the well known solutions for the critically balanced Kolmogorov spectrum ($\alpha = 5/3, b = 1$) and the anisotropic Iroshnikov-Kraichnan spectrum ($\alpha = 2, \beta = 1/2$) can be reproduced (*Goldreich and Sridhar*, 1995, 1997; *Ng and Bhattacharjee*, 1997). Interestingly, the relation $k_\parallel \propto k_\perp^{2/3}$ arises as a universal scaling, which results from the assumption of a constant ratio $\tau_\mathrm{A}/\tau_\mathrm{nl}$ (*Galtier et al.*, 2005).

Within the kinetic range the problem of ambiguity is even greater. While the dominance of Alfvén waves on scales $k\rho_i \ll 1$ is agreed upon in the solar wind, the dominant wave mode on kinetic scales is yet to be identified. As discussed in Section 2.2.5, the most probable candidates are kinetic Alfvén waves and whistler waves, but it is experimentally very difficult to distinguish between them. The dispersion relation has to be measured and the observations are inconclusive so far because of the large measurement uncertainties (*Sahraoui et al.*, 2010; *Narita et al.*, 2011; *Perschke et al.*, 2013; *Roberts et al.*, 2013). However, all measurements coincide to such a degree as they detect predominantly fluctuations with wave vectors perpendicular to the background magnetic field, $k_\perp \gg k_\parallel$. Note, that other phenomena such as ion-Bernstein waves or simply convected structures may also play important roles in the turbulent cascade at kinetic scales (*Perschke et al.*, 2013; *Roberts et al.*, 2013). From a dimensional point of view, the difference between kinetic Alfvén waves and whistler waves is negligible because both linear wave periods scale as $\tau_\mathrm{w} \propto (k_\parallel k_\perp)^{-1}$. Therefore, the linear

relationship in the kinetic range amounts to

$$3\alpha + \beta = 8 \tag{2.58}$$

for both waves, which shows that it is impossible to determine the wave mode from the estimation of the spectral index alone (*Galtier et al.*, 2005). Other theories that are in accordance with Equation (2.58) include weak whistler turbulence with a spectral index of 2.5 (*Galtier and Bhattacharjee*, 2005; *Narita and Gary*, 2010) as well as strong KAW turbulence (*Boldyrev and Perez*, 2012) and strong whistler turbulence when the parallel cascade is weak (*Galtier et al.*, 2005) both with a slope of 8/3.

2.2.8 Estimation of the Background Magnetic Field

It is generally agreed upon that the background magnetic field introduces an anisotropy for the turbulent fluctuations in space plasmas (*Montgomery and Turner*, 1981; *Matthaeus et al.*, 1990; *Wicks et al.*, 2012). However, there are currently two schools of thought regarding the definition of this background magnetic field. The traditional approach is to define the background magnetic field by the arithmetic average over the complete time series:

$$\mathbf{B}_0 = \frac{1}{N} \sum_{i=1}^{N} \mathbf{B}_i \ , \tag{2.59}$$

where N is the number of samples. This is the global mean magnetic field. We will almost exclusively apply this method throughout Chapter 3 and refer to it simply as the mean magnetic field. The advantage of this method is that it allows us to work with discrete data blocks of arbitrary length, e.g., 10 min time series, for which the parameters of interest - field-to-flow angle θ, RMS δB, spectral index κ, etc. - can be calculated.

The second school of thought propagates the so-called local mean magnetic field. The idea behind this approach is schematically visualized in Figure 2.6. Here, a large scale fluctuation (wave 1) experiences a background magnetic field $\mathbf{B}_0$ that is close to the global field. In contrast, a small scale and high frequency wave packet (wave 2) on top of the large wave primarily experiences a magnetic field that is a superposition of the large scale fluctuation of wave 1 and the global field. This magnetic field is the local magnetic field $\mathbf{B}_{\mathrm{loc}}(f, t)$ and it depends explicitly on the size or frequency of the wave packet and its location or, in case of a time series, the time of observation (*Cho et al.*, 2002). For large scales and low frequencies, the local magnetic field should asymptotically approach the global magnetic field but there is no unique way to describe a local background field.

Horbury et al. (2008) introduced a construction formula based on a wavelet transformation, which sorts the wavelet coefficients into discrete field-to-flow angle bins. The subsequent averaging is then carried out not over a continuous

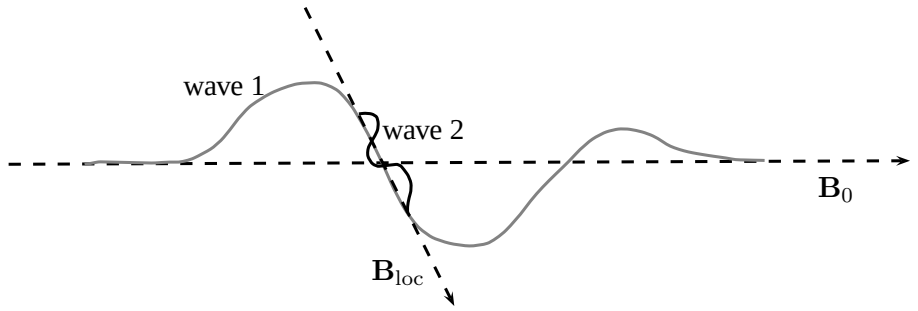

Figure 2.6: *Schematic of the global magnetic field* $\mathbf{B}_0$ *and the local magnetic field* $\mathbf{B}_{\mathrm{loc}}$ *(dashed lines). The large wave 1 (gray) experiences a large scale magnetic field equal to the global magnetic field. In contrast, the small scale and high frequency wave 2 (black) experiences the magnetic field modified by the fluctuation of wave 1. This local magnetic field* $\mathbf{B}_{\mathrm{loc}}$ *depends on the size and the location of wave packet 2.*

time interval, but over separate instances in time, during which a similar field-to-flow angle is observed. Thus, it yields an angle dependent power spectrum, $P(f, \theta)$. This method has since been used in several other studies (*Podesta*, 2009; *Osman and Horbury*, 2009; *Chen et al.*, 2010a; *Wicks et al.*, 2010). Recent observations in the solar wind indicate that only in such a local magnetic field frame, it is possible to resolve the spectral anisotropy $\kappa(\theta)$, i.e., the change of the spectral index as a function of the field-to-flow angle (*Tessein et al.*, 2009; *Chen et al.*, 2011). Note, however, that the application of a local magnetic field analysis after *Horbury et al.* (2008) requires much longer time intervals than the global field analysis in order to obtain enough coverage in each field-to-flow angle bin.

In Saturn's magnetosphere, the magnetic field, the plasma parameters and the observed spectral densities change considerably during an orbit of Cassini. This is unlike the solar wind, where a measurement under nearly homogeneous conditions can last several days. The spectral anisotropy, which can be observed in a local frame, is most likely only measurable for very small angles, say $\theta \lesssim 20^\circ$ (see Chapter 4). However, due to the near corotation of the plasma in Saturn's plasma sheet, most of the field-to-flow angles are much greater than 20° despite of a general sweepback of the magnetic field (*Wilson et al.*, 2009). Therefore, we expect the effect of spectral anisotropy to be negligible compared to the potential variations caused by inhomogeneous plasma conditions. In this thesis, we focus on the analysis of inhomogeneities of the Saturnian system with respect to local time and longitudinal asymmetries. Therefore, we prefer the global magnetic field, because it allows us to easily analyze the spatial distribution of parameters that are obtained at discrete times at locations.

2.2.9 Dissipation

The dissipation of plasma turbulence is still hardly understood. In contrast to hydrodynamic turbulence, where collisions between particles are the main dissipation mechanism, the mean free path of particles in astrophysical or space plasmas often exceeds the size of the system. This means that the plasma is effectively collisionless, which applies to the solar wind (*Belcher and Davis*, 1971) and also in a lesser extent to plasma in Saturn's middle magnetosphere (*Delamere et al.*, 2007; *Fleshman et al.*, 2013). Thus, the main contributor to dissipation are believed to be wave-particle interactions. However, due to the limited resolution of the instruments used for in-situ turbulence measurements, which only reach to the beginning of the dissipation range, there is no broadly accepted theory on the dissipation mechanisms in space plasmas.

Although the interactions of the fluctuations are nonlinear, a promising ansatz for the estimation of the dissipation rate are linear wave damping rates (*Howes et al.*, 2014b). Linear wave damping has been the subject of several recent studies (*Stawicki et al.*, 2001; *Howes et al.*, 2006; *Sahraoui et al.*, 2010; *Podesta et al.*, 2010). A substantial damping of the wave is expected when the damping rate becomes comparable to the wave frequency ω. In the case of kinetic Alfvén turbulence damping in the inertial or MHD range is negligible but gets important close to $k_\perp \rho_i \sim 1$, where the Alfvén mode transforms into the kinetic Alfvén mode (*Howes et al.*, 2006). The exponential decay in the power spectra, which was found to fit recent observations in the high frequency solar wind, is believed to be caused by such a linear wave damping (*Alexandrova et al.*, 2009, 2012).

The potential damping mechanisms include cyclotron and Landau damping and describe how energy is transferred from the wave to the particle, i.e., wave-particle interactions. The resonant condition for ion cyclotron and Landau damping is given by

$$\omega - k_\parallel v_\parallel \sim n\Omega_{\mathrm{ic}} \ , \tag{2.60}$$

where $v_\parallel$ denotes the resonant particle's speed parallel to the magnetic field. In Equation (2.60), $n \geq 1$ represents the ion cyclotron resonance and $n = 0$ the Landau resonance. The ion cyclotron resonance takes place when the Doppler-shifted wave electric field, which a particle experiences, becomes comparable to multiples of the ion cyclotron frequency (*Chen*, 1990; *Matthaeus et al.*, 1990). This type of resonance leads to perpendicular heating of the resonant particle (*Howes et al.*, 2008; *Cranmer and van Ballegooijen*, 2012).

In the case of $n = 0$, Landau damping takes place. Nonlinear Landau damping can be interpreted as the trapping of particles with a velocity close to the wave phase speed by the wave potential (*Chen*, 1990). When the wave amplitude is small, particles with a velocity close to the phase speed of the wave experience linear Landau damping. If the particle's speed is lower than the phase speed, it will gain energy from the wave, while a particle faster than the phase speed will loose energy to the wave. However, plasmas with a velocity distribution

close to a Maxwellian hold more slower than faster particles and thus the Landau resonance effectively drains energy from the waves and therefore from the turbulent cascade (*Chen*, 1990). After *Schekochihin et al.* (2009) Alfvén waves are affected by ion Landau damping at scales close to the ion gyro radius, while kinetic Alfvén waves are subject to electron Landau damping. Consequently, KAW turbulence ultimately leads to heating of electrons.

The damping rates at the respective resonances for ion cyclotron and Landau damping are anisotropic with respect to the wave vector. Ion cyclotron damping is strong when the wave frequency is close to the ion cyclotron frequency, $\omega \sim \Omega_{\mathrm{ci}}$, which happens for large $k_{\parallel}$, while Landau damping is strong for large $k_{\perp}$ (*Leamon et al.*, 1999; *Howes et al.*, 2006, 2008; *Cranmer and van Ballegooijen*, 2012). For a critically balanced cascade with $k_{\perp} \gg k_{\parallel}$, it can be shown that strong ion cyclotron damping is reached only far in the dissipation range. However, electron Landau damping of kinetic Alfvén waves already dominates the dissipation process at the associated large perpendicular wave numbers (*Schekochihin et al.*, 2009).

In order to estimate the dissipated energy per unit time from our observations, we assume a stationary turbulent cascade. Based on this simple principle one can estimate the dissipation rate by the energy transfer rate along the cascade within the inertial range. Although we can extract information on the total amount of energy with this method, it is not clear how exactly the energy is dissipated. Dissipation through wave-particle interactions may lead to anisotropic heating or the formation of current sheets that can accelerate particles through reconnection and thus generate a strongly non-Maxwellian velocity profile (*Leamon et al.*, 2000; *Dmitruk et al.*, 2004; *Chian and Muñoz*, 2011; *Perri et al.*, 2012). However, it is not the aim of this thesis to analyze the damping *mechanisms* of plasma turbulence. Instead, we are interested in the total energy carried by turbulent fluctuations to estimate the impact on the energy budget of Saturn's magnetosphere. For that matter, we derive a heating rate for magnetic fluctuations in Section 3.4.5, where we assume the energy flux along the cascade to be completely and isotropically deposited into the system as heat. In Section 4.2.3, we examine the effects of anisotropic damping in **k**-space on the measured power spectral densities.

2.3 Observations in the Solar Wind

Before we focus on observations in Saturn's magnetosphere in the next chapter, we shortly present some important and characteristic observations in the solar wind that support the theory of a critically balanced (kinetic) Alfvén wave cascade as a natural process in plasma turbulence. This is of particular interest because we compare our results in Saturn's magnetosphere with those in the solar wind. In Chapter 4, we carefully check if the observations presented here are in accordance with a critically balanced cascade, an interpretation often made without exact knowledge of the spectral anisotropy that is determined by the

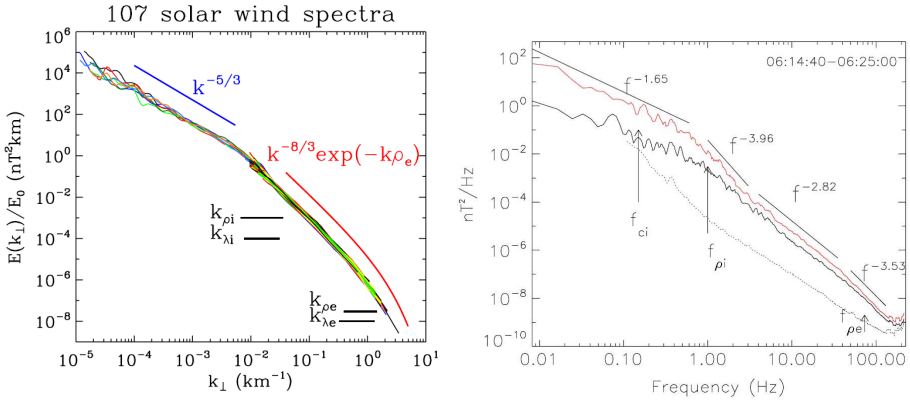

Figure 2.7: *PSD of magnetic fluctuations in the solar wind measured with CLUSTER from MHD to electron scales. Left: Results from Alexandrova et al. (2012), where an exponential model, $P \propto k_{\perp}^{-8/3} \exp(-k_{\perp}\rho_e)$, leads to the best fit in the kinetic range. Right: PSD of magnetic fluctuations parallel (black line) and perpendicular (black line) to the magnetic field from Sahraoui et al. (2010). After the first spectral break at the ion gyro radius, a steeper transition range is observed before the spectra flatten out in the ion kinetic range. At electron scales there is another spectral break followed by a power-law with spectral index* 3.53*.*

theory.

2.3.1 Magnetic Power Spectral Densities

Power spectral densities (PSD) in the solar wind have been measured since more than 30 years (*Matthaeus and Goldstein*, 1982; *Tu et al.*, 1984). Since then, modern technology has dramatically increased the measurements' accuracy and resolution. Recent observations of magnetic field fluctuations cover not only MHD and ion kinetic scales ($k > \rho_i^{-1}$) but also electron kinetic scales with $k > \rho_e^{-1}$.

Figure 2.7 (left) shows latest results obtained by *Alexandrova et al.* (2012) from observations in the solar wind by the CLUSTER spacecraft. The PSD were transformed into wave number space assuming Taylor's frozen-in hypothesis and the spectral energy was normalized so that all spectra fit nicely on top of each other. It is clearly visible that the MHD range exhibits a Kolmogorov like spectral slope of around 5/3. At kinetic scales close to both ion gyro radius and ion inertial length, the Alfvén waves evolve to kinetic Alfvén waves and a spectral break is observed. After the break the PSD steepens toward a slope of approximately 8/3. This is somewhat steeper than the 7/3 slope presented in Section 2.2.6, but we will later see in Chapter 4 that this discrepancy might be explained by damping of the fluctuations. *Alexandrova et al.* (2012) find that an

exponential model

$$P(k_\perp) \propto k_\perp^{-8/3} \exp(-k_\perp \rho_e) \tag{2.61}$$

best fits the data. The change of the spectral index around electron scales is explained by damping leading to an exponential decay as it is observed for the dissipation range of hydrodynamic turbulence.

Sahraoui et al. (2010) made similar observations with CLUSTER in the solar wind and interpret the change of the spectral index as a second spectral break. They used a power-law of spectral slope ∼3.5 to fit this electron kinetic range. An example PSD of their results is shown in Figure 2.7 (right), where the black line shows the energy of fluctuations parallel to the magnetic field, $P_\parallel$, and the red line the energy of fluctuations perpendicular to the magnetic field, $P_\perp$. The power anisotropy is large in the MHD range, $P_\perp/P_\parallel \geq 10$, which is a common observation in the solar wind (*Belcher and Davis*, 1971; *Osman and Horbury*, 2009; *Wicks et al.*, 2010; *TenBarge et al.*, 2012). The steep power-law range with a slope of 3.96 is interpreted as a transition range from MHD to kinetic scales associated with ion dissipation (*Sahraoui et al.*, 2010; *Smith et al.*, 2012). Although both results yield slightly different spectral indices and the electron scale observation is interpreted differently, both PSD show the same characteristics. In Chapter 3, we show that these characteristics of the power spectra, namely spectral breaks at ion scales and steep slopes in the kinetic range of ∼2.6, similarly apply to fluctuations in Saturn's magnetosphere.

2.3.2 Observations of Intermittent Fluctuations

The statistics of the fluctuations in the solar wind has been analyzed extensively with experimentally derived probability density functions (PDF) and structure functions (*Burlaga*, 1992; *Sorriso-Valvo et al.*, 1999, 2001; *Hnat et al.*, 2003; *Kiyani et al.*, 2009; *Salem et al.*, 2009; *Zimbardo et al.*, 2010). The flatness, i.e., the normalized fourth order statistical moment, is found to increase drastically starting from a value close to 3 on MHD scales (*Bruno et al.*, 2003; *Alexandrova et al.*, 2008a). This has also been observed in simulations of MHD turbulence (*Cho and Lazarian*, 2009; *Wan et al.*, 2009) and is characteristic of intermittency and also of the dissipation range in HD turbulence (*Frisch*, 1995).

Figure 2.8 shows the flatness obtained from HELIOS and CLUSTER measurements in the solar wind using a scale dependent wavelet estimation (*Alexandrova et al.*, 2008a). At large scales the flatness of ∼3 indicates that the PDF is close to Gaussian. The power-law like increase of the flatness with frequency shows that the scaling exponent is not a linear function of statistical order n (see Equation (2.17)), which indicates multifractal fluctuations (*Kiyani et al.*, 2013). This increase is drastically enhanced in the kinetic range. The intermittency can be estimated with the local intermittency measure presented by *Farge* (1992) as shown in the inset in Figure 2.8. The increasing flatness is thus in accordance with an increased intermittency and may indicate the formation of current sheets (*Perri et al.*, 2012).

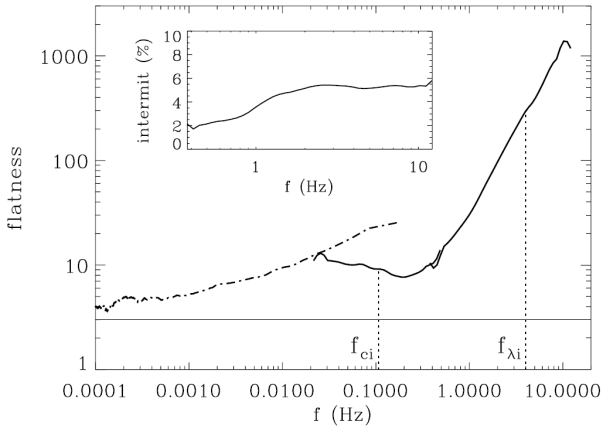

Figure 2.8: *Flatness as a function of frequency in spacecraft frame from Alexandrova et al. (2008a). The solid line shows HELIOS data and the dashed line data from CLUSTER. At frequencies higher than the ion cyclotron frequency, $f_{\rm ci}$, the flatness increases like a power-law.The inset shows the intermittency of the fluctuations.*

2.3.3 Spectral Anisotropy

The critically balanced cascade predicts that the spectral index κ is a function of the field-to-flow angle θ. The first analysis of such a spectral anisotropy, $\kappa(\theta)$, was made by *Horbury et al.* (2008) using 30 days of magnetic field data from Ulysses in the high speed solar wind. Their results are shown in Figure 2.9 (left). Here, the spectral anisotropy $\kappa(\theta)$ is shown for 10° angle bins. The spectral index has been obtained in a frequency range of $f = 15{-}98\,\mathrm{mHz}$ which corresponds to MHD scales. *Horbury et al.* (2008) used a wavelet based method to construct spectra in a local mean magnetic field frame. Similar results were later reported by several other authors (*Podesta*, 2009; *Osman and Horbury*, 2009; *Wicks et al.*, 2010). The choice of the reference frame seems to be particularly important for the spectral anisotropy, as *Tessein et al.* (2009) found no such anisotropy in a global magnetic field frame. Spectral anisotropy in a local magnetic field frame has also been measured in the kinetic range, $k_\perp \rho_i > 1$, by *Chen et al.* (2010a). They used CLUSTER data from 2002 to obtain the spectral indices from second order structure functions. Their results are shown in Figure 2.9 (right) for fluctuations parallel (red) and perpendicular (blue) to the local mean magnetic field. The results have been presented as indicative for a critically balanced cascade.

Both results - a monotonically decreasing spectral index from 2 to 5/3 and ∼3.5 to 8/3 - are interpreted as consistent with a critically balanced cascade on MHD and kinetic scales, respectively. For the MHD range *Forman et al.* (2011) showed that the results of *Horbury et al.* (2008) are in agreement with a critically balanced cascade, but they used a mathematical transformation that forbid them to analyze the function $\kappa(\theta)$ or the PSD directly. An attempt to reconstruct the

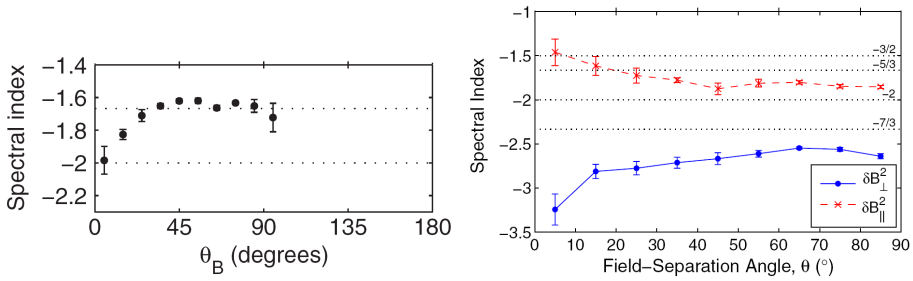

Figure 2.9: *Left: spectral anisotropy $\kappa(\theta)$ calculated in the range $f = 15-98\,mHz$ for $10°$ angle bins as measured by Horbury et al. (2008) on MHD scales. Right: spectral anisotropy for fluctuations parallel (red) and perpendicular (blue) to the local mean magnetic field as obtained by Chen et al. (2010a).*

energy distribution in **k**-space has recently been published by *He et al.* (2013), which indicates that the measured spectral anisotropy may indeed be caused by an anisotropy in wave vector space corresponding to the critical balance theory by *Goldreich and Sridhar* (1995). Also there are numerical simulations indicating that a critically balanced cascade is formed by Alfvén (*Cho and Vishniac*, 2000; *Maron and Goldreich*, 2001; *Cho et al.*, 2002) and kinetic Alfvén turbulence (*TenBarge and Howes*, 2012).

Despite of these recent findings that support the critically balanced (kinetic) Alfvén wave conjecture, the results presented here lack a complete explanation. Although the observed spectral indices at $\theta \sim 0°$ and $\theta \sim 90°$ are close to what is expected for KAW turbulence, the exact functional dependence of the spectral index on the field-to-flow angle on MHD and kinetic scales is unknown. There are no theoretical considerations on how a critically balanced cascade might look like for intermediate angles $0° < \theta < 90°$ in the measured PSD. We will therefore analyze the functional dependence, $\kappa(\theta)$, of these critically balanced cascades in Chapter 4. There, we show that the critically balanced KAW turbulence leads to a surprising spectral shape of the PSD and is unlikely to be the only cause of the observed spectral anisotropy. Instead, the anisotropic damping term presented in Equation (2.61) is substantial for a smooth variation of the spectral index from small to large angles.

CHAPTER 3

Turbulence at Saturn

In this Chapter, we explore Saturn's magnetosphere, present its structure and dynamics, and analyze magnetic field data of in-situ measurements obtained by the spacecraft Cassini in the years from 2004 to 2009. We present one of the two major results of this thesis, namely the existence of a kinetic range turbulent cascade in Saturn's magnetosphere and its implications on the magnetospheric energy budget. We also show that the turbulence exhibits several asymmetries with respect to local time and planetary longitude.

We begin this chapter with a review of the general characteristics of Saturn's magnetosphere obtained from measurements in the Cassini era. First, we discuss the general structure of the planet and its magnetosphere in Section 3.1. We show that the magnetosphere of the second largest planet of our solar system is to a major degree internally controlled and explain some of the dynamic magnetospheric processes in more detail in Section 3.2. Then, we come to the analysis of turbulent magnetic field fluctuations, which has been carried out in the framework of this thesis. In Section 3.3, we investigate in detail the magnetic fluctuations in a case study of Cassini's second orbit. As described in Section 3.4, the energy that is ultimately injected into the magnetosphere through the fast rotation of the planet is nonlinearly transferred to smaller scales, where the magnetic fluctuations form a consistent turbulent cascade. The cascade has important implications for the energy budget of the system and is shown to substantially heat the magnetospheric plasma. The dependence of the derived parameters on local time and planetary longitude is discussed in Section 3.5. For a presentation of the Cassini mission and the instruments that are important for our observations, the reader is referred to Appendix A. An extensive review of Cassini observations at Saturn is given by *Dougherty et al.* (2009). The most parts of Sections 3.3 and 3.4 have been published in *von Papen et al.* (2014).

3.1 Planetary Properties of Saturn

Saturn is the second largest planet of our solar system and is named after the roman god of agriculture. It is particularly famous for its rings, which were first

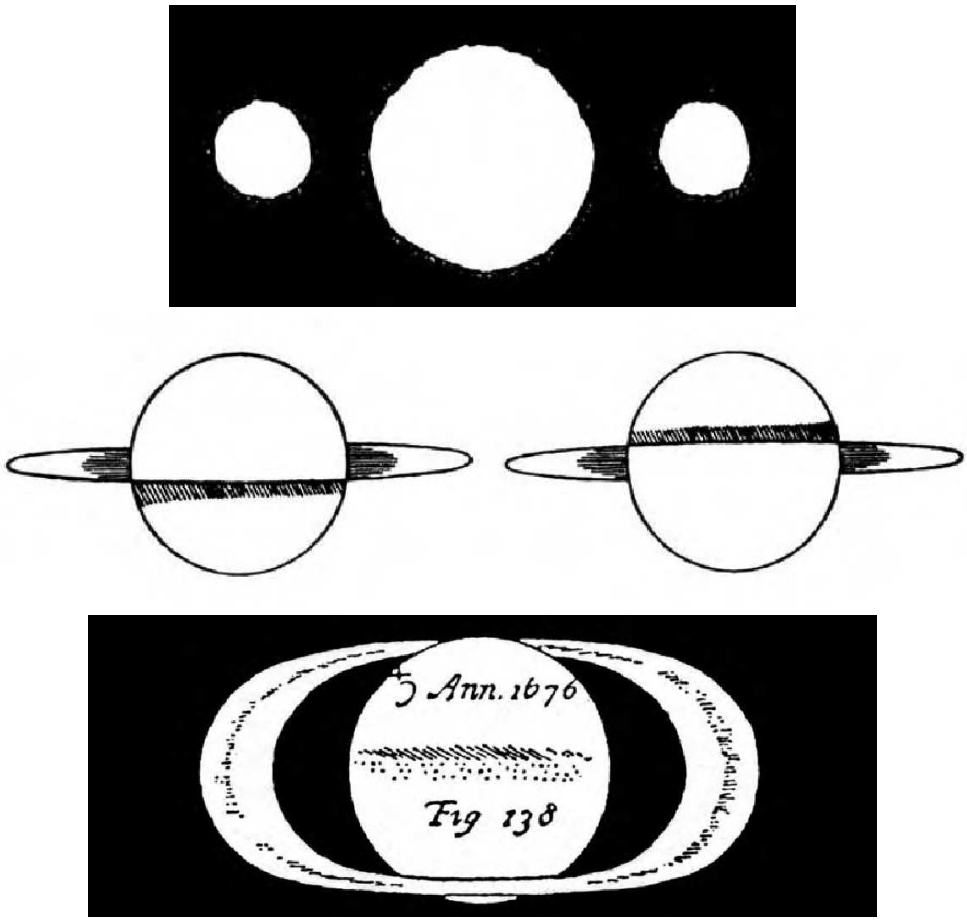

Figure 3.1: *Historical drawings illustrating the discovery of Saturn's rings. Galilei mistook them for two moons (top), while C. Huygens correctly interpreted them as rings in the equatorial plane (middle). G. D. Cassini later recognized the division of the rings (bottom). Figure from Harland (2007).*

discovered by *Galileo Galilei* (1564-1641) in 1610. However, *Galilei* mistook the rings for two moons as can be seen in his drawing shown in Figure 3.1 (top). Later, *Christiaan Huygens* (1629–1695) recognized the ring structure in 1659 (Figure 3.1, middle), followed by the discovery of a dark division between the rings by *G. D. Cassini* (1625–1712) shown in Figure 3.1 (bottom).

The planet Saturn is a gas giant located at an average distance of 9.54 AU from the Sun with a mass of 95 times that of Earth and an equatorial radius of $1\,R_\mathrm{s} = 60268\,\mathrm{km}$ (defined at 1 bar atmospheric pressure). The flattening $f = (a - c)/a$, which quantifies the relation between equatorial radius a and polar radius c, is 0.09796 for Saturn. This is almost 30 times larger than Earth's flattening (*NASA*, 2014). Table 3.1 summarizes the most relevant parameters in comparison with those of Earth. Saturn's atmosphere consists primarily of

	Saturn	**Earth**
Planetary Parameters		
Equatorial radius [km]	$1\,R_\mathrm{s} = 60268$	$1\,R_\mathrm{E} = 6378$
Mass [10^{24} kg]	568.36	5.9726
Mean density [$\mathrm{kg\,m^{-3}}$]	687	5514
Flattening	0.09796	0.00335
Equatorial magnetic field [nT]	20000	31000
Magnetic dipole moment [$\mathrm{T/m^{-3}}$]	$4.6 \cdot 10^{18}$	$7.75 \cdot 10^{15}$
Average IMF magnitude [nT]	0.5	4
Magnetopause standoff distance	$25\,R_\mathrm{s}$	$10\,R_\mathrm{E}$
Dipole tilt	$< 1°$	$10.5°$
Orbital Parameters		
Semi major axis [AU]	9.54	1
Sidereal orbit period [days]	10759.22	365.256
Sidereal rotation period [h]	$\sim$10.7	23.9345
Obliquity	26.73°	23.44°

Table 3.1: *Basic parameters of Saturn compared to those of Earth (NASA, 2014; Gombosi et al., 2009; Achilleos et al., 2008).*

molecular hydrogen (H_2, 96%) and helium (He, 3%) (*NASA*, 2014). The planetary mass is - even more than at Jupiter - centrally concentrated in a core of 15−20 Earth masses (*Dougherty et al.*, 2009, Ch. 4). The visible surface, i.e., the atmospheric cloud top, is in constant motion and rotates differentially. Figure 3.2 shows a photograph of the largest storm since 1990 which was detected in December, 2010, taken by the spacecraft Cassini. One can clearly see band patterns of clouds and the turbulent storm tail, which ultimately encircles the whole planet. It takes Saturn 29.4 years to orbit around the Sun. The obliquity of Saturn, i.e., the maximal angle between its equatorial plane and the solar ecliptic, is 26.7° (*NASA*, 2014). Therefore, strong annual changes are expected, caused by asymmetric heating of the hemispheres. The spacecraft Cassini arrived at Saturn on July 2004 during southern summer, which lasted until equinox on 11 August 2009.

3.1.1 Saturn's Moons

More than 60 moons orbit the planet most of which have diameters below 200 km. The largest moon is Titan, located at $20.3\,R_\mathrm{s}$, with a radius of 2575 km. Titan's dense atmosphere consists of mostly nitrogen and has been investigated in many Cassini flybys and also by the probe Huygens (*Harland*, 2007). The most important moon for magnetospheric dynamics, however, is located at $3.9\,R_\mathrm{s}$. It is the moon Enceladus and despite of its small size, with a radius of just 250 km, it is the main source of the magnetospheric plasma. Other moons with mean radii of more than 100 km include Mimas (radius 199 km, distance to Saturn $3.1\,R_\mathrm{s}$),

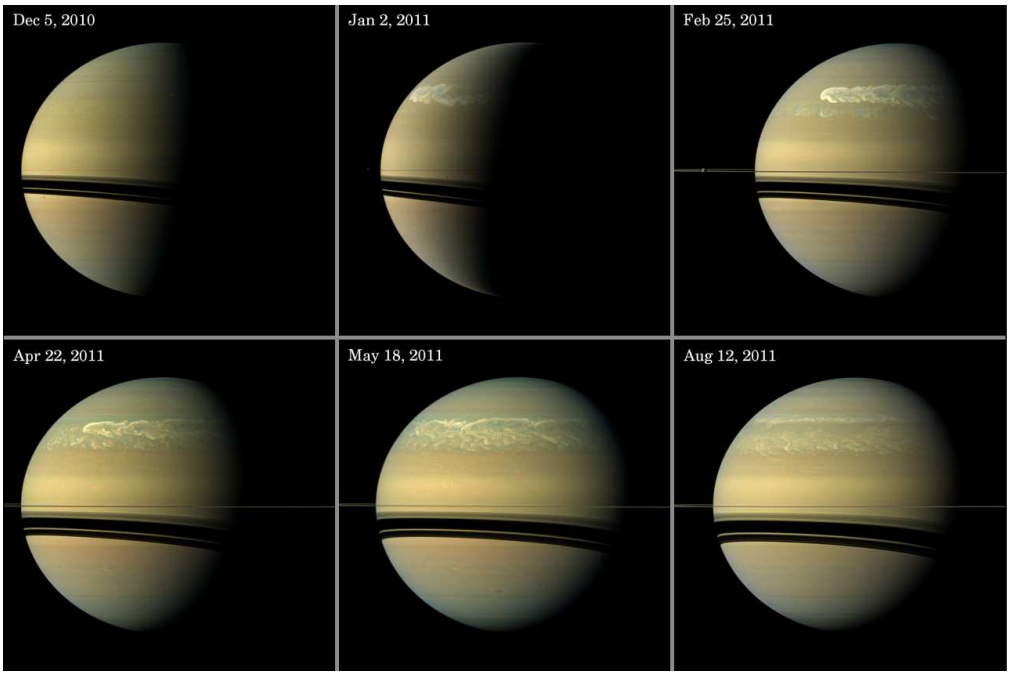

Figure 3.2: *Evolution of the greatest storm observed on Saturn since 1990. The Feb. 25 and Aug. 12 images are true color [NASA/JPL-Caltech/Space Science Institute].*

Tethys (531 km, 4.9 R_s), Dione (562 km, 6.3 R_s), Rhea (763 km, 8.7 R_s), Hyperion (139 km, 24.6 R_s), Iapetus (735 km, 59.1 R_s) and Phoebe (107 km, 215 R_s) (*NASA*, 2014). Mimas, Enceladus, Tethys, Dione and Rhea are often referred to as the icy moons because of their surface of water ice.

The main source of neutrals inside Saturn's magnetosphere is the moon Enceladus. Several flybys found plumes near the south pole in the region of the characteristic tiger stripes emitting water group neutrals (H_3O, H_2O, OH, O) into the magnetosphere (*Dougherty et al.*, 2009, Ch. 21, and references therein). A photograph of these plumes taken by Cassini is shown in Figure 3.3. The amount of neutrals emitted through water jets from Enceladus' plumes to the magnetosphere is found to vary with time (*Saur et al.*, 2008). Estimations for the mass loss rate reach from 200 kg/s up to 1600 kg/s (*Saur et al.*, 2008; *Sittler et al.*, 2008; *Gombosi et al.*, 2009; *Bagenal and Delamere*, 2011). The neutrals form a large torus centered at Enceladus' orbit and eventually get ionized by electron impact, charge exchange and photo ionization (*Cassidy and Johnson*, 2010; *Fleshman et al.*, 2013). However, neutrals remain the main constituent of particles in the magnetosphere and outweigh ions by a factor of ∼12 (*Bagenal and Delamere*, 2011).

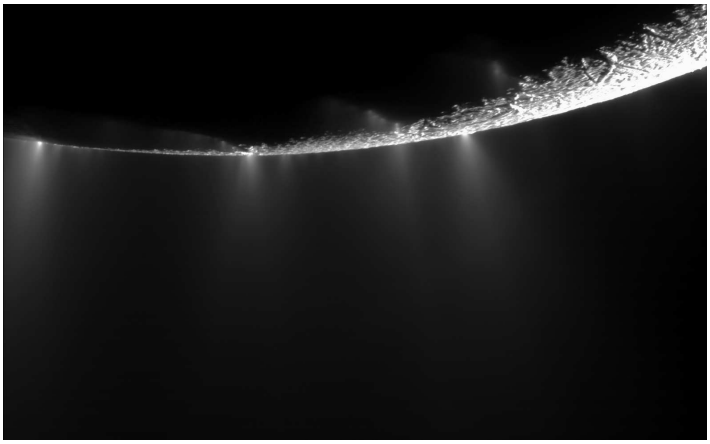

Figure 3.3: *Plumes at Enceladus' south pole emitting water group neutrals captured by Cassini's narrow angle camera on Nov 21, 2009 [NASA/JPL/Space Science Institute]. These plumes are the main source of neutrals in Saturn's magnetosphere.*

3.1.2 Magnetospheric Structure

The magnetosphere of Saturn is after Jupiter's the second largest of the solar system. It acts as an obstacle to the solar wind because the planetary magnetic field generally inhibits the solar wind plasma from entering the magnetosphere. The characteristic shape is caused by the incident solar wind, which leads to compression on the day side and to the formation of an elongated tail on the night side. A schematic of the magnetosphere is shown in Figure 3.4. The region, where the supersonic solar wind decelerates to subsonic speeds is called the bow shock. Past the bow shock is the magnetosheath, which is characterized by anisotropic heating and turbulent plasma (*Bavassano Cattaneo et al.*, 2000; *Alexandrova and Saur*, 2008). The magnetopause is defined by the area on which the solar wind pressure equals the planetary magnetic field pressure. Hence, it bounds the region which is mainly controlled by the planetary magnetic field. The magnetopause standoff distance, which is the shortest radial distance from Saturn to the magnetopause at the subsolar point, is found at $22{-}27\,R_\mathrm{s}$ depending on solar wind pressure (*Achilleos et al.*, 2008, 2010).

Due to the high conductivity and nearly collisionless nature of the plasma, the frozen-field theorem given by Equation (2.25) can be used to describe the plasma motions on large scales. Accordingly, the plasma stays on its magnetic field line and corotates around the planet. Because the rotation of the planet is very fast ($\sim$11 h), strong centrifugal forces act on the plasma and confine it in the magnetic equator, where it forms a plasma sheet and leads to radially stretched field lines. It is found that the plasma sheet is distorted by the solar wind into a bowl-shaped structure, which is shown in Figure 3.5 (*Arridge et al.*, 2008a). In the beginning of the Cassini observations, southern summer conditions led to a northward displacement of the plasma sheet. The vertical displacement of the

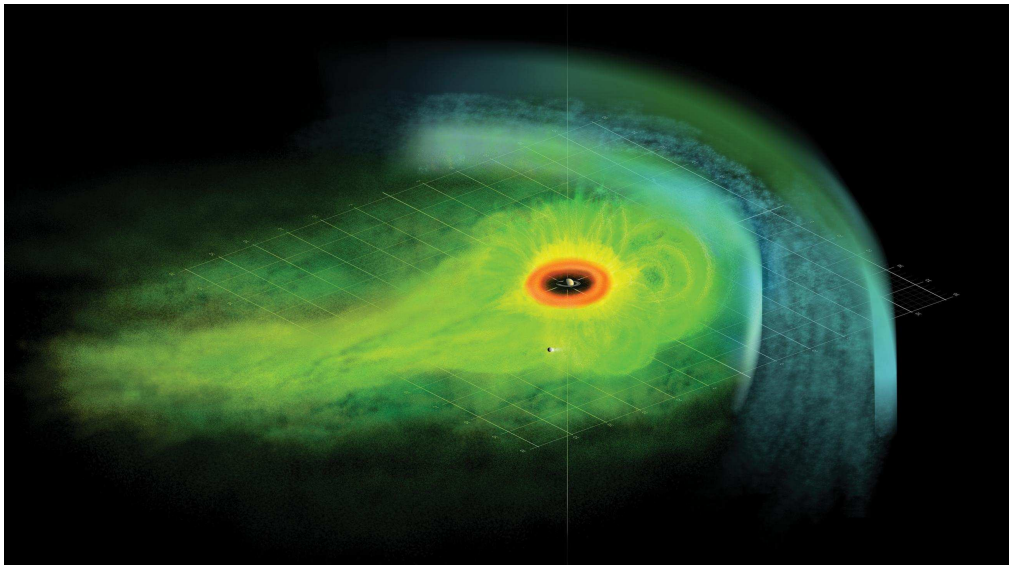

Figure 3.4: *Illustration of Saturn's magnetosphere with the moon Titan for reference. The neutral cloud is shown as red ring around Saturn while the plasma is shown in green and gets more tenuous along the tail. The incident solar wind is decelerated at the bow shock and is deflected around the magnetopause in the highly turbulent magnetosheath (blue colors) [NASA/JPL/JHUAPL].*

plasma sheet above the rotational equator can be approximated by

$$z_{\mathrm{cs}} = \left[r - R_{\mathrm{H}} \tanh\left(\frac{r}{R_{\mathrm{H}}}\right) \right] \tan(\theta_{\mathrm{SUN}}) \ , \tag{3.1}$$

where r is the equatorial distance to Saturn in units of R_{s}, R_{H} is the so-called hinging distance and θ_{SUN} the angle of Saturn's obliquity (*Arridge et al.*, 2008a). It is found that $R_{\mathrm{H}} \sim 25\,R_{\mathrm{s}}$, i.e., the hinging can be observed on the day side only during low solar wind pressure when the magnetopause standoff distance is larger than $25\,R_{\mathrm{s}}$. However, ∼60% of the time the magnetopause is situated closer to the planet (*Achilleos et al.*, 2008). In the range $6-20\,R_{\mathrm{s}}$, where we analyze the magnetic field fluctuations, this vertical distortion of the plasma sheet is less than $1.5\,R_{\mathrm{s}}$. The lobes, which are characterized by hot and tenuous plasma, are located on higher latitudes than the plasma sheet. Magnetic fluctuations in these lobes are very low in the frequency range covered by the magnetometer so that spectra from this region may even be used to test the spectral noise level of the magnetometer (*Cornilleau-Wehrlin et al.*, 2003).

Plasma Properties in the Plasma Sheet

The plasma in Saturn's magnetosphere consists mainly of water group ions with a mean ion mass of 18 amu stemming from Enceladus' neutral cloud (*Krimigis*

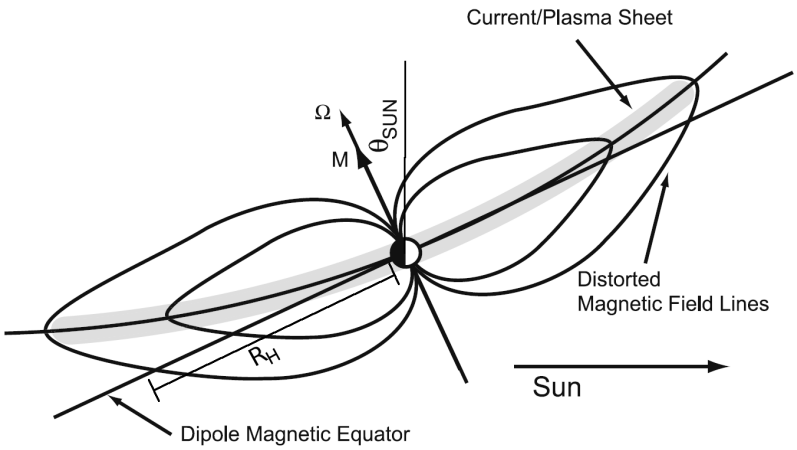

Figure 3.5: *Schematic of Saturn's magnetosphere configuration: the plasma is concentrated on elongated magnetic field lines in the magnetic equator. Due to the solar wind pressure the plasma sheet is displaced northward during southern summer, characterized by the hinging distance* R_{H}*. (modified from Arridge et al., 2008a).*

et al., 2005; *Sittler et al.*, 2008). Minor sources are the solar wind, Saturn's ionosphere and sputtering from the rings and moons. However, only the input from the solar wind may amount to a substantial fraction of the plasma produced from Enceladus. *Bagenal and Delamere* (2011) estimate that 0.1% of solar wind plasma is able to enter the magnetosphere, which leads to a production rate of only 3 kg/s. This is much less than the production estimates for Enceladus.

The thermal or cold ion and electron population with temperatures of 10−100 eV are predominantly found close to the magnetic equator (*Sittler et al.*, 2008; *Thomsen et al.*, 2010). Their energetic counterparts, on the other hand, are much more dispersed. Although their density is significantly less, e.g., a factor of around 100 for electrons in the middle magnetosphere, their contribution to plasma pressure exceeds that of the thermal plasma population outside of 9 R_{s} (*Sergis et al.*, 2010; *Schippers et al.*, 2008). *Thomsen et al.* (2010) analyzed the two main constituents of this thermal magnetospheric plasma, namely water group ions, W^+, and protons, H^+, using data from the Cassini Plasma Spectrometer (CAPS, *Young et al.* (2004)). For times when the CAPS field of view was pointing in corotation direction, they showed that the densities in a range 6−17 R_{s} could well be fitted by a power-law (see also *Thomsen et al.*, 2014). Figure 3.6 (bottom) shows the derived densities for the respective ion populations as a function of radial distance. They also measured the densities as a function of latitude from which they were able to derive the scale heights of the associated plasma species. The coefficients of their best fitted models are given in Table 3.2. The coefficients for the scale height given in Table 3.2 are taken from a fit in the range $6 \leq L \leq 7$, where L is the L shell in units of

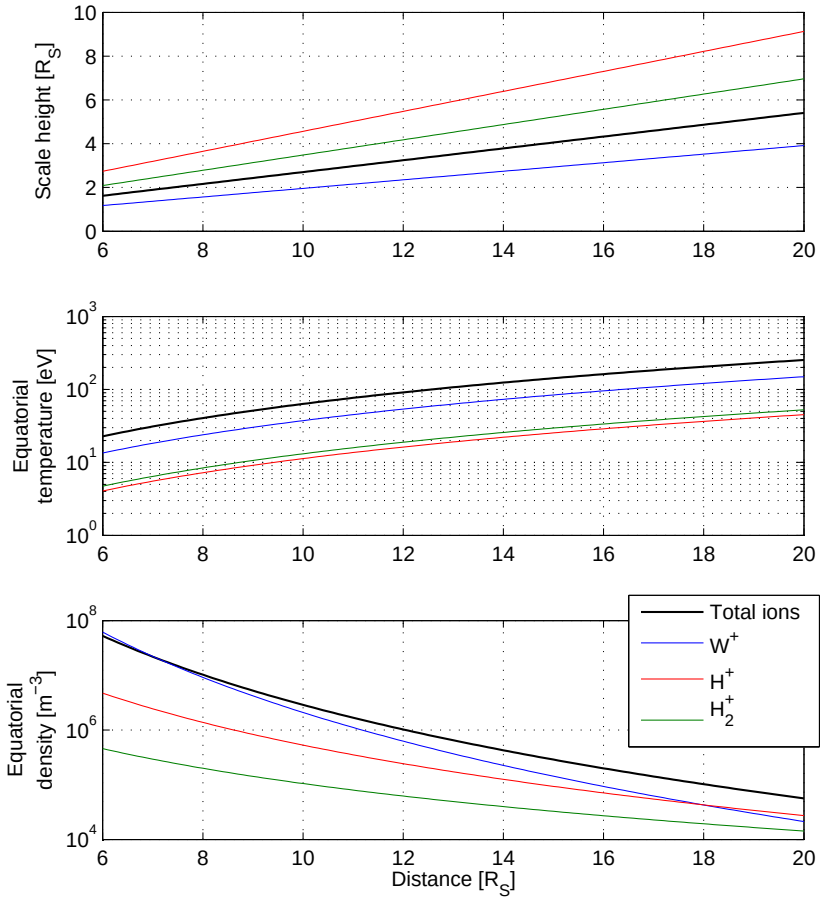

Figure 3.6: *Scale height (top), equatorial temperature (middle) and equatorial density (bottom) of total ions, water group W^+, hydrogen H^+ and molecular hydrogen H_2^+ ions in Saturn's magnetosphere as a function of radial distance to Saturn. Models derived after Thomsen et al. (2010).*

Saturn radii. Figure 3.6 (top) shows the calculated scale heights for the total ions, water group ions, protons, and molecular hydrogen. The such derived scale heights, however, should only be seen as a rough estimate because the derivation is based on a dipole magnetic field, which is not well justified at larger distances to Saturn.

The centrifugal force concentrates the ions along the magnetic field line toward the magnetic equator. The thermal energy of the ions, in particular the ion temperature parallel to the background magnetic field $T_{\parallel}$, opposes this force and leads to a spread of the plasma sheet in vertical direction. *Hill and Michel* (1976) showed for the case of Jupiter that the scale height may be thought of

Parameter	H^+	W^+	Total Ions
C	$1.01 \cdot 10^4$	$8.72 \cdot 10^6$	$1.38 \cdot 10^6$
m	4.28	6.62	5.68
A	3.19	22.9	23.8
B	1.6	8.7	4.56

Table 3.2: *Coefficients for plasma density models in units of cm^{-3} after Thomsen et al. (2010). A power-law model ($n = CL^m$) describes the radial dependence and an exponential model ($n = A\exp(-Bx)$) the latitudinal dependence, where $x = 1 - \cos^6\theta$, for a given L shell.*

as a centrifugal scale height H_c of a spin aligned dipole (see also *Bagenal and Sullivan*, 1981), which is defined by the ratio of thermal energy per mass to the centrifugal force,

$$H_c = \sqrt{\frac{2k_B T_i}{3m_i \Omega^2}} \ , \tag{3.2}$$

where Ω is the rotation frequency of the plasma. After *Thomsen et al.* (2010), the mean corotational frequency of the plasma is $\Omega = 0.6 \cdot \Omega_S$, where we use $\Omega_S = 10.8\,\mathrm{h}$ as the planetary rotation period (*Gurnett et al.*, 2011). Solving Equation (3.2) for T, we are thus able to estimate the equatorial temperatures of the ions. Figure 3.6 (middle) shows the such derived equatorial temperatures of the ion populations for a 60% corotating magnetosphere. These results have recently been validated using a more extensive data set (*Thomsen et al.*, 2014).

It is interesting to note the increase of ion temperature with radial distance to Saturn. It is reasonable to believe that the plasma flux at Saturn is stationary, i.e., production, transport and loss rates are equal on large time scales. As the plasma is produced deep inside the magnetosphere near Enceladus, it has to be transported radially outward to get lost along the magnetotail. During this transport the plasma expands, which is expected to happen almost adiabatically because the plasma is nearly collisionless. In conclusion, the temperatures of the ion populations are expected to decrease with radial distance. However, the opposite is observed, as can be seen in Figure 3.6 (middle). A similar increase of temperatures has been found by *Sittler et al.* (2008) for the ions and by *Schippers et al.* (2008) for the cold ($< 1\,\mathrm{keV}$) and hot electron populations.

The increase of thermal ion temperatures in combination with the radially increasing energetic ion pressure (*Sergis et al.*, 2009), suggests that energy is deposited into the system as the plasma moves radially outward. *Bagenal and Delamere* (2011) estimate that a total of $75-630\,\mathrm{GW}$ are needed to heat the thermal and suprathermal plasma populations to their observed temperatures. It is currently an open question, how exactly this plasma heating occurs. Part of it may come from the pickup gyrational energy of newly born ions (*Thomsen et al.*, 2010). However, we show in the later analysis of magnetic field data in Section 3.4, that the dissipated energy carried by turbulent fluctuations amounts

to a substantial part of the required energy.

3.1.3 Rotation Period

Due to the differential rotation of the visible and measurable atmosphere, Saturn's rotation period cannot be accurately estimated from observations of the surface. A good estimator for the rotation period was found in the so-called Saturn kilometric radiation (SKR), which is a modulation of auroral kilometric radio emissions at around 500 kHz. A similar observation was made at Jupiter, where a decametric radiation is modulated with the planet's magnetic field rotation period (*Carr et al.*, 1983). Because the source of the magnetic field is likely in the deep interior of the planet, the derived period is believed to reflect the internal rotation (*Kurth et al.*, 2007). Before Cassini arrived at Saturn in July, 2004, the planet had already been visited by the spacecraft Pioneer 11 as well as Voyager 1 and 2 in 1979-1981. From that era, a very fast planetary rotation period of $10^{\mathrm{h}}39^{\mathrm{m}}24^{\mathrm{s}}$ had been detected by *Desch and Kaiser* (1981). However, ongoing observations of the SKR by the spacecraft Ulysses and later with Cassini led to differences of the derived period of ∼1% from the one measured by Voyager (*Galopeau and Lecacheux*, 2000; *Gurnett et al.*, 2005), which cannot reflect an actual change in Saturn's rotation. The real rotation period of Saturn is still subject of debate (see, e.g., *Carbary and Mitchell*, 2013, and references therein).

Saturn Longitude System

The first Saturn Longitude System (SLS) was based on the SKR periodicities found by *Desch and Kaiser* (1981). The changes in the modulation period, however, were so big that a series of longitude systems were proposed to account for the variations in time. The SKR signal itself has no longitudinal variation, i.e., it is detected independent of the location of the observer. It is believed that the SKR emissions are triggered when a certain orientation of the magnetic field with regards to a position fixed in local time is reached (*Desch and Kaiser*, 1981; *Warwick et al.*, 1981).

The basic approach in the derivation of the new longitude systems SLS2 and SLS3 was to measure the SKR periodicities during Cassini's orbits with its Radio and Plasma Wave Science (RPWS) instrument (*Gurnett et al.*, 2004) and fit a polynomial of 3rd and 5th order, respectively, to the obtained data (*Kurth et al.*, 2007, 2008). *Kurth et al.* (2008) define the SLS3 system as follows: Let λ_{sun} be Saturn's subsolar longitude, i.e., the longitude of the planet that points toward the Sun. Additional to a fixed sidereal rotation period of $2\pi/\omega = 10.7928\,\mathrm{h}$, *Kurth et al.* add a phase correction term $\Phi(T)$ which is time dependent. The subsolar longitude then takes the form

$$\lambda_{\mathrm{sun}} = C_0 + \omega T - \Phi(T) \ , \tag{3.3}$$

where the constant $C_0 = 100°$. This stems from Voyager observations in the original SLS system: *Warwick et al.* (1981) found that the SKR brightens when

	Value	Std. dev.	Units
C_1	86.6681	± 20.7	$^\circ$
C_2	-2.7537	± 0.31	$^\circ\,\mathrm{d}^{-1}$
C_3	$4.7730 \cdot 10^{-3}$	$\pm 1.50 \cdot 10^{-3}$	$^\circ\,\mathrm{d}^{-2}$
C_4	$-4.8755 \cdot 10^{-6}$	$\pm 2.96 \cdot 10^{-6}$	$^\circ\,\mathrm{d}^{-3}$
C_5	$3.5653 \cdot 10^{-9}$	$\pm 2.48 \cdot 10^{-9}$	$^\circ\,\mathrm{d}^{-4}$
C_6	$-9.1485 \cdot 10^{-13}$	$\pm 7.51 \cdot 10^{-13}$	$^\circ\,\mathrm{d}^{-5}$

Table 3.3: *Coefficients and their respective standard deviations for the phase correction term in Equation* (3.4) *as given by Kurth et al. (2008).*

Saturn is thus oriented with regards to the Sun. The phase correction term $\Phi(T)$ is given as a polynomial of 5th order

$$\Phi(T) = C_1 + C_2 T + C_3 T^2 + C_4 T^3 + C_5 T^4 + C_6 T^5 \ , \tag{3.4}$$

where $T = t - T_0 - R(t)/c$ in days with T_0 being January 1, 2004, and $R(t)/c$ is the one-way light time correction, which is the time that the signal takes to travel to Cassini's position $R(t)$ with light speed c. The coefficients C_i are given in Table 3.3 together with their uncertainties.

In their presentation of the SLS3 longitude system *Kurth et al.* (2008) also mention the occurrence of a second SKR signal, which was found to have a slightly shorter period. In further analyses it became clear that this second period was connected to a SKR signal, which originated from the northern polar region, while the first SKR signal was appointed to a source in the southern polar region (*Gurnett et al.*, 2009). The fact that the southern signal is much stronger than the northern signal may be explained by asymmetric solar illumination of the poles. Before equinox in 2009, the southern hemisphere experienced summer and was constantly illuminated by the Sun. The solar irradiance leads to an increased ionization of the atmosphere, which in turn enhances the Pedersen conductivity. This may lead to stronger field-aligned currents that increase the coupling to the plasma sheet relative to the northern signal (*Gurnett et al.*, 2009). Indeed, the variations shown as a function of time in Figure 3.7 clearly reflect the importance of equinox at Saturn (*Gurnett et al.*, 2011).

Based on these findings, a new longitude system, SLS4, has been derived which includes both modulation periods and is valid until October, 2009 (*Gurnett et al.*, 2011)[1]. Similar results have been found by *Lamy* (2011)[2], who provides SKR derived periods that are valid until July, 2010. For our analysis in this chapter, we apply the SLS4 system after *Lamy* (2011) as it allows us to investigate a larger data set. Both SLS4 systems lack verification through a peer reviewed process, so that we compare our results with the older SLS3 system

[1]Accessible under `http://www-pw.physics.uiowa.edu/sls4/`.
[2]Accessible under `http://www.lesia.obspm.fr/kronos/`.

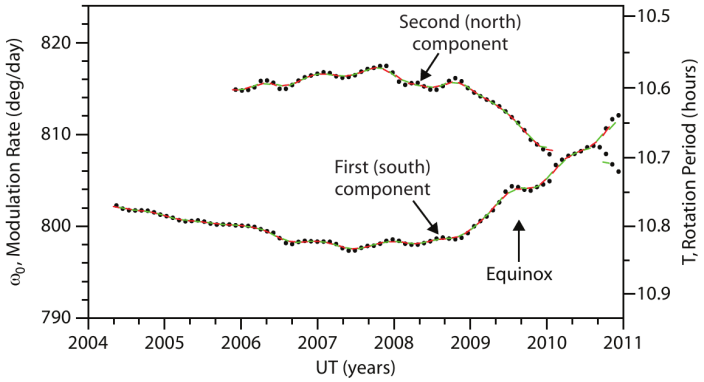

Figure 3.7: *Variation of SKR periodicities originating from the northern (SLS-N) and southern (SLS-S) hemispheres. With equinox approaching the two periods change more quickly and eventually reach equal periods. Red and green lines give running averages. Figure from Gurnett et al. (2011).*

where necessary. However, using data from the respective valid time intervals we find that our results are robust with respect to the chosen longitude system. After convergence of the signals in 2010, the SKR periods became much harder to detect. In magnetic field data, the northern signal was found to dominate but abrupt variations were detected unlike the steady changes before (*Provan et al.*, 2013). Interesting insights are to be expected from ongoing measurements.

Periodicities in Saturn's Magnetic Field

The tilt of the magnetic dipole axis with respect to Saturn's spin axis is less than 1° and the planetary magnetic field is found to be nearly axisymmetric with an equatorial magnetic field strength of 20000 nT (*Dougherty et al.*, 2005; *Burton et al.*, 2010). In contrast to Jupiter where the magnetic dipole axis is tilted with respect to the rotation axis, the rotation period should therefore not be detectable in magnetic field data. However, *Espinosa et al.* (2003) found a modulation in Voyager data with a period close to the one derived from SKR. They explained this modulation in terms of a *camshaft*: an equatorial magnetic anomaly that rotates at a fixed longitude around the planet and generates a compressional fast mode wave. The availability of better quality data provided by Cassini allowed the improvement of this model. It has been shown that the magnetic field oscillations are coupled to the SKR signals and both northern and southern periods can be seen in the data (e.g. *Gurnett et al.*, 2007; *Andrews et al.*, 2010, 2012; *Provan et al.*, 2013; *Southwood and Cowley*, 2014).

The measured signal can be explained by two magnetic field patterns that rotate around the planet with the respective northern and southern SKR periods. They are thought of as perturbative fields imposed on Saturn's internal axisymmetric magnetic field (*Dougherty et al.*, 2005; *Bunce et al.*, 2007). Figure 3.8

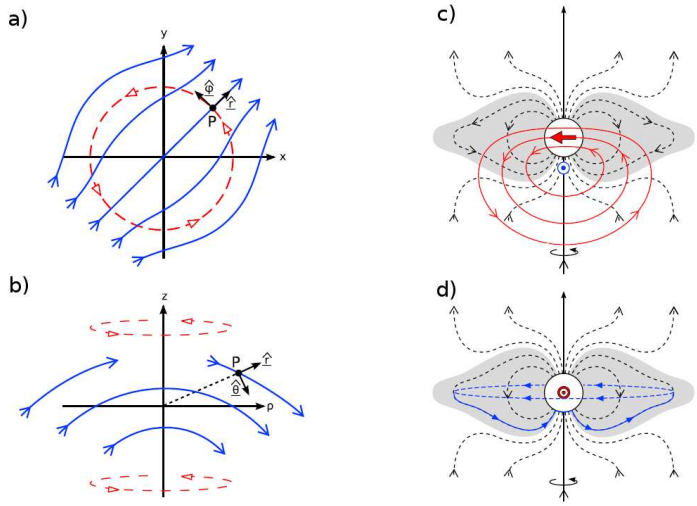

Figure 3.8: *Field lines of perturbative magnetic field pattern for southern SKR signal. (a) quasi-uniform perturbation field (blue arrows) in the equatorial plane and (b) in the meridional plane; (c) noon-midnight meridional plane with Sun to the right and red arrows indicating the quasi-dipolar perturbation field. The blue vector pointing out of the plane indicates direction of underlying current. (d) Current system shown as blue lines in a plane orthogonal to c) that may cause the magnetic field perturbations. Red vector out of the plane indicates direction of quasi-dipolar perturbation. Figures modified from Andrews et al. (2010).*

shows an example of the perturbative magnetic field (a,b,c) and the associated current system (d) from southern SKR source (*Andrews et al.*, 2010). When this pattern rotates around the planet it causes a sinusoidal perturbation, where B_r is in phase with B_θ (b) and the azimuthal component B_ϕ has a phase difference of 90° with respect to B_r (a). Here, we used KRTP coordinates, where $\mathbf{e}_r$ is directed radially away from Saturn, $\mathbf{e}_\phi$ in corotation direction, and $\mathbf{e}_\theta = \mathbf{e}_\phi \times \mathbf{e}_r$ completes the right-handed system.

The red lines in Figure 3.8 (c) show the perturbative magnetic field lines in the noon-midnight meridional plane with the Sun located to the right. The gray shaded area denotes the closed magnetic field region, where for times before equinox the southern signal is dominant. This pattern can be explained by the currents in the dusk-dawn meridional plane shown by blue lines in Figure 3.8 (d). The currents flow from left to right in the plane and close along the magnetic equator. This system was advanced to include surface currents along the open closed magnetic field boundary, which act to partly shield the signal emanating from the northern polar cap. Thus, the dominance of the southern signal in the closed field line region and a fractional leakage of the signals to the opposite hemispheres could be explained (*Andrews et al.*, 2012; *Southwood and Cowley*, 2014).

The maximum SKR intensity is found when the magnetic field of the rotating pattern shown in Figure 3.8 is directed roughly tailwards toward 2 h local time (*Andrews et al.*, 2010). It can be shown that the perturbations of B_r cause the magnetic equator to rock up and down, while the variation of B_θ causes the magnetic pressure to oscillate with the planetary period (*Arridge et al.*, 2011; *Andrews et al.*, 2010). We discuss these observations in terms of potential energy injections later in Section 3.2.3.

3.2 Plasma Dynamics in Saturn's Magnetosphere

Saturn's magnetosphere is a very dynamic environment. In this section we present important observations from the Cassini era that are crucial to understand for the interpretation of magnetic field measurements in Saturn's plasma sheet. The observed phenomena cover a large range of scales and are in part related to plasma production and transport processes as well as current sheet dynamics induced by the varying solar wind conditions. In the aspect of plasma turbulence it is of specific interest if these dynamics inject energy into the system, which may then be nonlinearly cascaded to smaller scales. Also, some of the observed phenomena may affect our spectral analysis of magnetic field data and therefore have to be thoroughly investigated.

3.2.1 Plasma Production: Ion Cyclotron Waves

Neutrals emanating from Enceladus' plumes rotate around Saturn on Kepler orbits and form an extended neutral cloud (*Fleshman et al.*, 2013; *Cassidy and Johnson*, 2010). The plasma, which nearly corotates with the planet, has a much higher azimuthal velocity and therefore constantly overtakes the neutrals. Hence, when a neutral collides with an ion and charge exchange takes place, the newly formed ion is much slower than surrounding plasma and the corotating magnetic field lines. Hence, it experiences an electric field $\mathbf{E} = -\mathbf{v} \times \mathbf{B}_0$ in radial direction away from Saturn perpendicular to the background magnetic field $\mathbf{B}_0$. The electric field generates a radial current, which is closed in the ionosphere by field-aligned Birkeland currents, and accelerates the plasma via $\mathbf{j} \times \mathbf{B}_0$ forces. Thus, the rotational torque to accelerate the plasma in azimuthal direction comes ultimately from the planetary rotation (*Vasyliunas*, 1983). As the ion moves with respect to the magnetic field, it starts to gyrate perpendicular to the magnetic field with the ion cyclotron frequency Ω_i. This leads to an unstable ring distribution of energy, which may trigger ion cyclotron waves propagating parallel to the magnetic field (*Leisner et al.*, 2006) and non-propagating mirror mode waves (*Russell et al.*, 2006). These waves are thus an indicator of pickup processes. Such ion cyclotron waves have been frequently observed in Saturn's inner magnetosphere ($< 6\,R_\mathrm{s}$) (*Russell et al.*, 2006; *Leisner et al.*, 2006, 2011). They can be easily identified in power spectra of magnetic field measurements, where they lead to elevated energy of the perpendicular magnetic field components at the respective ion cyclotron frequency. As we analyze power spectra

in terms of turbulent cascading processes, the dominance of ion cyclotron waves inside $6\,R_s$ inhibits us from an investigation of this region. Therefore, we confine our analysis to distances greater than $6\,R_s$.

3.2.2 Plasma Transport: Interchange Instability

The plasma is produced deep inside Saturn's magnetosphere close to Enceladus' orbit from where it is slowly transported outward. The density is found to peak at $\sim 4\,R_s$ and drops with distance to Saturn close to a power-law as has been found by *Thomsen et al.* (2010) (see Figure 3.6). Combined with the centrifugal force acting on the nearly corotating plasma, this leads to a large scale instability, which drives so-called flux-tube interchanges (*Hill and Michel*, 1976). This instability is conceptually equivalent to a Rayleigh-Taylor instability of a dense fluid on top of a lesser dense fluid with a centrifugal instead of gravitational force. Here, flux-tubes that contain dense and cold plasma are radially displaced outward in interchange with flux-tubes containing hot and tenuous plasma from farther out.

These interchange processes are usually observed as sharp diamagnetic cavities, i.e., a strong decrease of magnetic pressure, in Saturn's magnetosphere in a range of approximately $6-10\,R_s$ (*Leisner and Russell*, 2005; *André et al.*, 2005, 2007). However, sometimes the opposite is observed: interchange processes associated with an increase of magnetic pressure (see, e.g., event E in *André et al.*, 2007). The flux-tube interchanges can also be seen in CAPS and MIMI (Magnetospheric Imaging Instrument, *Krimigis et al.* (2004)) data as characteristic signatures of energetic ($> 1\,\mathrm{keV}$) ions and electrons (*Mauk et al.*, 2005; *Burch et al.*, 2005; *André et al.*, 2007; *Hill et al.*, 2005; *Müller et al.*, 2010) and have been simulated in numerical models of Saturn's magnetosphere (*Liu et al.*, 2010). Figure 3.9 shows measurements of magnetic field pressure and electron energies during several interchange events observed in the outbound leg of Cassini's Revolution A around Saturn (Rev A) and the results of numerical simulations of Saturn's middle magnetosphere in the left and right panel, respectively. During the outbound leg of Rev A (see also Section 3.3.5 for a spectral analysis of MAG data) the CAPS data (lower panel) show a significant increase in hot ($> 1\,\mathrm{keV}$) electrons inside the regions of increased pressure, e.g., around 19:05 UT and 19:30 UT. At the same time the cold electron population with energies $\sim 10\,\mathrm{eV}$ vanishes.

The azimuthal cross section of the flux-tubes has been estimated from the length of the observed diamagnetic depression and the corotation velocity at the respective location as less than $1\,R_s$ (*Leisner and Russell*, 2005). However, the radial extent of the flux-tubes may be much larger (*Burch et al.*, 2005; *Liu et al.*, 2010). It is interesting to note that in the vicinity of flux-tube interchanges, an enhanced wave activity has been detected. These include transverse broadband ultra low frequency waves (*Leisner and Russell*, 2005), narrow banded electron cyclotron waves and whistler mode chorus emissions (*Hospodarsky et al.*, 2008; *Menietti et al.*, 2008). It is also reasonable to expect the generation of Alfvén

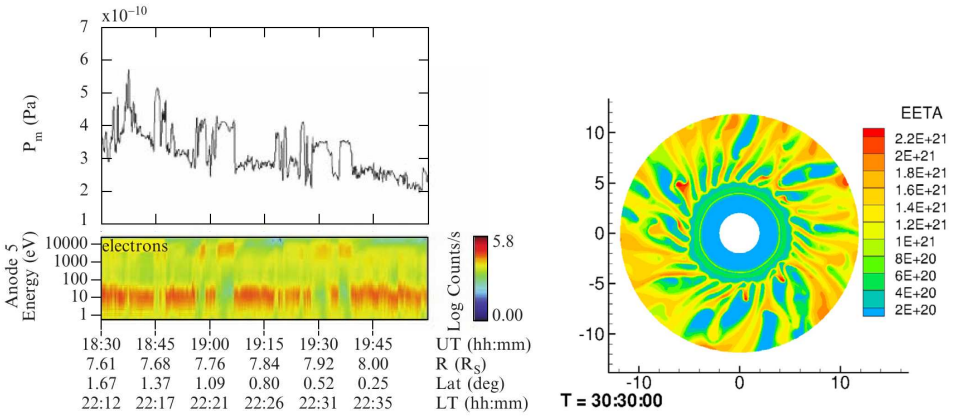

Figure 3.9: *Left: observations of magnetic pressure (MAG) and electron energies (CAPS) from André et al. (2007) during a period of several flux-tube interchanges, right: quasi steady state of numerical simulation of the interchange instability in Saturn's magnetosphere from Liu et al. (2010), where the color represents flux-tube ion content in ions/Wb.*

waves from such strong magnetic disturbances. Flux-tube interchanges may therefore be seen as a means of energy injection for turbulent fluctuations.

There is another class of interchange events that arise from reconnection in the magnetotail and usually last much longer (up to 20 h) and contain even more energetic plasma of hundreds of keV (*Thomsen et al.*, 2013). These particle injections from the magnetotail can also create large corotating clouds of energetic neutral atoms (ENA) when the hot plasma reaches the inner magnetosphere and charge exchange with atoms from the neutral cloud takes place (*Mitchell et al.*, 2009; *Krupp et al.*, 2009). *Mitchell et al.* (2009) argue that the azimuthal pressure gradient caused by the energetic particle injections may produce field-aligned currents that are linked to SKR generation.

3.2.3 Current Sheet Dynamics

Cassini data showed the presence of an azimuthally directed ring current in Saturn's magnetic equator ranging from $6\,R_\mathrm{s}$ up to the magnetopause on the day side at $20\,R_\mathrm{s}$ (*Krimigis et al.*, 2007; *Sergis et al.*, 2010). The region of strong current signatures in the plasma sheet is therefore also-called the current sheet. The main drivers of this current are the plasma pressure gradient inside $\sim 18\,R_\mathrm{s}$ and the centrifugal force outside of this distance, which act to balance the radially inward directed curvature stress of magnetic field lines (*Arridge et al.*, 2007; *Kellett et al.*, 2010). The induced magnetic field is opposed to the background planetary magnetic field at the inner edge of the current sheet. *Kellett et al.* (2009) find that the current sheet on the day side has a mean half-thickness of $\sim 1.5\,R_\mathrm{s}$.

Due to the strong centrifugal force, the magnetic field is stretched into a

magnetodisc configuration, whose extent on the day side is controlled by the dynamic solar wind pressure. In a highly compressed state, when the magnetopause standoff distance is found inside Titan's orbit, the current sheet is less strong and the magnetic field adopts a quasi-dipolar configuration (*Arridge et al.*, 2008b; *Achilleos et al.*, 2010; *Jia et al.*, 2012a). The solar wind also distorts the current sheet into a bowl shape away from the equator. This effect is strongest at solstice, when the inclination of Saturn with regards to the solar wind direction and therefore the exerted force on the current sheet is maximal (*Arridge et al.*, 2008a). The dynamical state of the current sheet can also be seen in flapping motions of the magnetic equator, which is defined at $B_r = 0$ (*Jia et al.*, 2012b). Several crossings of the equator are often observed in a short period of order $10-20\,\mathrm{min}$ (*Arridge et al.*, 2007). Radial currents in the current sheet close field aligned currents that enforce corotational acceleration of the plasma (*Vasyliunas*, 1983). It has also been shown that patterns of radial currents rotate around Saturn with the SKR periods of northern and southern sources (*Andrews et al.*, 2010, 2012; *Provan et al.*, 2013; *Southwood and Cowley*, 2014). These patterns are shown in Figure 3.8 and constantly stir the plasma sheet, thus transferring energy from the planet into the magnetosphere.

In summary, the current sheet is a dynamic structure driven from internal (planetary) as well as external (solar wind) sources. It is reasonable to assume that internal sources lead to a potential longitude dependence of magnetospheric parameters while external sources are reflected in potential local time asymmetries. As the current sheet is host of a substantial part of Saturn's magnetospheric plasma, approximately $10^6\,\mathrm{kg}$ of plasma are expected in the magnetodisc (*Arridge et al.*, 2008b), its dynamics are a major contribution to the turbulent magnetic field fluctuations.

3.3 Turbulent Magnetic Field Fluctuations

In the preceding Sections we have presented the general properties of Saturn's magnetosphere as they have been previously found by several authors. After some basic considerations for plasma turbulence at Saturn, we present the data for our analysis of magnetic field fluctuations at Saturn. We discuss these fluctuations in detail in a case study of Cassini's second orbit and show that a turbulent cascade is able to develop in Saturn's magnetosphere. We also analyze the statistical properties and compare them to solar wind observations.

3.3.1 Basic Considerations for Magnetospheric Turbulence

In this section, we shortly summarize the magnetospheric dynamics originating from internal and external sources in order to discuss them in the framework turbulence. We consider these dynamics as potential energy injection mechanisms, which work on a large range of scales. Let us first discuss the external sources: energy injection on large scales is caused by varying solar wind conditions, which compress the magnetosphere on the day side and severely alter

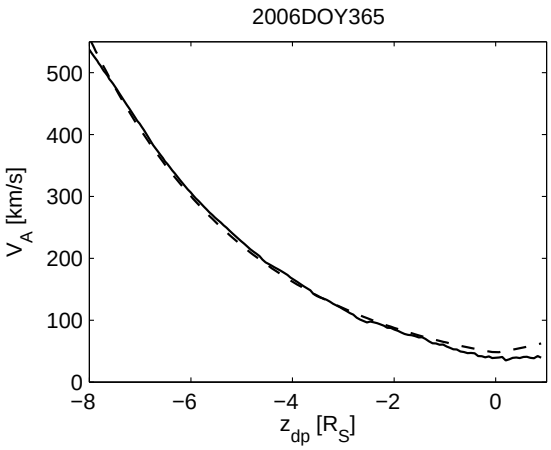

Figure 3.10: *Alfvén speed V_A as a function of height over magnetic equator z. Solid line: Alfvén speed calculated from measured background magnetic field B_0 and density model ϱ from Thomsen et al. (2010); dashed line: exponential fit used to estimate a transit time of $\tau_H \sim 2.3\,h$.*

the structure of the day side current sheet (*Achilleos et al.*, 2010). The magnetopause moves several Saturn radii inwards during high pressure periods and compresses the plasma in the magnetosphere. The solar wind pressure varies on time scales of days, although corotating interaction regions can lead to faster variations driving additional dynamics in the magnetotail and cusps (*Jackman et al.*, 2004; *Kimura et al.*, 2013). The effect of external sources are strongest in the outer magnetosphere, where the magnetodisc develops during low pressure states.

The potential energy injections due to internal sources are directly or indirectly connected to Saturn's fast rotation: the rotating pattern of radial currents, which leads to a rocking of the current sheet on time scales of Saturn's rotation period (*Andrews et al.*, 2010); flux-tube interchanges, which are sporadically observed inside $10\,R_\mathrm{s}$ on scales less than $1\,R_\mathrm{s}$ and which are linked to plasma wave generation (*Leisner and Russell*, 2005); plasma shear flow as the observations of *Thomsen et al.* (2010) indicate; and current systems that accelerate newly born ions to corotation speeds. Due to the large extent of the neutral cloud the latter should happen regularly over a region of roughly $4{-}9\,R_\mathrm{s}$ (*Mauk et al.*, 2005; *Fleshman et al.*, 2013; *Cassidy and Johnson*, 2010). The temperature anisotropy which goes along with ion pickup further leads to instabilities favoring the generation of ion cyclotron and mirror mode waves (*Russell et al.*, 2006). Lastly, we note large scale convection patterns needed to shed off the internally produced plasma. It is believed that a mixture of Dungey and Vasyliunas cycle control the magnetospheric plasma transport. Although these processes have not yet been observed directly, there are indicators for their existence, e.g., plasmoid formation or auroral activity in the midnight to dawn sector (*Cowley et al.*, 2005; *Jackman et al.*, 2008; *Jia et al.*, 2012a).

In conclusion, Saturn's magnetosphere can be seen as rich in instabilities on several time and length scales, which cause magnetic field perturbations. But how are these phenomena linked to our analysis and why should a turbulent cascade develop in Saturn's magnetosphere? Most of the energy injection mechanisms have characteristic length scales much larger than an ion gyro radius and frequencies much lower that the ion cyclotron frequency. Therefore, the magnetic perturbations associated to the energy injections happen on MHD scales and generate Alfvén waves. These waves propagate along magnetic field lines until they are reflected at density gradients, e.g., close to the ionosphere. Thus, the Alfvén waves travel back and forth and are able to nonlinearly interact with counter-propagating waves. Most of these interactions happen in the plasma sheet.

This can be seen in Figure 3.10, where we show the Alfvén speed as a function of height over magnetic equator z (solid line) obtained during a high inclination orbit of Cassini in December, 2006. Cassini crossed the magnetic equator at $10\,R_\mathrm{s}$, where the scale height is $H = 2.7\,R_\mathrm{s}$. The measured velocity profile, $V_\mathrm{A}(z)$, can well be fitted by an exponential function (dashed line). Here, we used the density profile given by *Thomsen et al.* (2010) to estimate the transit time, i.e., the time it takes for an Alfvén wave to travel from one hemisphere to another, as

$$\tau_H(r) = \int_S^N \frac{1}{V_\mathrm{A}(z,r)} \mathrm{d}s \ , \tag{3.5}$$

where the integration is from southern to northern ionosphere along the magnetic field line. However, the Alfvén speed V_A increases dramatically in the lobes because of the low plasma density. As a rough estimation, we may simplify Equation (3.5) and integrate the fitted exponential function along the high inclination orbit, which is approximately in vertical direction.

This estimation results in a transit time of $\sim$2.3 h using infinite integration boundaries. More than half of that time, namely 1.4 h, is spent inside $\pm 3\,R_\mathrm{s}$ so that we can assume a major part of the interactions to happen inside the plasma sheet. Note, that the density gradient between plasma sheet and lobe may already be strong enough to partially reflect the Alfvén waves so that part of the wave packet does not leave the plasma sheet at all (see *Wright*, 1987; *Jacobsen et al.*, 2007, for Alfvén wave reflection in Jupiter's plasma sheet). We can therefore expect the excited Alfvén waves to be able to travel numerous times along the magnetic field lines, so that many interactions between counter-propagating wave packets will take place in the plasma sheet. These interactions are the necessary condition for a turbulent cascade to develop.

We have now laid the cornerstone for our turbulence analysis: We have shown that a sufficient number of energy injection mechanisms exist in Saturn's magnetosphere. These injection mechanisms create Alfvén waves which travel along the magnetic field lines, are reflected and interact with each other predominantly

in the plasma sheet. In the absence of strong dissipation, which is the case in the nearly collisionless magnetospheric plasma at Saturn, these are the requirements for plasma turbulence. We may therefore begin with our analysis of turbulent magnetic field fluctuations in the following sections.

3.3.2 Processing of Magnetic Field Data

We analyze magnetic field data from Cassini's flux-gate magnetometer (FGM) of the MAG experiment (*Dougherty et al.*, 2004) measured in Saturn's plasma sheet. The magnetic field data is obtained from the Planetary Data System (PSD[3]) in KRTP (Kronocentric Radial Theta Phi) coordinates, which is a Saturn centered spherical coordinate system. Here, $\mathbf{e}_r$ points from Saturn to Cassini, $\mathbf{e}_\phi = \mathbf{e}_\mathrm{s} \times \mathbf{e}_r$ points in the direction of corotation from dawn to dusk ($\mathbf{e}_\mathrm{s}$ is aligned with Saturn's spin axis) and $\mathbf{e}_\theta = \mathbf{e}_\phi \times \mathbf{e}_r$ points in latitudinal direction from north to south, thus forming a right handed coordinate system. We also use a magnetic field-aligned Cartesian coordinate system (x, y, z), where $\mathbf{e}_z = \mathbf{B}_0/B_0$ is aligned with the global mean magnetic field $\mathbf{B}_0 = \langle \mathbf{B} \rangle$ (where $\langle * \rangle$ means temporal average), $\mathbf{e}_y = \mathbf{e}_v \times \mathbf{e}_z$ is perpendicular to the plasma velocity and the mean magnetic field and $\mathbf{e}_x = \mathbf{e}_y \times \mathbf{e}_z$ is quasi-parallel to the plasma velocity, thus completing the right handed system. Here, we use the plasma velocity relative to the Cassini spacecraft, $\mathbf{v} = \mathbf{v}_\mathrm{pl} - \mathbf{v}_\mathrm{cas}$, where we assume $\mathbf{v}_\mathrm{pl}$ to be purely azimuthal with 60% of strict corotation speed (*Thomsen et al.*, 2010). The magnetic field data is interpolated onto a temporal equidistant grid of $\Delta t = 0.14\,\mathrm{s}$. The maximal sampling frequency of the FGM is 32 Hz.

Power spectral densities (PSD) of 10 min time series are estimated in field-aligned coordinates using a wavelet transform

$$W_i(t,p) = \sum_{j=1}^{N} b_i(t,\Delta t)\ \Psi\left(\frac{t_j - t}{p}\right), \quad i = x, y, z \tag{3.6}$$

where Ψ is a Morlet mother wavelet and p the wavelet period with the equivalent Fourier frequency $f = (1.03p)^{-1}$ (*Farge*, 1992; *Torrence and Compo*, 1998). We use increment time series

$$b_i(t,\tau) = B_i(t+\tau) - B_i(t) \tag{3.7}$$

with time separation $\tau = \Delta t$ to suppress the slowly varying background field of Saturn (i.e., we prewhiten the data according to *Bieber et al.* (1993)). This leads to wavelet coefficients

$$W_\parallel^2 = |W_z|^2, \quad W_\perp^2 = |W_x|^2 + |W_y|^2 \tag{3.8}$$

for fluctuations parallel and perpendicular to the mean magnetic field, respec-

[3] `http://ppi.pds.nasa.gov`

tively. Note, that these fluctuations are defined with respect to the global magnetic field. For spectra of time series longer than 10 min the field-aligned system is less accurate due to variations of the background magnetic field. Therefore, we calculate wavelet coefficients

$$W_{\parallel}^2 = |W_{|B|}|^2 \tag{3.9}$$

from the magnetic field strength $|\mathbf{B}(t)|$ and use

$$W_{\perp}^2 = \sum_{i=x,y,z} |W_i|^2 - W_{\parallel}^2 \ . \tag{3.10}$$

This allows us to determine the energy of the fluctuations and their orientation with respect to a local mean magnetic field (*Alexandrova et al.*, 2008b; *Horbury et al.*, 2008). Compressible fluctuations will be well approximated by fluctuations of the magnetic field strength according to Equation (3.9), if the relative fluctuation is small, $\delta B/B_0 \ll 1$. This condition is usually well satisfied within Saturn's middle magnetosphere. The PSD of a component i of the magnetic field is calculated as

$$P_i(f) = \frac{1}{4\sin^2(\pi f \Delta t)} \frac{2\Delta t}{N} \sum_{j=1}^{N} |W_i(t_j, f)|^2 \ , \tag{3.11}$$

where the factor $\left(4\sin^2(\pi f \Delta t)\right)^{-1}$ ensures energy conservation (i.e., post-darkening according to *Bieber et al.* (1993)). Note, that when we refer to the corresponding wavelet spectra as parallel or perpendicular, we are referring to the diagonal components of the spectral tensor and not to the direction of wave vector $\mathbf{k}$ or relative plasma flow $\mathbf{v}$ with respect to the global magnetic field $\mathbf{B}_0$.

To analyze the statistical nature of the fluctuations and to estimate the intermittency, we calculate the flatness F. This can be done directly from centered increment time series $b_i'(t,\tau) = b_i(t,\tau) - \langle b_i(t,\tau)\rangle$ for different temporal separations $\tau = n \cdot \Delta t$:

$$F_i(\tau) = \frac{\left\langle b_i'(t,\tau)^4 \right\rangle}{\left\langle b_i'(t,\tau)^2 \right\rangle^2} \ . \tag{3.12}$$

A Gaussian distribution results in a value of $F = 3$. The scale dependent flatness can be used to test the fluctuations for intermittency. We note, that it is also possible to estimate the flatness from wavelet coefficients (*Alexandrova et al.*, 2008a). However, this method yields qualitatively the same results and, therefore, we restrict our analysis to the flatness calculated with Equation (3.12).

3.3.3 Measured Parameters of the Magnetic Field

In this section, we provide a basic overview on the data used for the analysis and present characteristic parameters derived from the magnetic field data. To gain a basic understanding of the system, we present in Figure 3.11 parameters

derived from the magnetic field measurements: a) background magnetic field B_0, b) gyro radius, ρ_W, and inertial length, λ_W, of the dominant water group ion species, c) thermal ion plasma $\beta_i = p/p_B$, i.e., we neglect the pressure of the suprathermal population and d) the Alfvén velocity V_A. The results are obtained from 10 min time series during the equatorial orbits of Cassini from 2004-2009 (see also Section 3.5.1). The parameters denoted with a red line in Figure 3.11 (b,d) (λ_w, v_co) are derived solely from the basic magnetospheric model given by *Thomsen et al.* (2010) and thus show no scatter. For the analyses in this thesis, we use the density of water group ions calculated with the power-law model given in Table 3.2 according to

$$n_W = 8.72 \cdot 10^{12}\, r^{-6.62} \cdot e^{-\frac{|z-z_\mathrm{cs}|}{H_W}} \ , \tag{3.13}$$

where r is in units of Saturn radii and z is the height of the spacecraft over the geographic equator. This density is further corrected according to the scale height of water group ions, H_W, with respect to the center of the plasma sheet (Equation (3.1)). The temperature of the plasma is derived according to Equation (3.2). In Figure 3.11, we only show data deep inside the plasma sheet with $|z|/H < 0.1$, where H is the plasma scale height of total ions.

From Figure 3.11a, it is visible that the magnetospheric magnetic field in the equatorial region inside 12 R_s is close to a dipole field (red line, $\propto r^{-3}$). However, beyond that distance the magnetic field decreases less strong due to the radially stretched magnetic field lines in magnetodisc configuration. Compared to the solar wind, the magnetic field is strong as it reaches almost 100 nT at 6 R_s. The gyro radius and inertial length generally increase with distance to Saturn and differ significantly only inside 10 R_s. In the outer magnetosphere, they reach values of more than 1000 km, which is about ten times larger than the average gyro radius at 1 AU. The thermal ion plasma β_i, which can be expressed in terms of gyro radius and inertial length as $\beta_i = \rho_\mathrm{w}^2/\lambda_\mathrm{w}^2$, is generally less than or around unity with a maximum reached at $\sim$13 R_s. Inside 8 R_s the plasma β_i even drops to 0.1. This states the importance of the planetary magnetic field for the magnetospheric plasma dynamics. In the solar wind, where the ion plasma is usually on the order of unity (*Bruno and Carbone*, 2005, Ch. 12), such low values are only found sporadically.

In Figure 3.11d, we can see that the Alfvén speed V_A is generally comparable to the plasma velocity v_pl. This is unlike the solar wind, where usually $V_\mathrm{A} \ll v_\mathrm{pl}$. The speed of the spacecraft is negligible compared to the plasma speed, which nearly triples in the middle magnetosphere from 6−20 R_s. This strong change in the velocity profile is reflected in the measurement: dependent on the distance to Saturn, a structure of fixed size that is convected over the spacecraft would appear at different frequencies in the spacecraft frame. To compare measurements at different locations, we therefore have to transform our observation in spacecraft frame into the rest frame of the plasma. However, the fact that $V_\mathrm{A} \sim v_\mathrm{pl}$ complicates this transformation, which we discuss in Section 3.3.4.

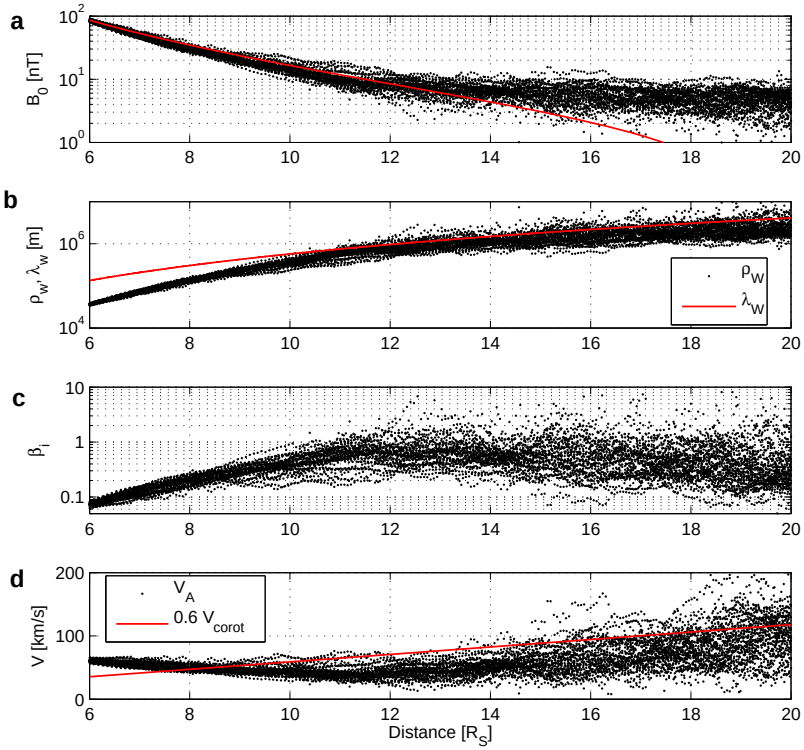

Figure 3.11: *Basic parameters in Saturn's magnetosphere derived from magnetic field data of* 10 *min time series: a) background magnetic field* B_0 *(black dots) and dipole field (red line), b) gyro radius* ρ_w *(black dots) and inertial length* λ_w *(red line) of water group ions, c) thermal ion plasma* β_i *and d) Alfvén speed* V_A *(black dots) and mean plasma corotation speed* $v_\mathrm{pl} = 0.6 \cdot \Omega_\mathrm{s} r$ *(red line).*

We estimate the energy of the fluctuations in Saturn's magnetosphere with the average root-mean-square of the components $i = x, y, z$ of the 10 min time series according to

$$\delta B = \sqrt{\delta B_x^2 + \delta B_y^2 + \delta B_z^2} \ , \tag{3.14}$$

where $\delta B_i = \sigma_i$ is the standard deviation of the ith component. The RMS generally reflects the energy of low frequencies because they contain most of the energy of the time series. This can be seen in the power spectral densities, which usually follow a negative power-law with most power in the lowest resolved frequencies. To minimize the influence of the varying internal magnetic field over the 10 min time range, we subtract a linear mean before we compute the RMS. This has proven to be more efficient than subtraction of an internal magnetic field model based on Cassini measurements (*Dougherty et al.*, 2005; *Bunce et al.*,

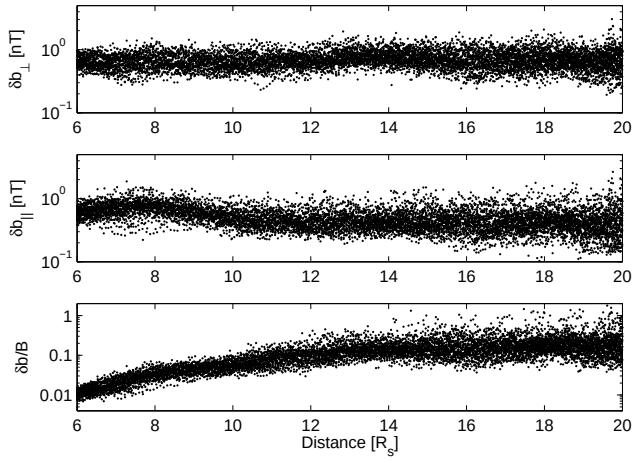

Figure 3.12: *Top: RMS of fluctuations perpendicular to the mean magnetic field $\delta B_\perp$, middle: RMS of fluctuations parallel to the magnetic field $\delta B_\parallel$, and bottom: relative fluctuation energy $\delta B/B_0$. The relative fluctuation energy shows a clear radial dependence, while the RMS of perpendicular and parallel fluctuations are rather constant. Parallel fluctuations are slightly increased close to Saturn indicating stronger compressional fluctuations.*

2007). The results are shown in Figure 3.12 for $|z|/H < 0.1$, where the top panel shows the energy of fluctuations perpendicular to the magnetic field, $\delta B_\perp = \sqrt{\delta B_x^2 + \delta B_y^2}$, the middle panel shows the fluctuations parallel to the magnetic field, $\delta B_\parallel = \delta B_z$, and the bottom panel shows the relative fluctuation energy $\delta B/B_0$.

From the radial profiles in Figure 3.12, it can be seen that the fluctuations $\delta B_\perp$ are quite constant and homogeneous throughout Saturn's magnetosphere. The RMS $\delta B_\parallel$ is slightly increased at $8\,R_\mathrm{s}$ close to Saturn, which indicates that compressible fluctuations are enhanced at this distance. Still, also the parallel fluctuations vary only slightly in the analyzed range of $6{-}20\,R_\mathrm{s}$. The relative fluctuation level $\delta B/B_0$ is generally weak with $\delta B/B_0 < 0.1$ inside $9\,R_\mathrm{s}$ but increasing with distance. Such small relative fluctuations may lead to the assumption of a weak turbulent cascade close to Saturn. However, later we see that the large scale fluctuations are primarily controlled by magnetospheric processes and the RMS may therefore be misleading in the interpretation of the turbulence characteristics. In general, the absence of systematic changes of the RMS within the equatorial region of the plasma sheet indicates a certain homogeneity of the magnetosphere.

3.3.4 On the Geometry of the Observations

An important aspect for the analysis of the fluctuations' spectral densities as a function of frequency in spacecraft frame is the measurement geometry. The important question we have to answer is: what is the corresponding wave vector direction of the magnetic fluctuations, which Cassini measures? The relative velocity of the plasma bulk flow with respect to Cassini in Saturn's magnetosphere is on the order of the Alfvén velocity (see Figure 3.11), which means that Taylor's hypothesis cannot be applied as straight-forward as, e.g., in the solar wind. To apply Taylor's frozen-in approximation we have to show that 1) the fluctuation velocity is much smaller than the bulk flow velocity and 2) the wave frequency in the plasma frame, ω, is much smaller than the Doppler shift in frequency created by the waves propagating past the spacecraft (*Taylor*, 1938). From the measured data, we can show that the Alfvén velocity fluctuations $\delta V_\mathrm{A} = \delta B/\sqrt{\mu_0 \varrho}$ are indeed much smaller than the relative plasma velocity ($\langle \delta b/v \rangle = 0.05$) and the Alfvén velocity ($\langle \delta b/V_\mathrm{A} \rangle = 0.07$). However, to show the second point, we have to make certain assumptions that we now explain in detail.

Turbulent fluctuations are known to cascade preferentially perpendicular to the background magnetic field (e.g. *Matthaeus et al.*, 1990; *Bieber et al.*, 1996; *Sahraoui et al.*, 2010), which results in wave numbers $k_\perp \gg k_\parallel$. This allows us to express the angle Φ_{kv} between wave-vector $\mathbf{k}$ and relative plasma flow velocity $\mathbf{v}$ through the angle θ between $\mathbf{B}_0$ and $\mathbf{v}$, namely $\cos\Phi_{kv} \simeq \sin\theta$ (e.g. *Mangeney et al.*, 2006; *Bourouaine et al.*, 2012). In Saturn's magnetosphere, the plasma flow is nearly perpendicular to the mean magnetic field ($\theta \sim 90°$). Thus, the frequency measured in spacecraft frame can be written as

$$\begin{aligned} 2\pi f &= \mathbf{k}\cdot\mathbf{v} + \omega \\ &\simeq k_\perp v \sin(\theta) + \omega \end{aligned} \tag{3.15}$$

and we are left to show that $k_\perp v \sin(\theta) \gg \omega$. In the case of kinetic Alfvén waves the linear wave frequency according to Equation (2.47) is $\omega \sim k_\parallel V_\mathrm{A} k_\perp \rho_i$. Hence, Taylor's hypothesis is applicable if

$$\begin{aligned} k_\perp v &\gg k_\parallel V_\mathrm{A} k_\perp \rho_i \\ \Leftrightarrow \quad \frac{v}{V_\mathrm{A}} &\gg k_\parallel \rho_i \ . \end{aligned} \tag{3.16}$$

The left-hand side of Equation (3.16) is approximately unity because $v_\mathrm{rel} \sim V_\mathrm{A}$ and we already used $\theta \sim 90°$. This means that $k_\parallel \rho_i \ll 1$ must be fulfilled. However, kinetic Alfvén waves only exist in this regime. Therefore, Taylor's hypothesis can be applied in case of turbulence with $k_\perp \gg k_\parallel$ and fluctuations caused by kinetic Alfvén waves or convected structures with $\omega = 0$ (see also *Howes et al.*, 2014a). For Alfvén waves with $\omega \sim k_\parallel V_\mathrm{A}$, Equation (3.16) reduces to $1 \gg k_\parallel/k_\perp$, which is given according to our basic assumption of a primarily perpendicular cascade.

It is also possible to argue with the phase velocity of KAW, $v_\mathrm{ph} = \omega/k \sim$

$V_\mathrm{A}\cos(\theta_{kB})$, where θ_{kB} is the angle between wave vector $\mathbf{k}$ and magnetic field $\mathbf{B}_0$ (*Baumjohann and Treumann*, 1997, Eq. (10.181)). Dividing Equation (3.15) by $k_\perp \sim k$ (since $k_\perp \gg k_\parallel$), we find that $v_\mathrm{rel} \gg V_\mathrm{A}\cos(\theta_{kB})$ must be fulfilled. For turbulence with wave vectors $k_\perp \gg k_\parallel$ this is true because the perpendicular phase velocity for $\theta_{kB} \sim 90°$ is very low and thus much smaller than the plasma bulk flow in Saturn's magnetosphere. Fluctuations due to whistler waves, however, violate Taylor's hypothesis because $v_\mathrm{ph}(\theta{\sim}90°) \geq V_\mathrm{A}$ and their wave vectors are not restricted to $k_\parallel \rho_i \ll 1$ (*Howes et al.*, 2014a). Therefore, we can only interpret our results in terms of KAW turbulence.

Using thermal ion temperatures T and densities ϱ corrected for the height over the plasma sheet (*Achilleos et al.*, 2008; *Thomsen et al.*, 2010), we can calculate the ion gyro radius ρ_i (with $T_\perp \approx T$) and the ion inertial length λ_i to transform the observed frequency f to normalized perpendicular wave numbers

$$k_\perp s = \frac{2\pi f}{v\sin(\theta)} s \ , \tag{3.17}$$

where $s = \rho_i, \lambda_i$ denotes the ion gyro radius or the ion inertial length, respectively. Accordingly, power spectra $P(f)$ are transformed to the corresponding normalized wave number spectra

$$E(k_\perp s) = \frac{v\sin(\theta)}{2\pi s} P(f) \ , \tag{3.18}$$

which assures energy conservation: $\int Es\,\mathrm{d}k_\perp = \int P\,\mathrm{d}f$. Alternatively, we use a frequency normalization, $f \to f/f_\mathrm{ci}$, with respect to the ion cyclotron frequency.

3.3.5 Case Study of Cassini's Second Orbit

In this section, we discuss the second orbit (Rev A) of Cassini around Saturn from 26 to 28 October 2004, where we analyze in detail the magnetic field fluctuations found in Saturn's magnetosphere and the inherent magnetospheric dynamics. We show that magnetic fluctuations cover all measured frequencies and turbulent spectra with well-defined power-laws are observed. At MHD scales the shape of the spectra and the nature of fluctuations are controlled by large scale processes in the magnetosphere, while at kinetic scales ($k_\perp \rho_W > 1$) all spectra are similar. Figure 3.13 shows the trajectory of Cassini during its second orbit around Saturn in Kronocentric Solar Magnetic (KSM) coordinates. In this coordinate system the x-axis points to the Sun, the y-axis to dawn and the z-axis lies in the plane spanned by the x-axis and Saturn's spin axis. During the whole orbit Cassini stays inside the scale height of the plasma sheet reaching a maximum of $|z|/H = 0.9$ at $7\,R_\mathrm{s}$.

The magnetic field data measured during the inbound leg of Rev A is shown in Figure 3.14 in KRTP coordinates. The given time is relative to midnight on 26 October 2006. In the beginning of the interval shown, shortly after Cassini's Titan flyby, the spacecraft is in the northern geographic hemisphere ($z > 0$) but

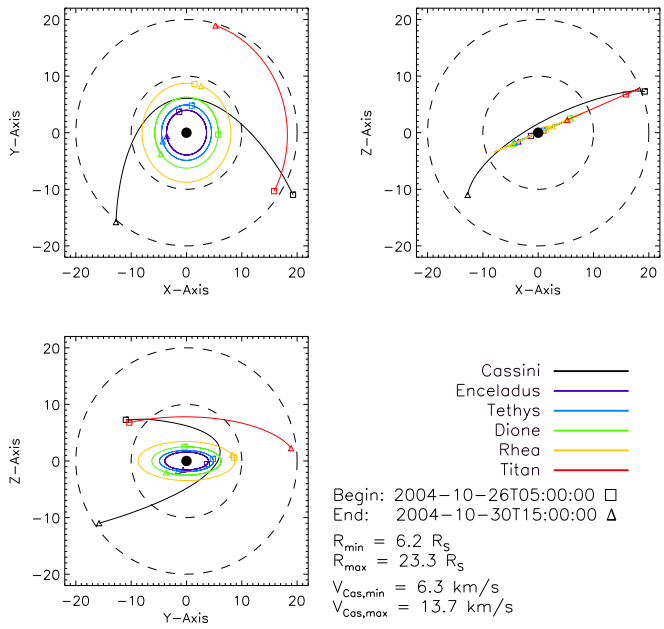

Figure 3.13: *Trajectory of Cassini's second orbit around Saturn (Rev A) in KSM coordinates. During the whole orbit Cassini stays inside the plasma sheet with* $|z|/H < 1$.

in the southern magnetic hemisphere. This is by definition the region where the radial magnetic field is negative. It crosses the magnetic equator from south to north not until $t \sim 31\,\mathrm{h}$. The magnetopause during this orbit was found at around $22\,R_\mathrm{s}$ (*Arridge et al.*, 2008a). The turbulent magnetic field in interval A and the multiple crossings of $B_r = 0$ indicate that Cassini is inside the current sheet and that the current sheet is in motion. After the crossing, Cassini enters a region of less activity before the magnetic field increases dipolar-like and three distinct flux-tube interchanges are observed.

During the whole inbound leg, the B_ϕ component exhibits a long period oscillation. The period with roughly 12 h in spacecraft frame is a little longer than Saturn's rotation period due to the orbit of Cassini. During the first minimum in B_ϕ at $r \sim 15\,R_\mathrm{s}$, Cassini is at longitude ∼90° (SLS4) and local time 11.5 h. This is close to the subsolar longitude of ∼100°, which means that the SKR is near maximum at that time (*Kurth et al.*, 2007). During SKR maxima, the radial quasi-uniform perturbation field points to a local time of 2 h leading to minima in B_ϕ at $5\,h$ and 11 h local time (see also Fig. 1 of *Andrews et al.*, 2010). Thus, the oscillations in B_ϕ can be explained with the proposed quasi-uniform perturbation field caused by the rotating patterns shown in Figure 3.8 and the plasma cam as described in Section 3.1.3. We now turn to look at the power spectral densities during Rev A to see if these large scale fluctuations may cascade to smaller scales.

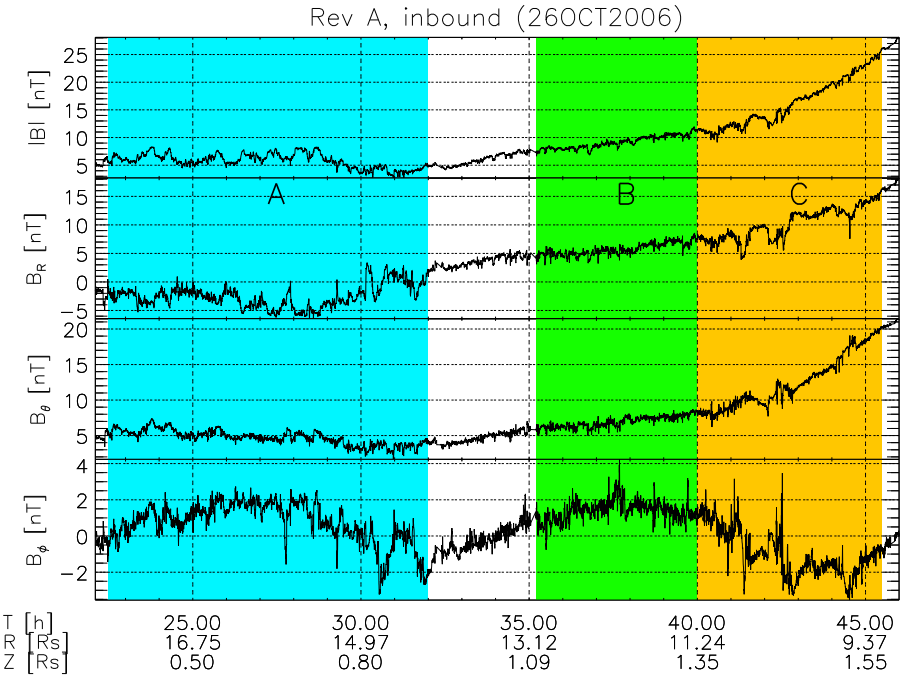

Figure 3.14: *Magnetic field strength $|B|$ and magnetic field components in KRTP coordinates during inbound leg of Rev A (starting at 22 h on October 26, 2004). Cassini flies through the turbulent ring current plasma (22.5−32 h), crosses the magnetic equator at ∼31 h from south to north and then enters a more quiet region. Three discrete flux-tube interchange events can be identified as decreases in magnetic field strength from 41.3−44.5 h. Intervals A-C indicated with color.*

Figure 3.15 shows, for the same time interval as in Figure 3.14, the scalograms of compressible $W_{\parallel}(t,p)^2$ and Alfvénic $W_{\perp}(t,p)^2$ fluctuations using Morlet wavelets, as defined in Section 3.3.2 (Equations (3.9) and (3.10)). Ion gyro periods of H^+ and W^+ are marked as white lines on top of the scalograms. It is fairly visible that the low frequency fluctuations change considerably along the orbit. After Cassini leaves the turbulent current sheet at about 32 h, the spectral energy at large scales drops significantly. In the first step of the analysis, we present results from four distinct intervals A-D, which reflect approximately homogeneous regions according to the scalogram in Figure 3.15. The intervals from the inbound leg of Rev A at distances $r > 9\,R_s$ represent the planetary ring current (A), the quiet magnetosphere (B) and the magnetosphere during isolated flux-tube interchanges (C). Interval D from the outbound leg of Rev A (Figure 3.16) represents a region of radial plasma transport with mirror mode waves and a series of interchange events. We show that the difference in the governing physics in these regions only affects low frequency fluctuations, while the statistical features of high frequency fluctuations are consistent throughout the whole orbit.

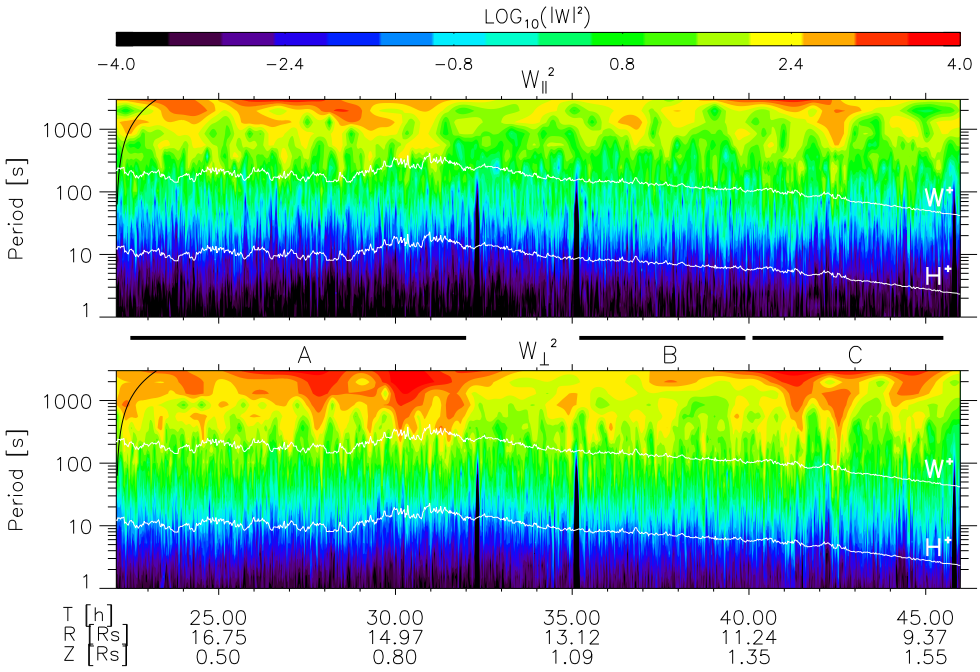

Figure 3.15: *Scalograms of fluctuations parallel (above) and perpendicular (below) to the local mean magnetic field during inbound leg of Rev A (same time interval as in Figure 3.14). Intervals A-C are marked with horizontal bars and energies are given are in nT^2/Hz. Data gaps are visible as black arcs and white lines indicate ion gyro periods of H^+ and W^+. During interval B there is significantly less energy in low frequency fluctuations. Flux-tube interchange events during interval C can be clearly identified in $W_\perp$ by enhanced energies on time periods between ∼200 s and ∼700 s.*

Interval A, $t = [22.5, 32]\,\mathbf{h}$

During this time interval, Cassini crosses the plasma sheet from south to north at a radial distance of ∼15 R_s, determined by the location where $B_r = 0$ (called zero crossing). The magnetic field fluctuates strongly throughout the whole interval with $\langle \delta B/B_0 \rangle = 0.14$ averaged over the whole interval. Multiple zero crossings of B_r indicate that the current sheet is in motion, flapping up and down over the spacecraft. This flapping motion with periods of around 15 min has also been observed by *Arridge et al.* (2008a).

Figure 3.17 A shows the power spectral density of magnetic fluctuations parallel $P_\parallel = P_{zz}$ to the mean field $\mathbf{B}_0 = B_0\mathbf{e}_z$ (black line) and the spectrum of Alfvénic fluctuations $P_\perp = P_{xx} + P_{yy}$ (yellow line) as a function of frequency f in the spacecraft frame. The maximal resolved frequency $f_{\max}$ of our spectral analysis is not only defined by the Nyquist frequency $f_N = 3.6$ Hz, but also by instrumental and quantization noise levels as well as aliasing noise. The FGM instrument as described by *Dougherty et al.* (2004) has a noise level of

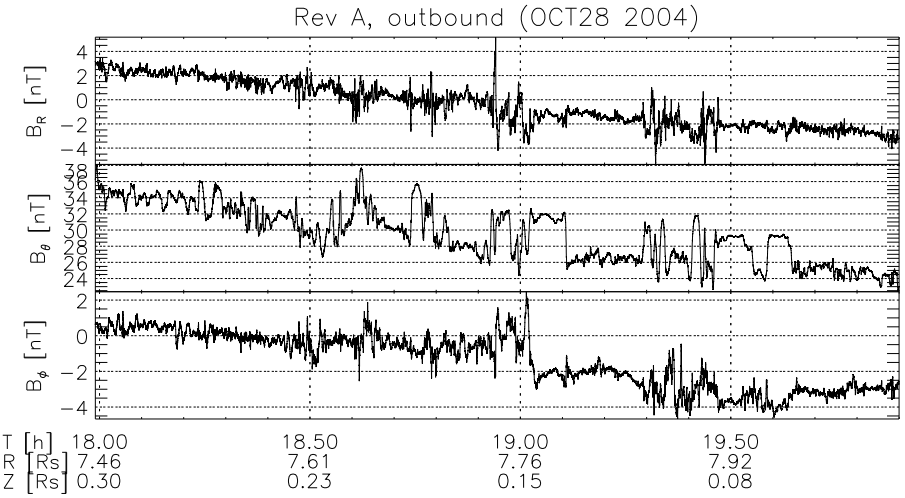

Figure 3.16: *Data from interval D on October 28, 2004 (outbound section of Rev A). Magnetic field component B_θ shows characteristic mirror mode oscillations from* $18{-}19\,h$ *(Russell et al., 2006) followed by a series of flux-tube interchanges (André et al., 2007).*

$n_\mathrm{i} = 25\,\mathrm{pT}^2/\mathrm{Hz}$ (which we assume to vary with $1/f$) and a resolution of $\Delta B = 4.9\,\mathrm{pT}$ in a $\pm 40\,\mathrm{nT}$ range and $\Delta B = 48.8\,\mathrm{pT}$ in a $\pm 400\,\mathrm{nT}$ range. We model the resulting quantization noise after *Russell* (1972) as

$$n_\mathrm{q} = \frac{\Delta B^2}{12 f_\mathrm{N}} \ . \tag{3.19}$$

The aliasing noise n_a is estimated according to *Podesta et al.* (2006) as

$$n_\mathrm{a} = \sum_{n=1}^{\infty} \frac{(f 2\Delta t)^\kappa}{(2n - f 2\Delta t)^\kappa} \cdot P(f) \ , \tag{3.20}$$

where κ is the spectral index of the underlying power-law. We assume the total noise to be the sum of instrumental, quantization and aliasing noise. This provides a very conservative estimation and likely upper limit on the real combined error. Thus, we define f_max as the frequency where the signal to noise ratio (SNR) is equal to 5. Any measurements below this ratio are considered as affected by noise. As far as the observed spectra are power-laws with negative spectral indices, the range of frequencies $f < f_{max}$ are characterized by SNR > 5. The dashed line in Figure 3.17 depicts the noise level for $P_\parallel$. In the case of interval A, we find that $f_\mathrm{max} = 0.4\,\mathrm{Hz}$.

In Figure 3.17A, at low frequencies $[4, 100] \cdot 10^{-4}\,\mathrm{Hz}$, which correspond to the MHD scales, one observes a power-law spectrum with a slope close to 5/3. This is consistent with a Kolmogorov cascade of strong turbulence. At around $10^{-2}\,\mathrm{Hz}$, close to the Doppler-shifted gyro radius of water group ions $f(\rho_W)$, a

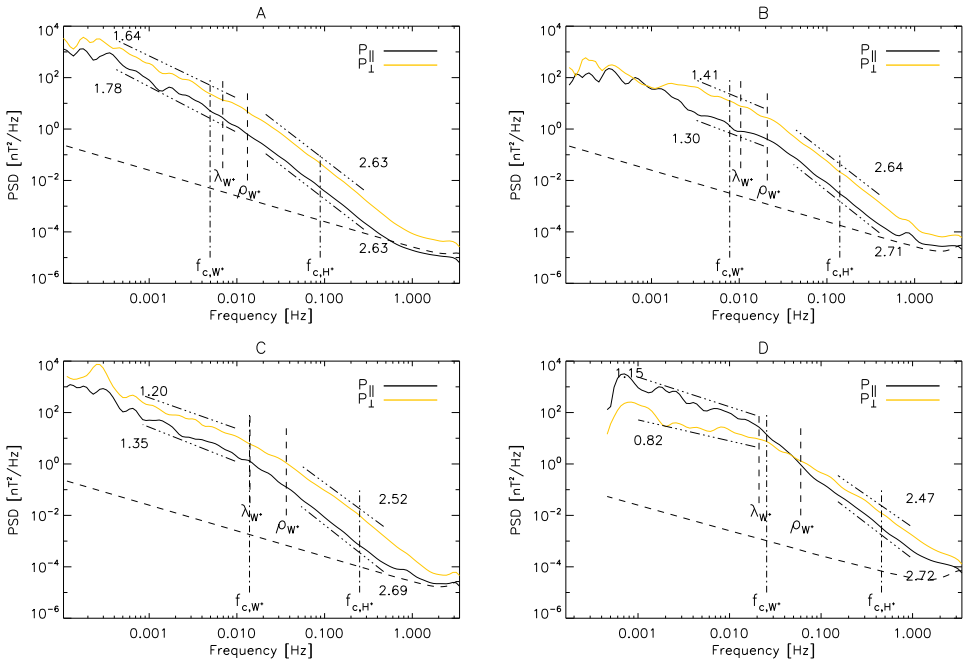

Figure 3.17: *Power spectra of intervals A-D. Mean ion cyclotron frequencies $f_{c,H}$ and $f_{c,W}$ (dash-dotted), and Doppler shifted gyro radii ρ_W and inertial lengths λ_W (dashed) marked with vertical lines. The noise level of $P_\parallel$ is shown as a dashed line with slope $1/f$. Also shown are linear fits to power-law spectral ranges. Fluctuations perpendicular to the magnetic field $P_\perp$ are generally stronger than those parallel to it $P_\parallel$ with exception of interval D, where mirror mode activity is observed at low frequencies.*

spectral break is observed, which we denote with break frequency f_b. At higher frequencies, $f > f_b$, there is another power-law with spectral index 2.63 for both compressible and Alfvénic fluctuations. In the following, we call this range of scales the kinetic range. One may also note that the Alfvénic fluctuations, $P_\perp$, dominate the compressible fluctuations, $P_\parallel$, both at MHD and kinetic scales. On MHD scales, the variance anisotropy is $P_\perp/P_\parallel \simeq 4$ and on kinetic scales, fluctuations become even more strongly anisotropic with $P_\perp/P_\parallel \simeq 8$. In terms of compressibility, we observe $P_\parallel/|P| = 0.2$ within the MHD range and $P_\parallel/|P| = 0.11$ within the kinetic range.

The PSD only give information on the second order statistical moment. Information of higher order moments can be extracted from the probability density functions (PDF) of the incremental magnetic fluctuations $b(t, \tau)$. Figure 3.18 (left) shows the PDF of three components of magnetic fluctuations in KRTP coordinates for time interval A. The black line corresponds to a scale of $\tau = 2\,\mathrm{s}$, the green PDF represents $\tau = 9\,\mathrm{s}$ and the red line shows the $\tau = 100\,\mathrm{s}$ time scale. The flatness is calculated using Equation (3.12) and is given in the legends of Figure 3.18. One observes a clear deviation from a Gaussian distribution as

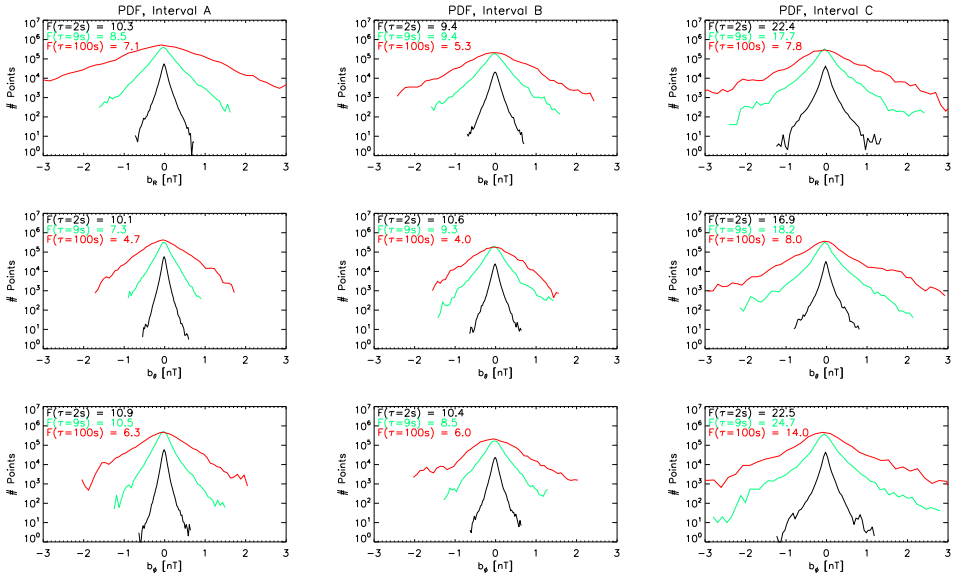

Figure 3.18: *PDF of increment time series of intervals A-C for different lags and components in KRTP coordinates. Vertical shifts (green line* $\times 10$*, red line* $\times 100$*) are applied for visualization purposes. The tails of the PDF are growing with frequency rendering the PDF increasingly non-Gaussian as reflected by increasing flatness values* $F(\tau)$ *shown in upper left corner.*

the time scale decreases, which is usually observed for a turbulent cascade (see e.g. *Bruno and Carbone*, 2005). The flatness as a function of temporal separation τ for each magnetic field component is shown in Figure 3.19. To compute the flatness without strong influence of the planetary magnetic field, we have subtracted the internal field beforehand (*Dougherty et al.*, 2005; *Burton et al.*, 2010). Colored arrows indicate the break frequencies f_b as estimated from Figure 3.17. Here, we can also directly compare the results of the different intervals. For interval A, the flatnesses generally increase smoothly like a power-law from a near Gaussian distribution ($F = 3$) at $\tau \sim 1\,\mathrm{h}$ to $F = 10$ at $\tau = 10\,\mathrm{s}$. This indicates the presence of a developed turbulent cascade. The lesser increase of flatness for $\tau < 10\,\mathrm{s}$ is most-likely caused by a decreasing signal-to-noise ratio. As the noise is nearly Gaussian this would ultimately lead to a flatness of $F = 3$.

Interval B, $t = [35.2, 40]\,\mathbf{h}$

After the last zero crossing of B_r at 32 h, Cassini enters a more quiet region ($\langle \delta B/B_0 \rangle = 0.07$), where the mean magnetic field is beginning to increase dipole-like. In the spectrum of magnetic fluctuations (Figure 3.17 B), we observe significantly less activity in low frequencies compared to interval A. The power-law range is reduced and follows a flatter power-law than during time interval A, which suggests that other physical processes control the low frequency range than during interval A. The characteristic anisotropy, $P_\perp/P_\parallel > 1$, is not

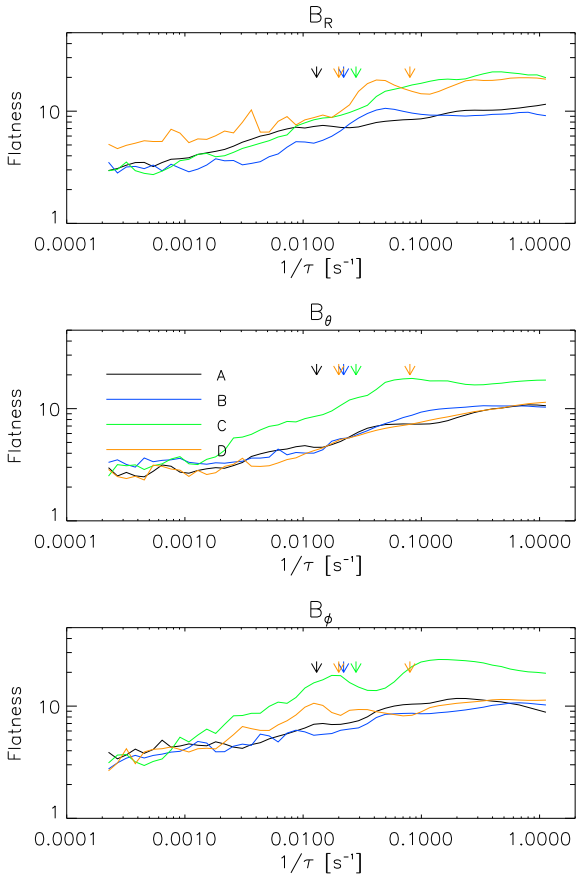

Figure 3.19: *Flatness as a function of τ calculated with Equation* (3.12) *for intervals A-D and for magnetic field components B_R (top), B_ϕ (middle) and B_θ (bottom). Colored arrows indicate the break frequency f_b as estimated from Figure 3.17. For all intervals there is a power-law increase in flatness at frequencies $f > 10^{-3}$ Hz.*

observed for frequencies less than 10^{-3} Hz. If we assume this frequency as an upper bound for the energy injection scale, we will get $L \sim v/(2\pi f) \sim 0.1\,R_s$. This indicates the lack of large scale magnetic perturbations in that interval, which might be the reason why the cascade is not developed at lower frequencies.

The spectral break frequency $f_b \simeq 2 \cdot 10^{-2}$ Hz stays in the same range as within interval A and remains close to the Doppler-shifted gyro radius of water group ions: $f(\rho_W) = 0.021$ Hz. On smaller scales, $f > f_b$, there is a power-law range with a slope similar to the one in interval A. The total spectral energy is slightly higher than during interval A and the maximal resolved frequency is $f_{\max} = 0.51$ Hz. The PDF of magnetic fluctuations during interval B shown in Figure 3.18 (middle) have similar characteristics as those of interval A. This can be verified in Figure 3.19, where the increase of the flatness with frequency $1/\tau$ is almost identical to interval A. This is an interesting result as the time

series in Figure 3.14 look rather different in intervals A and B. As the flatness is characteristic of the near dissipation range, the similarity might indicate a common dissipation process on comparable scales in both intervals.

Interval C, $t = [40, 45.5]$ **h**

During interval C, there are three isolated flux-tube interchange events (at $t = [41.3, 42.2, 44.5]$ h, best visible in B_r, see Figure 3.14), which have been previously identified by *André et al.* (2007). During these events, flux-tubes containing hot tenuous plasma from farther out interchange with flux-tubes containing cold dense plasma from farther inside (*Hill et al.*, 2005; *Mauk et al.*, 2005). This usually causes a decrease in magnetic pressure. These events are often linked with plasma wave activity and increased flux of hot electrons (*Gombosi et al.*, 2009). During all three events, an increased hot electron flux (20−100 keV) was detected. This could be verified from data taken by LEMMS (Low Energy Magnetospheric Measurement System), which is part of the MIMI instrument onboard Cassini (*Krimigis et al.*, 2004).

Figure 3.17 C shows a low frequency power-law range comparable to the one in interval A. However, the slope is considerably shallower with values of 1.2 and 1.4 for fluctuations perpendicular and parallel to the mean magnetic field, respectively. From the scalograms in Figure 3.15, it is clear that the low frequency energy is significantly enhanced during the flux-tube interchanges. The small peak at around $f \sim 3 \cdot 10^{-4}$ Hz corresponds to a length of $\sim 0.5\, R_\mathrm{s}$ and reflects the size of the largest flux-tube interchange. There is a clear spectral break at around $f_b \sim f(\rho_W) \sim 0.03$ Hz and again a power-law for high frequency fluctuations with a slope $\sim$2.6 as seen in the other intervals. As is the case for interval A, the variance anisotropy $P_\perp/P_\parallel$ is increased for $f > f_b$. This corresponds to a decrease of the level of compressibility with $P_\parallel/|P| \simeq 0.2$ within the MHD range and $P_\parallel/|P| \simeq 0.07$ within the kinetic range. Usually, in the solar wind the inverse situation is observed, i.e., an increase of the compressibility across the ion spectral break (*Alexandrova et al.*, 2008a; *Kiyani et al.*, 2013). This suggests that large scale magnetospheric processes control the turbulence at MHD scales in Saturn's magnetosphere.

The PDF of the magnetic fluctuations during interval C in Figure 3.18 (right) have elongated tails, which is reflected by large flatness values of $F \sim 10$ at relatively large periods of $\tau \sim 100$ s. The larger flatness can be clearly seen in Figure 3.19, where interval C clearly shows an enhanced intermittency compared to the intervals A and B. The flatness increases strongly in the B_θ and B_ϕ component and deviates from the other observed flatnesses at a frequency of $f \sim 10^{-3}$ Hz, reaching values of $F = 20$ at $\tau = 100$ s in case of B_ϕ. It is reasonable to believe that this strong increase is caused by the flux-tube interchanges observed in this interval. A detailed analysis of this feature is beyond the scope of this thesis, but it is highly recommended as it might lead to further insight on the dissipation mechanisms of plasma turbulence. Here, we restrict our interpretation to the general trend seen in the data, which is in accordance with observations of in

the solar wind.

Interval D, $t = [66, 67.9]$ h

Very close to Saturn, the fluctuations are more compressible. The magnetic field data of interval D can be seen in Figure 3.16. *Russell et al.* (2006) describe the oscillations in the beginning of the interval (18−18.5 h of October 28, 2004) as mirror mode waves with "less sharp sides" than the series of flux-tube interchange events that follow later (see Figure 3.9 (left) and Fig. 9.36 of *Gombosi et al.* (2009) for a multi-instrument analysis of this interval). These mirror mode waves are best visible in the B_θ component.

In the turbulent spectra in Figure 3.17 D one observes PSD with $P_\parallel > P_\perp$ at frequencies lower than the ion cyclotron frequency of water group ions, which is characteristic of mirror modes. The mean amplitude of these mirror modes is $\delta B_\parallel \simeq 3\,\mathrm{nT}$ and the relative parallel fluctuation is $\delta B_\parallel / B_0 \simeq 0.12$. The spectra have a double kink shape (*Voitenko and De Keyser*, 2011) with two spectral breaks at 0.02 Hz and 0.08 Hz. The steeper part in between these two spectral breaks might correspond to the ion dissipation range as described in *Smith et al.* (2012). At frequencies higher than the second break frequency, the spectrum is again a well defined power-law with spectral indices 2.5 for perpendicular fluctuations and 2.7 for compressible ones.

In Figure 3.19, the flatness for interval D is a little higher in the B_R component than for intervals A and B. Interestingly, there is no difference in the flatness for the B_θ component, where the compressible mirror modes are observed. There is a local maximum in the flatness of the B_R component between the break frequencies, at $1/\tau \sim 0.04\,\mathrm{s}^{-1}$, which is characteristic of the presence of coherent structures. However, despite of these slight differences, the general behavior still shows a power-law like increase, thus indicating intermittency.

Conclusions of Case Study

During Rev A, Cassini encountered regions dominated by the planetary ring current, a quiet interval in the plasma sheet, flux-tube interchanges characteristic of the middle magnetosphere and mirror mode wave activity close to Saturn. Ion cyclotron waves, which frequently occur in the inner magnetosphere (*Leisner et al.*, 2006), are not observed in the analyzed intervals. The intervals reflect quite well the dynamic nature of Saturn's middle magnetosphere. Although magnetic field data show distinct behavior in all subintervals, there are certain statistical similarities of the fluctuations, which are omnipresent. We can resume that:

1. During all intervals, magnetic fluctuations have power-law spectra with flatter spectra at MHD scales and steeper spectra within the kinetic range. The limit between these two spectral ranges, i.e., the spectral break f_b, is observed within the frequency range $f_b \in [1, 8] \cdot 10^{-2}\,\mathrm{Hz}$, which is in the

vicinity of the Doppler-shifted water group ion gyro radius and inertial length.

2. At MHD scales, the spectral index varies between 0.8 and 1.7 with a less developed power-law in interval B. The spectral shape and power are likely controlled by large scale magnetospheric processes.

3. Within the kinetic range the spectral slope is always close to 2.6.

4. Fluctuations in the frequency range $f > f_b$ are mainly perpendicular to the mean magnetic field resulting in a variance anisotropy $P_\perp/P_\parallel \geq 4$ corresponding to a compressibility level of $P_\parallel/|P| \leq 0.2$.

5. The flatness of each interval increases like a power-law with frequency from a near normal distribution to values $F \geq 10$, thus showing more bursty or intermittent behavior. There seems to be no significant change of flatness around the break frequency.

The findings listed above are characteristic of turbulence in a magnetized plasma. In the solar wind, power spectra with a break in the vicinity of ion scales are usually observed. The important difference is that the low frequency range is controlled by large scale magnetospheric processes such as current sheet flapping, mirror modes or flux-tube interchanges. However, at high frequencies, i.e., within the kinetic range of scales, the turbulent spectrum is very similar to what is observed in the solar wind (see Section 2.3). In the next section, therefore, we perform a large statistical study of the kinetic range turbulent spectra within the magnetosphere of Saturn using the first seven orbits of Cassini.

3.4 Statistical Analysis of Kinetic Range Turbulent Cascade

In the previous section we considered magnetic spectra taken over 2−10 hours in order to describe both, MHD and kinetic range scales. Here, we use data from the first seven orbits of Cassini around Saturn divided into 10 min blocks, for which we calculate power spectral densities. These 10 min time intervals are well suited for the analysis of the kinetic range (*Alexandrova et al.*, 2012). On the one hand, the interval is long enough to study fluctuations shortly after the spectral break at $f \sim 10^{-2}$ Hz, and on the other hand, the shortness of the time series ensures a nearly homogeneous background.We restrict the analysis to data obtained between 6.5−17 R_s to avoid time series dominated by ion cyclotron waves usually found in Saturn's inner magnetosphere (*Leisner et al.*, 2006) and to make sure we are far enough from the magnetopause at $r \sim 20\,R_\mathrm{s}$ (*Arridge et al.*, 2008b). Further, we discard all data with gaps exceeding 0.14 s and data with $\delta B < 0.1$ nT or $\delta B > 3$ nT to avoid lobe regions and unphysical spikes in the data, respectively. With these restrictions, 270 blocks are discarded and we

work with 1180 blocks. Another 44 blocks inside $7.5\,R_s$ are removed by hand because of visible ion cyclotron resonances in the spectra.

Figure 3.20 shows the total PSD ($|P| = P_\perp + P_\parallel$) without separation into parallel and perpendicular components as was done in Figure 3.17 for the case study. In Figure 3.20a all 1136 measured spectra are shown, calculated with a Morlet wavelet transform as defined in Section 3.3.2. The red lines (one for resolution $\Delta B = 4.9\,\mathrm{pT}$ and one for $\Delta B = 48.8\,\mathrm{pT}$) indicate the noise levels of the MAG instrument, determined as explained in Section 3.3.5. We calculate the relative power of the spectra, $\langle P/P_0 \rangle$, with respect to a reference spectrum P_0 measured at $13.5\,R_s$. This relative power can also be used as an estimator of the relative turbulence level. Here, the average $\langle * \rangle$ is taken in the range $0.1\,\mathrm{Hz} < f < \min(f_{\max}, 0.6)\,\mathrm{Hz}$ corresponding to the kinetic range. As discussed in Section 3.3.5, $f_{\max}$ is calculated for SNR > 5. The relative power is quite variable throughout the magnetosphere and needs to be studies further. Figure 3.21 (left column) shows the correlation of $\langle P/P_0 \rangle$ with radial distance, thermal pressure of water group ions, magnetic pressure and ion plasma β_i. The correlations with radial distance and thermal pressure are particularly good ($c = \mp 0.7$). The strong correlation with radial distance indicates that the relative spectral power rather reflects the magnetospheric structure than the turbulence characteristics that we are interested in.

Therefore, in Figure 3.20b, we use the transformation to a normalized wave number $k_\perp \rho_W$ and calculate a similar relative spectral power $\langle E/E_0 \rangle$ for the normalized spectra $E(k_\perp \rho_W)$. Here, the average $\langle * \rangle$ is taken in the kinetic range $k_\perp \rho_W = [2, 50]$. E_0 is the reference spectrum according to P_0. The right column of Figure 3.21 shows the relative spectral power $\langle E/E_0 \rangle$ as a function of radial distance, thermal and magnetic pressure and ion plasma β_i. As the normalized spectra $E(k_\perp \rho_W)$ reflect the scales in the plasma frame, they are not affected by the variation of the plasma speed with radial distance to Saturn. Consequently, with exception of ion plasma β_i, the correlations for normalized spectra are less than those for raw frequency spectra.

In Jupiter's magnetosphere, the relative spectral power was found to peak at radial distances, where the corotation of the magnetosphere breaks down (*Saur et al.*, 2002, 2003) and similar correlations of relative power of frequency-spectra with plasma parameters such as temperature, magnetic and kinetic energy have been observed in the solar wind (*Grappin et al.*, 1990; *Alexandrova et al.*, 2009, 2013), although the radial evolution of the solar wind is likely controlled by different processes. In Saturn's magnetosphere, we find that only the observed power of frequency-spectra, $P(f)$, as well as k-spectra, $P(k)$, depend on radial distance, thermal pressure $n_W k T_W$ of water group ions and magnetic pressure $B^2/(2\mu_0)$. The normalized spectra, $E(k_\perp \rho_W)$ as well as $E(f/f_{c,W})$ and $E(k_\perp \lambda_W)$, seem to be independent of radial distance. This affirms that not only the plasma velocity, but also the background magnetic field strongly influences the spectral analysis. We conclude that normalized frames are more suitable for our turbulence analysis in Saturn's magnetosphere than raw frequency spectra.

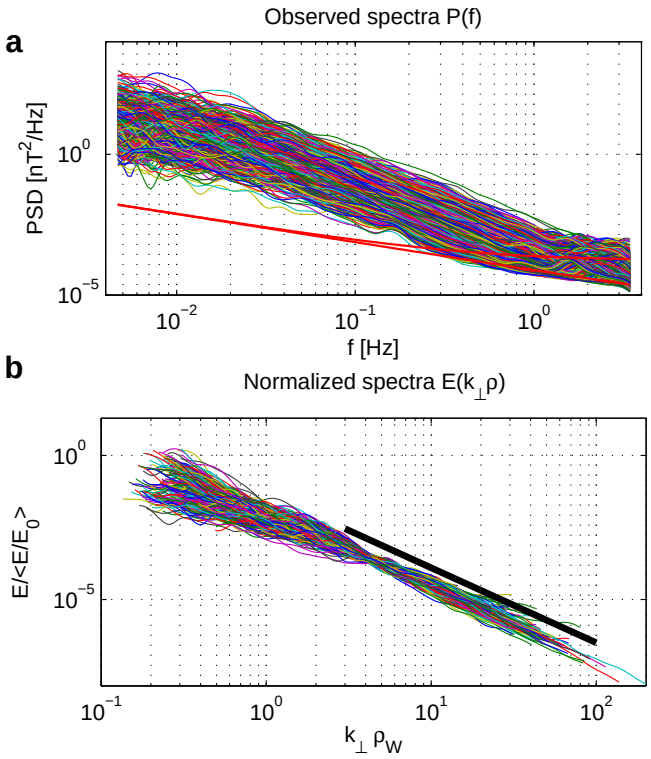

Figure 3.20: *a) Measured spectra $P(f)$ of all* 1136 *analyzed* 10 *min blocks. Dashed lines show noise levels of MAG instrument. b) Normalized power spectra $E/\langle E/E_0\rangle$ as a function of $k_\perp\rho_W$, where $\langle E/E_0\rangle$ is averaged power in range $k_\perp\rho_W = [2, 50]$ with respect to a reference spectrum E_0. The spectral break is found at $k_\perp\rho_W \sim 2$. The black line shows a slope of* 2.6.

In Figure 3.20b, we show the spectra $E(k_\perp\rho_W)$ normalized by their respective spectral power in the kinetic range, $\langle E/E_0\rangle$. We cut frequencies $f < 0.02\,\mathrm{Hz}$ and $f > f_{\max}$ because of strong oscillations at low frequencies and flattening of the PSD at high frequencies due to noise. The similar spectral shape of all PSD indicates that the underlying turbulent cascade is consistent in the analyzed data set.

3.4.1 Spectral Index within the Kinetic Range

One of the important characteristics of turbulence is the spectral index within the inertial range, where a turbulent cascade takes place. Determination of its value can help to choose a good model to describe the turbulence. First of all, we determine the range of scales, in which the spectral index is nearly constant. For different radial distances r, we calculate the spectral slope for frequency spectra $P(f)$, for spectra normalized by water group ion cyclotron frequency $E(f/f_{c,W})$, and for spectra as a function of $k_\perp\rho_W$ and $k_\perp\lambda_W$. To

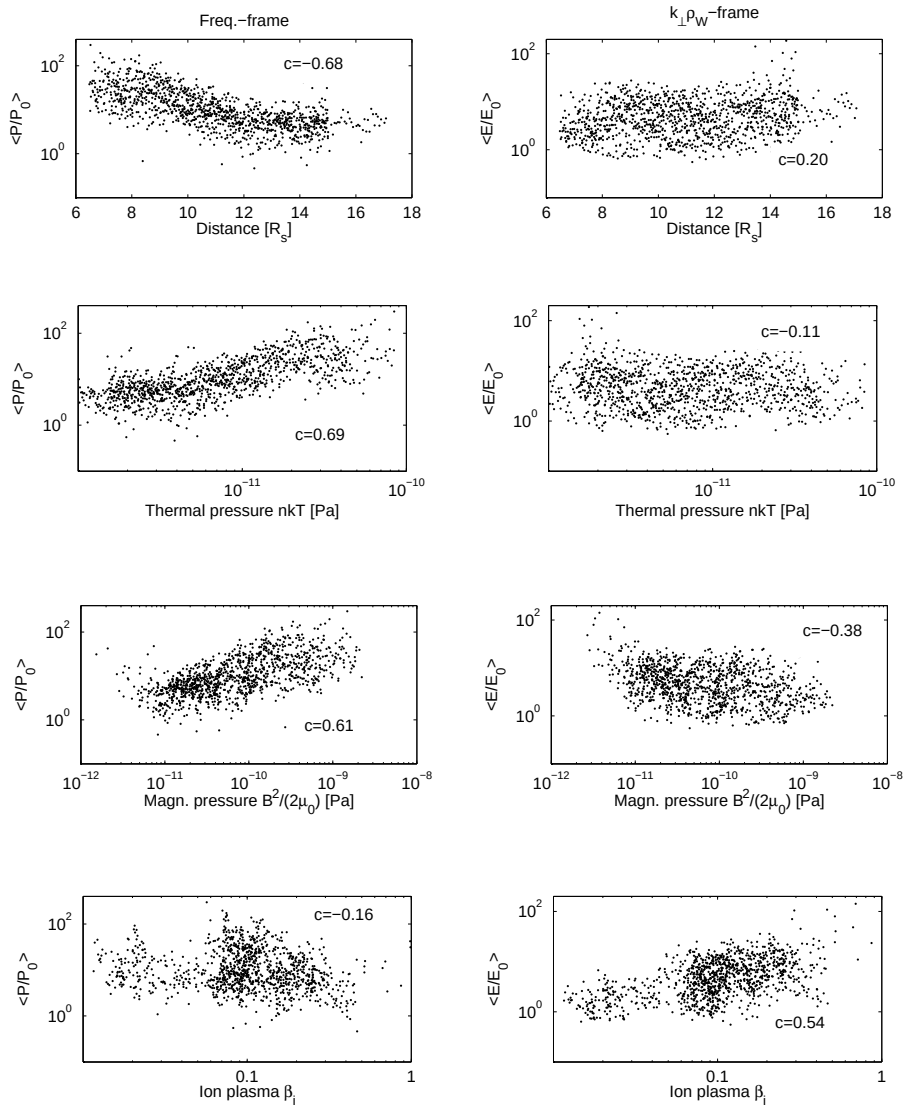

Figure 3.21: *Relative spectral power $\langle P/P_0 \rangle$ (left column) for raw frequency spectra and $\langle E/E_0 \rangle$ (right column) for $k_\perp \rho_W$-spectra as a function of radial distance from Saturn, thermal and magnetic pressure and ion plasma β_i. Double logarithmic correlations c given in the respective panels.*

determine the range of constant spectral slope, we perform a sliding window fit: For frequency spectra $P(f)$ observed in spacecraft frame, we calculate the spectral slope in a window $[f', 5f']$ with left corner frequency f' increasing from $f_b \simeq 0.01\,\mathrm{Hz}$. As discussed in Section 3.3.5 we only take into account data with

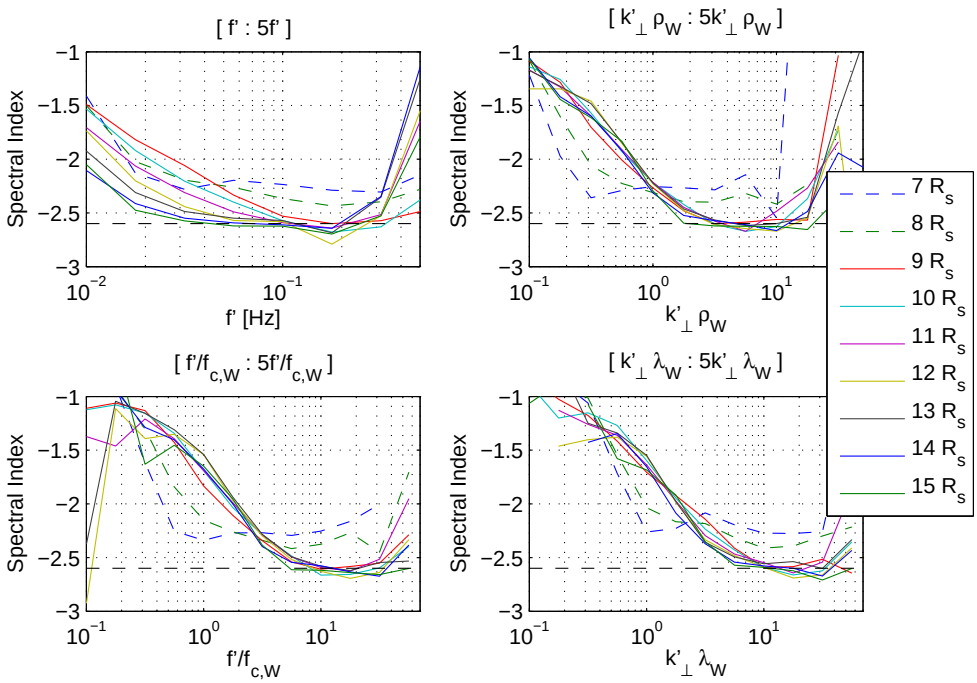

Figure 3.22: *Average spectral indices for* $1\,R_\mathrm{s}$*-bins obtained in a sliding window fit. The* x*-axis values indicate the start of the fit and the window size is given in the title of the plots. The spectral break is reflected by a rapid change of slope at low frequencies. Convergence toward a constant slope (*2.6 *shown as horizontal black dashed line) depends on radial distance for fits in spacecraft frame (top left) but is independent of radial distance in normalized frames. A distinct behavior is observed for* $r < 8\,R_\mathrm{s}$*.*

SNR > 5. The such obtained results are then averaged within radial bins of $1\,R_\mathrm{s}$ to account for possible changes with radial distance from Saturn. In Figure 3.22 (top left), we see that the such estimated spectral indices, $\kappa(f, r)$, decrease rapidly at low frequencies, which results from the sliding window moving over the spectral break f_b. They converge toward approximately 2.6 (shown as black dashed line) within the frequency range $f' = [0.05, 0.3]\,\mathrm{Hz}$ for radial distances $r > 13\,R_\mathrm{s}$. This means that the spectral indices are nearly constant in the range $f = [0.05, 1.5]\,\mathrm{Hz}$. However, the convergence toward a spectral index of 2.6 depends strongly on radial distance. An ever shorter frequency range of constant spectral indices for $r < 13\,R_\mathrm{s}$ indicates that the spectral break is found at higher frequencies closer to Saturn.

In contrast, using normalizations $f \to k_\perp s$ according to Equation (3.15) with $s = \rho_W, \lambda_W$ or $f \to f/f_{c,W}$, we obtain the other results shown in Figure 3.22. Here, the convergence toward a spectral index of 2.6 is consistent for all radial distances (with exception of $r \leq 8\,R_\mathrm{s}$, where we observe a distinct convergence

	$\kappa^{\mathbf{k}\rho}$	$\kappa^{\mathbf{k}\lambda}$	$\kappa^{\mathbf{fc}}$
$\mathbf{r < 8\,R_s}$	2.30 ± 0.39	2.26 ± 0.26	2.31 ± 0.31
$\mathbf{r > 9\,R_s}$	2.58 ± 0.25	2.52 ± 0.23	2.55 ± 0.22

Table 3.4: *Mean and standard deviation of spectral indices. The ranges, over which the spectral indices are determined, are* $k_\perp \rho_W = [2, 50]$, $k_\perp \lambda_W = [5, 100]$, *and* $f/f_{c,W} = [5, 100]$.

behavior toward a shallower spectral index of ∼7/3). This indicates a strong correlation of the spectral break with these characteristic scales and frequencies and shows that the turbulent cascade in Saturn's magnetosphere is controlled by characteristic length scales in the rest frame of the corotating plasma. A range of constant spectral indices is observed for $k_\perp \rho_W = [2, 50]$, $k_\perp \lambda_W = [5, 100]$, and $f/f_{c,W} = [5, 100]$.

Figure 3.23 shows the radial distributions of spectral indices $\kappa^{k\rho}$ (top), $\kappa^{k\lambda}$ (middle) and κ^{fc} (bottom), calculated within the range, where the spectral indices are observed to be nearly constant, $k_\perp \rho_W = [2, 50]$, $k_\perp \lambda_W = [5, 100]$, $f/f_{\mathrm{c,W}} = [5, 100]$, respectively. The error bars of the spectral indices are obtained from the least-squares fit to the PSD. It can be seen that the spectral indices $\kappa^{k\rho}$ are fairly constant outside $9\,R_\mathrm{s}$ and change toward shallower spectra farther inside. This result is robust as it is also observed for $\kappa^{k\lambda}$ and κ^{fc}. Thus, it is independent of the specific method of normalization. Interestingly, the distance of $9\,R_\mathrm{s}$ coincides with a boundary found by *Schippers et al.* (2008, 2012), where the electron temperature maximizes and the pitch angle distribution of suprathermal electrons changes from pancake-like inside $9\,R_\mathrm{s}$ to field-aligned outside $9\,R_\mathrm{s}$. This change has also been observed by *Saur et al.* (2006). Figure 3.24 shows a histogram of the observed spectral indices for radial distances $r < 8\,R_\mathrm{s}$ and $r > 9\,R_\mathrm{s}$. Here, we show the histogram of the spectral indices $\kappa^{k\rho}$ with a red line, the blue line gives the histogram of $\kappa^{k\lambda}$, calculated for $k_\perp \lambda_W$-spectra, and the green line indicates the histogram of κ^{fc}, determined from the $f/f_{c,W}$-spectra. The vertical lines show spectral indices of 8/3 and 7/3. The weighted averages and the corresponding standard deviations of the spectral indices for $r < 8\,R_\mathrm{s}$ and $r > 9\,R_\mathrm{s}$ are given in Table 3.4. Outside $9\,R_\mathrm{s}$, the histogram in Figure 3.24 has a nearly Gaussian distribution, which indicates that the magnetosphere is nearly homogeneous and the cascade is consistent. In contrast, the distribution of spectral indices inside $8\,R_\mathrm{s}$ is skewed toward shallower slopes. This may be explained from Figure 3.23, where it can be seen that the slopes are increasingly flatter the closer to Saturn they are observed.

Our results are close to what is found in the solar wind within the kinetic range of scales (*Alexandrova et al.*, 2009; *Sahraoui et al.*, 2010; *Alexandrova et al.*, 2012; *Bourouaine et al.*, 2012) and can be explained in the framework of different turbulent models. The shallower slope, which we observe close to Saturn, namely $\langle \kappa(r{<}8\,R_\mathrm{s}) \rangle = 2.3 \pm 0.3$ is close to 7/3, which characterizes strong KAW turbulence (*Howes et al.*, 2006; *Schekochihin et al.*, 2009). Outside $9\,R_\mathrm{s}$ our

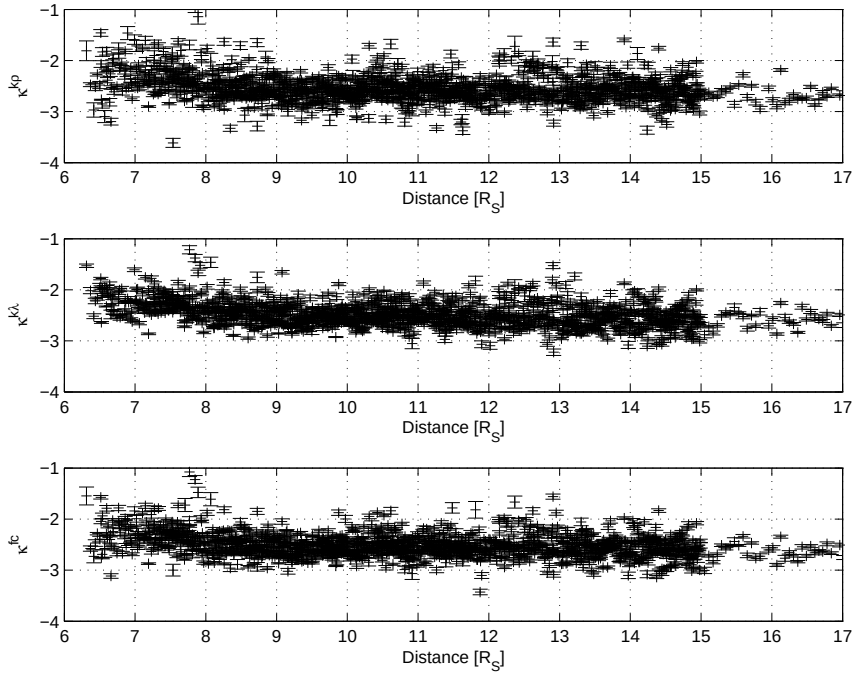

Figure 3.23: *Radial profile of spectral indices $\kappa^{k\rho}$ (top), $\kappa^{k\lambda}$ (middle) and κ^{fc} (bottom) obtained by least squares fit in the range $k_\perp \rho_W = [2, 50]$, $k_\perp \lambda_W = [5, 100]$, $f/f_{\mathrm{c,W}} = [5, 100]$, respectively, for* SNR > 5. *All radial profiles show similar results with a generally shallower slope inside* $9\,R_\mathrm{s}$.

results are consistent with strong KAW turbulence (*Howes et al.*, 2006; *Boldyrev and Perez*, 2012) and strong whistler turbulence (*Galtier et al.*, 2005) with slopes of 7/3 and 8/3 as well as strong compressible Hall turbulence as proposed by *Alexandrova et al.* (2008a). The spectral index of 2.58 ± 0.25 is also in agreement with 2.5 for weak whistler wave turbulence (*Narita and Gary*, 2010), weak KAW turbulence (*Howes et al.*, 2011a) and weak incompressible Hall-MHD turbulence (*Galtier*, 2006). However, as we show in Section 4.2.3, the measured spectral index κ is not identical with the spectral index of the underlying turbulence theory. Especially in the kinetic range, damping on electron scales can steepen the spectra significantly. Note also, that for electron temperatures $T_e \sim T_i$, the electron gyro radius is only a factor of $\sim$50 smaller than the ion gyro radius. Therefore, we cannot exclude that the fit range reaches up to electron scales, where a steeper slope is expected. In summary and according to our later results in Section 4.4, we conclude that our results may best be explained by strong KAW turbulence after *Howes et al.* (2006), which proposes a slightly shallower slope of 7/3.

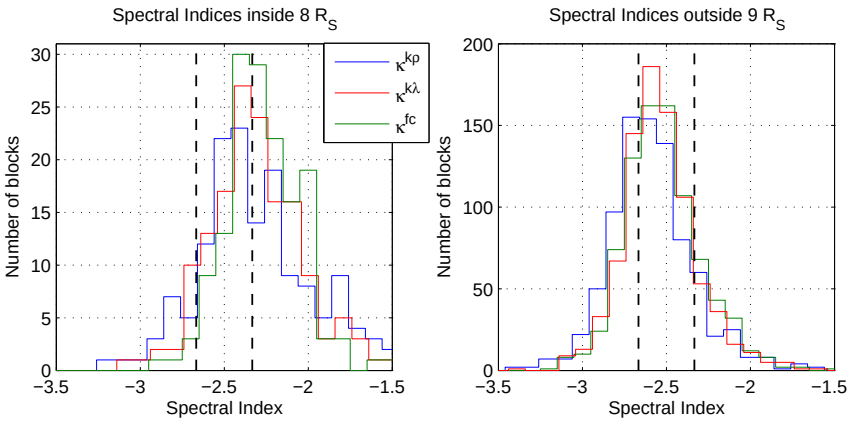

Figure 3.24: *Histogram of spectral indices $\kappa^{k\rho}$, κ^{kd} and κ^{fc} for distances $r < 8\,R_s$ (upper panel) and $r > 9\,R_s$ (lower panel). Vertical dashed lines indicate slopes of 8/3 and 7/3. Outside $9\,R_s$, a nearly Gaussian distribution is observed while the distribution inside $8\,R_s$ is skewed with larger tail toward shallower slopes.*

3.4.2 Intermittency of Fluctuations

Another general statistical property of turbulent flows is intermittency, which is observed as deviation from Gaussianity of the PDF of turbulent fluctuations. This deviation is scale dependent, as we have already seen in Section 2.3.2. Intermittency is observed in the solar wind on MHD scales (e.g. *Burlaga*, 1992; *Sorriso-Valvo et al.*, 2001; *Salem et al.*, 2009) and on kinetic scales (*Alexandrova et al.*, 2008a; *Kiyani et al.*, 2009; *Perri et al.*, 2012). To check if this intermittency depends on radial distance to Saturn, we calculate the mean flatness $F = (F_x + F_y + F_z)/3$ in radial bins of $1\,R_s$. Figure 3.25 shows the such averaged flatness calculated from Equation (3.12) as a function of $1/\tau$. As expected from our case study in Section 3.3.5, the flatness increases with frequency as a power-law independent of distance to Saturn. The power-law increase of the flatness with frequency indicates that the fluctuations are increasingly intermittent and demand a multifractal description. However, the slope of the power-law is quite shallow. It is comparable to what is observed by *Alexandrova et al.* (2008a) in the inertial range of solar wind fluctuations. In the kinetic range they observe a steeper slope. We note, that the mean flatness shown here can only represent the general trend in the data. As we have seen in Figure 3.19, the details of the flatness during different intervals can be rather different. The calculation of the flatness using a wavelet based method as described in *Alexandrova et al.* (2008a), yields the same power-law increase as presented in Figure 3.25.

A power-law increase of flatness indicates intermittency and the formation of coherent structures (*Mangeney*, 2012) and is therefore characteristic of strong turbulence. This narrows down the models, that can explain our results, to strong KAW turbulence (*Schekochihin et al.*, 2009; *Boldyrev and Perez*, 2012),

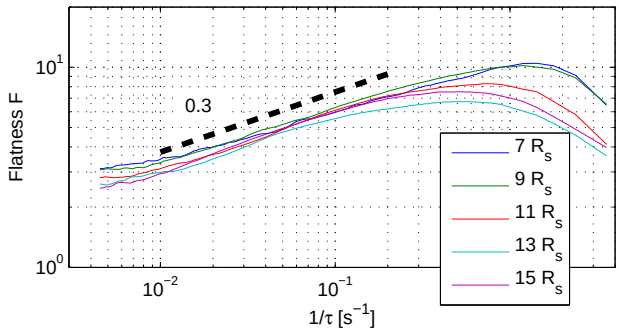

Figure 3.25: *Mean flatness* $F = (F_x + F_y + F_z)/3$ *averaged within radial bins of* $1\,R_s$ *calculated with Equation* (3.12) *as functions of* $1/\tau$. *The power-law increase indicates intermittency of the fluctuations. The decrease of flatness values for* $f > 0.5\,Hz$ *is caused by a decreasing SNR at the corresponding high frequencies.*

strong whistler turbulence after *Galtier et al.* (2005), and strong compressible Hall-MHD turbulence after *Alexandrova et al.* (2008a). At smaller scales, $f > 0.5\,\mathrm{Hz}$, the flatness begins to decrease again because of a decreasing signal to noise ratio in the corresponding high frequency range. As the noise is approximately Gaussian, this leads to decreasing values ultimately approaching the flatness value for Gaussian white noise: $F = 3$.

Interestingly, the averaged flatness functions at different radial distances shown in Figure 3.25 match very well in the frequency frame of the spacecraft. In contrast, the spectral indices in Figure 3.22 are best represented in a normalized rest frame of the plasma. This contradictions may indicate either influence of the instruments onboard Cassini or effects caused by waves that violate Taylor's hypothesis. Here, we must leave a more detailed analysis of this phenomenon to future studies. However, understanding of the flatness may yield further insight on the dissipation of the fluctuations.

3.4.3 Correlation of Spectral Indices with Field-to-Flow Angle

Here, we examine if the variance of spectral indices κ can be explained with a critically balanced cascade. Originally proposed by *Goldreich and Sridhar* (1995) for strong Alfvén wave turbulence, critical balance leads to a dependence of the spectral index on the field-to-flow angle θ (see Section 2.3). This arises as a consequence of anisotropy in $\mathbf{k}$-space and the fact, that a one-dimensional measurement only reflects a slice of the three-dimensional $\mathbf{k}$-space depending on the geometry of the measurement. If critical balance holds, the spectral slope will be much steeper for small angles θ. With a critical balance of $k_\parallel \sim k^{1/3}$ and scaling of $k_\perp^{-7/3}$ for $\theta = 90°$ in case of strong KAW turbulence (*Schekochihin et al.*, 2008, 2009), this leads to a scaling of $k_\parallel^{-5}$ for $\theta = 0°$ (*Cho and Lazarian*, 2004).

However, in our results, we do not see a correlation of κ with θ. This may be explained by the fact that 90% of our data have angles $\theta > 74°$ and the dependence of spectral index on θ is not linear (see Section 4.2). Therefore, our analysis cannot rule out that the turbulence inside Saturn's magnetosphere is critically balanced. Note, that we applied a global background magnetic field for this analysis and that a spectral anisotropy can most likely only be observed in the local magnetic field (*Cho et al.*, 2002; *Horbury et al.*, 2008). Analyses in the solar wind have shown that global magnetic field methods do not to reproduce the spectral anisotropy of a critically balanced cascade (*Tessein et al.*, 2009). Still, even local magnetic field methods may not show a spectral anisotropy for angles $\theta > 74°$, which can be seen from our study in Section 4.3.2. Only at significantly lower angles, a measurable change of the spectral slope might be observed. We propose to conduct a local magnetic field analysis in the future to verify our assumptions. Here, a study in the outer magnetosphere, where the background magnetic field is more variable and the relative fluctuation $\delta B/B_0$ stronger than close to Saturn, should yield the best results.

3.4.4 Compressibility Level

Analyzing the compressibility level $\langle E_\parallel/E \rangle$ of the fluctuations, where brackets mean ensemble average with geometrical mean[4], can yield information on the type of waves involved in the turbulent cascade. *TenBarge et al.* (2012) showed by evaluating the collisionless Vlasov-Maxwell equations that the variance anisotropy (and so the compressibility) depends strongly on plasma parameters such as the ion plasma β_i or on the angle between wave vector and magnetic field. The compressibility level is equivalent in information to the variance anisotropy $E_\perp/E_\parallel$ according to

$$\frac{E_\parallel}{E} = \left(1 + \frac{E_\perp}{E_\parallel}\right)^{-1} . \tag{3.21}$$

Similar to what has been reported for solar wind data (*Leamon et al.*, 1998; *Chen et al.*, 2010a), the compressibility in our data is generally below $E_\parallel/E = 1/3$, which is the compressibility of isotropic fluctuations. This means that transverse fluctuations are generally more energetic than compressible fluctuations. Figure 3.26 shows the compressibility level as a function of $k_\perp \rho_W$ averaged within radial bins of 1 R_s for frequencies $10^{-2}\,\mathrm{Hz} < f < 0.6\,\mathrm{Hz}$. The differences between different radial bins are rather small so that the results can be considered consistent throughout the magnetosphere. A similar result is produced from the normalizations $k_\perp \lambda_W$ and $f/f_{c,W}$.

[4]We use the geometrical mean because the distribution of the logarithms of the parameter are close to Gaussian while for the normal parameter it is strongly non-Gaussian. Therefore, a geometrical mean better reflects the average value, see also Appendix B.

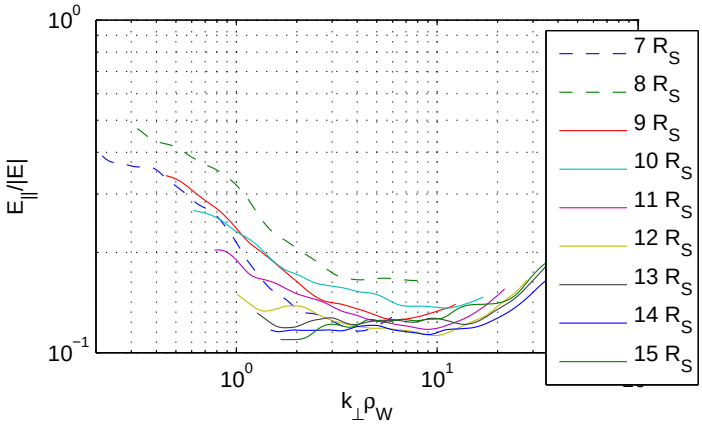

Figure 3.26: *Compressibility level $\langle E_\parallel/E \rangle$ averaged within radial bins of $1\,R_\mathrm{s}$. The compressibility decreases from isotropy ($E_\parallel/E = 1/3$) observed close to Saturn to $\langle E_\parallel/E \rangle \simeq 0.1$. The minimum is reached for frequencies higher than the spectral break at $k_\perp\rho_W \simeq 2$. For $k_\perp\rho_W \geq 18$ ($k_\perp\rho_H \geq 1$) the compressibility is found to increase again.*

For $k_\perp\rho_W < 2$ and inside $\sim$11 R_s the fluctuations are found to be increasingly compressible. Unfortunately, our measurements at large distances to Saturn do not cover such small scales. Therefore, it is unclear if the increased compressibility reflects physical processes that only happen close to Saturn or if the same would be observed farther out for much lower frequencies. Generally, the compressibility decreases with $k_\perp\rho_W$ to $\langle E_\parallel/E \rangle \simeq 1/8$, i.e., the anisotropy increases with $k_\perp\rho_W$ to $\langle E_\perp/E_\parallel \rangle \simeq 7$, reaching its minimum at scales slightly smaller than the spectral break, which was found at $k_\perp\rho_W \simeq 2$ (Figure 3.20). For $k_\perp\rho_W \geq 16$, which is approximately $k_\perp\rho_H \geq 1$, we find that the compressibility increases again. Similar observations have been made at 1 AU in the solar wind (*Alexandrova et al.*, 2008a; *Podesta and TenBarge*, 2012; *Salem et al.*, 2012). *Podesta and TenBarge* (2012) and *Salem et al.* (2012) show that this is in agreement with KAW turbulence as derived from the Vlasov-Maxwell dispersion relation. However, the increase of compressibility in our observations could also be explained by a decreasing signal to noise ratio, which ultimately leads to the isotropic value of compressibility. We note, that the application of a local magnetic field might yield slightly different results. However, the results of the case study, which is analyzed in a local magnetic field frame, are in accordance with the observations presented in Figure 3.26.

3.4.5 Turbulent Plasma Heating Rates

The continuous presence of a turbulent cascade has consequences for the energy budget of magnetospheric plasma as has been shown in the case of Jupiter's magnetosphere by *Saur* (2004). As the temperature profile measured in Sat-

urn's magnetosphere shows a non-adiabatic increase with distance from Saturn, there is need for a plasma heating mechanism. Here, we test if the dissipation of the fluctuations' energy can account for the 75−630 GW needed to heat an adiabatically expanding plasma to the temperatures measured in Saturn's plasma sheet (*Bagenal and Delamere*, 2011). The phenomenological approach we follow here is unable to tell how exactly the energy is dissipated. Therefore, we don't know if the energy goes into ion or electron heating and which dissipation mechanism is at work. *Schekochihin et al.* (2009) suggests, however, that the cascaded energy splits at the spectral break corresponding to the ion gyro radius, where it is decided how much energy goes into ion heating. A KAW cascade beyond the spectral break then ultimately leads to electron heating. We note that this process may be asymmetric with regards to the background magnetic field or lead to non-Maxwellian velocity profiles. However, for the sake of simplicity and because we expect the energy to be converted into heat eventually, we discuss the transferred energy in terms of a heating rate.

In the framework of turbulence, the energy of the fluctuations at low frequencies is transported without energy loss through the inertial range until it reaches the dissipation range, where the energy is converted into heat. Assuming a quasi-steady state process, the energy transport rate ϵ is constant at any scale and therefore also equal to the dissipation rate. For the estimation of the plasma heating rate density q, we use methods based on *Leamon et al.* (1999) (q_L) and *Saur* (2004) (q_S). We assume a turbulent cascade of kinetic Alfvén waves according to the gyrokinetic approach of *Howes et al.* (2006) and *Schekochihin et al.* (2009) because this theory is suited to explain our observations. The energy transport rate in terms of the total energy E_tot is

$$\epsilon \sim \frac{E_\mathrm{tot}}{\tau_\mathrm{tr}} \sim E_\mathrm{tot}\frac{\tau_\mathrm{KAW}}{\tau_\mathrm{nl}^2} \ , \tag{3.22}$$

where we use a transfer time $\tau_\mathrm{tr} \sim \tau_\mathrm{nl}^2/\tau_\mathrm{KAW}$. According to our derivations in Section 2.2.6, $\tau_\mathrm{KAW} \sim (k_\perp \rho_i k_\parallel b)^{-1}$ is the linear wave period of kinetic Alfvén waves and $\tau_\mathrm{nl} \sim (k_\perp \delta b)^{-1}$ is the nonlinear time with fluctuation $\delta b = k_\perp \rho_i \delta B/\sqrt{\mu_0 \varrho}$ in velocity units. Inserting this in Equation (3.22) and using $E_\mathrm{tot} \sim \delta B^2/(\mu_0 \varrho)$, we find

$$\epsilon \sim \frac{\delta B^4}{\mu_0^2 \varrho^2}\frac{k_\perp^3 \rho_i}{k_\parallel V_\mathrm{A}} \ . \tag{3.23}$$

Comparing the characteristic time scales, we can estimate if the turbulence at Saturn is weak ($\tau_\mathrm{KAW} < \tau_\mathrm{nl}$) or strong ($\tau_\mathrm{KAW} \sim \tau_\mathrm{nl}$ for a critically balanced cascade). For that matter, we use as characteristic parallel scale of the system the total ion scale height of the plasma sheet, $H \sim k_\parallel^{-1} \sim 2{-}5\,R_\mathrm{s}$, with values from *Thomsen et al.* (2010) and for the characteristic perpendicular scales $\ell_\perp \sim k_\perp^{-1} \sim v \cdot \tau_c$. Here, we estimate the correlation time τ_c by the time, where the auto-correlation function reaches a value of $1/e$, for each component of the 10 min time series and subsequently average the components' correlation times

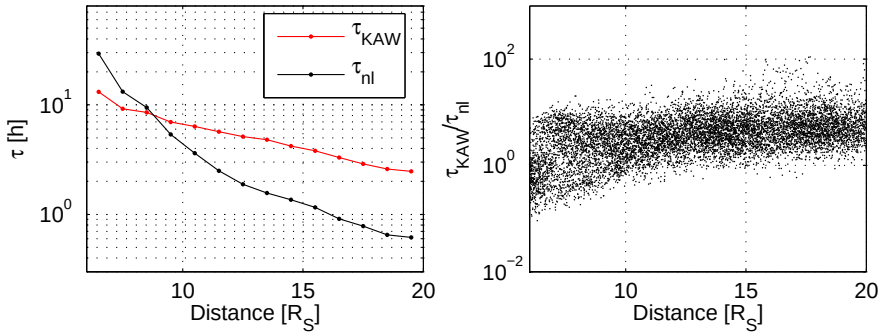

Figure 3.27: *Left: Nonlinear time τ_{nl} and kinetic Alfvén time τ_{KAW} averaged in $1\,R_{\mathrm{s}}$-bins as a function of radial distance to Saturn. Right: Ratio of characteristic times $\tau_{\mathrm{KAW}}/\tau_{\mathrm{nl}}$ of all 10 min time series. Generally, we estimate that $\tau_{\mathrm{nl}} < \tau_{\mathrm{KAW}}$, which indicates strong turbulence.*

τ_i according to $\tau_c = (\tau_x + \tau_y + \tau_z)/3$. The such calculated τ_c is on average 50 s in the plasma sheet. This leads to characteristic length scales perpendicular to the magnetic field of $\ell_\perp \sim 1000{-}5000\,\mathrm{km}$. In Saturn's middle magnetosphere, we generally find that $\tau_{\mathrm{nl}} < \tau_{\mathrm{KAW}}$. The results of our observations are shown in Figure 3.27, where the characteristic times, averaged in radial bins of $1\,R_{\mathrm{s}}$, are shown in the left panel and the ratio of the two times, $\tau_{\mathrm{KAW}}/\tau_{\mathrm{nl}}$, for all analyzed 10 min (of the extended data set, see Section 3.5.1) is shown in the right panel. Only inside $9\,R_{\mathrm{s}}$, the nonlinear time is comparable or even larger than the kinetic Alfvén time: $\tau_{\mathrm{nl}} \gtrsim \tau_{\mathrm{KAW}}$. This further corroborates our interpretation that we are observing strong turbulence. Therefore, we further use $\tau_{\mathrm{KAW}} \sim \tau_{\mathrm{nl}}$, which can be expressed as $k_\perp \delta B/\sqrt{\mu_0 \varrho} \sim k_\parallel V_{\mathrm{A}}$.

Having chosen a turbulence model, we can calculate the heating rate density $q \sim \epsilon\varrho$ in $\mathrm{W\,m^{-3}}$. After *Leamon et al.* (1999), using conservation of energy $\delta B^2 = P(f)f$ with the observed power spectra $P(f)$ in spacecraft frame and $k_\perp \simeq 2\pi f/(v\sin(\theta))$, Equation (3.23) gives

$$q_{\mathrm{L}}(f) \sim \frac{P(f)^{3/2} f^{7/2}}{\sqrt{\mu_0^3 \varrho}} \left(\frac{2\pi}{v\sin(\theta)}\right)^2 \rho_W \tag{3.24}$$

for strong KAW turbulence. As this heating rate is a function of frequency, we average the heating rate density $q_{\mathrm{L}}(f)$ in the kinetic range of the spectrum ($k_\perp \rho_W = [2, 50]$), where it is approximately constant. Another way to estimate the heating rate density is according to *Saur* (2004). He estimates the energy not from the power spectral densities but from the RMS δB of the time series. For strong KAW turbulence this approach yields

$$q_{\mathrm{S}} \sim \frac{\delta B^3}{\sqrt{\mu_0^3 \varrho}} \frac{\rho_W}{v^2 \tau_c^2}\ . \tag{3.25}$$

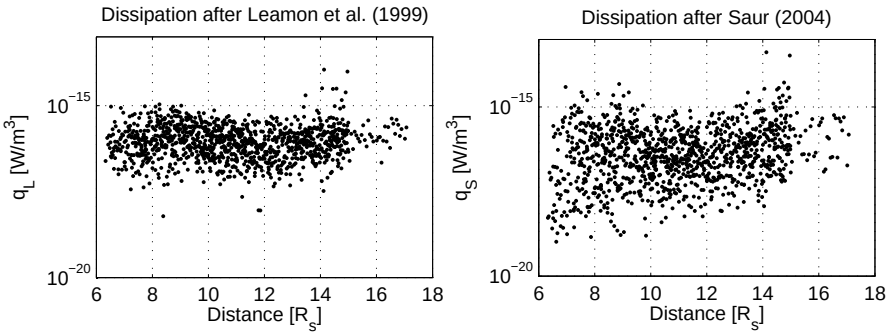

Figure 3.28: *Plasma heating rate densities q_{L} (left) and q_{S} (right) as functions of radial distance from Saturn for strong KAW turbulence.*

The resulting profiles of dissipated energy are shown in Figure 3.28 and are fairly similar. After *Leamon et al.* (1999), the strongest heating occurs at $\sim 9\,R_{\mathrm{s}}$, i.e., near the orbit of Rhea, whereas the heating rate density after *Saur* (2004) slightly increases with distance from Saturn. Integrating the heating rate densities over the volume of the plasma sheet from $6\,R_{\mathrm{s}}$ to $17\,R_{\mathrm{s}}$, where we use $2H$ as thickness of the plasma sheet, we arrive at total heating rates of $Q_{\mathrm{S}} \sim 120 \cdot 10^9\,\mathrm{W}$ and $Q_{\mathrm{L}} \sim 150 \cdot 10^9\,\mathrm{W}$ provided by dissipation of turbulent fluctuations in the middle magnetosphere. Note, that we restrict our calculation to the analyzed region and that the plasma sheet is larger than the integration volume. In the next section, we apply an extended data set that reaches up to $20\,R_{\mathrm{s}}$, which is close to the magnetopause standoff distance. This data set yields the similar radial profiles as shown in Figure 3.28, i.e., there is no further increase of heating rates beyond $17\,R_{\mathrm{s}}$. However, due to the larger integration volume, the total dissipation rate amount to $140 - 160\,\mathrm{GW}$ for the extended data set.

The obtained heating rates are in agreement with estimations by *Bagenal and Delamere* (2011) ($75{-}630\,\mathrm{GW}$) of how much power is needed to heat the plasma to the observed temperatures. However, the estimated values depend strongly on the underlying plasma and/or turbulence models. The results indicate that turbulent dissipation in general plays a substantial role for the energy budget and may help to explain the puzzling high plasma temperatures in Saturn's magnetosphere.

3.5 Asymmetries of Magnetospheric Turbulence

Various parameters in Saturn's magnetosphere, e.g., the magnetic field and the plasma density (*Espinosa et al.*, 2003; *Burch et al.*, 2009; *Andrews et al.*, 2010), as well as transient magnetospheric phenomena like injection events, energetic neutral atoms and flux-tube interchanges (*Krimigis et al.*, 2005; *Müller et al.*, 2010; *Kennelly et al.*, 2013) have been found to depend on longitude and/or local time (see e.g. *Carbary and Mitchell*, 2013, for a review on periodicities found at Saturn). In this section, we analyze if the derived parameters from our observa-

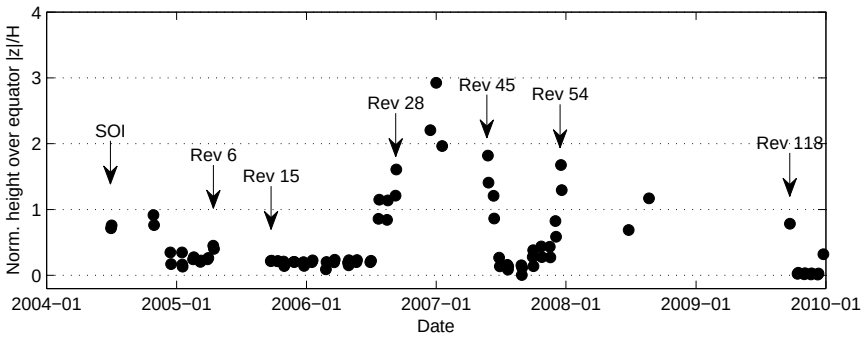

Figure 3.29: *Height over geographic equator, $|z|/H$, normalized by the scale height of the plasma sheet for each analyzed orbit. Shown are the maximal heights during the analyzed intervals. The polar phases of Cassini span from late 2006 to early 2007 and from 2008 to mid 2009. Names of revolutions given for orbits at the beginning and end of the equatorial phases.*

tions and the associated turbulent heating rate also show such variations with respect to local time or planetary longitude. The aim is to link the turbulence to observed magnetospheric phenomena and to find out if and how the existence of a turbulent cascade physically affects magnetospheric processes or is itself affected.

3.5.1 Extended Data Set

To research the asymmetries in Saturn's magnetosphere, we use an extended data set, which covers 43 orbits mostly from the equatorial phases of Cassini: SOI, Rev's A-C, 3-6, 15-28, 35-37, 45-54, 73, 81, and 118-123. Figure 3.29 shows the maximal normalized height $|z|/H$ over the equator during the analyzed interval of each of the 43 orbits. The polar phases of Cassini were excluded from the analysis because Cassini is located in the plasma lobes during the largest part of the respective orbits. The polar phases include some higher inclination orbits in mid 2005 (Rev's 7-14), Rev's 29-44 from late 2006 to early 2007 and Rev's 55-117 from 2008 to mid 2009. The two orbits (Rev's 73 & 81) during the second polar phase are only analyzed over a short interval around the center of the plasma sheet, so that the height shown in Figure 3.29 does not reflect the true orbit.

The orbits covered in the extended data set projected onto the equatorial plane as a function of distance and local time are shown in the left panel of Figure 3.30. We show only those parts where $|z| \leq H$, which is why some orbits have only short arcs. The middle and right panel of Figure 3.30 show the coverage as a function of local time and longitude, respectively. Here, we use radial bins of $1\,R_\mathrm{s}$, local time bins of 1 h and SLS4 bins of 5°. Dark blue colors show bins with two or less data points and thus represent sparsely sampled locations. The local

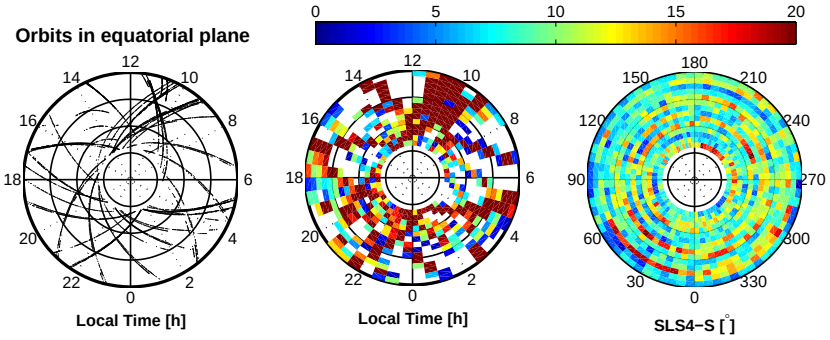

Figure 3.30: *Left panel: Cassini's orbits projected onto the equatorial plane. Middle and right panel: coverage of data as a function of local time and longitude (SLS4), respectively. The colors show the number of blocks falling into each bin. Dark blue colors represent low coverage (< 4). Circles are drawn every* $5\,R_\mathrm{s}$ *for* $r = 5{-}20\,R_\mathrm{s}$.

time coverage is limited around post-noon (∼14 h), midnight (0 h), and post-dawn (6−9 h) in the outer part ($r > 10\,R_\mathrm{s}$) of the magnetosphere and, therefore, some white spaces appear in the middle panel of Figure 3.30. However, there is very good coverage around pre-noon (∼10 h) and in the middle magnetosphere ($r = 6{-}15\,R_\mathrm{s}$) of the night side. As a function of longitude, the coverage is sufficient to compute reasonable averages throughout the whole analyzed area.

For the extended data set, we use the following thresholds to make sure that Cassini is located in the plasma sheet and not in the lobes or even outside the magnetopause. Additional to the threshold of the RMS ($0.1\,\mathrm{nT} < \delta B < 3\,\mathrm{nT}$), which was already used in the statistical study in Section 3.4, we also use restrictions on the maximum increment, $\Delta b < 1\,\mathrm{nT}$, to filter out spikes in the data. We further restrict the normalized height over the magnetic equator, $|z| \leq H$, to be smaller than or equal to the scale height H of total ions and restrict the background magnetic field to $B \geq 2\,\mathrm{nT}$. The latter condition is to make sure that Cassini is inside the magnetopause. A larger and much more conservative threshold of $B \geq 5\,\mathrm{nT}$ had been applied to the data for testing purposes, which yielded similar results to those presented here. This affirms that magnetopause effects are minimal if not absent in our results. The magnetopause crossings can be identified by a sudden drop of magnetic pressure and the onset of strongly turbulent magnetosheath fluctuations (see, e.g., *Arridge et al.*, 2008a). To exclude moon plasma interactions, we only use data where Cassini is at a distance of at least $2\,R_\mathrm{s}$ from any of the icy moons or Titan. Finally, we remain with 9505 10 min time series for the analysis in this section.

Longitude Systems There are currently two SLS4 systems publicly available, one from *Lamy* (2011) (valid until July 2010) and one from *Gurnett et al.* (2011)

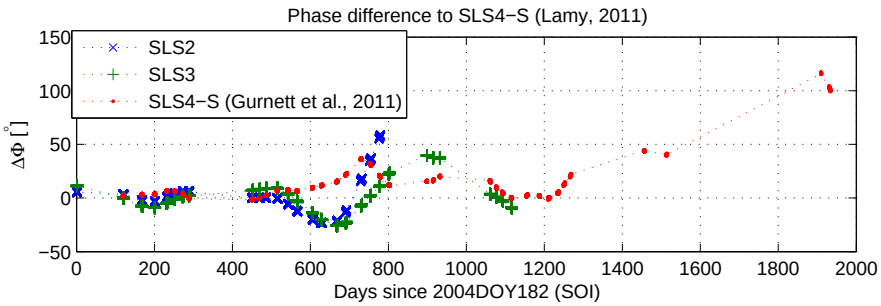

Figure 3.31: *Phase difference* $\Delta\Phi$ *for the southern period of SLS2, SLS3 (Kurth et al., 2007, 2008), and SLS4 (Gurnett et al., 2011) with regards to SLS4 according to Lamy (2011). With exception of the last two covered orbits the difference to SLS4 (Gurnett et al., 2011) is less than* 50°*. Note, that SLS2 and SLS3 are only for valid until day* 788 *and day* 1135*.*

(valid from 12 September 2004 until 16 October 2009). Although both lack verification through a peer review process, we decided to use the SLS4 system because we would be unable to analyze all our data with the SLS3 system, which is only defined until day of year (DOY) 222 of 2007. Here, we use the SLS4 system according to *Lamy* (2011) because it covers the whole time interval of our data set. However, we cross checked our results presented in this section with those obtained from longitudes given by *Gurnett et al.* (2011) and the older SLS3 system using data from the respective valid time intervals, which yielded no significant differences. Therefore, we only present results from SLS4 (*Lamy*, 2011) in this thesis.

A comparison of the used longitude system with the SLS4 system given by *Gurnett et al.* (2007) and the former systems SLS2 and SLS3 (*Kurth et al.*, 2007, 2008) is visualized in Figure 3.31, which shows the phase differences $\Delta\Phi$ with regards to SLS4 by *Lamy* (2011). 750 d and 1200 d after Saturn Orbit Insertion (SOI, counting from DOY182 2004 onward) the SLS2 and SLS3 phases, respectively, start to deviate by more than 50° from SLS4. This is in accordance with the range up to which these systems are valid, namely DOY240 2006 (788 d) for SLS2 and DOY222 2007 (1135 d) for SLS3. The difference to SLS4 given by *Gurnett et al.* (2011) is usually $< 50°$ with exception of the latest orbits after Cassini's polar phase from $\sim$1500 d−1900 d.

3.5.2 Root Mean Square of Fluctuations

We begin the analysis of our observations with the root-mean-square or standard deviation of the magnetic fluctuations, δB, from 10 min time series in units of nT. The RMS mainly reflects the energy of low frequency fluctuations because they contain most of the power in the time series. The contribution of high frequency or kinetic range fluctuations to the RMS is negligible. To minimize the influence of the background magnetic field, we subtracted a linear fit from the

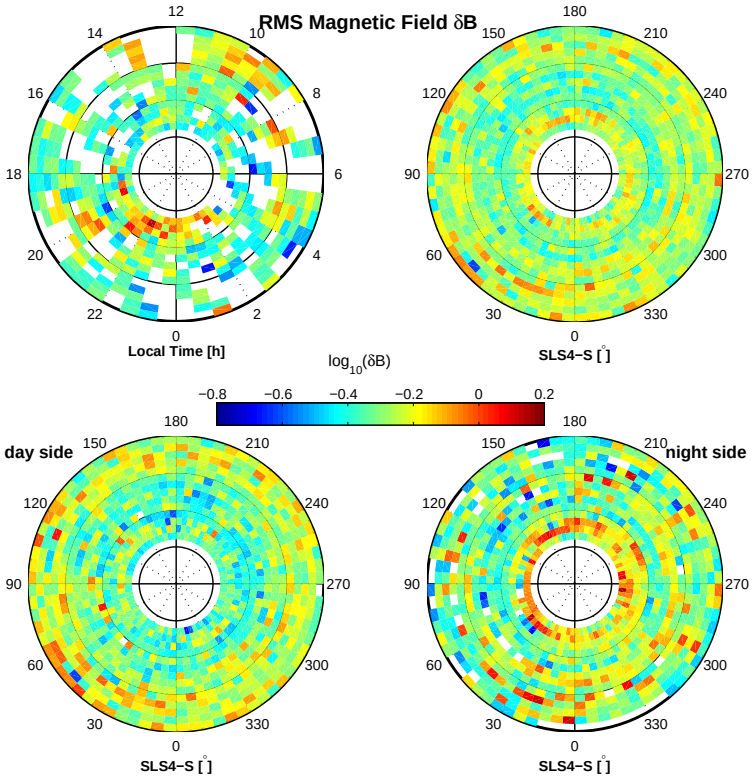

Figure 3.32: *Root-mean-square δB of 10 min time series with subtracted linear fit as a function of local time (top left) and longitude SLS4 (top right). The bottom row shows the longitude distribution on the day side (6−18 h) and on the night side (18−6 h) of the magnetosphere. Concentric circles are drawn every 5 R_S for $r = 5{-}20\,R_S$.*

10 min time series before computing the RMS. The result is shown in Figure 3.32 as a function of local time (top left), longitude (top right), and as a function of longitude for data obtained on the day side (6 h < LT < 18 h) and night side (LT < 6 h and LT > 18 h) of the magnetosphere (bottom left and right, respectively). Concentric black circles denote the distance at every 5 R_S starting from 5 R_S distance from Saturn to the outermost circle at 20 R_S. The data in each bin is averaged geometrically because of the near log-normal distribution of the parameter (see Appendix B for an analysis of the statistical distribution of δB).

From the local time distribution it seems that there are two local maxima: one around pre-noon in the outer part of the analyzed area ($r > 15\,R_S$) and one around midnight in the inner magnetosphere ($r < 10\,R_S$). In the longitude distribution (top right) the energy is more homogeneously distributed. However,

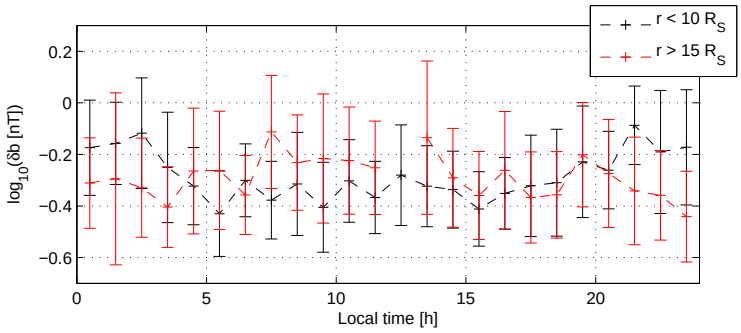

Figure 3.33: *Root-mean-square δB of 10 min time series as a function of local time. Shown are geometrical averages for distances inside $10\,R_s$ and outside $15\,R_s$ and the corresponding standard deviations of the mean logarithms.*

before interpreting these findings, it is worth while to look at the averages of δB and their standard deviations, e.g., inside $10\,R_s$ and outside $15\,R_s$, as a function of local time in Figure 3.33. Here, we see that the spread of the parameters is actually very large and the error bars overlap at all times. This indicates that the parameter - even though it seems to be ordered in local time - is primarily controlled by other processes that account for the large scatter. Hence, we have to be cautious when interpreting the data shown in the color coded distribution maps because the respective confidence bounds are not indicated.

In Figure 3.33 it seems that there are two opposite patterns in the data inside $10\,R_s$ and outside $15\,R_s$: the former peaks around midnight and the latter peaks at pre-noon at $\sim$8 h. However, the coverage in the morning sector and post-noon is not very good, which complicates the exact localization and interpretation of the pre-noon peak. The increased activity of the fluctuations may be due to waves generated by an oscillating magnetopause (*Clarke et al.*, 2006), which would trigger fluctuations peaking around noon. A peak at dawn, on the other hand, would be consistent with a modulation of field-aligned currents (FAC) as proposed by *Southwood and Kivelson* (2009). They argue that corotating plasma from the outer magnetosphere is being compressed as it enters the dawn side and a modulation of the swept back field lines ($B_\phi > 0$ in the southern hemisphere) appears, which is caused by the corotating magnetic field pattern shown in Figure 3.8. This modulation is believed to be linked to the generation of SKR. MHD Simulations by *Jia et al.* (2012b) indicate that the FAC are strongest at 6−12 h local time. It is reasonable to believe that these field-aligned currents are linked to increased magnetic field fluctuations. It is also interesting to note that *Mitchell et al.* (2009) found periodic enhancements of energetic neutral atoms (ENA) in the dawn sector at distances $15-20\,R_s$ linked to auroral brightenings and SKR activity. They suspect the azimuthal pressure gradients corresponding to the ENA enhancements to drive field-aligned currents and thus to be responsible for the generation of SKR and auroral brightening.

Around midnight, where we also observe strong fluctuations (Figure 3.32), *DeJong et al.* (2011) found an increased flux of trapped electrons at $8\,R_\mathrm{s}$ and *Kennelly et al.* (2013) observed an increased occurrence rate of young interchange events. The latter are usually linked to magnetic field depressions, high-frequency waves seen in RPWS data, and/or energetic particles that show dispersion signatures in MIMI and CAPS data (*André et al.*, 2007; *Mauk et al.*, 2005; *Chen et al.*, 2010b). *Müller et al.* (2010) find that these injection events occur mostly in the midnight-to-dawn sector and *Chen et al.* (2010b) find most events around at a distance of $\sim 7.5\,R_\mathrm{s}$, which is roughly consistent with our observation in Figure 3.33. A careful check of the time series corresponding to the most energetic fluctuations in this section showed that the high RMS values are predominantly caused by fluctuations δB_z parallel to the magnetic field. The interpretation of an increased occurrence of interchanges may therefore be a reasonable explanation for our observations.

The day side longitude distribution of the RMS in Figure 3.32 (bottom left) shows that the local maximum found at pre-noon for $r > 15\,R_\mathrm{s}$ is not restricted to a certain longitude as it leads to increased fluctuations observed at all longitudes at the corresponding distances. Neither are the energetic fluctuations inside $10\,R_\mathrm{s}$ around midnight restricted to a certain longitude range (bottom right). Although the day side seems to host more energetic fluctuations, a separate integration of the RMS over day and night side plasma sheet yields an energy difference of only 4%. On the night side there seems to be a longitudinal asymmetry with more energy around 300° longitude, which we discuss in detail in the next sections.

3.5.3 Relative Spectral Power on Kinetic Scales

To examine in more detail the fluctuations' energy in the kinetic range, we now analyze the relative spectral power $\langle E/E_0 \rangle$ of the turbulent cascade as introduced in Section 3.4. In contrast to the RMS of the time series, which mostly reflects low frequency energy, $\langle E/E_0 \rangle$ represents the spectral power on kinetic scales as it is averaged in the range $2 < k_\perp \rho_W < 50$. Therefore, it is a better estimate for the turbulence intensity of the considered KAW cascade (*Alexandrova et al.*, 2009).

Figure 3.34 shows that the local time and longitude distribution of the relative spectral power $\langle E/E_0 \rangle$ has basically the same characteristics as the RMS in Figure 3.32. However, the power at pre-midnight close to Saturn ($< 10\,R_\mathrm{s}$) is not as strongly enhanced as in the RMS. This is consistent with our hypothesis that the midnight peak in RMS is mainly caused by compressional fluctuations. As has been shown in our case study in Section 3.3.5, compressible fluctuations caused by mirror mode waves or interchange events predominantly affect the low frequency spectral power (see Figure 3.17d). However, the elevated energy of the compressional component does not reach into the kinetic range, where we estimate the relative spectral power.

The longitudinal distribution indicates an elevated energy at around 300°,

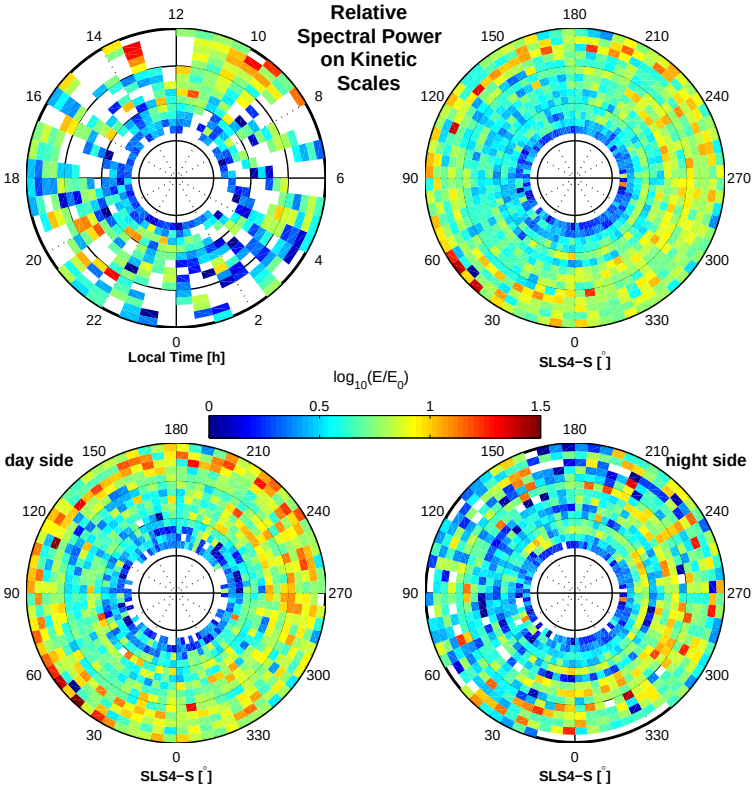

Figure 3.34: *Relative spectral power* $\langle E/E_0 \rangle$ *of* 10 *min time series as a function of local time (top left) and longitude SLS4 (top right). The bottom row shows the longitude distribution on the day side* (6−18 *h) and on the night side* (18−6 *h) of the magnetosphere. Circles are drawn every* 5 R_s *for* $r = 5{-}20\,R_s$.

which is best visible on the night side. This asymmetry can also be seen in the RMS, although less clearly. It seems to be strongest at radial distances 10−15 R_s and, indeed, examining the relative spectral power in that range (Figure 3.35) we see a sinusoidal variation with peak energy at 294° and 300° for the day and night side, respectively. However, the spread of the relative spectral power is larger than the amplitude of the sinusoid. This indicates that the influence of other magnetospheric processes that are independent of longitude. Note, that the longitude range of elevated energy is in accordance with findings of increased plasma density for electrons by *Gurnett et al.* (2007) and ions by *Burch et al.* (2009). In the next section, we analyze if the change of spectral power also changes the turbulence characteristics, namely the spectral index of the cascade.

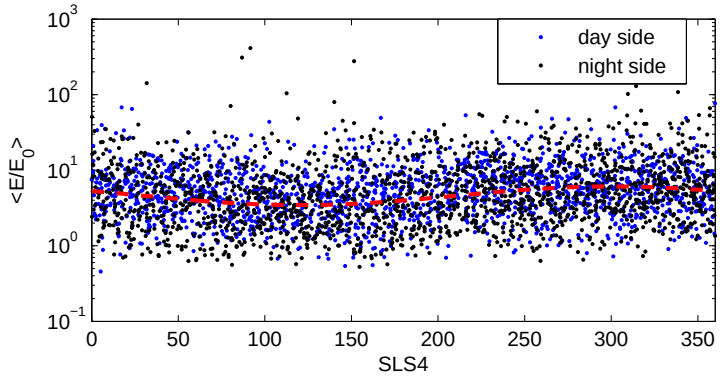

Figure 3.35: *Relative spectral power* $\langle E/E_0 \rangle$ *of* 10 *min time series for distances* $10{-}15\,R_\mathrm{s}$. *Blue dots indicate observations on the day side and black dots observations on the night side magnetosphere. The red dashed line shows a least-squares sinusoid fit to the data with peak phase at* 300°.

3.5.4 Spectral Index

We discuss the distribution of spectral indices $\kappa^{k\rho}$ to study how the asymmetries in the energy of the time series may affect the turbulent cascade. From the theory laid out in Chapter 2, we expect the spectral index to be constant and independent of the RMS or spectral power. However, the fitting range over which we determine the spectral slope does depend on the spectral power because a large spectral energy in the kinetic range results in a larger signal-to-noise ratio and thus a longer fitting range. Therefore, in case the spectral index changes with growing frequency, we might see a variation of the slope that correlates with the relative spectral power.

Figure 3.36 shows the distribution of the spectral index as a function of local time and longitude. From the local time distribution (top left) it is evident that the enhanced RMS at pre-noon coincides with steeper spectral slopes. The variation is strongest outside $15\,R_\mathrm{s}$: between $8{-}12$ h local time the mean spectral slope is 2.63 ± 0.23 compared to 2.49 ± 0.28 at local times $20{-}24$ h for $r > 15\,R_\mathrm{s}$. Further analyses reveal that the spectral index is weakly correlated ($c = -0.33$) with the relative spectral power in the kinetic range, $\langle E/E_0 \rangle$, such that a higher spectral energy correlates with steeper slopes. This correlation is shown in Figure 3.37 and might be explained by power spectra steepening with frequency. Such steepening may be caused by damping on electron scales, which is already detectable in the ion kinetic range (see Section 4.2.3) and has been observed in the solar wind (*Alexandrova et al.*, 2012). In Figure 3.37, it can also be seen that the spread of spectral indices is greater at lower energies and we that the error of the fit is weakly correlated ($c = -0.33$) with the spectral power $\langle E/E_0 \rangle$. However, this can be understood by the fact that the fitting range is longer and the signal-to-noise ratio is larger for higher spectral energy, which consequently leads to a smaller error for the fit of the spectral slope.

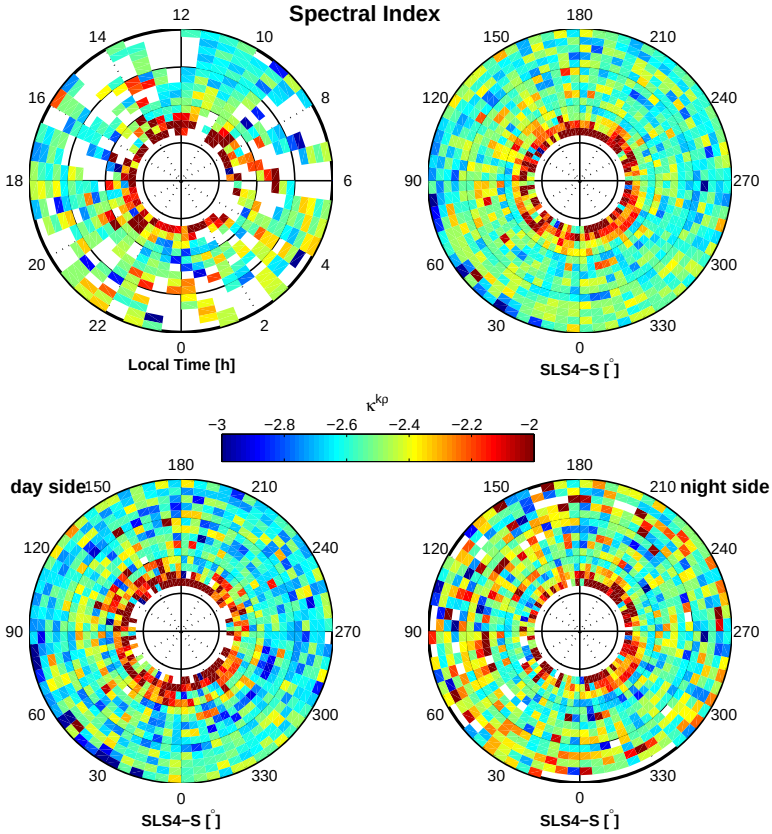

Figure 3.36: *Spectral index $\kappa^{k\rho}$ of 10 min time series as a function of local time (top left) and longitude SLS4 (top right). The bottom row shows the longitude distribution on the day side (6−18 h) and on the night side (18−6 h) of the magnetosphere. Circles are drawn every 5 R_s for r = 5−20 R_s.*

The longitudinal variation (Figure 3.36, top right) of the spectral index is very weak. Slightly steeper spectra are found around ∼300° caused by the correlation with the relative spectral power $\langle E/E_0 \rangle$. However, the spectral indices are more uniformly distributed than the relative spectral power, although the day side (bottom left) spectra are a little steeper than the night side (bottom right) spectra outside 9 R_s ($\kappa_{day} - \kappa_{night} = 0.05$). This can be seen in the bottom row of Figure 3.36 and is mainly the result of the higher energy on the day side. The shallower spectra inside 9 R_s are generally visible by red colors close to Saturn in all distributions. This indicates that the shallower slopes are caused by a process independent of local time and longitude. In summary, the slight changes of the spectral index with local time and longitude are generally very

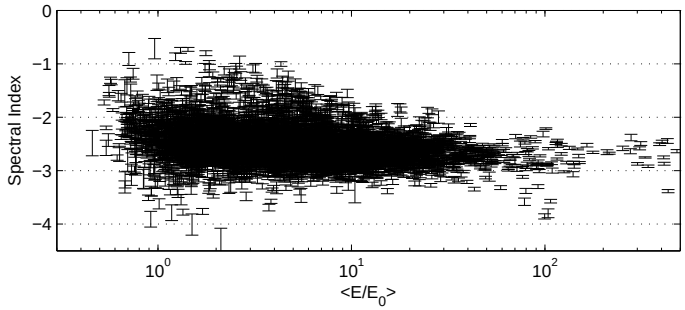

Figure 3.37: *Spectral index $\kappa^{k\rho}$ for distances $r > 9\,R_\mathrm{s}$ as a function of relative spectral power $\langle E/E_0 \rangle$. Both the spectral index κ and its error $\Delta\kappa$ (obtained from least-squares fit to the PSD) are weakly correlated with the spectral energy. The spread of the spectral indices is much less at higher energies.*

small and, thus, do not indicate a change in the nature of the turbulent cascade. The averaged spectral index for distances $r > 9\,R_\mathrm{s}$ in the extended data set is $\left\langle \kappa^{k\rho} \right\rangle = 2.54 \pm 0.33$. This is in accordance with our result of 2.58 ± 0.25 obtained in Section 3.4.1.

3.5.5 Turbulent Heating Rates

After finding systematic changes in the energy of the fluctuations with regards to local time and slight variation of the spectral index toward somewhat steeper slopes on the day side, we now analyze the turbulent heating rate densities. We discuss the energy transfered along the kinetic range turbulent cascade and analyze its asymmetric dissipation in the magnetosphere. In Section 3.4.5 we have estimated the heating rate using two different methods given by equations Equation (3.24) and Equation (3.25), which we now apply to the extended data set. Figure 3.38 shows the local time and longitude distribution of the local turbulent heating rate density q_L after *Leamon et al.* (1999) and Figure 3.39 the heating rate q_S after *Saur* (2004). Three features are clearly visible in both distributions: (1) The dissipation rate shows an enhanced heating at pre-noon similar to the RMS and relative spectral energy, (2) The day side is heated more strongly than the night side, and (3) the turbulent heating seems to be ordered in longitude with increased heating at around 300°.

From the local time distributions (Figure 3.38 and 3.39, top left), it is visible that the heating is much stronger in the pre-noon sector. This shows that the strong large scale fluctuations observed in the RMS are cascaded to smaller scales, where they heat the plasma. The midnight peak close to the planet, however, is not as pronounced because the compressible energy of the mirror mode waves and the injection events is not transferred to smaller scales in the same way as the Alfvénic fluctuations. The longitude distributions of the heating rates q_L and q_S shown in Figure 3.38 and 3.39 (top right), respectively, indicate

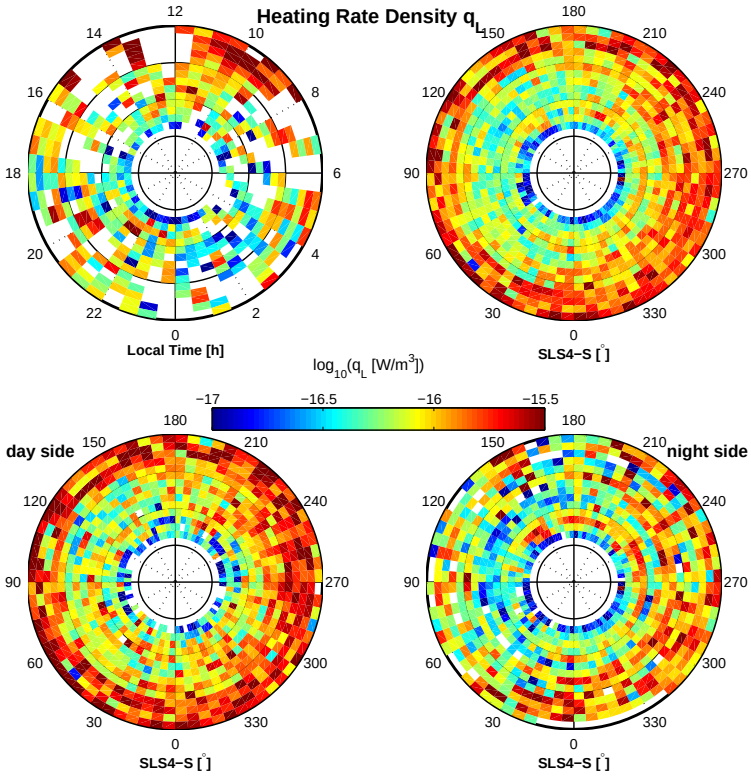

Figure 3.38: *Turbulent heating rate density q_L from 10 min time series as a function of local time (top left) and longitude SLS4 (top right). The bottom row shows the longitude distribution on the day side (6−18 h) and on the night side (18−6 h) of the magnetosphere. Circles are drawn every 5 R_s for $r = 5$−20 R_s.*

an intensified heating at around 300°. This asymmetry strongly correlates with the relative spectral power, $c > 0.93$, on both day and night side. This affirms that the strong turbulent heating can be explained by an increased flux of energy along the cascade. The outer region of the magnetosphere ($r > 15\,R_\mathrm{s}$) is heated more strongly on the day side, which stems from the increased heating in the pre-noon sector. This feature is not ordered in longitude and, hence, obscures any longitudinal dependence that might be present outside $15\,R_\mathrm{s}$. In contrast, the night side has a visibly distinct peak at ∼300° in the outer magnetosphere.

The longitudinal variation in the distribution of q_S is less clear than the one obtained from q_L. Compared to q_L, the heating rates q_S are generally lower and show a stronger radial increase with distance to Saturn. The radial dependence of q_S is in part controlled by the correlation time τ_c, which causes a positive correlation ($c = 0.55$) with radial distance. However, errors of τ_c may be caused by

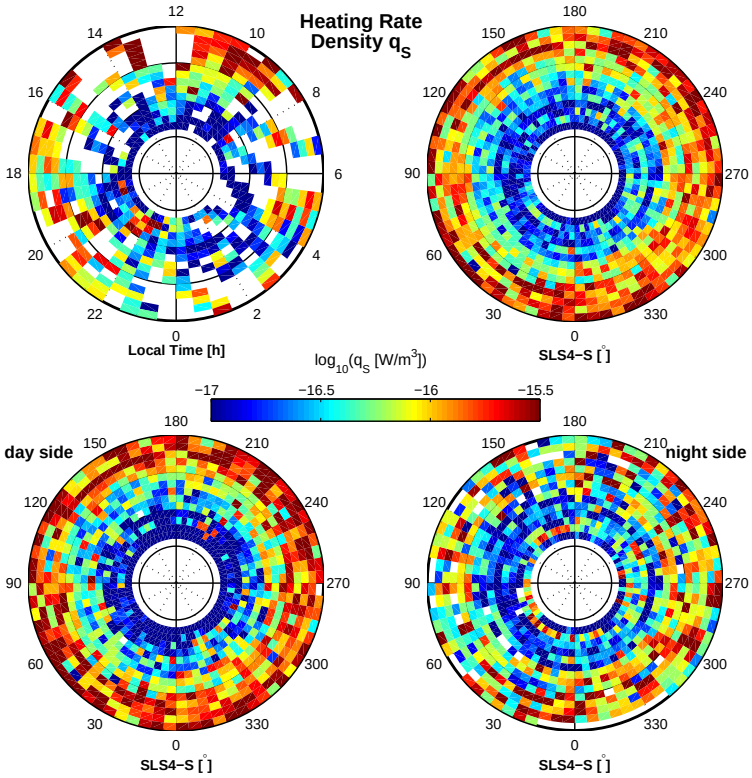

Figure 3.39: *Turbulent heating rate density q_S from 10 min time series as a function of local time (top left) and longitude SLS4 (top right). The bottom row shows the longitude distribution on the day side (6−18 h) and on the night side (18−6 h) of the magnetosphere. Circles are drawn every 5 R_s for $r = 5$−20 R_s.*

large scale magnetospheric processes, which strongly affect the auto-correlation function of the magnetic field time series. These errors may thus explain the difference between the two heating rates. Integration of the heating rate densities from 6-20 R_s over the plasma sheet using the scale height of water group ions according to Equations (3.24) and (3.25) yields a total of 140-160 GW. Using the total ion scale height, according to the estimation in Section 3.4.5, we find an even stronger heating of 190−220 GW. Both estimations are in agreement with our prior ones and the slightly larger values are primarily caused by the larger integration volume (6-20 R_s compared to formerly 6-17 R_s).

Looking in particular at the heating rates at distances $10 < r < 15\,R_s$ in Figure 3.40, we further analyze the longitudinal variation of both q_L (top) and q_S (bottom). The Figure shows the heating rates for each 10 min time series on both day and night side. The red line depicts a sinusoid ($\hat{y}$), which was fitted

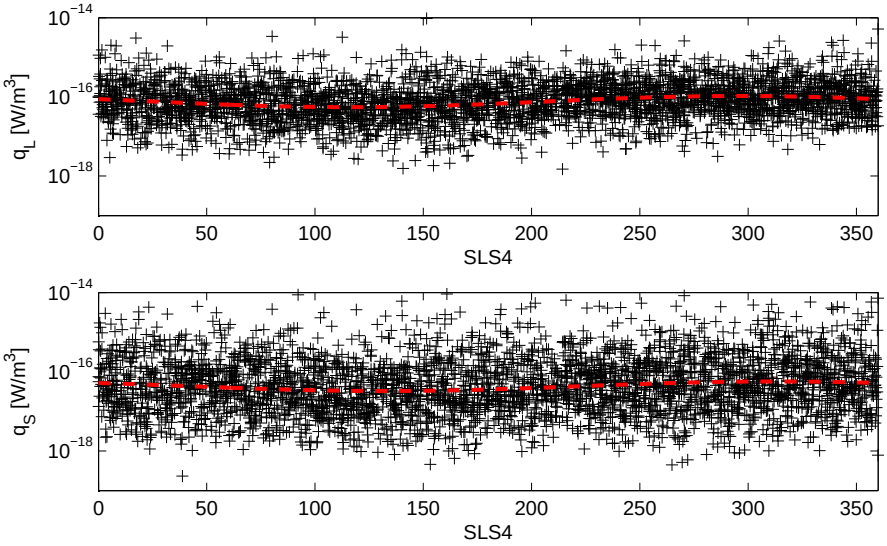

Figure 3.40: *Turbulent heating rate densities q_L and q_S from 10 min time series as a function of longitude for radial distances $10\,R_\mathrm{s} < r < 15\,R_\mathrm{s}$. Red line shows a sinusoid with peak at 296° for q_L in the top panel and 312° for q_S in the bottom panel.*

to the data peaking at ∼300° for both heating rates. It is clear that the spread of the parameters is much larger than the amplitude of the sinusoids. Indeed, if we subtract the model $\hat{y}$ from the data y, the mean sum of squares

$$\sigma^2_{y-\hat{y}} = \sum \frac{(y-\hat{y})^2}{n-3} \tag{3.26}$$

with respect to the sinusoidal model will be only marginally lower than the variance

$$\sigma^2_{y} = \sum \frac{(y-\bar{y})^2}{n-1} \tag{3.27}$$

with respect to the mean $\bar{y} = \langle y \rangle$. Percentually, the decrease is 4% in the case of q_L and 1% in the case of q_S. This gives an idea of how much of the spread can be explained by the model. Despite of this small decrease, the fit $\hat{y}$ may still be an improvement compared to the simple mean of the heating rate $\bar{y}$. The statistical significance of such an improvement is tested in the following paragraph.

Significance Test

To estimate the significance of the sinusoidal fit, we use the statistical F-test (see e.g. *Bevington and Robinson*, 2003, chapter 11.4). Here, we test the null hypothesis that the data y can be explained by a simple model with one degree of freedom, i.e., a constant mean value $\bar{y} = \langle y \rangle$, against the hypothesis that the

data is best fitted by a model $\hat{y}$ with three degrees of freedom ($p = 3$). This model is given by

$$\hat{y} = c_0 + c_1 \cdot \sin(m \cdot x - c_2) \ , \tag{3.28}$$

where x is the longitude and $m = 1$ the order of the sinusoid. The parameters c_i are determined by a least squares fit to the logarithmic heating rate densities. First, we compute the sum of squares associated to the simple model, S_1, and the sum of squares associated to the extended model with three degrees of freedom, S_3:

$$S_1 = \sum_{i=1}^{n} (y - \bar{y})^2 \qquad\qquad S_3 = \sum_{i=1}^{n} (y - \hat{y})^2 \ , \tag{3.29}$$

where n is the number of data points. According to *Bevington and Robinson* (2003) the key parameter F of this test can be considered as the improvement due to the extended model divided by the sum of squares of the extended model. This parameter is further normalized with the number of data points n and the associated degrees of freedom p, which yields

$$F = \frac{(S_1 - S_3)}{S_3} \cdot \frac{(n - p)}{(p - 1)} \ . \tag{3.30}$$

The test statistic F follows a Fisher F_{n-p}^{p-1}-distribution, for which we can calculate a critical value F_c given a percentual certainty that we want to exceed (*Wishart*, 1947; *David*, 1949). Here, we use a 95% certainty, which means that the probability of the improvement from the sinusoidal model to happen by chance is 5%. Hence, if $F > F_c$, the null hypothesis needs to be rejected and the extended model will be a significant improvement to the data. In the case of Figure 3.40, we find that the fit leads to a significant improvement with $F/F_c = 25.5$ for q_{L} and $F/F_c = 8.4$ for q_{S}. Using the SLS3 system for data up to DOY222 2007, we find a similarly significant improvement with $F/F_c = 24.5$ for q_{L} and $F/F_c = 10.0$ for q_{S}. This again indicates the accuracy of the SLS4 system.

However, we also want to mention the limits of the applied significance test. The F-test as shown in Equation (3.30) is only valid for variables y, which are normally distributed. Therefore, we work with the logarithms of the heating rates since q_{L} and q_{S} are approximately log-normal distributed. However, the variables y also need to be statistically independent. Strictly speaking, this is not the case for the present data set: it is unreasonable to believe that a measurement 10 min later is completely independent of the measurement before because the plasma conditions and the magnetospheric environment change on time scales much longer than 10 min. Hence, the results of this significance test have to be treated with caution and we thus proceed with a further and more detailed study, where we analyze the single orbits of Cassini separately.

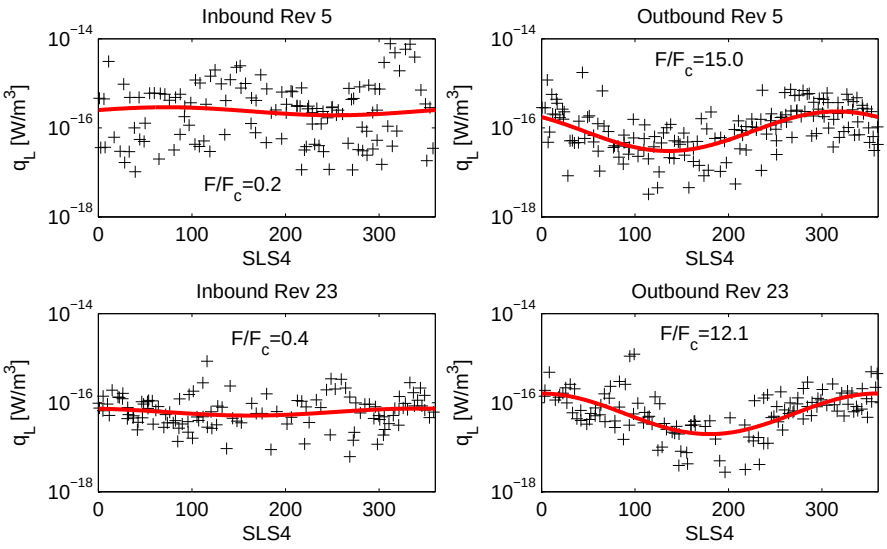

Figure 3.41: *Turbulent heating rates q_L of 10 min time series during in- and outbound legs of Rev 5 (top row) and Rev 23 (bottom row) as functions of longitude (black crosses) and their respective sinusoidal fits (red line). Unlike Figure 3.40, no additional restrictions on radial distance r have been applied here.*

Analysis of Single Orbits

A careful analysis of the in- and outbound legs of single orbits shows that the heating rates of some orbits strongly depend on longitude, whereas others completely lack this correlation. As an example for this on and off correlation, we show in Figure 3.41 the heating rates during Rev 5 (top row) and Rev 23 (bottom row) as black crosses. It is interesting to see how strongly the results differ between the in- and outbound legs although less than 24 h have passed. The values of the F-test are given in the legend of the plots and show that both outbounds are well described by a sinusoidal variation (red line). Their mean sum of squares $\sigma^2_{y-\hat{y}}$ with respect to the model $\hat{y}$ is decreased by more than 31% compared to the variances σ^2_y. Another aspect is the phase of the sinusoid, which is not constant but varies from 316° during Rev 5 to 360° during Rev 23.

In total, we find that 65% of all orbits exhibit a significant ($F/F_c > 1$) longitude dependence described by a simple sinusoidal variation. This percentage can even be increased if we restrict our analysis to shorter vertical distances from the plasma sheet center. The correlation between heating rate and longitude stems mostly from the power of the fluctuations in the kinetic range, $P(f)^{3/2}$ in Equation (3.24), and therefore reflects real energetic changes instead of mere geometric variations that arise, e.g., from the density model $\varrho(r, z)$ controlled by the location of the spacecraft. The same results are found from the analysis in the SLS3 system, which could be expected because the phase drift between the

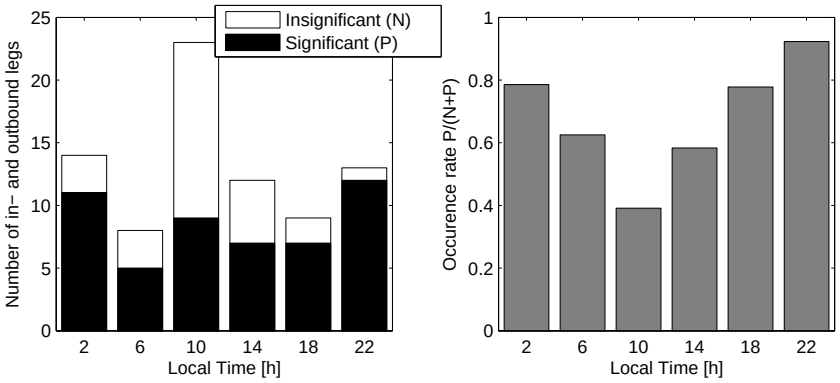

Figure 3.42: *Left: Histogram of in- and outbounds showing a significant correlation of heating rate with longitude (P) in white and those without significant correlation (N) in black as a function of local time in 4 h bins. Right: Occurrence rate of significant correlations (P/(N + P)) showing an increased probability of significant correlations in the pre-midnight sector (16 − 4 h).*

two systems is so slow that it is negligible during a single orbit. However, we might expect a difference in the absolute peak phases of the models. The average peak phases for q_{L} are quite variable and peak at a mean longitude of 295°, 305° and 312° for SLS4 after *Lamy* (2011), SLS4 after *Gurnett et al.* (2011), and SLS3 (*Kurth et al.*, 2008), respectively, but the uncertainty in all systems is very large with ±80°. A seasonal change of the phase cannot be verified from the data. For the statistically significant fits, the relative improvement of the variance is on average $\left\langle (\sigma_y^2 - \sigma_{y-\hat{y}}^2)/\sigma_y^2 \right\rangle = 20\%$ for SLS4 (*Lamy*, 2011) when the fitted model is subtracted from the data.

Figure 3.42 (left) shows the total number of in- and outbounds during which a significant ($F/F_c > 1$) correlation was found (positive) in black and those where no correlation was found (negative) in white. The data is shown as a function of local time in 4 h bins, which is approximately the local time range covered during a single in- or outbound leg. On the right hand side of Figure 3.42, we show the occurrence rate, which we estimate as the number of positive orbits (P) divided by the total number of orbits ($N + P$) in that bin. It can be seen that the occurrence rate increases strongly from 10 h, where it is minimal, to 22 h local time. Thus, the chance to find a significant correlation of the heating rate with longitude is highest in the pre-midnight sector.

3.5.6 Discussion and Comparison with Recent Observations

The fact that a sinusoidal model significantly improves the fit of the turbulent heating rate in 65% of all cases shows that the magnetic fluctuations and their associated turbulent dissipation are controlled by an asymmetry in the magneto-

sphere rotating with the planetary period. This asymmetry is more pronounced in the pre-midnight sector. Numerical simulations indicate that the plasma in this sector, in contrast to the dawn-to-noon sector, experiences less pressure and is generally slower because it is not compressed by the asymmetric shape of the magnetosphere (see, e.g., *Jia et al.*, 2012a; *Chané et al.*, 2013, for Saturn's and Jupiter's magnetosphere, respectively). This compression may mask or dominate any longitudinal correlation of plasma parameters. Note, that the asymmetry discussed here is not fixed in the plasma frame, which sub-corotates around the planet (*Wilson et al.*, 2008; *Thomsen et al.*, 2010).

We observe that the $m = 1$ correlation with longitude can get lost in less than 24 h, which shows that eventually other processes may dominate or disturb the longitudinal dependence. We cannot determine with sufficient certainty if the longitude dependence is lost completely or if it moves to higher order ($m > 1$) models. A test with $m = 2$ still yields a significant fit for 35% of the orbits although with a much lesser improvement of the variance of only 9%. Also, the mean test value of all significant fits is much smaller: $\langle F/F_c \rangle = 2.0$ for $m = 2$ compared to $\langle F/F_c \rangle = 6.0$ for $m = 1$. All analyses have been carried out in SLS3 and the two SLS4 longitude systems using data in the respective valid time intervals leading to robust results with respect to the applied longitude system. The fact that the extended data sets (up to December 2009) of the SLS4 systems lead to the same results (e.g., maximum turbulent heating at $\sim$300°) as the shorter data set in SLS3 (valid until August 2007) indicates that both SLS4 systems map the phase drift of Saturn's rotation appropriately.

There may be a transient process that disturbs the magnetosphere and thus destroys the correlation of the heating rate with longitude. The time scale of such a process would have to be at least on the order of hours. On the one hand, if its duration was much shorter, it should not be able to affect the correlation of a complete in- or outbound section. On the other hand, the change from disturbed to undisturbed state has to be quick enough for the effect to vanish in less than 24 h as has been observed for the examples in Figure 3.41. Also, large areas of the magnetosphere are affected as the in- and outbounds usually cover $\sim$4 h of local time. Such variations can only be caused by large scale processes. *Achilleos et al.* (2010) showed that the solar wind pressure can dramatically change the magnetospheric configuration. It is therefore reasonable to believe that a contracting magnetosphere during the onset of strong solar wind pressure may lead to a decorrelation of our $m = 1$ model especially around dawn and noon, where the plasma is compressed by the magnetopause boundary. Strong substorm activity as it is observed by *Jackman et al.* (2008) on the time scales of hours may also be causing such decorrelations. Although such reconnection events usually happen outside $20\,R_\mathrm{s}$, the inflowing plasma, which has been indirectly observed by huge corotating ENA clouds, may travel farther inside and disturb the magnetospheric plasma (*Mitchell et al.*, 2005).

It is interesting to compare our results with recent $m = 1$ models proposed in the literature. The increased turbulent heating at $\sim$300° is consistent with a

maximum electron density found by *Gurnett et al.* (2007) around 330° and an increased ion density found by *Burch et al.* (2009) between 270° and 50°. In the frame of the rotating magnetic field pattern proposed by *Andrews et al.* (2010), the positive B_ϕ perturbation maximizes at 340°. This rotating perturbation is connected to a rotating field-aligned current system, which is believed to drive the SKR signal (*Southwood and Kivelson*, 2009). It is interesting to note that during SKR maximum, when the subsolar longitude is 100°, the maximum heating rate at $300° \pm 80°$, points to local times of 17−4 h. This is exactly the sector, where most of the significant correlations are found. The correlation between longitude and heating rate may thus by explained by an increased heating of the night side during SKR maximum.

There may also be correlations with auroral activity at Saturn. Auroras have been extensively analyzed with regards to asymmetries in local time and longitude (*Lamy et al.*, 2009; *Nichols et al.*, 2010; *Carbary and Mitchell*, 2013; *Lamy et al.*, 2013; *Bunce et al.*, 2014). In a statistical study *Nichols et al.* (2010) showed that the aurora brightness is modulated with the SKR period. *Carbary* (2013) find that the aurora intensity peaks between longitudes of $140° - 280°$ and that the poleward displacement of the southern auroral arc is maximal around 340°. The latter is in accordance with the location of the plasma cam (*Burch et al.*, 2009; *Gurnett et al.*, 2007) and our turbulent heating rate maximum. However, *Lamy et al.* (2009) find that the auroral UV power and the SKR intensity both peak at local times 7−9 h, which is exactly opposite to the pre-midnight sector, where we observe maximal correlation of turbulent heating rate with longitude.

We can only speculate what the cause of the increased heating rate is. Given our results, it seems plausible that it is connected to the plasma cam and the increased plasma density at these longitudes. A possible scenario is that the dissipation of turbulent fluctuations leads to increased electron temperatures (after *Schekochihin et al.* (2009), the kinetic cascade heats electrons only), which in turn causes an increased ionization rate of the neutral cloud and thus leads to a higher plasma density (*Delamere and Bagenal*, 2008). However, another scenario in contrast to the preceding argument is that the heating is *caused by* the denser plasma. The higher density of the plasma results in an increased kinetic energy per volume $\varrho \delta b^2$ which is equal (on MHD scales) or nearly equal (on kinetic scales) to the magnetic energy of the fluctuations $\delta B^2/\mu_0$.

Unfortunately and despite of clear correlation of our results with previously observed phenomena by other authors, this thesis can not provide a physical explanation to link together all magnetospheric phenomena, such as increased turbulent heating, plasma density, SKR activity and auroral brightenings. In contrast, we may even find contradicting arguments when we try to separate cause and effect. Is strong turbulent heating caused by a rotating convection cell or does the turbulent heating contribute to it? Do field aligned currents drive turbulence or are electrons accelerated by turbulent dissipation. It is beyond the scope of this thesis to answer these questions. Therefore, we have to settle for having presented new interesting results of asymmetric turbulent heating in

Saturn's magnetosphere that will hopefully help to find a joint interpretation of all phenomena.

3.6 Conclusion

In this chapter, we have presented for the first time a statistical analysis of magnetic field fluctuations in the plasma sheet of Saturn's middle magnetosphere in the framework of turbulence. The turbulent spectra are characterized by a spectral break at characteristic water group ion scales and frequencies, f_b, which separates the MHD and kinetic range of scales. This spectral break is found at varying frequencies in spacecraft frame but appears at a fixed position independent of radial distance from Saturn for spectra normalized by the water group ion gyro radius ρ_W, the ion inertial length λ_W or the ion cyclotron frequency $f_{c,W}$. The relative power density of raw frequency spectra is found to depend on the ion thermal (nkT) and magnetic pressure ($B^2/(2\mu_0)$) as well as on radial distance from Saturn. The normalized spectra do not show such correlations anymore. Instead, for $k\rho_W$- and $f/f_{c,W}$-spectra, only a weak correlation is observed with ion plasma β_i. This indicates that these normalized frame is best suited for our analysis.

Power law spectral ranges at MHD scales show variable slopes of 0.8 up to 1.7 and are likely controlled by large scale magnetospheric processes, such as current sheet flapping, mirror mode activity and flux-tube interchanges. At high frequencies, $f > f_b$, there is a continuously present power-law spectral range. In this kinetic range, the spectral index of the trace of the spectral tensor is $\kappa_< = -2.3\pm0.3$ inside $8\,R_\mathrm{s}$ and $\kappa_> = -2.6\pm0.3$ for distances $r > 9\,R_\mathrm{s}$. These observed spectral slopes might be explained with theoretical spectral indices for strong and weak turbulence of KAW and whistler waves. Note, that the measured slopes may be steeper than the theoretical values due to additional damping on electron scales, which we discuss in the next chapter. Strong KAW turbulence (*Howes et al.*, 2011a) gives a slope of 7/3, whereas weak KAW turbulence after *Howes et al.* (2011a), weak Hall-MHD turbulence after *Galtier* (2006), and weak whistler turbulence after *Narita and Gary* (2010) lead to a slope of 2.5. Weak turbulence has also been observed in Jupiter's middle magnetosphere by *Saur et al.* (2002) in the inertial range. Strong KAW and whistler turbulence with a slope of 8/3 as proposed by *Boldyrev and Perez* (2012) and *Galtier et al.* (2005), respectively, and compressible Hall-MHD turbulence as described by *Alexandrova et al.* (2008a) equally well explain our results.

The observed compressibility level $E_\parallel/E$ is qualitatively in agreement with observations in the solar wind (*Leamon et al.*, 1998; *Chen et al.*, 2010a). The observation of an increasing $E_\parallel/E$ for $k_\perp\rho_H > 1$ is in accordance with the expected behavior of KAW as predicted by linear Vlasov-Maxwell theory (*Podesta and TenBarge*, 2012; *Salem et al.*, 2012). However, it might as well be explained with an increasing contribution of noise. We find that large scale fluctuations closer to Saturn ($< 11\,R_\mathrm{s}$) are increasingly compressible. It is unclear if the

same would be observed farther away from Saturn for corresponding low frequencies, which are outside the coverage of our data. The fluctuations are found to have increasingly non-Gaussian statistics for smaller scales. The observation of a power-law increase of the flatness indicates a multifractal nature of the fluctuations. It is also indicative for the build up of coherent structures and intermittency (*Mangeney*, 2012) and therefore strong turbulence. Similar results have been obtained in the solar wind (*Alexandrova et al.*, 2008a; *Salem et al.*, 2009).

We find that for radial distances $r < 9\,R_\mathrm{s}$, the nonlinear time τ_nl is on the order of the kinetic Alfvén time τ_KAW. Outside this distance, we find $\tau_\mathrm{nl} < \tau_\mathrm{KAW}$, which further corroborates that we observe strong turbulence. This narrows down the list of applicable models to describe the turbulence inside the plasma sheet of Saturn to strong KAW and whistler turbulence. However, whistler turbulence violates Taylor's hypothesis and thus cannot be explained from our analysis. Therefore, only strong KAW turbulence after *Howes et al.* (2006) is in agreement with the complete range of measured spectral slopes. We showed that the existence of such a turbulent kinetic Alfvén wave cascade substantially influences the magnetospheric energy budget. An estimated $140-160\,\mathrm{GW}$ is dissipated by turbulent magnetic field fluctuations in case of a critically balanced cascade. These estimates are on the same order of magnitude as $75-630\,\mathrm{GW}$ as estimated by *Bagenal and Delamere* (2011) which are needed to heat the plasma to the measured temperatures. This indicates that turbulent fluctuations also have important implications for overall properties of Saturn's magnetosphere and need to be taken into account to describe the energy budget in Saturn's magnetosphere.

We have further shown that the magnetic fluctuations show increased activity at distances $r > 15\,R_\mathrm{s}$ in the pre-noon sector and close to the planet inside $10\,R_\mathrm{s}$ near midnight. The latter activity seems to be mostly caused by compressible low frequency fluctuations connected to interchange events. The increased activity around pre-noon in particular and a higher spectral energy $E(k\rho)$ in general weakly correlate with observations of slightly steeper spectra. This may indicate that the spectral index is not constant along the PSD but slowly steepens toward higher wave numbers. Such a behavior is in agreement with a near dissipation range at electron scales.

The heating rate that we have estimated from the turbulent cascade on kinetic scales shows strong asymmetries in local time and longitude (SLS4 south). This asymmetry strongly correlates with the spectral energy and thus reflects an increased energy flux along the cascade. It peaks at pre-noon and shows a significant longitudinal $m = 1$ variation for 65% of all orbits in our extended data set covering 43 orbits from July 2004 to December 2009. The turbulent heating rate peaks at a longitude of $300^\circ \pm 80^\circ$, which coincides with increased plasma density (*Gurnett et al.*, 2007; *Burch et al.*, 2009), a maximum B_ϕ perturbation of a rotating magnetic field pattern (*Andrews et al.*, 2010) and poleward displacement of the southern auroral arc (*Carbary*, 2013). The longitudinal modulation

is especially pronounced in the pre-midnight sector, which coincides with the local time range of $300° \pm 80°$ when the subsolar longitude is 100°. This indicates that turbulent dissipation rate in the pre-midnight sector is significantly higher during SKR maximum.

As the energy transferred along the kinetic turbulent cascade is ultimately deposited into electrons (*Schekochihin et al.*, 2008), it would be interesting to look for longitudinal anomalies in the electron temperature. Such an analysis could shed more light on the actual dissipation mechanism of the cascade of kinetic Alfvén waves and the subsequent energy transport to other populations in Saturn's magnetosphere. In the next chapter, we present a numerical tool to calculate reduced PSD, which we apply to the measurements presented in this chapter. The successful qualitative reproduction of the observed features, namely the radial distribution of spectral indices, further corroborates that the magnetic field fluctuations can indeed be explained by a critically balanced KAW cascade. Also it indicates that the turbulent energy is primarily deposited into the hot electron population.

CHAPTER 4

Modeling Turbulent Spectra

Power spectral densities from in-situ measurements of single spacecraft are generally obtained in a one-dimensional reduced form. This means, that actually many different waves of different wavelengths and with different propagation directions are observed at the same frequency in spacecraft frame. Therefore, many waves contribute to the spectral density $P(f)$ at a certain frequency f. However, the turbulence models we have discussed in Chapter 2 are formulated in three-dimensional wave vector space. In this three-dimensional **k**-space, each wave vector **k** is assigned a certain energy. The measurement geometry determines, which of these wave vectors map to a certain frequency in spacecraft frame. Although this fact is very well known, there are to date no numerical tools to perform such a forward calculation. Hence, we derive in this chapter a numerical scheme to forward calculate reduced spectra from three-dimensional energy distributions determined by theoretical considerations for turbulence.

The idea behind this is two-fold: on the one hand we want to test the implications of certain turbulence theories on the reduced power spectra by forward calculation from a given energy density in **k**-space. Thus, we can explicitly analyze functional dependencies, e.g., the spectral index $\kappa(f, \theta, L)$ as a function of frequency f, field-to-flow angle θ, and outer scale L for a critically balanced cascade. On the other hand, the tool enables us to construct synthetic power spectra, which we can compare to measurements, e.g., our observations at Saturn. This forward modeling can be used as a new interpretation method, as it allows for the first time to analyze from first principles if observations are in accordance with a certain theory. Thus, we gain further insight into the mechanisms of the turbulent cascade.

Before we introduce our model, we examine the general form of the underlying correlation tensor in Section 4.1, which is closely related to the spectral tensor. Using symmetry arguments, we show that the diagonal elements of the spectral tensor consist of only two independent scalar functions that describe the transverse and the compressional fluctuations. These functions define the energy or power as a function of the three-dimensional wave vector **k** and can be expressed analytically for certain turbulence theories, such as critically balanced

or 2D+slab turbulence. The energy distribution or model in **k**-space can be used to compute the power spectral tensor for given measurement geometries and enables us to analyze the integral characteristics of different turbulence theories from MHD to dissipation scales. In Section 4.2, we study the characteristics of a critically balanced cascade of (kinetic) Alfvén waves. We add empirical and anisotropic damping terms and analyze their contributions to the reduced spectra. We show that the PSD develop toward a quasi-perpendicular shape, i.e., the spectral index is not constant with growing frequency in spacecraft frame.

In Section 4.3, we compare the modeled spectra with real measurements in the solar wind and confirm the applicability of the model and the interpretation of the results in terms of critical balance. We further move on to our observations in Saturn's magnetosphere in Section 4.4. Here, we successfully reproduce some of the results obtained in the previous chapter, which corroborates our former interpretation. Also, we show that the change of spectral indices inside $9\,R_\mathrm{s}$ might be explained by damping at scales controlled by the hot electron population.

4.1 General Form of the Spectral Tensor

Here, we derive the general form of the correlation tensor $R_{ij}(\mathbf{x},\mathbf{r})$ of incompressible magnetic fluctuations after *Matthaeus and Smith* (1981). This tensor is directly related to the spectral tensor, which can be obtained from the correlation tensor by Fourier transformation. Let $B_i(\mathbf{x})$ denote the i'th component of the magnetic field, then

$$R_{ij}(\mathbf{x},\mathbf{r}) = \langle B_i(\mathbf{x}) B_j(\mathbf{x}+\mathbf{r}) \rangle \tag{4.1}$$

is the correlation tensor of the magnetic field. The vector $\mathbf{x}$ denotes the location of the measurement and vector $\mathbf{r}$ the spatial displacement. If we further demand homogeneity of the problem, the tensor will be independent of the location, so that we may drop the variable $\mathbf{x}$. Experimentally, $R_{ij}(\mathbf{r})$ can be considered as a two-dimensional matrix $R_{ij}(\mathbf{r}) \in \mathbb{R}^{3\times3}$ according to the three components of the magnetic field. It can be shown that the correlation tensor can be decomposed as

$$R_{ij}(\mathbf{r}) = R^\mathrm{S}_{ij}(\mathbf{r}) + R^\mathrm{A}_{ij}(\mathbf{r}) \ , \tag{4.2}$$

where $R^\mathrm{S}_{ij} = R^\mathrm{S}_{ji}$ is a symmetric proper tensor and $R^\mathrm{A}_{ij} = -R^\mathrm{A}_{ji}$ is an antisymmetric proper tensor (see e.g. *Oughton et al.*, 1997). With regards to these tensors, *Matthaeus and Smith* (1981) reach the following conclusions:

(1) The diagonal of the correlation tensor is always symmetric: $R_{ii} = R^\mathrm{S}_{ii}$.

(2) Based on the work of *Robertson* (1940): If $R_{ij}(\mathbf{r})$ is assumed to be invariant under rotation about a given vector $\mathbf{b}$, the correlation tensor can be written as the sum of the vectors fundamental to the problem and the fundamental

invariants δ_{ij} and ϵ_{ijk} each multiplied with a scalar function dependent on $\mathbf{r}\cdot\mathbf{b}$ and/or $\mathbf{r}\cdot\mathbf{r}$.

(3) R^{S}_{ij} and R^{A}_{ij} are separately solenoidal: $\partial_{r_i} R^{\mathrm{S}}_{ij} = \partial_{r_j} R^{\mathrm{S}}_{ij} = 0$ and $\partial_{r_i} R^{\mathrm{A}}_{ij} = \partial_{r_j} R^{\mathrm{A}}_{ij} = 0$.

Based on these conclusions, it is possible to construct a general form of the correlation tensor, which we may later use to describe turbulent fluctuations.

4.1.1 Rotational Symmetry Along Mean Magnetic Field

In plasma turbulence, one expects the statistical characteristics of the fluctuations to be symmetric with regards to the mean magnetic field $\mathbf{b} = \mathbf{B}_0/B_0$. Therefore, we assume the correlation tensor to be invariant under rotations about $\mathbf{b}$ so that the decomposition according to point (2) can be applied. It should be noted that this is a strong assumption and although this feature has not been proven, we use it in this derivation because it severely simplifies the general form of the tensor. However, there are strong indications that the fluctuations are indeed rotational symmetric (*Wicks et al.*, 2012). Together with the results of (1) and (3), the correlation tensor can be written as

$$
\begin{aligned}
R_{ij}(\mathbf{r}) &= R^{\mathrm{S}}_{ij}(\mathbf{r}) + R^{\mathrm{A}}_{ij}(\mathbf{r}) && (4.3)\\
R^{\mathrm{S}}_{ij}(\mathbf{r}) &= A\delta_{ij} + Br_ir_j + C(b_ir_j + b_jr_i) + Db_ib_j \\
&\quad + E(r_i\epsilon_{jkl}b_kr_l + r_j\epsilon_{ikl}b_kr_l) \\
&\quad + F(b_i\epsilon_{jkl}b_kr_l + b_j\epsilon_{ikl}b_kr_l) && (4.4)\\
R^{\mathrm{A}}_{ij}(\mathbf{r}) &= G\epsilon_{ijk}r_k + K\epsilon_{ijk}b_k\ , && (4.5)
\end{aligned}
$$

where A, B, D, E and G are functions of even power of r and $\mathbf{r}\cdot\mathbf{b}$, and C, F and K are odd functions in $\mathbf{r}\cdot\mathbf{b}$ and even in r (*Matthaeus and Smith*, 1981). Note, that the scalar functions $A\ldots K$ are not all independent of each other. This general form is still too complex to work with but it can be further simplified.

4.1.2 Fourier Transform of the Correlation Tensor

As we are primarily interested in computing the power spectral densities, we now turn to the spectral tensor

$$
S_{ij}(\mathbf{k}) = \frac{1}{(2\pi)^3}\int \mathrm{d}\mathbf{r}\, R_{ij}(\mathbf{r})\mathrm{e}^{-\mathbf{kr}}\ , \tag{4.6}
$$

which is the Fourier transform of the correlation matrix. The conclusions (1)-(3) apply equally in $\mathbf{k}$-space, so that we can immediately write down the general form of the spectral density matrix in case of axisymmetry with respect to the

mean magnetic field:

$$\begin{aligned} S_{ij}(\mathbf{k}) &= \tilde{A}\delta_{ij} + \tilde{B}k_ik_j + \tilde{C}(b_ik_j + b_jk_i) + \tilde{D}b_ib_j \\ &\quad +\tilde{E}(k_i\epsilon_{jkl}b_kk_l + k_j\epsilon_{ikl}b_kk_l) \\ &\quad +\tilde{F}(b_i\epsilon_{jkl}b_kk_l + b_j\epsilon_{ikl}b_kk_l) \\ &\quad +\tilde{G}\epsilon_{ijl}k_l \ . \end{aligned} \tag{4.7}$$

As stated earlier, the scalar functions are not independent of each other. Based on the ansatz of *Montgomery and Turner* (1981), the spectral tensor may be decomposed as

$$\mathbf{S}(\mathbf{k}) = \sum_{i,j=1}^{2} A_{ij}\mathbf{e}_i\mathbf{e}_j \tag{4.8}$$

with the basis vectors

$$\mathbf{e}_3 = \frac{\mathbf{k}}{k} \ , \quad \mathbf{e}_2 = \frac{\mathbf{k}\times\mathbf{b}}{|\mathbf{k}\times\mathbf{b}|} \quad \text{and} \quad \mathbf{e}_1 = \mathbf{e}_2 \times \mathbf{e}_3 \ . \tag{4.9}$$

Now, we are left with four independent scalar functions $A_{11}, A_{22}, A^{\mathrm{S}}$ and A^{A} with $A_{12} = A^{\mathrm{S}} + iA^{\mathrm{A}}$ that completely describe the spectral tensor. Contributions from $i, j = 3$ to Equation (4.8) vanish because the magnetic field is assumed to be solenoidal (*Montgomery and Turner*, 1981). Using $\mathbf{b} = \mathbf{e}_3 = \mathbf{e}_z$ so that $\mathbf{k}\cdot\mathbf{b} = k_z$, the functions A_{ij}, A^{S} and A^{A} can be identified with the functions of Equation (4.7) as follows

$$\tilde{A} = A_{22} \tag{4.10}$$

$$\tilde{B} = -\frac{k^2A_{22} - k_z^2A_{11}}{k^2(k^2 - k_z^2)} \tag{4.11}$$

$$\tilde{C} = \frac{k_z}{k^2 - k_z^2}(A_{22} - A_{11}) \tag{4.12}$$

$$\tilde{D} = \frac{k^2}{k^2 - k_z^2}(A_{11} - A_{22}) \tag{4.13}$$

$$\tilde{E} = -\frac{k_z}{k(k^2 - k_z^2)}A^{\mathrm{S}} \tag{4.14}$$

$$\tilde{F} = \frac{k}{k^2 - k_z^2}A^{\mathrm{S}} \tag{4.15}$$

$$\tilde{G} = \frac{i}{k}A^{\mathrm{A}} \ . \tag{4.16}$$

This leads to the general form of the spectral tensor

$$\begin{aligned} S_{ij} &= A_{22}\delta_{ij} - \frac{k^2 A_{22} - k_z^2 A_{11}}{k^2 k_\perp^2} k_i k_j \\ &\quad + \frac{k_z}{k_\perp^2}(A_{22} - A_{11})(b_i k_j + b_j k_i) \\ &\quad + \frac{k^2}{k_\perp^2}(A_{11} - A_{22}) b_i b_j \\ &\quad - \frac{k_z}{k k_\perp^2} A^{\mathrm{S}}(k_i \epsilon_{jkl} b_k k_l + k_j \epsilon_{ikl} b_k k_l) \\ &\quad + \frac{k}{k_\perp^2} A^{\mathrm{S}}(b_i \epsilon_{jkl} b_k k_l + b_j \epsilon_{ikl} b_k k_l) + \frac{i}{k} A^{\mathrm{A}} \epsilon_{ijl} k_l \ , \end{aligned} \tag{4.17}$$

where $k_\perp^2 = k^2 - k_z^2$ and ϵ_{ijk} denotes the totally antisymmetric Levi-Civita tensor.

4.1.3 Diagonal Elements of the Spectral Tensor

The power spectral densities P_i that we derived from measurements in Saturn's magnetosphere are auto spectra, which means that they are given by the diagonal elements S_{ii} of the spectral tensor. The interpretation of turbulent spectra observed in the solar wind is in most cases also restricted to the diagonal elements or even only the trace of the spectral tensor. As these elements are the simplest to describe because they do not involve the helicities of the respective plasma parameter, we drop the off-diagonal elements in Equation (4.17) and write:

$$\begin{aligned} S_{ii}(\mathbf{k}) &= A_{22} - \frac{k^2 A_{22} - k_z^2 A_{11}}{k^2 k_\perp^2} k_i^2 \\ &\quad + 2\frac{k_z}{k_\perp^2}(A_{22} - A_{11}) b_i k_i \\ &\quad - \frac{k^2}{k_\perp^2}(A_{22} - A_{11}) b_i^2 - \underbrace{2\frac{k_z}{k k_\perp^2} A^{\mathrm{S}} k_i \epsilon_{ikl} b_k k_l}_{\chi} \ , \end{aligned} \tag{4.18}$$

which is equivalent to Equation (20) of *Oughton et al.* (1997). Here, we may set the function χ to zero, which is equivalent to the assumption of mirror symmetry and leads to a vanishing magnetic helicity. While it severely simplifies the general form of the spectral tensor, this assumption is only valid in case of balanced turbulence. Here, balanced means that the same amount of energy is transported parallel and anti-parallel to the mean magnetic field. Although this is also a prerequisite for critically balanced turbulence and a commonly used approximation, it is strictly not the case for solar wind turbulence (*Wicks et al.*, 2010; *Forman et al.*, 2011; *Turner et al.*, 2012). However, we set $\chi = 0$ and

further use $T = A_{22}$, $P = A_{11}$, so that we arrive at (*Wicks et al.*, 2012)

$$S_{xx}(\mathbf{k}) = \left(1 - \frac{k_x^2}{k_\perp^2}\right) T + \frac{k_x^2 k_z^2}{k_\perp^2 k^2} P \tag{4.19}$$

$$S_{yy}(\mathbf{k}) = \left(1 - \frac{k_y^2}{k_\perp^2}\right) T + \frac{k_y^2 k_z^2}{k_\perp^2 k^2} P \tag{4.20}$$

$$S_{zz}(\mathbf{k}) = \frac{k_\perp^2}{k^2} P \ . \tag{4.21}$$

This set of equations describe the final and most simplest form of the diagonal components of the spectral tensor. The trace of the tensor is $\mathrm{tr}\,(S(\mathbf{k})) = T + P$, where T is a scalar function that describes the energy distribution of toroidal, i.e., shear-Alfvénic, fluctuations while the scalar function P describes the poloidal, i.e., pseudo-Alfvénic, fluctuations. The latter are the incompressible limit of the slow mode (*Goldreich and Sridhar*, 1995; *Cho and Lazarian*, 2005). *Cho et al.* (2002) find from their simulation of driven incompressible MHD turbulence that the power in shear- and pseudo-Alfvén modes are approximately equal ($T \sim P$), which would further reduce Equations (4.19)-(4.21) to

$$S_{ii}(\mathbf{k}) = \left(1 - \frac{k_i^2}{k^2}\right) T \ . \tag{4.22}$$

If pseudo-Alfvén modes were absent ($P = 0$), Equations (4.19)-(4.21) would reduce to

$$S_{ii}(\mathbf{k}) = \left(1 - \frac{k_i^2}{k_\perp^2}\right) T \ , \quad \text{if } i = x, y \tag{4.23}$$

and there would be no energy in fluctuations along the background magnetic field ($S_{zz} = 0$). However, from solar wind measurements, it can be seen that generally $P \neq T$ and $P \neq 0$. At this point, we need to propose reasonable estimates for the scalar functions T and P. In case of a critically balanced turbulent cascade, we can deduce the energy distribution for T from the derivations presented in Section 2.2.4, which describe the Alfvénic fluctuations. Moreover, according to *Lithwick and Goldreich* (2001), slow mode waves are passively cascaded by Alfvén waves, which means that the same scaling can be expected for the poloidal fluctuations P (*Schekochihin et al.*, 2009). Due to the fact that $k_\perp \gg k_\parallel$ for a critically balanced cascade, we can estimate the proportionality between the two functions from the measured variance anisotropy

$$\frac{P_\perp}{P_\parallel} = \frac{k^2}{k_\perp^4}\frac{T}{P} + \frac{k^2 k_z^2}{k_\perp^4}\frac{T}{P} + \frac{k_z^2}{k_\perp^2} \approx \frac{T}{P} \ . \tag{4.24}$$

Observations in the solar wind show that usually $T \gg P$ (*Bieber et al.*, 1996; *Hamilton et al.*, 2008; *TenBarge et al.*, 2012), which means the error of this approximation should be rather small. However, we note that the influence of poloidal fluctuations increase in the kinetic range and that recent findings

indicate a slightly different scaling of the poloidal fluctuations (*Podesta and TenBarge*, 2012; *Forman et al.*, 2013; *Chen et al.*, 2010a).

As we are able to estimate the scalar function P according to Equation (4.24), we can now proceed to describe the diagonal elements of the spectral tensor with a single scalar function T. This function depends on the three-dimensional wave vector $\mathbf{k}$ but since we assume axisymmetry along the mean magnetic field, this dependence further reduces to $T(\mathbf{k}) = T(k_\perp, k_\parallel)$. Each wave vector represents a fluctuation with a certain wavelength along a certain direction in space. These fluctuations are non-propagating, completely uncorrelated to each other and also have a constant angle to the mean magnetic field, i.e., global and local mean magnetic field are identical in our model. For magnetic power spectral densities, the scalar function T is in units $\mathrm{nT^2\,m^3}$. In the next section, we describe a possible energy distribution for Alfvénic turbulence based on the theoretical considerations of *Goldreich and Sridhar* (1995).

4.2 Numerical Results of Critical Balance Model

Here, we introduce and discuss our turbulence model ranging from MHD to electron scales, which allows us to calculate one-dimensional reduced PSD for arbitrary measurement geometries. We focus on the theory of a strong critically balanced turbulent cascade as originally proposed by *Goldreich and Sridhar* (1995) for Alfvénic turbulence. It has been further developed to include ion kinetic range of scales (*Howes et al.*, 2008; *Schekochihin et al.*, 2009) and the electron range of scales (*TenBarge et al.*, 2013). Observations indicate that it correctly describes solar wind turbulence (*Horbury et al.*, 2008; *Podesta*, 2009; *Chen et al.*, 2010a), although these observations could not be tested explicitly. However, with the forward model derived in this section, we are able to check if the observations are, in fact, in agreement with critical balance. According to *Goldreich and Sridhar* (1995), the energy distribution on MHD scales is given by

$$E(\mathbf{k}) \sim \frac{B_0^2}{k_\perp^{10/3} L^{1/3}}\; f\left(L^{1/3}\frac{k_\parallel}{k_\perp^{2/3}}\right)\;, \tag{4.25}$$

where "$f(u)$ *is a positive, symmetric function of* u*, that becomes negligibly small, when* $|u| \gg 1$". It is this function $f(u)$, which contains the critical balance relation on MHD scales

$$k_\parallel \sim L^{-1/3} k_\perp^{2/3}\;, \tag{4.26}$$

where L denotes the outer scale on which the energy is isotropically injected into the system. It is also this term, which leads to spectra anisotropy, i.e., different scalings depending on the field-to-flow angle θ between plasma velocity $\mathbf{v}$ (relative to the observing spacecraft) and background magnetic field $\mathbf{B}_0$. *Cho et al.* (2002) find that the function, which explains their simulation results of

incompressible MHD turbulence best, is

$$E_{\mathrm{MHD}}(k_\perp, k_\parallel) = \left(\frac{B_0^2}{L^{1/3}}\right) k_\perp^{-10/3} \exp\left(-L^{1/3}\frac{|k_\parallel|}{k_\perp^{2/3}}\right) \ . \tag{4.27}$$

This distribution describes the Alfvénic fluctuations, which means we can use $T = E_{\mathrm{MHD}}$ on MHD scales. According to Equation (4.24), this also defines the poloidal function $P = \frac{P_\parallel}{P_\perp} T$. Besides the exponential function used in Equation (4.27), there are several different possibilities to describe $f(u)$, e.g., Dirac Delta, Heaviside or Gauss functions. Whichever function one chooses, it results in a similar spectral anisotropy depending on the field-to-flow angle θ (*Forman et al.*, 2011; *Turner et al.*, 2012), which is also shown in Figure C.1 in Appendix C for the case of our forward calculation. For $\theta = 90°$ the one-dimensional PSD scales as $P(f) \propto k^{-5/3}$ and for $\theta = 0°$ as $P(f) \propto k^{-2}$ in the inertial range. The power-law behavior can be shown analytically only for these two extreme cases. In the literature, however, it is often implicitly assumed that the spectra in the intermediate range $0° < \theta < 90°$ also follow power-laws and that the spectral index κ is independent of frequency. Later, we see that this latter assumption is indeed incorrect.

4.2.1 Power Spectral Density in Frequency Space

If we want to compare theoretical considerations for energy densities in three-dimensional **k**-space with measured PSD, we need to calculate the reduced one-dimensional spectrum in frequency space $P(f)$ from the spectral tensor given in Equations (Equation (4.19))-(4.21). Generally, this is not possible. However, we may assume a frozen-in flux and apply Taylor's hypothesis. This, of course, needs to be verified with $\mathbf{k}\cdot\mathbf{v} \gg \omega$, where $\mathbf{k}\cdot\mathbf{v}$ is the frequency of structures or fluctuations being convected over the spacecraft with velocity $\mathbf{v}$ and ω is the frequency of the corresponding wave in the plasma frame. If Taylor's hypothesis is applicable, the diagonal elements of the reduced spectral tensor in frequency space $P_{ii}(f)$ can be obtained by integrating the three-dimensional energy densities $S_{ii}(\mathbf{k})$ over a plane perpendicular to the flow direction $\mathbf{v}$ (*Fredricks and Coroniti*, 1976):

$$\begin{aligned} P_{ii}(f) &= \int_{-\infty}^{\infty} \mathrm{d}t\, e^{i2\pi f t} \int_{-\infty}^{\infty} \mathrm{d}k^3\, S_{ii}(\mathbf{k})\, e^{-i\mathbf{k}\cdot\mathbf{v}t} \\ &= \int_{-\infty}^{\infty} \mathrm{d}^3k\, S_{ii}(\mathbf{k})\, \delta(2\pi f - k_x v\sin(\theta) - k_z v\cos(\theta)) \ . \end{aligned} \tag{4.28}$$

Here, we assumed that the z-axis is parallel to the background magnetic field ($\mathbf{e}_z \parallel \mathbf{B}_0$) and $\mathbf{e}_y = \mathbf{e}_z \times \mathbf{v}$, so that $\mathbf{e}_x$ lies in the plane spanned by $\mathbf{B}_0$ and $\mathbf{v}$, which is sometimes called the quasi-parallel direction (*Bieber et al.*, 1996). If we rotate this coordinate system by the field-to-flow angle θ about the y-axis such

that

$$k'_x = k_x \sin(\theta) + k_z \cos(\theta) \tag{4.29}$$
$$k'_y = k_y \tag{4.30}$$
$$k'_z = -k_x \cos(\theta) + k_z \sin(\theta) \ , \tag{4.31}$$

then k'_x will be aligned with $\mathbf{v}$ and the plane of integration lies in the $y'-z'$ plane. Hence, Equation (4.28) becomes

$$P_{ii}(f) = \frac{1}{v} \int_{-\infty}^{\infty} \mathrm{d}^3k' \, S_{ii}(\mathbf{k}') \, \delta\left(\frac{2\pi f}{v} - k'_x\right) \ . \tag{4.32}$$

The Delta function can be evaluated, which reduces the dimensions of the integration volume from three to two, and we use $k_x^* = \frac{2\pi f}{v}$. This wave number is determined by the frequency f in spacecraft frame and the plasma speed v relative to the spacecraft. Note, that several different wave vectors map to the same frequency in spacecraft frame. In fact, the power spectral density $P_{ii}(f)$ is determined by integration over a plane with normal vector $\mathbf{k} = (k_x \sin(\theta), 0, k_z \cos(\theta))$. This two-dimensional integration over the energy distribution in $\mathbf{k}$-space can be evaluated numerically.

In the rotated frame $\mathbf{k}'$, the diagonal components of the spectral tensor $S'_{ii}(\mathbf{k}')$ takes on a lengthy form, which is given in Appendix C. Here, we only show the form of Equation (4.27) in the rotated frame, which can be written as

$$\begin{aligned} E'_{\mathrm{MHD}} &= \left(\frac{B_0^2}{L^{1/3}}\right) \left((k_x^* \sin(\theta) - k'_z \cos(\theta))^2 + k_y'^2\right)^{-5/3} \\ &\quad \cdot \exp\left(-L^{1/3} \frac{|k_x^* \cos(\theta) + k'_z \sin(\theta)|}{\left((k_x^* \sin(\theta) - k'_z \cos(\theta))^2 + k_y'^2\right)^{1/3}}\right) \ . \end{aligned} \tag{4.33}$$

The scalar functions T' and P' can be inserted in Equation (4.32) using Equations (4.19)-(4.21) in the rotated form. Thus, we are able to numerically calculate the power spectral densities $P_{ii}(f)$ in spacecraft frame. For the sake of completeness, we describe in Appendix C the complete set of applied equations in the rotated frame and also give the MATLAB code used for the numerical evaluation.

4.2.2 Transition from MHD to Kinetic Scales

When the observed Doppler-shifted frequencies reach scales close to the characteristic ion scales, such as the gyro radius ρ_i or the ion inertial length λ_i, the MHD approximation breaks down and one needs to take into account kinetic equations to describe the plasma dynamics. For the remainder of this paper we use the gyro radius as the controlling kinetic scale and argue with the derivation of *Howes et al.* (2008) for kinetic Alfvén waves (KAW). However, similar results can be obtained with a Hall-MHD approach and the inertial length as

the controlling scale. The associated critical balance on ion kinetic scales is

$$k_{\parallel} \sim L^{-1/3} \rho_i^{-1/3} k_{\perp}^{1/3} \tag{4.34}$$

as has been derived in Section 2.2.6. This relation must be incorporated into the function of Equation (4.25) to describe the critical balance on kinetic scales.

We model the transition from MHD to kinetic scales as an abrupt change in the function $E_{\mathrm{MHD}}(\mathbf{k})$ at $k_{\perp}\rho_i = 1$. Let us denote the function E_{MHD}, given in Equation (4.33), as the one applicable for $k_{\perp}\rho_i \leq 1$ and E_{KAW} as the one applicable for $k_{\perp}\rho_i \geq 1$. At $k_{\perp}\rho_i = 1$, both energy distributions must be equal, i.e., $E_{\mathrm{MHD}}(k_{\perp}\rho_i{=}1) = E_{\mathrm{KAW}}(k_{\perp}\rho_i{=}1)$. Also, the kinetic energy distribution E_{KAW} must scale as $P \propto k_{\perp}^{-7/3}$ for $\theta = 90°$ (*Howes et al.*, 2008) and should be structurally equivalent to the distribution on MHD scales given by Equation (4.27). These requirements are fulfilled in the expression

$$E_{\mathrm{KAW}} = \left(\frac{B_0^2}{L^{1/3}\rho_i^{1/3}}\right) k_{\perp}^{-11/3} \exp\left(-L^{1/3}\rho_i^{1/3}\frac{|k_z|}{k_{\perp}^{1/3}}\right) , \tag{4.35}$$

which we have written in unprimed coordinates for the sake of brevity. At even smaller scales, we approach the electron gyro radius ρ_e and the energy distribution changes once again from E_{KAW} to E_{ED}. Here, Landau damping is supposed to weaken the cascade so that there is no more parallel transfer of energy (*Sridhar and Goldreich*, 1994; *Howes et al.*, 2008). The electron or dissipation range fluctuations are modeled as a function E_{ED} with a critical balance according to $k_{\parallel} \propto k_{\perp}^{0}$ (*TenBarge et al.*, 2013). A functional form that satisfies equality at $k_{\perp}\rho_e = 1$ of E_{KAW} and E_{ED} can be given by

$$E_{\mathrm{ED}} = \left(\frac{B_0^2}{L^{1/3}\rho_i^{1/3}}\right) k_{\perp}^{-11/3} \exp\left(-L^{1/3}\rho_i^{1/3}\rho_e^{1/3}|k_z|\right) \tag{4.36}$$

with an associated critical balance of

$$k_{\parallel} \sim L^{-1/3} \rho_i^{-1/3} \rho_e^{-1/3} . \tag{4.37}$$

It can be shown that this leads to a scaling of $P_{\perp} \propto k_{\perp}^{-8/3}$ for the perpendicular cascade ($\theta = 90°$) and an exponential decay $P_{\parallel} \propto \exp(-k_{\parallel})$ for the parallel cascade ($\theta = 0°$). Note, that this exponential decay for the parallel cascade is not associated to the exponential damping observed by *Alexandrova et al.* (2012) and given in Equation (2.61). As we show in the next section, it is also unlikely that a spectral slope much steeper than the perpendicular slope can be observed at all for a critically balanced KAW cascade at such small scales.

Cascade toward Quasi-Perpendicular Spectra

While Equation (4.32) can be integrated analytically for angles $\theta = 0°$ and $\theta = 90°$, it can only be numerically evaluated for intermediate angles $0° < \theta < 90°$. Such a numeric integration is carried out for the first time and the results are shown in Figure 4.1. The expected spectral slopes are inserted as black lines to guide the eye. For this example, we restricted the calculation of the PSD to Equations (4.27) and (4.35), i.e., the change of the cascade at electron scales, $k_\perp \rho_e > 1$, is not included. We use plasma parameters characteristic of the solar wind at 1 AU, namely $v = 600\,\mathrm{km/s}$, $\rho_i = 100\,\mathrm{km}$, $B = 1\,\mathrm{nT}$ and $L = 10^9\,\mathrm{m}$ (*Schekochihin et al.*, 2009; *Chen et al.*, 2010a) and plot the resulting PSD for several field-to-flow angles as a function of normalized wave number $k\rho_i$.

We note two interesting features in this plot: (1) the spectral break moves to lower frequencies for smaller angles, e.g., it is found already at $k\rho_i \sim 0.1$ for $\theta = 5°$. It is also increasingly smeared out at lower frequencies. Tests have shown that the onset of the spectral break can well be estimated by $k\rho_i \sim \sin(\theta)$. Note, that this corresponds to $k_\perp \rho_i$, the same normalization that we applied in Chapter 3. (2) The spectra for non-zero angles are steepened in a short range around the break and then flatten out to a slope of 7/3 at higher frequencies. The smaller the angle θ, the longer the range, where PSD are steeper than 7/3. A similar result is shown in Figure 5 of *Forman et al.* (2011) but is not discussed there. We emphasize the importance of this result as it contradicts the commonly assumed constancy of the spectral index with frequency. In the following of this section, we will focus on this second feature and explain it as a geometrical or sampling effect.

To analyze the change of the spectral index in detail, we show in Figure 4.2 the spectral slope as a function of $k\rho_i$ for the PSD shown in Figure 4.1. The spectral indices for the extreme cases $\theta = 0°$ and $\theta = 90°$ behave as expected and change to steeper slopes of $\kappa = 5$ and $\kappa = 7/3$, respectively, after their respective spectral breaks. Interestingly, the slopes for angles $0° < \theta < 90°$ steepen at their respective spectral breaks toward a value larger than 7/3 but then flatten out again. Eventually, all of these spectra reach a spectral index of 7/3 according to the perpendicular slope.

The flattening of the PSD, although puzzling at first, can be explained with the anisotropic distribution of power in **k**-space. Figure 4.3 shows logarithmically equidistant iso-contours of power in a double-logarithmic plot of k_x vs. k_z. We see the characteristic slopes of the critical balance relations 2/3 and 1/3 in the MHD and KAW regime, respectively. Recall, that the reduced one-dimensional spectrum is calculated by integrating over a plane given by

$$k_x \sin(\theta) = \frac{2\pi f}{v} - k_z \cos(\theta) \ . \tag{4.38}$$

Projections of these planes into the $k_x - k_z$ plane are shown as dashed lines in Figure 4.3 for an angle $\theta = 1°$ at logarithmically equidistant frequencies $f = 10^{-4} - 10\,\mathrm{Hz}$. For $\theta = 0°$, these dashed lines would be horizontal and

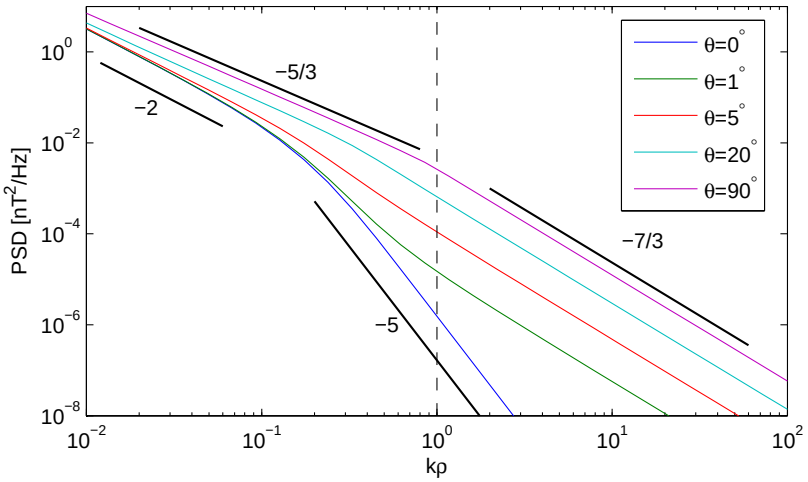

Figure 4.1: *PSD for different angles θ as a function of $k\rho_i$ with plasma parameters characteristic of solar wind turbulence ($L = 10^9\,m$, $v = 600\,km/s$, $\rho_i = 10^5\,m$). The vertical dashed line shows the Doppler-shifted gyro-radius ρ_i for $\theta = 90°$. The spectral break for small θ is observed at significantly lower frequencies. At high frequencies all spectra tend toward a slope of $7/3$.*

parallel to the k_x-axis and for $\theta = 90°$ they would be vertical and parallel to the k_z-axis. However, due to the double-logarithmic nature of the plot, the dashed lines for intermediate angles θ are curved. Due to the linear relation of k_x and k_z in equation 4.38, the point of maximum curvature grows as $k_z \sim k_x$. This means it grows faster than both critical balance relations $k_\parallel \sim k_\perp^\gamma$ for the MHD ($\gamma = 2/3$) and kinetic ($\gamma = 1/3$) range of scales. Hence, for increasing frequencies f, the plane of integration given by Equation (4.38) effectively has only contributions from the part seemingly perpendicular to the k_x-axis in the double-logarithmic plot. It is this feature that causes the spectral slope of the PSD to asymptotically approach its perpendicular value at high frequencies.

An analytic estimation for this argument may be derived assuming a two-dimensional **k**-space ($k_\parallel$, $k_\perp$) and a critically balanced cascade controlled by a Dirac Delta function instead of the exponential function in Equation (4.27). This seems to be a very strong assumption but it has been shown that there are only minor differences between the spectral anisotropy of PSD controlled by an exponential and a Dirac Delta function (*Forman et al.*, 2011; *Turner et al.*, 2012). On the other hand, the implications of a two-dimensional wave vector space need a more detailed discussion. Here, it is important to clarify the three-dimensional geometry of the problem. In Figure 4.3, we see a slice along the k_x-k_z plane. While the plane of integration is two-dimensional and expands straight in k_y direction, the energy distribution is three-dimensional and axisymmetric with respect to k_z. This means that the plane of integration intersects with the Dirac

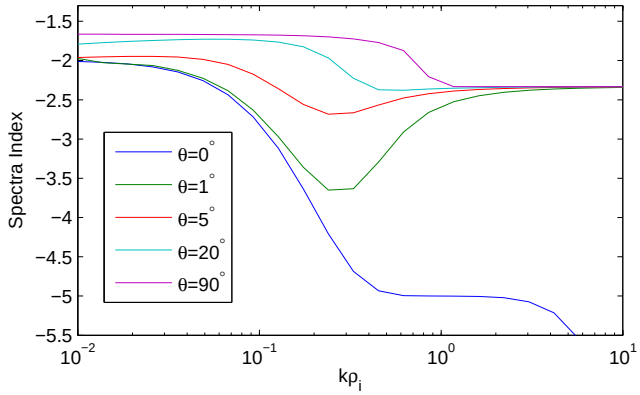

Figure 4.2: *Spectral index as a function of $k\rho_i$ for different field-to-flow angles θ. The change of spectral slope toward the perpendicular slope of 7/3 is clearly visible for all angles $\theta > 0°$. Only for exactly parallel spectra $\theta = 0°$ a spectral index of 5 is obtained. The decrease of the respective spectral index at $k\rho_i > 2$ is due to numerical reasons.*

Delta planes for $k_z > 0$ and $k_z < 0$ in a complicated curve, which is given by a cubic equation and depends on the field-to-flow angle θ. However, most of the energy on the plane of integration given by Equation (4.38) resides at $k_y = 0$ and decreases strongly with growing wave number in y-direction. Also, the two-dimensional approximation leads to a very good fit of our three-dimensional model results. Therefore, we assume that the effect of a merely two-dimensional wave vector space is negligible for our following derivation.

In two dimensions, the energy distribution of critical balance controlled by a Dirac Delta function can be written as

$$E_2(k_\perp, k_\parallel) \propto k_\perp^{-\kappa}\, \delta\Big(|k_\parallel| - L^{-1/3}\rho_i^{\gamma-2/3}k_\perp^{\gamma}\Big) \ , \tag{4.39}$$

where $\kappa = [5/3, 7/3]$ are the one-dimensional spectral indices and $\gamma = [2/3, 1/3]$ the critical balance exponents on MHD and kinetic scales, respectively (see also *Grappin and Müller*, 2010). The intersection of these two planes ($|\pm k_\parallel| \sim k_\perp^{2/3}$) with the plane of integration given by Equation (4.38), where $k_x = k_\perp$ and $k_z = k_\parallel$, are two points, positive $k_{\parallel,1}(k_{\perp,1})$ and negative $-k_{\parallel,2}(k_{\perp,2})$, whose locations are depicted in Figure 4.4. Field-to-flow angles smaller than 90° yield $k_{\perp,1} < k_{\perp,0} < k_{\perp,2}$, where

$$k_{\perp,0} = \frac{2\pi f}{v \sin(\theta)} \tag{4.40}$$

is the wave number corresponding to $k_\parallel = 0$. Note, that we do not need to make any assumptions regarding the energy at zero parallel wave number. The two locations $k_{\perp,1/2}$ are uniquely defined by the critical balance conditions, Equations

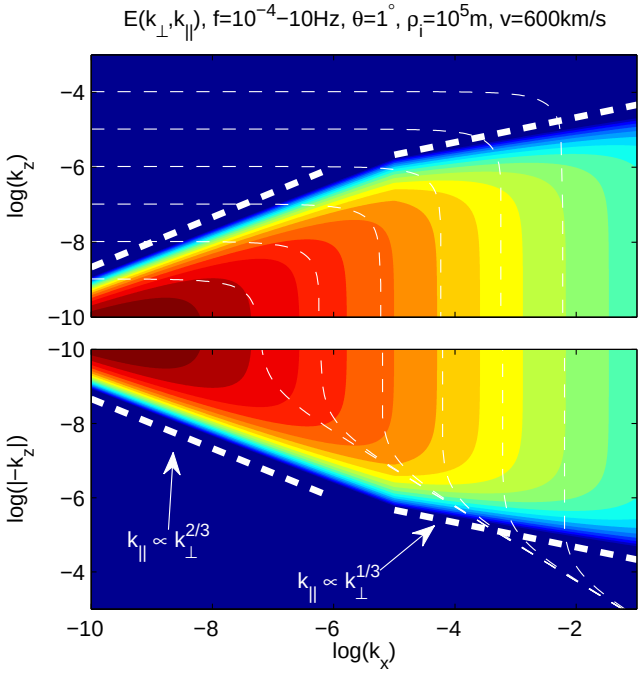

Figure 4.3: *Logarithmically equidistant iso-contours of energy distribution in* **k***-space in arbitrary units calculated with Equations (4.27) and (4.35) for a fixed field-to-flow angle* $\theta = 1°$*. Thin dashed white lines show integration planes after Equation* (4.38) *for logarithmically equidistant frequencies* $f = 10^{-4}{-}10\,Hz$*. Due to the double-logarithmic plot these planes appear as curved lines. Thick white lines denote power-laws according to the critical balance exponents on MHD and kinetic scales.*

(4.26) and (4.34), and the integration plane, Equation (4.38). It follows that

$$\begin{aligned} k_{\perp,1/2} &= \frac{2\pi f}{v\sin(\theta)} \mp k_{\parallel,1/2}\cot(\theta) \\ &= \frac{2\pi f}{v\sin(\theta)} \mp L^{-1/3}\rho_i^{\gamma-2/3}k_{\perp,1/2}^{\gamma}\cot(\theta)\ . \end{aligned} \tag{4.41}$$

This equation can be written as a cubic polynomial to find its solution $k_\perp(\theta)$.

Let us now look at the energy E_2 in **k**-space that contributes to the integration over a plane with angle θ:

$$E_2 \propto k_{\perp,1}^{-\kappa} + k_{\perp,2}^{-\kappa}\ , \tag{4.42}$$

which is essentially the summation over both critical balance branches. In the following, we show that this energy asymptotically approaches $E_0 \propto 2k_{\perp,0}^{-\kappa}$ with increasing frequency, which corresponds to a scaling according to $\theta = 90°$. At a certain frequency $f_{\max}$, the measurement uncertainty will be greater than the

difference between the energies E_2 and E_0 and, therefore, the corresponding PSD will scale like the perpendicular cascade. To show this, we make the ansatz that the ratio E_2/E_0 be almost unity for all $f > f_{\max}$. Because we are working in logarithmic space, we demand

$$\log\left[\frac{k_{\perp,1}^{-\kappa} + k_{\perp,2}^{-\kappa}}{2k_{\perp,0}^{-\kappa}}\right] < \epsilon \ , \tag{4.43}$$

where $\epsilon > 0$ is arbitrary small. Later, we choose an ϵ according to typical measurement uncertainties for spectral slopes in solar wind observations. To proceed further, we approximate

$$k_{\parallel,1/2} \approx L^{-1/3}\rho_i^{\gamma-2/3}k_{\perp,0}^{\gamma} \ . \tag{4.44}$$

The error of this approximation is less than 2.2% for frequencies $f \geq 0.1\,\mathrm{Hz}$, $\theta \geq 5°$, and $\gamma = 1/3$, which we calculated by comparing it to the real solution of the cubic polynomial using Cardano's method. For solar wind data, this corresponds to the frequency range after the first spectral break. Now, we can write Equation (4.41) as

$$k_{\perp,1/2} \approx k_{\perp,0} \mp L^{-1/3}\rho_i^{\gamma-2/3}k_{\perp,0}^{\gamma}\cot(\theta) = k_{\perp,0} \mp \Delta \ . \tag{4.45}$$

Inserting this in Equation (4.43), we get

$$\left(1 - \frac{\Delta}{k_{\perp,0}}\right)^{-\kappa} + \left(1 + \frac{\Delta}{k_{\perp,0}}\right)^{-\kappa} < 2e^{\epsilon} \ . \tag{4.46}$$

If we expand Equation (4.46) to second order around $\Delta/k_{\perp,0} = 0$, we find that

$$\frac{\Delta}{k_{\perp,0}} < \sqrt{\frac{2e^{\epsilon} - 2}{\kappa(\kappa+1)}} \ . \tag{4.47}$$

Inserting $\Delta = L^{-1/3}\rho_i^{\gamma-2/3}k_{\perp,0}^{\gamma}\cot(\theta)$ and $k_{\perp,0} = 2\pi f/\left(v\sin(\theta)\right)$ into this equation finally yields

$$f_{\max} = \frac{v\sin(\theta)}{2\pi}L^{\frac{1}{3\gamma-3}}\rho_i^{\frac{2-3\gamma}{3\gamma-3}}\left(\frac{2e^{\epsilon}-2}{\kappa(\kappa+1)}\right)^{\frac{1}{2\gamma-2}}\cot^{\frac{1}{1-\gamma}}(\theta) \ . \tag{4.48}$$

For an appropriately chosen ϵ, the difference between energies E_2 and E_0 for all frequencies $f > f_{\max}$ is so small that the scaling will be quasi-perpendicular within measurement errors. We find that $\epsilon = 0.05$ in Equation (4.48) represents an uncertainty of the spectral index of $\Delta\kappa = \pm 0.1$ in the kinetic range and $\Delta\kappa = \pm 0.02$ in the MHD range. Note, that the change of slope is a pure sampling effect and does not mean that the nature of the turbulent cascade is changing at this frequency. This estimation can now tested with our three-dimensional

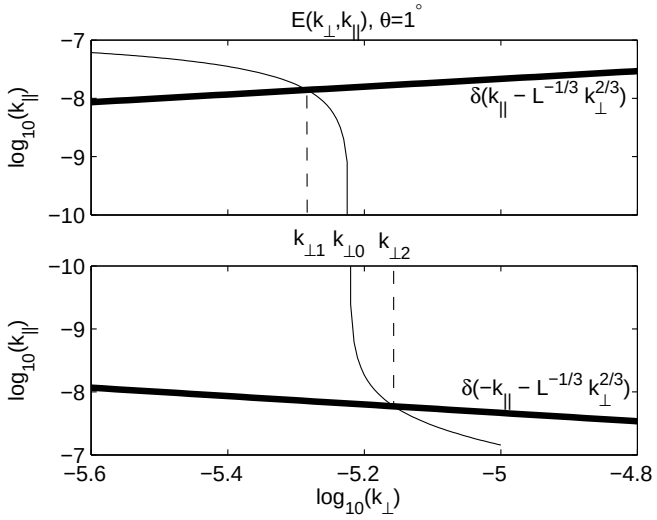

Figure 4.4: *Double-logarithmic plot of energy distribution given by Equation* (4.39) *(thick black line) in* $\mathbf{k}$*-space with thin black line showing plane of integration for a field-to-flow angle* $\theta = 1°$*. Black dashed lines indicate positions of* $k_{\perp,1/2}$*.*

model.

In Figure 4.5, we show how $f_{\max}$ varies with critical balance values $\gamma = [2/3, 1/3]$ as a function of field-to-flow angles $0° < \theta < 90°$. Naturally, for $\theta = 90°$ the corresponding spectral index is reached from the beginning of the cascade, while for $\theta = 0°$ the spectral index of the perpendicular cascade can never be reached. To test our estimation of $f_{\max}$, we calculate the PSD without a break at $k_\perp \rho_i \sim 1$, i.e., for Equations (4.33) and (4.35) separately, each extending over the whole range of wave vectors. From the such modeled PSD, we estimate a frequency $f'_{\max}$ for MHD and KAW turbulence defined by the frequency, where the spectral slope between two consecutive data points ($f_{n+1}/f_n \approx 1.3$) differs less than $\Delta\kappa = \pm 0.1$ from the spectral index 7/3 and less than $\Delta\kappa = \pm 0.02$ from 5/3. For the kinetic range, this is on the order of the usual measurement error in solar wind observations. The crosses in Figure 4.5 show the modeled results of the such determined $f'_{\max}$ and agree well with the estimation from Equation (4.48) for $\epsilon = 0.05$ (black and red lines for MHD and KAW, respectively).

The spectra in Figure 4.5 are computed for typical solar wind conditions of $v = 600\,\mathrm{km/s}$, $\rho_i = 100\,\mathrm{km}$ and $L = 10^9\,\mathrm{m}$, where the spectral break is found at a frequency $f \lesssim 1\,\mathrm{Hz}$ for the perpendicular cascade (see Figure 2.7). However, we find that the transition toward a quasi-perpendicular cascade for almost all field-to-flow angles ($\theta > 4°$) happens already below 1 Hz. We conclude that spectra of a critically balanced KAW cascade without damping on kinetic scales will almost exclusively be observed with a spectral index close to 7/3. Only for

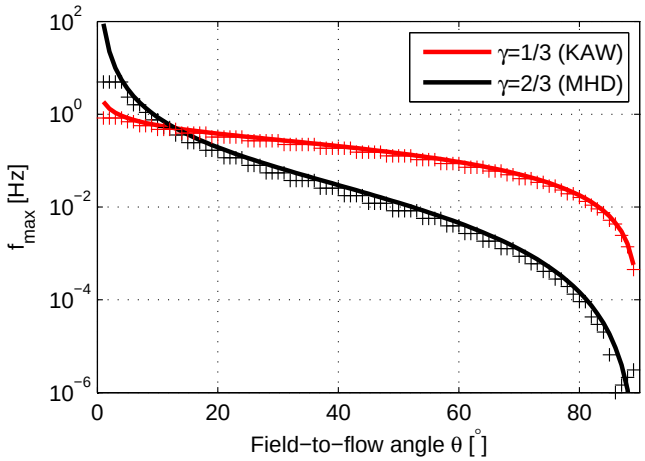

Figure 4.5: *Maximal frequency $f_{\max}$ as a function of θ for critical balance values $\gamma = [1/3, 2/3]$ using $\epsilon = 0.05$, outer scale $L = 10^9$ m and gyro radius $\rho_i = 10^5$ m. Black dots show $f'_{\max}$ obtained numerically from modeled PSD for $\Delta\kappa = 0.02$ on MHD and $\Delta\kappa = 0.1$ on kinetic scales.*

small angles and in a short frequency range between the first spectral break and 1 Hz a measurably steeper slope might be observed in the solar wind.

We stress the importance of this result: we have shown that the spectral index in a critically balanced cascade for intermediate field-to-flow angles $0° < \theta < 90°$ is not constant with growing frequency. Instead, it evolves toward a quasi-perpendicular slope. Therefore, we cannot expect to observe significantly steeper slopes than 7/3 over a broad frequency range in the solar wind in case of a critically balanced KAW cascade alone. Indeed, we see in Section 4.2.3 that such slopes only appear if the fluctuations are additionally subject to damping. This is a new result and has never been discussed in the literature, where it is often implicitly assumed that the PSD have a power-law shape with a constant spectral index that only depends on the field-to-flow angle. Although Figure 5 of *Forman et al.* (2011) implies that these authors calculated the same result, it is not discussed in their paper.

It is interesting to note, that a three-dimensional direct numerical simulation with strong guide field by *Grappin and Müller* (2010) produced a qualitatively similar transition toward a perpendicular cascade with a θ-independent slope, although the flattening of their spectra does not follow Equation (4.48). Also, the change of slope before $k\rho_i \sim 1$ for small angles, e.g., $P(\theta{=}5°)$ in Figure 4.1, slightly resembles the transition range (*Sahraoui et al.*, 2010) or ion dissipation range (*Smith et al.*, 2012), where the slopes are steeper than those in the MHD and kinetic range. *Voitenko and De Keyser* (2011) describe these double kink spectra as due to weakly dispersive fluctuations. PSD with this characteristic form have been observed by *Kiyani et al.* (2009), *Sahraoui et al.* (2010) and *Chen et al.* (2010a). However, their measured field-to-flow angles are much

greater than 5° (in the case of *Sahraoui et al.* (2010) 60°, not given for others). It is currently still under debate, which physical effect controls this range. At least for a critically balanced cascade with small field to flow angle, a possible explanation might be the effect presented here.

4.2.3 Anisotropic Damping

Several mechanisms have been proposed to dampen fluctuations on dissipative scales, e.g., ion-cyclotron damping, Landau damping and current sheet formation (*Matthaeus et al.*, 1990; *Leamon et al.*, 1999; *Dmitruk et al.*, 2004; *Howes*, 2009; *Schekochihin et al.*, 2009; *TenBarge et al.*, 2013). Most of the proposed mechanisms are anisotropic with regards to the background magnetic field, i.e., they affect wave numbers with certain direction to the mean magnetic field. In this section, we analyze how potential anisotropic damping terms that act on the energy distribution in three-dimensional **k**-space change the characteristics of reduced one-dimensional spectra. In **k**-space, damping may lead to a cut-off or exponential decay of the energy associated to the damped wave vector. In case of ion cyclotron resonance, the damping rate is low for $k_\parallel V_\mathrm{A} \ll \Omega_\mathrm{ci}$ and increases rapidly as $k_\parallel V_\mathrm{A}/\Omega_\mathrm{ci}$ approaches unity (*Howes et al.*, 2008; *Cranmer and van Ballegooijen*, 2012). We may therefore model the ion cyclotron damping as a cut-off at wave number $k_\parallel = \Omega_\mathrm{ci}/V_\mathrm{A}$, which can be seen as an upper bound of the effect of ion cyclotron damping. Recently, is has been found that reduced power spectra measured in the solar wind can empirically be described by

$$P(k_\perp) \propto k_\perp^{-\kappa} \exp(-k_\perp \rho_e) \tag{4.49}$$

as proposed by *Alexandrova et al.* (2012), who used a spectral index of $\kappa = 8/3$. This result could be reproduced by numerical gyrokinetic simulations that capture only electron Landau damping (*Howes et al.*, 2011b; *TenBarge et al.*, 2013). Hence, we might treat the exponential damping term of Equation (4.49) as a proxy for electron Landau damping.

Let us now investigate how these anisotropic damping terms, cut-off for parallel and exponential decay for perpendicular wave vectors in **k**-space, affect the PSD and the associated spectral anisotropy $\kappa(\theta)$. We will ion and electron gyro radii throughout this section as the controlling parameters for the onset of dissipation. However, the model can also be used to test other dissipative length scales, such as the inertial length. Note, that we apply the damping term of Equation (4.49) to three-dimensional **k**-space according to

$$E_\mathrm{damp}(\mathbf{k}) = E(\mathbf{k}) \cdot \exp(-k_\perp \rho_e) \ . \tag{4.50}$$

As we have seen in Section 4.2.1, the power at a certain frequency is obtained by integration over a two-dimensional plane. In contrast, the damping term depends on $k_\perp$ and is therefore axisymmetric with respect to k_z. This means that the integration along k_y includes perpendicular wave numbers larger than $k_\perp = 2\pi f/(v \sin\theta)$ corresponding to $k_y = 0$. Consequently, the effect of the

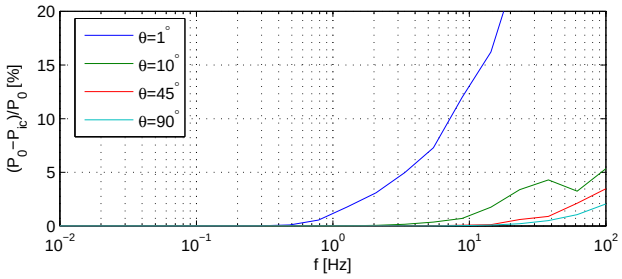

Figure 4.6: *Percentual difference* $(P_0 - P_{\mathrm{icr}})/P_0$ *of PSD with and without energy constrained to* $k_\parallel < \Omega_{\mathrm{ci}}/V_{\mathrm{A}}$ *as a function of frequency for several field-to-flow angles* θ*.*

exponential damping term is stronger when applied to three-dimensional **k**-space compared to a reduced one-dimensional spectrum. Therefore, we are able to produce similar results to those of Equation (4.49), although we apply a less steep spectral index of only 7/3 (see Figure 4.7).

From our assumption of critical balance, $k_\parallel \sim L^{-1/3}\rho^{\gamma-2/3}k_\perp^\gamma$ with $\gamma < 1$, it follows that usually $k_\perp \gg k_\parallel$ and, thus, that damping of perpendicular wave vectors is likely to be more effective than damping of wave vectors parallel to the mean magnetic field. It has been argued that the ion cyclotron resonance at $k_\parallel \sim \Omega_{\mathrm{ci}}/V_{\mathrm{A}}$ has only minor influence on a critically balanced cascade as it is reached only at very high perpendicular wave numbers $k_\perp$, where Landau damping already dominates (*Howes et al.*, 2008; *Schekochihin et al.*, 2009; *Cranmer and van Ballegooijen*, 2012). With our synthetic spectra we are now able to test this argument quantitatively.

In fact, if we model the ion cyclotron resonance with a cut-off at $k_\parallel = \Omega_{\mathrm{c,i}}/V_{\mathrm{A}}$, i.e., all energy residing in wave vectors with a parallel component exceeding this threshold is set to zero, we find only minor changes in the corresponding spectra P_{icr} compared to their undamped counterparts P_0. To quantify this effect, we show the relative difference $(P_0 - P_{\mathrm{icr}})/P_0$ in percent as a function of frequency for several angles θ in Figure 4.6. Only for quasi-parallel spectra, a detectable difference is observed. For $\theta = 1°$, the ion cyclotron damping starts to show at $f \sim 1\,\mathrm{Hz}$ and increases to 67 % at $f = 100\,\mathrm{Hz}$. Power spectra P_{icr} for frequencies $f \leq 100\,\mathrm{Hz}$ and field-to-flow angles $\theta \geq 10°$ differ less than 5 % from PSD without damping. However, one might think of systems, in which the ion-cyclotron resonance *does* change the form of the PSD significantly. Such systems must either be characterized by a critical balance exponent γ close to unity, or have a much smaller energy injection scale than the $L \sim 10^9 - 10^{10}\,\mathrm{m}$ found in the solar wind (*Howes et al.*, 2008; *Schekochihin et al.*, 2009), so that high $k_\parallel$ values are reached earlier in the cascade.

The damping of perpendicular wave vectors is much more effective. Figure 4.7 shows PSD with the same plasma parameters as in Figure 4.1 but additionally with extension to electron scales according to Equation (4.36), where we

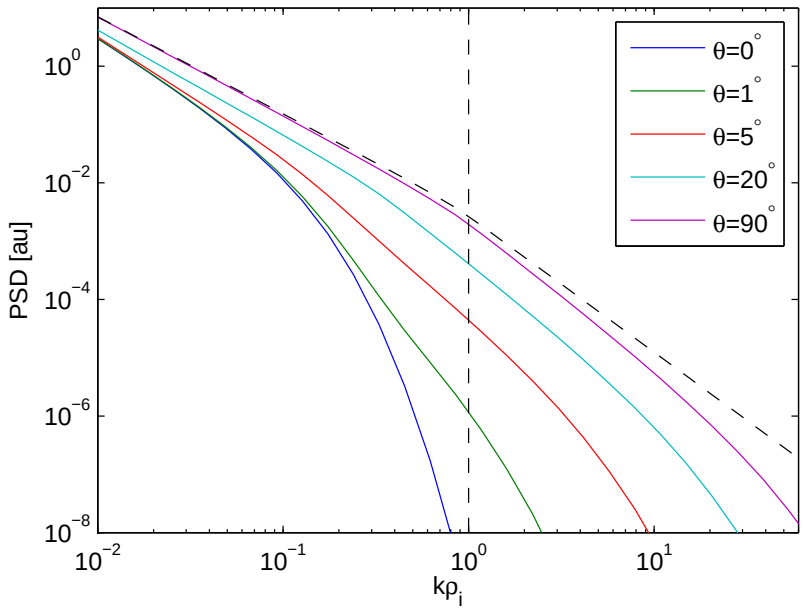

Figure 4.7: *PSD subject to damping according to Equation* (4.50) *as a function of* $k\rho_i$*, for several angles* θ *and an outer scale* $L = 10^9$ *m. The dashed line shows the PSD for* $\theta = 90°$ *without damping.*

use $T_i/T_e = 1$. Also, we applied the damping factor $\exp(-k_\perp \rho_e)$ acting on the energy distribution in **k**-space. As expected, the high frequency part is strongly affected and the damping leads to a characteristic exponential decay. The damping term dominates the effect of the energy distribution E_{ED} on electron scales and is found to be generally more effective at small angles θ. The latter can be understood considering the plane of integration given by Equation (4.38). The power at a certain frequency primarily stems from perpendicular wave numbers $k_\perp \sim 2\pi f/(v \sin\theta)$. For small angles θ, this involves larger $k_\perp$, which are more strongly damped, than a corresponding spectrum with angles close to 90°. Therefore, PSD for small angles are more affected by the damping term.

Although the damping sets in not before electron scales in wave vector space, the kinetic range of the PSD, $\rho_i^{-1} < k_\perp < \rho_e^{-1}$, is already affected: Figure 4.7 shows the undamped spectrum for $\theta = 90°$ as black dashed line and it is fairly visible, that the spectra subject to damping are steeper. In fact, we measure a spectral slope of ∼8/3 in the kinetic range for $P(\theta{=}90°)$ although the energy in **k**-space scales with 7/3. As T_i/T_e decreases or the electron gyro radius increases, the exponential decay moves to lower frequencies and further steepens the spectra. The two opposed mechanisms, flattening toward perpendicular slope and damping, can cancel each other out and lead to a range of seemingly constant slope. This shows that a close to power-law behavior of the measured PSD is not indicative of the absence of damping. Further, it shows that the

observed spectral slope is not necessarily the spectral index predicted by the underlying theory. Note, that we used this argument in Chapter 3 to explain the agreement of our observations in Saturn magnetosphere ($\kappa = 2.6$) with the KAW theory that predicts 7/3.

4.3 Application to Solar Wind Observations

By numerically evaluating Equation (4.32), it is possible to calculate power spectral densities $P_{ii}(f)$ for any component $i = x, y, z$ and any given plasma parameters. Here, we compare our results to in-situ measurements in the solar wind made by *Horbury et al.* (2008) in the MHD range and *Chen et al.* (2010a) in the kinetic range. *Podesta* (2009) has presented similar results, which are consistent with those from *Horbury et al.* (2008). We show that the measured spectral anisotropies are in accordance with our model and can thus be described by a critically balanced cascade. However, the influence of damping turns out to be more important than previously thought.

4.3.1 MHD Turbulence

From the assumption of critical balance, it follows that the trace of the PSD scales as $P \sim k_\perp^{-5/3}$ for $\theta = 90°$ and $P \sim k_\parallel^{-2}$ for $\theta = 0°$. Figure 4.8 shows that the transition between these two scalings is controlled by the outer scale L. It strongly affects the spectral anisotropy $\kappa(\theta)$ and it can be seen that the transition from parallel scaling 2 to perpendicular scaling 5/3 is much slower for small L. This reflects the evolution of the turbulent cascade along the critical balance path. While the energy is isotropic at the outer scale, it grows increasingly anisotropic as it cascades to smaller scales.

We can use this functional dependence of the spectral anisotropy to determine the value L, which best fits the observations of *Horbury et al.* (2008). They who used magnetic field data from the Ulysses spacecraft at 1.4 AU in the solar wind. For several outer scales L, we calculate the spectral anisotropy and fit the spectral indices $\kappa(L, \theta)$ to the results of *Horbury et al.* (2008). To evaluate the critically balanced power spectra, we use the complete set of energy distributions, E_{MHD}, E_{KAW} and E_{ED}, together with the anisotropic damping, i.e, a cut-off at the ion cyclotron resonance and exponential damping at electron scales according to Equation (4.50). From *McComas et al.* (2000), we estimate the proton gyro radius as $\rho_i = 1.9 \cdot 10^5$ m. Due to lack of a better estimate, we assume $T_i = T_e$ to calculate the electron gyro radius. For comparison, we also calculate the best fit for a slab+2-D turbulence model, where we use a spectral index of 2 for the slab component and 5/3 for the 2-D component (see, e.g., *Horbury et al.*, 2011, Eq. (3)). To quantify the goodness of fit we use a reduced error

$$\chi = \sqrt{\frac{1}{N} \sum_{i=1}^{N} \frac{(\kappa_i^{\mathrm{H}} - \kappa_i^{\mathrm{M}})^2}{\sigma_i^2}} \,, \tag{4.51}$$

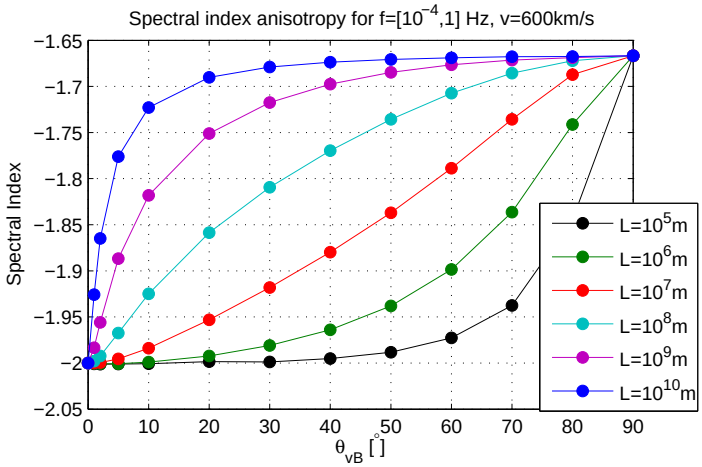

Figure 4.8: *Spectral anisotropy in the inertial range for different values of the outer scale L given in the legend. A smaller outer scale results in a slower transition of the spectral index from 2 to 5/3.*

where κ_i^{H} and σ_i are the spectral indices and their corresponding errors, respectively, taken from *Horbury et al.* (2008), N is the number of angle bins, and κ_i^{M} the modeled spectral indices, which are obtained in the same frequency range, 15−98 mHz, as those derived by *Horbury et al.* (2008). In general, the fit is much better for the critically balanced turbulence models ($\chi = 2.8-3.0$) than for the slab+2-D model ($\chi = 4.6$). We find that an outer scale of $L \sim 10^9$ m in the undamped case and $L = 10^{10}$ m for the damped cascade give the best results. Using the empirical formula

$$\frac{L}{\rho_i} \propto R^{0.13} \tag{4.52}$$

found by *Wicks et al.* (2010), where R is the radial distance to the Sun in units of AU, these outer scales map to $L = 6 \cdot 10^8$ m and $L = 6 \cdot 10^9$ m for the undamped and damped case, respectively. These values are in accordance with observations of the transition from k^{-1}-spectra to $k^{-5/3}$-spectra in the solar wind, which is believed to mark the end of the energy injection scale (*Schekochihin et al.*, 2009). The spectra at small angles θ are found to be steeper than $\kappa = 2$. This is because the spectral break at ion scales is found at lower frequencies for small angles and eventually falls into the fit range, i.e., the fit includes the steeper kinetic range cascade. For slab+2-D turbulence, we find the best fit has 30% slab and 70% 2-D turbulence, which is also in accordance with results obtained in the solar wind (*Bieber et al.*, 1996). Note, however, that we use two different spectral indices for slab and 2-D turbulence while *Bieber et al.* (1996) used the same slope for both slab and 2-D. The anisotropy of the power, $P(\theta)/P(\theta{=}5°)$, measured at a fixed frequency of $f = 61$ mHz is shown in Figure 4.10. The results of the damped critically balanced cascade well reproduce the anisotropy found by *Horbury et al.* (2008) for angles $\theta < 40°$ but overestimate the power

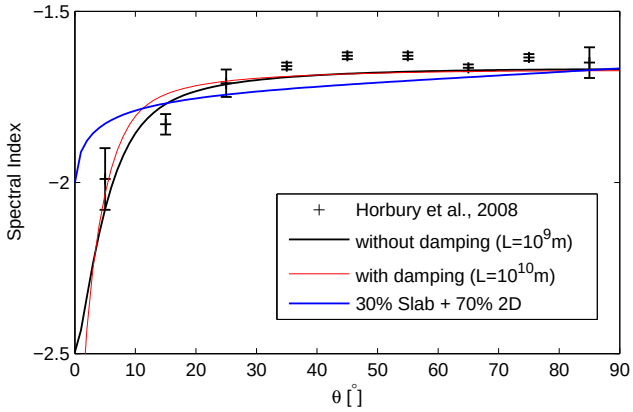

Figure 4.9: *Spectral anisotropy found by Horbury et al. (2008) (black crosses), as obtained from our model with an outer scale of $L = 10^9$ m for undamped (black line) and $L = 10^9$ m for damped (red line) critical balance, as well as for slab+2-D turbulence with 30% slab (blue line).*

at larger angles. The undamped cascade generally shows a lesser anisotropy but is in agreement with the measurements at $\theta \sim 90°$. Similar to what has been found for the spectral index, a critically balanced cascade fits the data much better than slab+2-D turbulence.

Given the simplicity of our parameters, we find that the presented fits to the results of *Horbury et al.* (2008) can be regarded as qualitatively successful reproduction of the observed data. Although *Forman et al.* (2011) showed that the observed spectral anisotropy is in agreement with a critical balance on MHD scales, this is the first time that these results have been analyzed with a model including a different kinetic range scaling and damping terms. The positive result of the fit indicates that the spectral anisotropy observed by *Horbury et al.* (2008) is indeed in accordance with a critically balanced cascade. Conversely, the successful fit with reasonable values for the outer scale proves that our model is applicable to measured data.

4.3.2 Kinetic Range Turbulence

For their analysis of kinetic range magnetic field fluctuations, *Chen et al.* (2010a) used data from CLUSTER during fast solar wind conditions with moderate plasma $\beta_i \sim 1$. They calculated the spectral index for perpendicular fluctuations using the wavelet method described by *Horbury et al.* (2008). For the modeled spectra, we choose outer scales $L = 10^9$ m for the undamped and $L = 10^{10}$ m for the damped cascade according to the fit to the *Horbury et al.* (2008) data. Ion and electron gyro radii as well as the bulk plasma velocity are given in Table 1 of *Chen et al.* (2010a) and the power anisotropy has been measured. The spectral anisotropy is given separately for parallel and perpendicular fluctuations. Accordingly, we use these values to calculate the PSD of perpendicular fluctu-

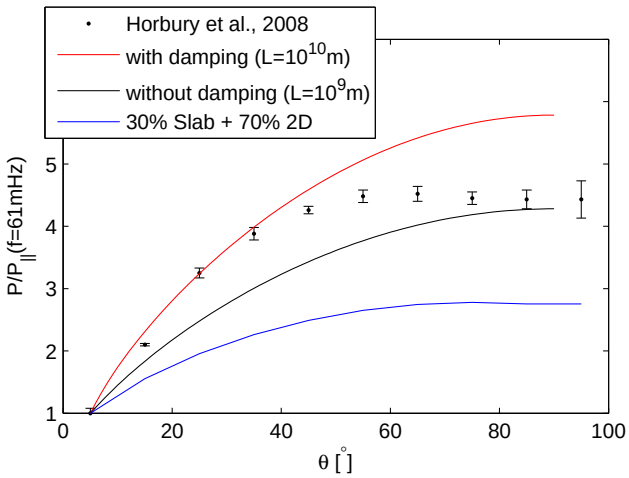

Figure 4.10: *Power spectral anisotropy $P(\theta)/P(\theta{=}5°)$ at frequency $f = 61\,mHz$. The results of damped and undamped critical balance are close to the results of Horbury et al. (2008) while slab+2-D turbulence underestimates the anisotropy.*

ations $P_\perp$ from which the spectral indices are derived. The spectral anisotropy of parallel fluctuations can not be successfully reproduced.

In Figure 4.11, we show the results obtained from our modeling and those presented in *Chen et al.* (2010a). Although both results for damped and undamped modeled spectra do not fit the data very well, the damped cascade shows at least a qualitatively similar functional dependence of the spectral slope on angle θ, i.e., the variation from $\theta = 0°$ to $\theta = 90°$ is smooth and not as abrupt as in the undamped case. The undamped cascade, in contrast, leads to spectral slopes of $\sim 7/3$ at almost all angles. Even at $\theta = 5°$, where the observed spectral index is ~ 3.25, the spectral index of the undamped cascade is still 2.43. This is the consequence of the transition toward a quasi-perpendicular slope as was elaborated in Section 4.2.2. The spectral index of the damped cascade on the other hand is 3.20 at $\theta = 5°$, and thus much closer to the observation. This shows that the observations of *Chen et al.* (2010a) are not in accordance with an undamped critically balanced KAW turbulent cascade.

The fact that an undamped cascade leads to a sharp increase of the spectral index at small field-to-flow angles, which appears rather step-like, has important implications for the interpretation of critically balanced plasma turbulence. It is often assumed that a critically balanced cascade can lead to any spectral slope, $7/3 \leq \kappa \leq 5$, between the extreme values at $\theta = 90°$ and $\theta = 0°$. However, we have shown in Equation (4.48) that the spectral index is $\sim 7/3$ for most angles and a smooth or slow variation of the spectral index, as seen in the results of *Chen et al.* (2010a), can therefore not be caused by critical balance alone. Instead, the effect of damping is essential to obtain steeper spectra at non-zero angles, which means that the measured functional dependence of the spectral

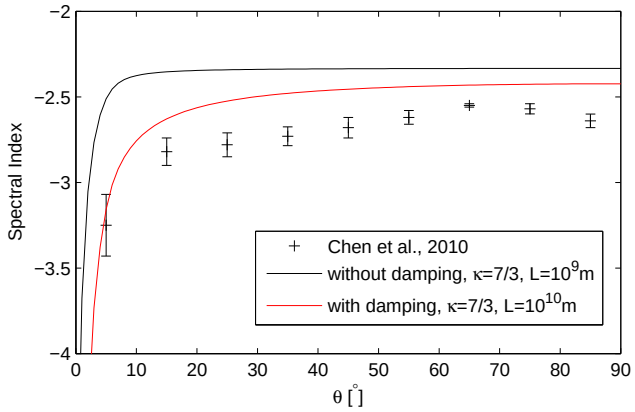

Figure 4.11: *Spectral anisotropy of fluctuations perpendicular to the local magnetic field derived by Chen et al. (2010a) (black crosses) for kinetic scales $k\rho_i = [1.5, 6]$ and numerically determined results for a critically balanced KAW cascade. While the spectral anisotropy of the damped cascade (red line) is similar to the measured data, the undamped cascade (black line) produces clearly different results.*

slope on angle, $\kappa(\theta)$, is to a large degree determined by the damping mechanism.

4.4 Modeling Spectral Densities at Saturn

In this section, we aim to reproduce the observed spectra in Saturn's magnetosphere with our synthetic spectra based on a critically balanced KAW turbulence. As we have shown in Section 3.3.4, Taylor's frozen-in approximation is valid in the case of nearly perpendicular kinetic Alfvén waves in Saturn's magnetosphere, which is a prerequisite for the application of our model. Although we are not able to validate that our observations are caused by KAW turbulence, we can check if they are in agreement with such a theory. Consistency between modeled and observed spectra, is thus at least indicative of the presence of a critically balanced KAW cascade in Saturn' magnetosphere. Further, we analyze on which scales the energy that is transferred along the cascade is dissipated. This may help to understand which electron population is energized by the turbulent fluctuations.

First, we model the spectrum of interval A from the second orbit of Cassini (see the case study in Section 3.3.5) to show which spectral characteristics of Saturn's magnetosphere our model is able to capture. Then, we proceed to model our complete data set of spectra from 10 min time series to analyze the radial distribution of spectral indices. We focus on the change of spectral slopes inside $9\,R_\mathrm{s}$, which so far could not be explained sufficiently. To model synthetic spectra in Saturn's magnetosphere, we use the parameters listed in Table 4.1. For the basic plasma parameters at Saturn - namely velocity, scale height, ion temperature and density - the same models as described in Section 3.1.2 are

Parameter	Description
$\mathbf{B}$	Magnetic field
θ	Field-to-flow angle
v	Plasma velocity
$L \sim 2H$	Outer scale
ρ_W	Water group ion gyro radii
ρ_e	Electron gyro radii
V_A	Alfvén velocity
$T/P \sim P_\perp/P_\parallel$	Power anisotropy

Table 4.1: *List of model input parameters needed to calculate synthetic spectra. We estimate the outer scale as twice the scale height and the ratio of toroidal to poloidal fluctuations from the measured power anisotropy.*

applied, which are based on observations by *Thomsen et al.* (2010). To calculate the electron gyro radius, which controls the onset of the empirical damping term in Equation (4.50), we use the electron temperature model given by *Schippers et al.* (2008, Table 1) derived from CAPS/MIMI measurements (*Young et al.*, 2004; *Krimigis et al.*, 2004). The field-to-flow angle θ is calculated assuming the plasma flow to be in azimuthal direction only. We further use the power anisotropy $P_\perp/P_\parallel$ to estimate the ratio T/P between toroidal and poloidal fluctuations' energy. The slopes of the modeled spectra are calculated from the trace of the synthetic spectral tensor.

4.4.1 Synthetic Power Spectral Densities for Rev A

The observed power spectral density during interval A of Rev A as shown in Figure 3.17a is an average over ∼10 h of data. During that time, the magnetospheric plasma parameters such as magnetic field direction, plasma velocity, and gyro radii change considerably. Because we cannot calculate synthetic spectra for time varying model parameters, we use hourly averages of the parameters instead. Figure 4.12 shows the variations of the mean magnetic field B_0, field-to-flow angle θ_{vB}, gyro radius ρ_w, and power anisotropy $P_\perp/P_\parallel$ during interval A as black crosses and the corresponding mean parameters used for modeling as red dots. It can be seen that the variations are well captured by the hourly averages. The synthetic spectral densities for each hour long interval k and component i are averaged to obtain the the spectra

$$P_\parallel = \sum_{k=1}^{10} \frac{1}{10} P_{z,k} \qquad\qquad P_\perp = \sum_{k=1}^{10} \frac{1}{10} \left(P_{x,k} + P_{y,k}\right) \tag{4.53}$$

for fluctuations parallel and perpendicular to the mean magnetic field of the whole interval A. In the model, all wave vectors are defined with respect to a constant magnetic field direction, i.e., for the modeled spectra the local and

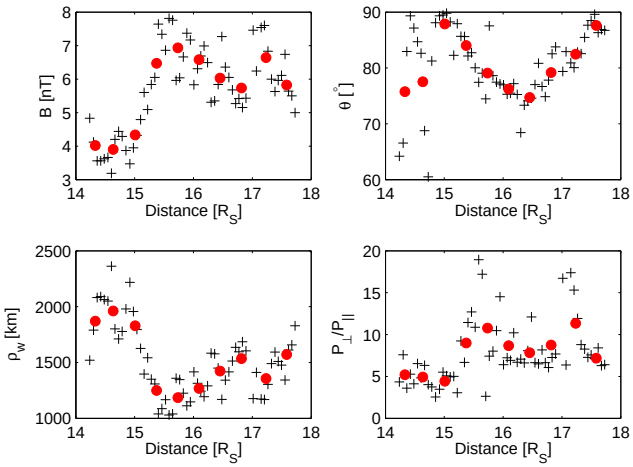

Figure 4.12: *Mean magnetic field B_0 (top left), field-to-flow angle θ (top right), gyro radius ρ_w (bottom left), and power anisotropy $P_\perp/P_\parallel$ (bottom right) obtained from 10 min time series during interval A of Rev A shown as black crosses and corresponding mean parameters used for modeling shown as red dots.*

global magnetic field frame are identical.

Equatorial temperatures have been derived by *Schippers et al.* (2008) for the cold or thermal ($< 100\,\mathrm{eV}$) and hot ($> 100\,\mathrm{eV}$) electron populations. These temperatures are needed for the calculation of the electron gyro radii, which control the empirical damping term in Equation (4.50). Here, we compare results for electron gyro radii derived from temperatures of the cold electron population with those derived for the hot population. The radial profiles of the temperatures and densities are shown in the left and right panel of Figure 4.13, respectively, together with the water group ion temperatures and densities for comparison. The model for the hot electrons is valid for distances up to $18\,R_\mathrm{s}$. The temperature of the cold population is more variable outside $15\,R_\mathrm{s}$ and thus only defined inside of that distance. However, due to the lack of a better estimate, we use the cold electron model also outside $15\,R_\mathrm{s}$. Both temperatures similarly peak at around $9\,R_\mathrm{s}$.

The density of the hot electron population n_h is significantly less than the density of the cold or thermal population n_c. The ratio of cold to hot electron densities is around 25 at $10\,R_\mathrm{s}$ decreasing to $\sim$7 at $20\,R_\mathrm{s}$. However, due to the much higher temperature of the hot electrons, the total energy residing in the population is a factor 5−10 higher than for the cold electrons (*Bagenal and Delamere*, 2011). With respect to the derived turbulent heating rates, we estimate how long it takes to heat each of the populations to their observed temperature. If we assume our derived turbulent heating rates, q_L and q_S, as the only energy source and neglect any energy sink, we may approximate this

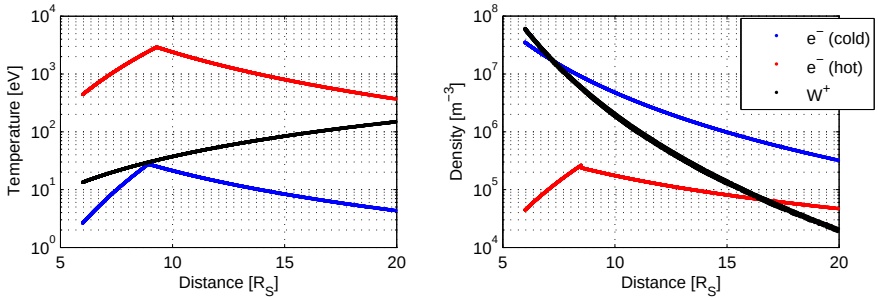

Figure 4.13: *Equatorial electron temperatures (left) and densities (right) for the hot (red) and cold (blue) electron populations after Schippers et al. (2008). For comparison, we also show the equatorial temperatures and densities of water group ions (black) as obtained from Thomsen et al. (2010).*

characteristic heating period according to *Saur* (2004) as

$$q\tau_{\mathrm{heat}} \sim \frac{3}{2} n k_B T \ , \tag{4.54}$$

where the left-hand-side describes the energy dissipated by turbulent fluctuations and the right-hand-side the total energy of the electron or ion population. Solving for time, we can calculate a characteristic heating period τ_{heat}. Figure 4.14 shows the radial profiles of $\langle\tau_{\mathrm{heat}}\rangle$ averaged in $1\,R_{\mathrm{s}}$ bins for hot and cold electrons as well as for water group ions and for both turbulent heating rates in units of days. Our estimation shows that it generally takes more than a day to heat the hot electron population to its observed temperature by turbulent dissipation. The cold electron and water group ion populations are heated more quickly and only inside $\sim 14\,R_{\mathrm{s}}$, it takes more than a day to reach the observed temperatures. Interestingly, both of these heating periods show a similar radial profile.

Although Equation (4.54) is only a rough approximation, it is illustrative in how much energy can be deposited into each population. We can see that Saturn's magnetosphere responds more robust to heating of the hot electrons because their energy reservoir is larger. The relatively short periods of less than a day for cold electrons and water group ions may be problematic in the sense that these populations would need to get rid of their energy very fast to keep the system stationary. In comparison, *Saur* (2004) derived turbulent heating periods for the middle magnetosphere of Jupiter and found that it takes $\sim$4 days to heat the ion population to the observed temperatures. At least for the hot electron population, this is comparable to what we observe here. It would be interesting to estimate corresponding heating periods for the suprathermal ions as well, but there is currently no model available. In general, heating by turbulent dissipation seems to be more effective at large distances to Saturn, where the characteristic heating periods are shorter.

In Figure 4.15, we compare the observed spectra of interval A with our

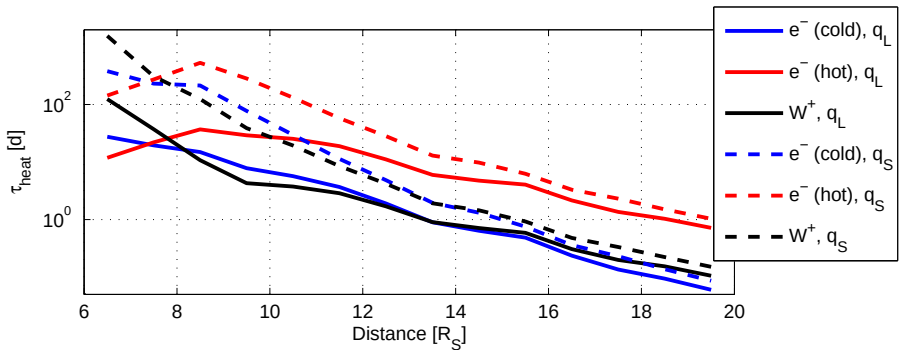

Figure 4.14: *Characteristic heating period* $\tau_{\mathrm{heat}} \sim 3n_e k_B T_e/(2q)$ *in days as a function of radial distance for the hot (red) and cold (blue) electron population as well as for water group ions (black). Periods for* q_{L} *are denoted by solid lines and those for* q_{S} *by dashed lines. Generally, it takes longer to heat the population of hot electrons than the populations of cold electrons and water group ions.*

modeled results. In the left panel, we only show the modeled spectra, P_{hot} and P_{cold}, which are calculated for hot and cold electron gyro radii, respectively. The gyro radii are given by

$$\rho_{e,c/h} = \frac{\sqrt{2m_e k_B T_{e,c/h}}}{eB} \ , \tag{4.55}$$

where T_{ec} and T_{eh} denote the cold and hot electron temperatures, respectively. The perpendicular and parallel fluctuations are shown in black and red colors, the spectra with damping at ρ_{ec} as dashed lines and those with damping at ρ_{eh} as dotted lines. The synthetic spectra are the output of our complete model with damping, i.e., Equations (4.27), (4.35), (4.36) and (4.50), using the hourly averaged parameters. The energy of the model is overestimated with respect to the observed spectra by a factor of ∼10 and, naturally, it lacks the flattening at higher frequencies, which is caused by noise. Clearly, the larger electron gyro radius of the hot electron population leads to an earlier onset of damping, which is visible as a slightly steeper slope for P_{hot}.

To better compare the results with the observation we apply an empirical energy correction factor of 1/10 and add noise to the synthetic spectra. The noise levels are computed according to Section 3.3.5 as the sum of magnetometer noise, quantization noise (Equation (3.19)), and aliasing estimated according to *Podesta et al.* (2006). The instrumental noise is actually measured and therefore must be added to the spectrum before calculating the aliasing. This leads to a synthetic spectrum given by

$$P_i'(f) = P_i(f)/c_E + 25{\cdot}10^{-6}/f + \frac{1}{6}\Delta B^2 \Delta t + A{\cdot}\left(P(f)/c_E + 25\cdot 10^{-6}/f\right) \ , \tag{4.56}$$

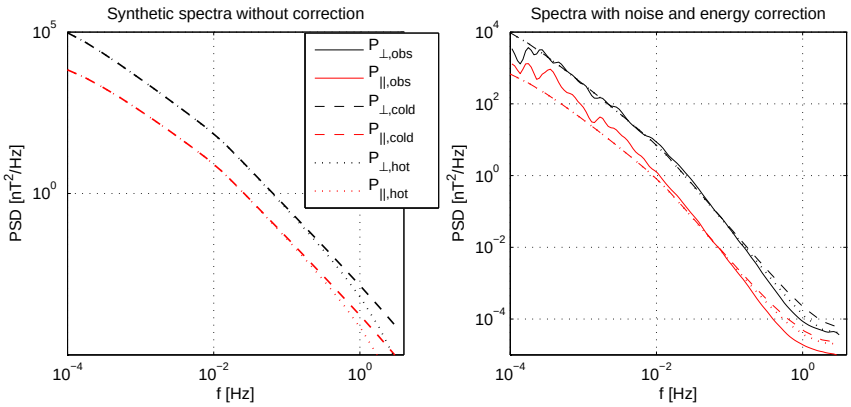

Figure 4.15: *Left: modeled spectra of fluctuations parallel (red) and perpendicular (black) to the local mean magnetic field computed from hourly averages during interval A of Rev A for hot and cold electron gyro radii (dashed and dotted lines, resp.). Right: modeled spectra with empirical energy correction (divided by 10) and added noise together with observed spectra (solid lines).*

where P_i is the synthetic spectrum without noise, $c_E = 10$ is the energy correction and the aliasing factor A is determined according to Equation (3.20) for a power-law of $\kappa = 7/3$. The second term on the right-hand-side of Equation (4.56) is the instrument noise ($25\,\mathrm{pT}^2$ at 1 Hz, $\propto f^{-1}$) and the third term is the quantization noise according to *Russell* (1972), where we use the quantization of the magnetic field data, e.g., $\Delta B = 4.9\,\mathrm{nT}$ in FGM range 1 (see Table A.2). The resulting spectra of Equation (4.56) are shown in the right panel of Figure 4.15. The spectra fit the observations qualitatively well, which shows that (1) the observations can generally be explained by a critically balanced turbulent cascade from MHD to electron scales formed by colliding (kinetic) Alfvén waves and (2) the basic plasma model (velocity, density, temperature) is appropriate to describe the measurements. The latter conclusion can be drawn from the coincidence of the spectral break for both synthetic and observed spectra at $f \sim 10^{-2}\,\mathrm{Hz}$. However, the fit is not perfect and we also need to discuss the discrepancies between model and observation. Also, the MHD ranges of the other intervals B-D of the case study do not fit the model at all as they show no characteristic Kolmogorov-like power-law.

We have already mentioned the energies of the modeled spectra, which do not correspond to the measurement. Hence, we need to normalize the synthetic spectra with measured spectral energies. Also, the model fits the perpendicular fluctuations better than those parallel to the magnetic field, which shows the limits of our simple approximation $P \propto T$. Further, it can be seen that the spectral slopes of the models in the kinetic range are somewhat shallower than the slope of the measured PSD. The spectra controlled by the hot electron population fit the observations generally better than those controlled by the cold

population. This may indicate that damping happens on scales ρ_{eh} rather than ρ_{ec} and thus a preferential heating of the hot electron population. However, the radial profiles of both electron temperatures are nearly identical so that the difference between the two gyro radii can be compensated by a simple factor in the damping term, e.g., $\exp(-10 \cdot k_\perp \rho_{ec})$. It may also indicate that the spectral index of 7/3 is not correct to describe the problem. *Boldyrev and Perez* (2012) propose a steeper slope of 8/3, which might better fit the observations if damping is negligible. However, the results in Figure 4.15 indicate that the turbulent spectra in Saturn's magnetosphere can be qualitatively modeled. An interpretation of the observations with the help of synthetic spectra based on KAW turbulence may thus yield further insight into what is controlling the turbulence characteristics in the magnetosphere. Therefore, we proceed to analyze the distribution of kinetic range spectral indices for our complete data set in the next section.

4.4.2 Reproduction of Distribution of Spectral Indices

In this section, we model the spectra of 10 min time series using the measured magnetic field data in the plasma sheet, the magnetospheric plasma model by *Thomsen et al.* (2010) and electron temperatures derived by *Schippers et al.* (2008). The aim is to analyze the radial profile of the spectral indices (see Figure 3.23) and to verify if the observations are in accordance with our interpretation in terms of a critically balanced cascade. As the basic plasma model that we use for Saturn's magnetosphere cannot reflect the exact plasma conditions during the measurement, we can only expect a qualitative fit to the data. As we did in the preceding section, we calculate spectra P_{cold} and P_{hot} for damping controlled by the cold and hot electron population, respectively. A systematic difference between the modeled results and the observed spectral indices may help to determine on which scales the dissipation occurs and which electron population is primarily heated by the turbulent cascade. However, such a conclusion may only be appropriate if a critically balanced KAW cascade with damping on electron scales is the proper model to describe the cascade, which is observed in Saturn's magnetosphere.

To compare the synthetic results with our observations, we carry out a forward modeling for each time series and compute the spectral slopes in the same frequency ranges as determined for the observed data, i.e., in the range $2 < k_\perp \rho_W < 50$ and for SNR < 5 of the respective measurement. As we have seen in the preceding section, our model does not sufficiently reproduce the spectral energy and must therefore be normalized. For that matter, we use the geometrical mean of the spectral power $\langle P \rangle$ in the respective fitting range. Noise is added to the spectra in a last step according to Equation (4.56). An example of a single 10 min time series spectrum and its corresponding synthetic spectra is shown in Figure 4.16. Inside the fitting range, depicted by two vertical lines, the three spectra are very similar. Their spectral indices are given in the legend of the Figure and the modeled results are close to the observed slope.

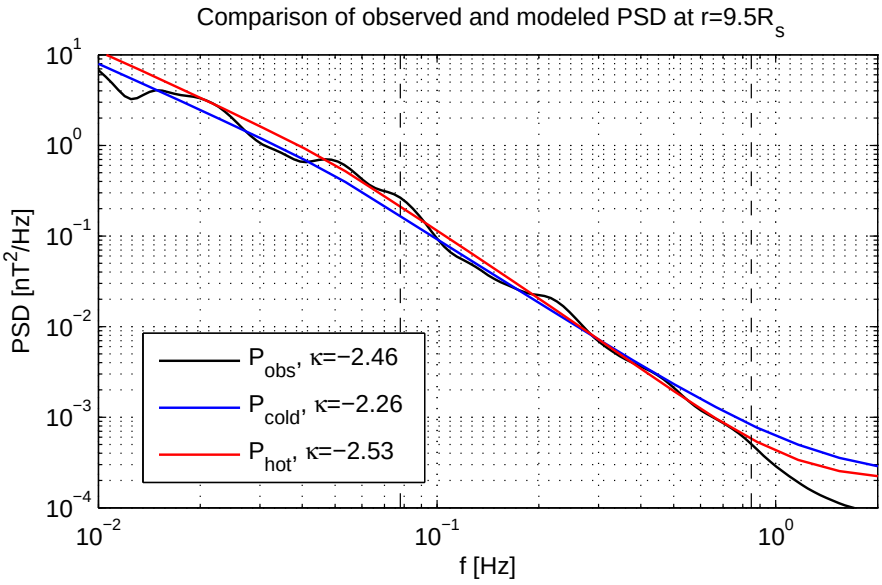

Figure 4.16: *Power spectral density of* 10 *min time series measured at a radial distance of* 9.5 R_s *(black line). The blue and red lines show synthetic PSD* P_{cold} *and* P_{hot}*, respectively, for damping controlled by the gyro radius of the corresponding electron population. Vertical dashed lines show the fitting range in which the spectral index is calculated. The determined value is given in the legend.*

The spectrum controlled by the hot electrons' gyro radius fits the observation slightly better. At frequencies higher than the fitting range, the noise level leads to a flattening, which is overestimated for both synthetic spectra. This may be due to our rather conservative estimation of the different noise sources to be uncorrelated (see Section 3.3.5).

Figure 4.17 shows the radial profile of spectral indices observed in Saturn's equatorial plasma sheet as black crosses (see also Figure 3.23). The spectral slopes for damping on cold electron scales (blue dots) are generally lower than the observations and close to the undamped spectral index of 7/3. This shows that the corresponding synthetic spectra have not yet reached dissipation scales, where the spectral energy decreases significantly. Damping on hot electron scales, on the other hand, leads to steeper spectra that agree much better with the observations. Clearly, the decrease of the electron temperature inside 9 R_s leads to shallower spectra because the damping is reduced for smaller electron gyro radii. This indicates that the change of slopes inside 9 R_s can be explained by damping effects. However, for larger distances ($> 12\,R_s$) the spectral indices κ_{hot} become shallower than the observations, which may indicate the presence of additional effects on the turbulent cascade that are not captured by our simple model.

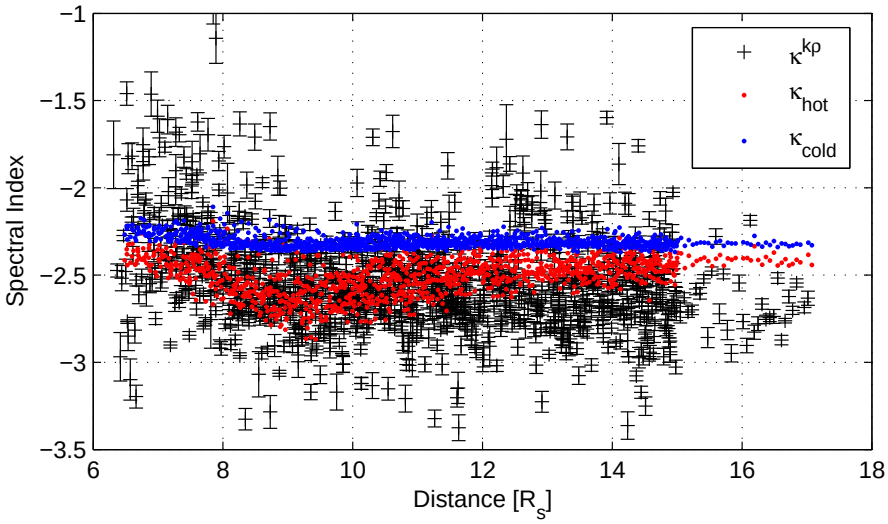

Figure 4.17: *Observed spectral indices obtained in Section 3.4.1 (see also Figure 3.23) shown as black crosses. Spectral indices of synthetic spectra are shown as dots for damping on cold (blue) and hot (red) electron scales. Damping on hot electron scales allows for a qualitative reproduction of the changing slopes inside* $9\,R_\mathrm{s}$.

In summary, the forward modeling of kinetic range spectra has provided a possible explanation for the changing spectral slopes inside $9\,R_\mathrm{s}$, which is solely based on first principles of a KAW cascade and an empirical term to describe damping on electron scales. Combined with our estimations of the characteristic heating period, our results indicate that the energy transferred along the kinetic range cascade is preferably deposited into the hot electron population. This may have important consequences for the pitch angle distribution and temperature anisotropy of that population and it would be interesting to analyze in more detail how exactly the energy is deposited into the electrons.

4.5 Conclusion

We present a numerical model to evaluate one-dimensional reduced PSD from a given energy distribution in **k**-space for arbitrary measurement geometries. Such a forward calculation for turbulent spectra from MHD to dissipation scales has been applied for the first time. Given a critically balanced **k**-space distribution of energy, we investigate the functional dependence on several plasma parameters such as the angle between plasma velocity and background magnetic field θ in the inertial, kinetic and dissipation range of scales. We show that the spectral slope of a critically balanced cascade is not constant but evolves with frequency toward a quasi-perpendicular slope. This new effect, which is caused by the anisotropic distribution in **k**-space, has not been described before. The PSD in this quasi-

perpendicular cascade range have a spectral slope corresponding to the spectral index of the perpendicular cascade $\kappa(\theta{=}90°)$. The maximal frequency, $f_{\max}$, where the transition to $\kappa(\theta{=}90°)$ is reached, is given in Equation (4.48). Under typical solar wind conditions, $f_{\max}$ is smaller than or on the same magnitude as the observed spectral break frequency. Therefore, significantly steeper slopes than the perpendicular spectra can only be explained by additional damping effects or by nearly parallel plasma flow ($\theta \lesssim 5°$). Inclusion of an empirical damping term $\exp(-k_\perp \rho_e)$ based on observations by *Alexandrova et al.* (2012), showed that the spectral index in the ion kinetic range $\rho_i^{-1} < k_\perp < \rho_e^{-1}$ can steepen measurably.

We validated our model with in-situ measured data, which show that turbulent fluctuations measured by *Horbury et al.* (2008) are in good agreement with a critically balanced cascade and less so with slab+2-D turbulence. In the kinetic range, we find qualitative agreement of the results of *Chen et al.* (2010a) with a damped critically balanced KAW cascade. While the spectral break and damping terms have only minor influence on the fit to the observations of *Horbury et al.* (2008), the inclusion of a damping term is essential to explain the results in the kinetic range. Indeed, spectral slopes for an undamped cascade differ strongly from the *Chen et al.* (2010a) results and are nearly constantly $\sim 7/3$, which is caused by the transition toward a quasi-perpendicular slope. This means that for a critically balanced KAW cascade, damping is an important contribution in the kinetic range. The measured spectral anisotropy, $\kappa(\theta)$, in this frequency range is to a large degree controlled by the nature of the damping mechanism.

The model is successfully applied to qualitatively reproduce power spectral densities measured in Saturn's magnetosphere. We have shown that a critically balanced KAW cascade is qualitatively in agreement with our observations in Saturn's magnetosphere and we are able to reproduce the location of the spectral break, which shows that the applied plasma model for the magnetosphere is appropriate. This indicates that our prior interpretation (Section 3.6) of a turbulent cascade formed by critically balanced kinetic Alfvén waves is correct. Forward modeling of each 10 min time series allows us to calculate synthetic spectral slopes, which can be compared to the measured radial profile of spectral indices. Here, the empirical damping term is an important factor as it steepens the synthetic spectra toward the observed slopes of generally $\kappa > 7/3$. Only for gyro radii of the hot electron population, damping becomes important and the fit to the data is sufficiently well. The change of spectral indices toward shallower slopes inside $9\,R_\mathrm{s}$ can thus be qualitatively explained by the effect of damping controlled by the underlying electron temperature profile. In contrast, spectral slopes for damping at ρ_{ec} (cold population) are too shallow to explain the observations and do not show a significant change at $9\,R_\mathrm{s}$.

These results indicate that the energy transferred along the turbulent cascade is predominantly deposited into the hot electron population. However, it must be noted that the applied damping term is an experimental fit to reduced spectra

in the solar wind (*Alexandrova et al.*, 2012) and there is so far no theoretical basis for its applicability in three-dimensional **k**-space. Also, it is not a priori clear that it can be used in a multi-species plasma with a high neutral fraction as it is found in Saturn' magnetosphere. As the radial profiles of both cold and hot electron populations are very similar, the difference between the effects of damping reduces to a simple constant factor in the exponential damping term. Therefore, the interpretation that the hot electron population controls the damping of the turbulent cascade is strictly inconclusive. Still, it has been shown that the application of our forward turbulence model generally leads to further insight into the system and it is an important step toward validating theories for turbulent magnetic fluctuations. A further development of the numerical model regarding the computation of the correct energy level and the inclusion of more turbulence models is therefore highly recommended.

CHAPTER 5

Summary

In the present thesis, we analyzed for the first time the statistics of magnetic field fluctuations inside Saturn's magnetosphere in the framework of turbulence. In Chapter 3, we showed that these fluctuations form a turbulent cascade on kinetic scales, which is constantly observed throughout the middle magnetosphere. Thus, a new laboratory for turbulence studies was introduced, which allows to observe turbulence in a system of low plasma β and strong background magnetic field B_0. A motivation for this study was to explain the large plasma temperatures that are measured in Saturn's magnetosphere. Although the plasma expands nearly adiabatically on its way out from deep inside the magnetosphere, where it is produced, the temperatures are found to increase with distance, which indicates a local heating mechanism (*Bagenal and Delamere*, 2011). Thus, we elaborated on the conjecture that turbulent dissipation is responsible for that heating.

Due to the pickup processes and the associated encounters of ion-cyclotron waves close to the planet and the influence of the magnetopause at large distances, we restricted our analysis to the plasma sheet in a range of $6.5 - 20\,R_\mathrm{s}$ (*Leisner et al.*, 2006; *Achilleos et al.*, 2008). A wavelet based case study of the second orbit of Cassini revealed power spectral densities characterized by a variable low-frequency power-law, a spectral break at frequencies f_b associated to characteristic ion scales and a steeper power-law range on kinetic scales. The low frequency fluctuations corresponding to MHD scales are characterized by large scale magnetospheric processes, such as current sheet flapping and flux tube interchanges. The spectrograms showed intermittent power enhancements and potential energy injections on the associated large scales. This might explain why a Kolmogorov-like power-law, indicating a strong turbulent cascade on MHD scales, was only sporadically observed, e.g., during the current sheet crossing of Cassini. However, the case study indicated that the spectral characteristics on kinetic scales are nearly homogeneous and quasi-stationary. Further, the obtained spectral indices of $\kappa \sim 2.6$ in the kinetic range and the increasing intermittency of the fluctuations matched characteristic observations of turbulence in the solar wind (*Alexandrova et al.*, 2013). Therefore, it was concluded

that a turbulent cascade is formed by magnetic fluctuations on kinetic scales in Saturn's magnetosphere.

The turbulent cascade on kinetic scales was analyzed with a data set covering a time interval from July 2004 up to December 2009. We used a simple plasma model (*Thomsen et al.*, 2010) to calculate the parameters needed to transform the measured frequency spectra into normalized wave vector spectra. This allowed us to compare spectra observed at different locations in Saturn's magnetosphere. It was found that the spectral break is best described in rest frame of the plasma normalized to the background magnetic field. At frequencies $f > f_b$, a consistent power-law range was detected in which the spectral indices were determined for a fixed range of normalized scales. The distribution of spectral indices as a function of radial distance revealed a systematic change at $9\,R_\mathrm{s}$. Inside that distance, the spectral slopes get shallower with decreasing distance to Saturn resulting in an average of $\alpha_< = 2.3 \pm 0.3$. Outside that distance, the spectral index shows no systematic changes leading to an average of $\alpha_> = 2.6 \pm 0.3$. These values are in agreement with predictions, amongst other theories, for a critically balanced KAW cascade (*Howes et al.*, 2006). This interpretation could be further substantiated in Chapter 4 through forward modeling of synthetic power spectra using the numerical tool developed in the framework of this thesis.

We further estimated how this turbulent cascade affects the energy budget of the planetary magnetosphere. The identification of a theoretical model to explain the observed magnetic field fluctuations in Saturn's magnetosphere permitted us to estimate the energy that is transferred along the turbulent cascade to smaller scales (*Leamon et al.*, 1999; *Saur*, 2004). For that matter, we assumed a stationary critically balanced KAW cascade, which yielded a total energy flux of 140-160 GW. According to *Schekochihin et al.* (2009), the energy transfered along this KAW cascade ultimately leads to electron heating. Therefore, the energy flux along the cascade can be interpreted as a turbulent heating or dissipation rate. A comparison with the energy needed to heat the plasma to its observed values, namely 75-630 GW, showed that turbulence plays a substantial role for the energy budget of Saturn's magnetosphere and may help to explain the puzzling high plasma temperatures measured in the magnetosphere. However, it remains an open question, which is beyond the scope of this thesis, how the dissipated energy is further transported in the Saturnian system.

In addition, the obtained results in Saturn's magnetosphere were examined for local time and longitudinal asymmetries. Here, we found stronger fluctuations and an increased heating rate at pre-noon and a significant sinusoidal ($m = 1$) variation with longitude for 65% of the analyzed orbits. Here, the dissipation rate was found to peak in a longitude sector $300° \pm 80°$ in both SLS4 systems (*Gurnett et al.*, 2011; *Lamy*, 2011). Tests showed that this increased heating rate density is primarily caused by an increased spectral power in the kinetic range and a larger RMS of the magnetic field fluctuations. Thus, the variation of the turbulent heating rate reflects an increased energy flux along

the cascade. Slight longitudinal changes of the spectral index may be explained by damping effects. Our results of a longitudinally asymmetric turbulent heating are in accordance with observations by *Gurnett et al.* (2007) and *Burch et al.* (2009), who found increased electron and ion densities, respectively, in the same longitude range. The sinusoidal variation of the heating rate is most pronounced in the local time sector of 17−4 h, which may indicate that the night side is more strongly heated during SKR maximum. However, it remains unclear what exactly causes the asymmetry and how it is physically connected to the various asymmetries observed in Saturn's magnetosphere.

In Chapter 4 of this thesis, we presented a newly developed numerical tool to calculate reduced power spectral densities from given energy densities in three-dimensional wave vector space. Such a forward calculation of turbulent spectra could be applied for the first time. Here, we focused on critically balanced turbulence (*Goldreich and Sridhar*, 1995) and were able to evaluate PSD for arbitrary measurement geometries covering a range from MHD ($k_\perp \rho_i < 1$) to dissipation scales ($k_\perp \rho_e > 1$) (*Howes et al.*, 2008; *Cho et al.*, 2002; *TenBarge et al.*, 2013). We assumed the turbulent fluctuations to be axisymmetric around the local mean magnetic field and estimated the pseudo-Alfvénic fluctuations to be passively cascaded by (kinetic) Alfvén waves. As a result, both poloidal and toroidal fluctuations follow the same scaling (*Lithwick and Goldreich*, 2001).

Extensive tests of the functional dependence of the PSD on field-to-flow angle θ, outer scale L, relative plasma velocity v and critical balance exponent γ, amongst others, have been carried out. It could be shown that the spectral index observed in one-dimensional reduced spectra is not constant along the cascade but is an explicit function of frequency in the spacecraft frame. We could show that the spectral slope of the PSD changes toward the value of the perpendicular cascade, $\kappa(\theta{=}90^\circ)$, for all non-zero field-to-flow angles. The frequency, $f_{\max}$, where this perpendicular slope is reached, was analytically estimated and the result checked with our model. For typical solar wind conditions at 1 AU, we find that $f_{\max} \lesssim 1\,\mathrm{Hz}$. This change toward a quasi-perpendicular cascade is a pure sampling effect and has not been discussed in the literature so far, although *Forman et al.* (2011) seem to come to a similar result. For the solar wind, this result has important implications. It follows that if the cascade is not damped, only in a short frequency range after the spectral break and only in case of small field-to-flow angles, a significantly steeper slope may be observed. For most field-to-flow angles, $\theta \gtrsim 10^\circ$, the observed slope will be quasi-perpendicular. This effect manifests in a shape that resembles the double kink spectra or transition range, which is sporadically observed (*Kiyani et al.*, 2009; *Sahraoui et al.*, 2010). Our analytical estimation suggests that this transition may be observed over a broad frequency range in case of small scale energy injection, i.e., small outer scales L.

To model potential anisotropic wave damping, e.g., ion cyclotron or Landau damping, we included a cut-off of energy acting on parallel wave vectors and an exponential decay acting on perpendicular wave vectors (*Schekochihin*

et al., 2009; *Alexandrova et al.*, 2012). We showed that the parallel cut-off only affects PSD with very small field-to-flow angles. For $\theta = 10°$, only 2% of the energy is drained by the cut-off at a frequency of 10 Hz and even less at lower frequencies. Thus, a damping mechanism dependent on parallel wave numbers is generally not effective for a critically balanced KAW cascade. On the other hand, an empirically derived damping term acting on perpendicular wave vectors controlled by the electron gyro radius proved to be highly effective. The effect of this damping term is already detectable in the ion kinetic range of the reduced spectra and may even mask the transition toward a quasi-perpendicular cascade. It leads to a frequency range in the PSD that appears as a power-law with steeper spectral slopes. In the case of our solar wind model, we find that for $\theta = 90°$ a spectral index of 8/3 is observed in the kinetic range, although the energy scales as $k_\perp^{-7/3}$. This shows that the measured spectral slope should not be confused with the spectral index of the underlying turbulence theory.

Our synthetic PSD were successfully applied to qualitative reproduce the results obtained by *Horbury et al.* (2008). This shows that they are in agreement with a critically balanced cascade and that damping is negligible for the observed spectral anisotropy. As the outer scale L is a controlling factor of the functional dependence $\kappa(\theta)$, we used the fit to their data to determine this parameter. This method resulted in a reasonable value for the energy injection scale of $L \sim 10^9$ m (*Schekochihin et al.*, 2009). This outer scale was further applied to analyze if recent observations on kinetic scales are also in agreement with a critically balanced KAW cascade (*Chen et al.*, 2010a). Here, the model fits the measurements only qualitatively but we find that the perpendicular damping term is substantial to generate a smooth transition of spectral indices from steep slopes at $\theta \sim 0°$ to shallow slopes at $\theta \sim 90°$. However, we propose to incorporate other theories into the model, e.g., KAW turbulence including intermittency effects (*Boldyrev and Perez*, 2012) with a slope of 8/3, that might better explain the data.

We applied the forward modeling of synthetic spectra to qualitatively reproduce the turbulent spectra measured in Saturn's magnetosphere. This substantiated our former interpretation that the magnetic fluctuations form a critically balanced turbulent cascade of kinetic Alfvén waves. We could derive a synthetic radial distribution of spectral indices to compare with our measurements. The change of spectral slopes inside $9\,R_\mathrm{s}$ was found to be qualitatively in accordance with damping on electron scales. As the temperatures of both thermal and hot electron population decrease inside of that distance, this leads to less strong damping and therefore shallower slopes. Damping at the hot electron gyro radii matches our observations best and indicates that the energy carried along the turbulent cascade primarily heats the hot electron population. This is further corroborated by our estimation of characteristic heating time scales, which yielded reasonable heating periods for the hot electron population comparable to those derived by *Saur* (2004) for Jupiter's magnetosphere. We note, however, the qualitative nature of these results as they are based on simple plasma models

and an empirically derived damping term.

Saturn's magnetosphere remains an interesting subject to future analyses as many questions have been raised that are still unanswered. Our spectral analyses indicate that the plasma in the magnetosphere is highly turbulent on kinetic scales and energy is transfered from large scale magnetospheric processes to electron scales. The forward calculation of synthetic power spectra based on first principles corroborates this interpretation and proved to be a valuable tool for the study of turbulent systems. We have further shown that dissipation of turbulent energy is substantial for the planetary energy budget and happens longitudinally asymmetric across the plasma sheet in accordance with observations of increased plasma density. From energy considerations, this turbulent heating may explain the non-adiabatic radial profile of plasma temperatures. Analyses on the effect of damping indicate that primarily the hot electron population is heated. Although the exact transfer of energy between electron and other plasma populations in the magnetosphere is still not well understood and, therefore, we cannot directly explain the high ion temperatures in Saturn's magnetosphere, we have presented in this thesis a new ansatz to solve this problem. We hope that our observations, together with our new forward modeling technique, will help to shed light on the complex and turbulent plasma dynamics in Saturn's magnetosphere.

APPENDIX A

Cassini: Mission and Instruments

The spacecraft Cassini was launched on the 15th of October, 1997, together with the Probe Huygens, which was deployed on 14th of January, 2004, during the third flyby of Saturn's moon Titan to analyze its atmosphere. A very detailed description of the mission and its instruments can be found in *Russell* (2003, 2004a,b). Figure A.1 shows a schematical drawing of the Cassini spacecraft and highlights its instruments. A complete list of the instruments onboard Cassini can be found in Table A.1.

After the launch of the spacecraft, a cruise phase of almost seven years followed, in which Cassini made swing-by's at Venus and Jupiter for gravitational assists. It entered Saturn's orbit (SOI) in July of 2004. The trajectory of the spacecraft is shown schematically in Figure A.2. Due to small changes in the beginning of the mission, the second to fourth orbits or revolutions are named Rev A, Rev B, Rev C, respectively, while the concurrent orbits are numbered. These numbered orbits begin with Rev 3, which is actually the fifth orbit and had its perigee in February, 2005 (*Seal*, 2005).

The MAG experiment, which we present in this chapter, consists of a scalar and vector helium magnetometer (S/VHM) and a three axis fluxgate magnetometer (FGM). Both magnetometer systems are mounted on an 11 m boom to minimize noise caused by the spacecraft. The technical characteristics and the general functionality of the two magnetometers described here are taken from *Dougherty et al.* (2004), where the experiment and its scientific goals are presented in detail. The data of the magnetometers is publicly available and was provided by the planetary data system (PDS).

A.1 Helium Magnetometer

The Helium magnetometer, which is mounted at the end of the magnetometer boom of the Cassini spacecraft, can be operated in a scalar and vector mode. The magnetic field strength is indirectly measured by a photo detector, which measures the light intensity behind a helium absorption cell. The instrument is shown in Figure A.3. Due to the presence of an ambient background magnetic

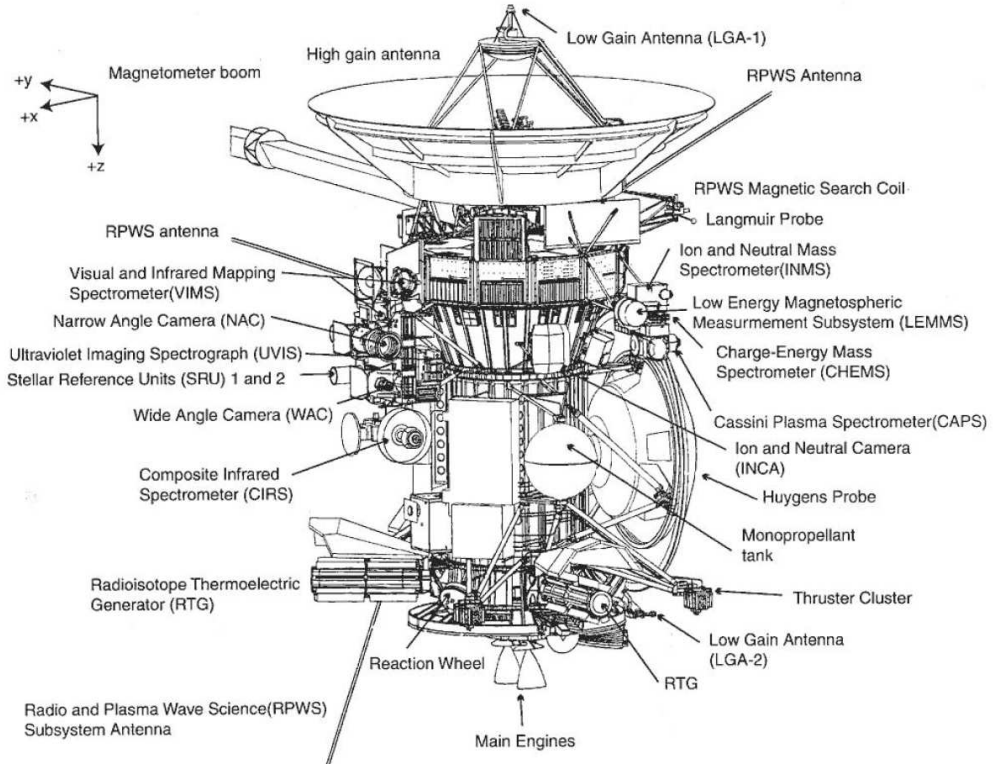

Figure A.1: *Drawing of the spacecraft Cassini and its instruments (Seal, 2005).*

field, the degenerate energy levels of the helium atoms are slit up, which is called the Zeeman effect. With circularly polarized radiation of 1083 nm it is possible to optically pump the helium, which is energized into a $^2S_1$ metastable state by radio frequency discharges. In a sufficiently pumped state, absorption of the circularly polarized light reaches a minimum.

The split up of the energy levels by the Zeeman effect is proportional to the background magnetic field strength. Using a frequency-modulated high-frequency sweep field, a transition between neighboring Zeeman levels can be induced. This happens at the Larmor frequency. The induced transition changes the spin of the electron and fills up the energy level that was emptied by optical pumping. Hence, the circularly polarized radiation of 1083 nm can be absorbed again and the resonance is measured by a decrease of light intensity behind the helium absorption cell. As the Larmor frequency is proportional to the background magnetic field, this method allows for the measurement of the magnetic field strength. The magnetic field strength can be measured in a range of $256 - 16384$ nT with very high precision. This allows highly accurate measurements very close to Saturn, which is important to characterize the internal magnetic field.

In the vector mode, it is possible to extract the vectorial magnetic field. The

Instrument	**Acronym**	**PI**
Cassini Plasma Spectrometer	CAPS	Young
Cosmic Dust Analyzer	CDA	Srama
Composite Infrared Spectrometer	CIRS	Flasar
Ion and Neutral Mass Spectrometer	INMS	Waite
Imaging Science Subsystem	ISS	Porco
Magnetometer	MAG	Dougherty
Magnetospheric Imaging Instrument	MIMI	Krimigis
Cassini Radar	RADAR	Elachi
Radio and Plasma Wave Science	RPWS	Gurnett
Radio Science Subsystem	RSS	French
Ultraviolet Imaging Spectrograph	UVIS	Esposito
Visible and Infrared Mapping Spectrometer	VIMS	Brown

Table A.1: *List of Instruments onboard the Cassini Orbiter, their Acronyms and respective Principal Investigators (PI) (Seal, 2005)*

	SHM	**VHM**	**FGM**
Sampling Rate	1 Hz	2 Hz	32 Hz
Dynamic Range, Resolution	256−16384 nT, 39 pT	±32 nT, 3.9 pT ±256 nT, 31.2 pT	±40 nT, 4.9 pT ±400 nT, 48.8 pT ±10000 nT, 1.2 nT ±44000 nT, 5.4 nT

Table A.2: *Technical properties of the instruments of the MAG experiment (Dougherty et al., 2004).*

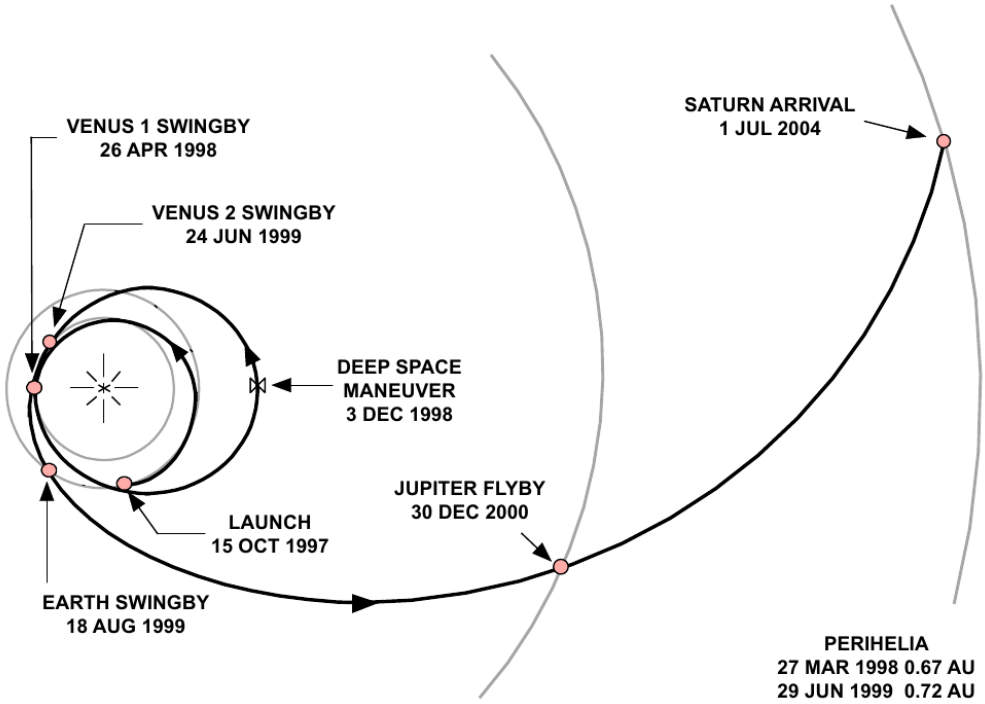

Figure A.2: *Trajectory of the Cassini-Huygens Mission from its launch in October, 1997, until Saturn Orbit Insertion (SOI) in July, 2004 (Seal, 2005).*

magnetic field direction influences the effectivity of the optical pumping by a factor $\cos^2\theta$, where θ is the angle between optical axis and background magnetic field. A set of three Helmholtz coils mounted around the absorption cell rotates a low frequency sweep field, which allows the detection of the single vector components of the magnetic field strength. The vector helium magnetometers can be operated in two different ranges as shown in Table A.2.

A.2 Fluxgate Magnetometer

The fluxgate magnetometer (FGM), shown in Figure A.4, is mounted halfway along the magnetometer boom. It consists of three high-permeability ring cores, which are winded by drive coils. Sense coils surround these cores and the drive coils. The three cores are mounted orthogonally on a ceramic platform. The drive coils are fed with an alternating current of 15.625 kHz and drive the cores into saturation. In the absence of an background magnetic field, the induced magnetic fields cancel out and there is no current induced in the sense coil. However, if a background magnetic field is present, the induced fields are asymmetric, which in turn induces a second harmonic of the drive frequency in the sense coil. This signal is proportional to the background magnetic field.

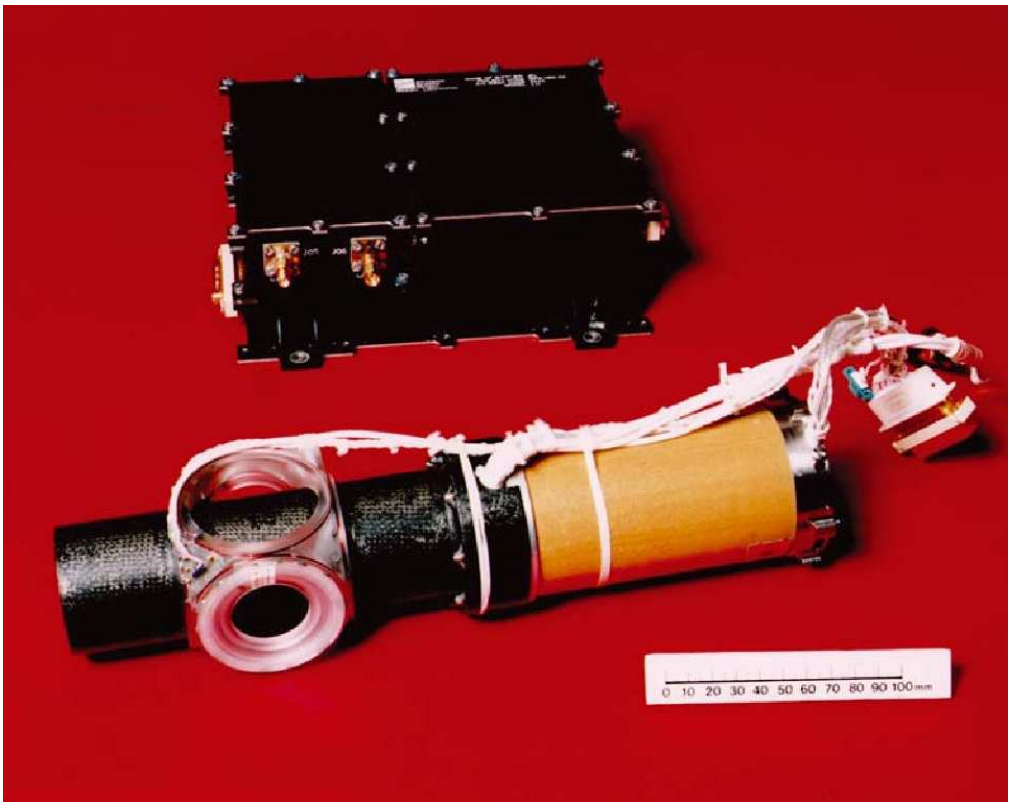

Figure A.3: *Picture of the scalar/vector helium magnetometer (bottom) and its electronics (top) (Dougherty et al., 2004).*

The fluxgate magnetometer allows for the best sampling of the presented magnetometers. It can reach sampling rates of up to 32 Hz. However, usually a lower sampling rate of ∼10 Hz is used, because the bandwidth to transmit data from Cassini to Earth is limited. The advantage of having a second system of magnetometers onboard Cassini is that the precision of the absolute measurement of the magnetic field can be enhanced. This is achieved through calibration of the FGM to the scalar helium magnetometer measurements. The noise of the FGM is given as $5\,\mathrm{pT}/\sqrt{\mathrm{Hz}}$ at 1 Hz and goes as f^{-1} in the respective power spectra (*Russell*, 1972). Dependent on the strength of the background magnetic field, the FGM works in different ranges with specific resolution given in Table A.2.

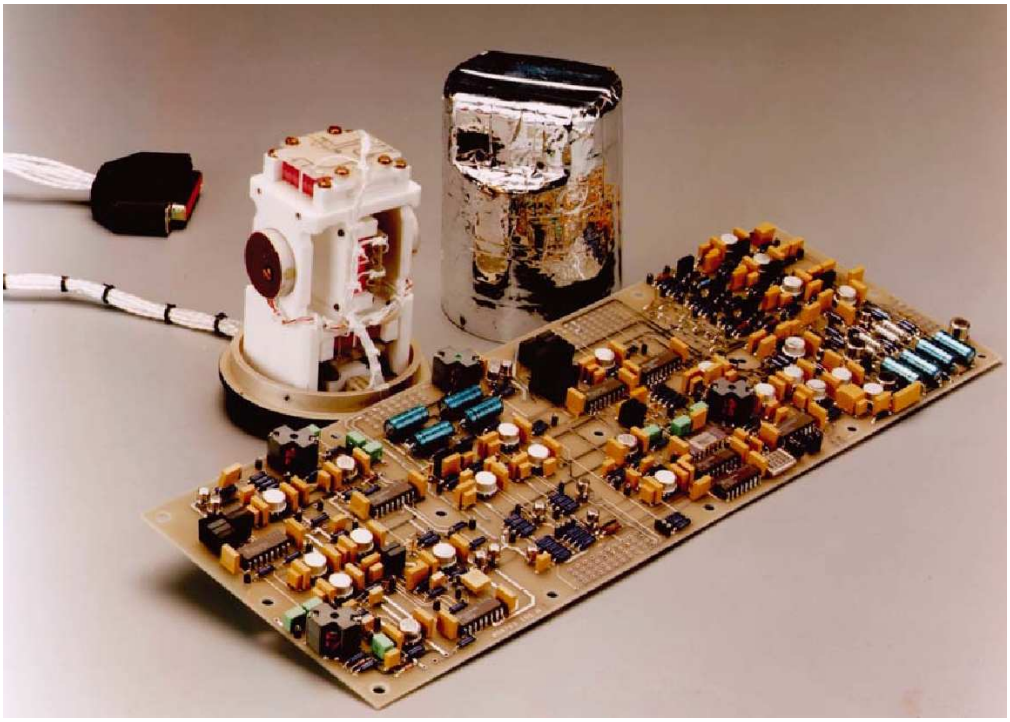

Figure A.4: *Picture of the fluxgate magnetometer (top) and its electronics (bottom) (Dougherty et al., 2004).*

APPENDIX B

Probability Density Functions of Measured Parameters

Any random variable x can be characterized by its probability density function (PDF). This function gives the probability p that the random variable x takes on a certain value x_i. Hence, the integral

$$\int \mathrm{d}x\, p(x) = 1 \tag{B.1}$$

is normalized because the probability that x takes an arbitrary value is 100%. If the PDF is given, one can calculate the statistical moments of the variable x. The first statistical moment

$$\langle x \rangle = \int \mathrm{d}x\, x\, p(x) \tag{B.2}$$

is the average value of the random variable. However, the mean value alone is not very meaningful. We also want to know about the spread of the random variable around the mean, i.e., the error of the mean. The general equation for statistical moments of order n is

$$\langle x^n \rangle = \int \mathrm{d}x\, x^n p(x)\ . \tag{B.3}$$

For a centered variable $x = x' - \langle x' \rangle$, Equation (B.3) gives the variance of the mean, $\sigma^2 = \langle x^2 \rangle$, for $n = 2$. The standard deviation σ, which is often used as an error estimate, is simply the square root of the variance. The statistical moments can be calculated for any order n and for a strictly stationary process, all of these moments must be time independent. We speak of a quasi-stationary process if the first two orders, mean and variance, are time independent. However, not all of the higher order moments are easily interpreted in a physical sense. In this

thesis, we deal with the normalized third order moment, i.e., the skewness

$$S = \frac{\langle x^3 \rangle}{\langle x^2 \rangle^{3/2}} \ , \tag{B.4}$$

which describes the asymmetry of the PDF with regards to the mean value, and the flatness

$$F = \frac{\langle x^4 \rangle}{\langle x^2 \rangle^{2}} \ , \tag{B.5}$$

which is the normalized fourth order moment describing the tails of the PDF. For a Gaussian or normal distribution with PDF

$$p(x) = \mathrm{e}^{-\frac{(x-\mu)^2}{2\sigma^2}} \ , \tag{B.6}$$

the mean μ and variance σ^2 give the center and the width of the function. Further, it can be shown that for a Gaussian distribution the skewness vanishes, $S = 0$, because the function is symmetric around the mean, and the flatness $F = 3$. Sometimes, the flatness is also called kurtosis or the excess kurtosis, $K = F - 3$, is used instead of the flatness. In case of a normal distribution we can use the following estimators for the mean μ and the variance σ^2:

$$\mu = \frac{1}{N}\sum_{i=1}^{N} x_i \qquad\qquad \sigma^2 = \frac{1}{N-1}\sum_{i=1}^{N}(x_i - \mu)^2 \ . \tag{B.7}$$

However, if the random variable is not normal distributed the such estimated mean value and variance might give misleading results. Here, a large skewness will mostly affect the estimate of the mean while the flatness leads to a wrong variance estimation. It is therefore strongly advised to check the PDF of the variable before using Equation (B.7).

A good approach is to compute the approximate PDF from the variable in form of a histogram. Figure B.1 (left) shows such histograms for the root mean square (RMS), δB, of magnetic fluctuations obtained in Saturn's magnetosphere from 10 min time series. The dotted line shows the Gaussian PDF, the blue line the distribution of the RMS and the black line the distribution of the logarithm of the RMS. We fitted a Gaussian to each distribution to compute their respective mean values and variances. Thus, we plot the normalized variables $(x - \mu)/\sigma$ so that the distributions can be compared to each other. From Figure B.1 (left), it can be seen that both distributions are non-Gaussian. However, comparing the values for skewness and flatness, we find that the logarithmic variable $\mathrm{RMS}_{\log}$ is much closer to a Gaussian than the variable RMS as shown in Table B.1. This shows that we can characterize the statistics of the random variable much better if we use Equation (B.7) with the logarithmically scaled variable, $\mathrm{RMS}_{\log}$, instead of the unscaled variable RMS.

Another way to visually inspect the PDF of the data is shown in Figure B.1 (right). These are so-called quantile-quantile plots (qq-plots) of the unscaled

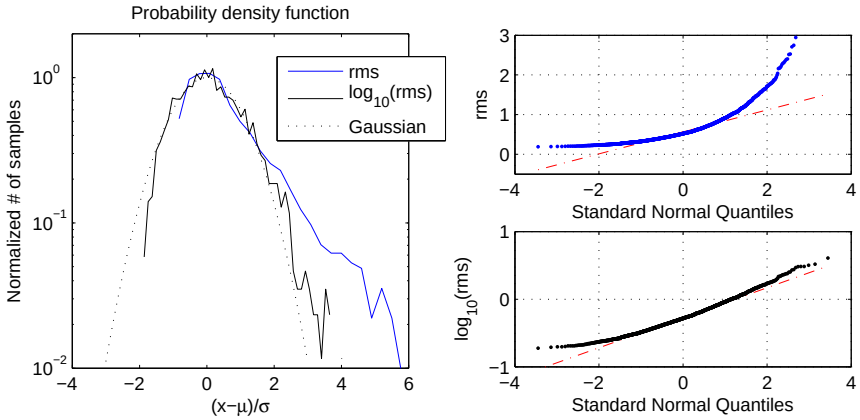

Figure B.1: *Left: Probability density functions of root mean square (RMS) of* 10 *min time series (blue line), the logarithm of the RMS (black line), and a Gaussian distribution (dotted line). Right: Quantile-quantile plots of the RMS (top) and the logarithm of the RMS (bottom) to visualize the difference to a normal distribution. A Gaussian distribution would result in a straight line depicted by the dash-dotted red line.*

	RMS	$\mathrm{RMS_{log}}$	Gaussian
Skewness	2.3	0.5	0
Kurtosis	11.9	3.0	3

Table B.1: *Skewness and flatness for variable RMS and logarithmic variable* $\mathrm{RMS_{log}}$ *as compared to values for a normal distribution.*

variable RMS (top) and the logarithmic variable $\mathrm{RMS_{log}}$ (bottom). To construct such a plot, the samples $x_1, x_2, \ldots, x_n$ of the random process are sorted by ascending value and then plotted next to each other at locations $[1, 2, \ldots, n]$. With the x-axis scaled such that the spacings between two successive points is inversely related to a Gaussian, any normal distribution results in a straight line as depicted by the red line in Figure B.1 (right). Clearly, the visual inspection of the qq-plots leads to the same result as the values in Table B.1 indicate.

For the data obtained in Saturn's magnetosphere, we find that the spectral power at a certain normalized wavenumber, $E(k_\perp \rho)$, is also nearly log-normal distributed. The same holds for the derived heating rates q_L and q_S or the magnetic field pressure at a fixed distance r to Saturn $P_B(r) = B(r)^2/(2\mu_0)$. In general, the flatness of the measured variables is slightly increased with respect to a normal distribution so that the error estimates, i.e., standard deviations, can be seen as conservative estimations. Therefore, we use geometrical averaging, i.e., computation of the mean and variance from logarithmically scaled variables, for these parameters in this thesis.

APPENDIX C

Numerical Evaluation of Power Spectral Density

In Chapter 4, we present and apply a numerical model to evaluate power spectral densities in frequency space, $P(f)$, from a given distribution of energy in $\mathbf{k}$-space. Here, we explain in detail the numerical scheme that we use for the calculation: Let us assume that we have an analytical expression $E(\mathbf{k})$, which defines the energy E for a wave vector $\mathbf{k}$. The wave vector is given in a coordinate system with the z-axis parallel to the background magnetic field $\mathbf{B}_0$, the x-axis in the plane spanned by the direction of the bulk plasma velocity $\mathbf{v}$ and $\mathbf{B}_0$, and the y-axis completing the right handed system. In case of critical balance, the energy distribution might, e.g., be given by Equations (4.27), (4.35), and (4.36):

$$E_{\mathrm{MHD}}(k_\perp, k_z) = \left(\frac{B_0^2}{L^{1/3}}\right) k_\perp^{-10/3} \exp\left(-L^{1/3}\frac{|k_z|}{k_\perp^{2/3}}\right) \tag{C.1}$$

$$E_{\mathrm{KAW}}(k_\perp, k_z) = \left(\frac{B_0^2}{L^{1/3}\rho_i^{1/3}}\right) k_\perp^{-11/3} \exp\left(-L^{1/3}\rho_i^{1/3}\frac{|k_z|}{k_\perp^{1/3}}\right) \tag{C.2}$$

$$E_{\mathrm{ED}}(k_\perp, k_z) = \left(\frac{B_0^2}{L^{1/3}\rho_i^{1/3}}\right) k_\perp^{-11/3} \exp\left(-L^{1/3}\rho_i^{1/3}\rho_e^{1/3}|k_z|\right) . \tag{C.3}$$

These equations are already normalized so that $E_{\mathrm{MHD}} = E_{\mathrm{KAW}}$ at $k_\perp\rho_i = 1$ and $E_{\mathrm{KAW}} = E_{\mathrm{ED}}$ at $k_\perp\rho_e = 1$, where ρ_i is the gyro radius of the ions under consideration (e.g. water group ions at Saturn) and ρ_e is the gyro radius of electrons.

The basic assumption for the applicability of the numerical evaluation is the validity of Taylor's frozen-in theorem, so that we can calculate the power spectral density in frequency space as

$$P_{ii}(f) = \frac{1}{v}\int_{-\infty}^{\infty} \mathrm{d}^3k'\, S_{ii}(\mathbf{k}')\,\delta\left(\frac{2\pi f}{v} - k_x'\right) . \tag{C.4}$$

Here, we use a primed coordinate system, where k'_x is parallel to the bulk plasma velocity $\mathbf{v}$. With respect to the familiar field-aligned coordinate system, in which $\mathbf{e}_z \| \mathbf{B}_0$, $\mathbf{e}_y$ perpendicular to both background magnetic field $\mathbf{B}_0$ and bulk plasma velocity $\mathbf{v}$, and $\mathbf{e}_x = \mathbf{e}_y \times \mathbf{e}_z$, the primed system is rotated about the y-axis by the angle θ and its components are given by

$$k'_x = k_x \sin(\theta) + k_z \cos(\theta) \tag{C.5}$$
$$k'_y = k_y \tag{C.6}$$
$$k'_z = -k_x \cos(\theta) + k_z \sin(\theta) \ . \tag{C.7}$$

S_{ii} is the spectral tensor with diagonal components

$$S_{xx}(\mathbf{k}) = \left(1 - \frac{k_x^2}{k_\perp^2}\right) T + \frac{k_x^2 k_z^2}{k_\perp^2 k^2} P \tag{C.8}$$
$$S_{yy}(\mathbf{k}) = \left(1 - \frac{k_y^2}{k_\perp^2}\right) T + \frac{k_y^2 k_z^2}{k_\perp^2 k^2} P \tag{C.9}$$
$$S_{zz}(\mathbf{k}) = \frac{k_\perp^2}{k^2} P \ . \tag{C.10}$$

The scalar functions T and P describe the toroidal and poloidal fluctuations, respectively. Here, we assume that

$$T = E \qquad \text{and} \qquad P = \gamma E \ , \tag{C.11}$$

where $\gamma = P_\parallel / P_\perp$ is the power anisotropy of the PSD. Inserting Equations (C.8)-(C.10) and (C.11) in Equation (C.4) we get

$$P_{xx}(f) = \frac{1}{v} \int_{-\infty}^{\infty} \mathrm{d}k'_y \mathrm{d}k'_z \left[\left(1 - \frac{k_x^2}{k_\perp^2}\right) E_{\mathrm{MHD}} + \frac{k_x^2 k_z^2}{k_\perp^2 k^2} \gamma E_{\mathrm{MHD}} \right]_{k'_x = \frac{2\pi f}{v}} \tag{C.12}$$
$$P_{yy}(f) = \frac{1}{v} \int_{-\infty}^{\infty} \mathrm{d}k'_y \mathrm{d}k'_z \left[\left(1 - \frac{k_y^2}{k_\perp^2}\right) E_{\mathrm{MHD}} + \frac{k_y^2 k_z^2}{k_\perp^2 k^2} \gamma E_{\mathrm{MHD}} \right]_{k'_x = \frac{2\pi f}{v}} \tag{C.13}$$
$$P_{zz}(f) = \frac{1}{v} \int_{-\infty}^{\infty} \mathrm{d}k'_y \mathrm{d}k'_z \, \frac{k_\perp^2}{k^2} \gamma E_{\mathrm{MHD}} |_{k'_x = \frac{2\pi f}{v}} \ . \tag{C.14}$$

For the sake of brevity, we used the unprimed coordinates in Equations (C.12)-(C.14). To include the empirical damping term according to Equation (4.50) (*Alexandrova et al.*, 2012), Equations (C.12)-(C.14) are simply multipled with $\exp(-k_\perp \rho_e)$. To numerically integrate these equations for the computation of power at a given frequency f, we now define a two dimensional grid in the

$y'-z'$-plane. This grid should be logarithmically spaced so that we define

$$k'_x = \frac{2\pi f}{v} \tag{C.15}$$

$$k'_{y,i} = 10^{\,k_{\min}+(i-1)\cdot\frac{k_{\max}-k_{\min}}{N}} \tag{C.16}$$

$$k'_{z,j} = \begin{cases} -k'_{y,N+1-j} & \text{for} j \le N \\ k'_{y,j-N} & \text{for} j > N \end{cases} , \tag{C.17}$$

where $i \in \{1 \dots N\}$, $j \in \{-N \dots -1, 1 \dots N\}$ and $k_{\min}$ and $k_{\max}$ determine the logarithmical boundaries of the integration. The unprimed coordinates may thus be written as

$$k_{x,j} = k'_x \sin(\theta) - k'_{z,j} \cos(\theta) \tag{C.18}$$

$$k_{y,i} = k'_{y,i} \tag{C.19}$$

$$k_{z,j} = k'_x \cos(\theta) + k'_{z,j} \cos(\theta) \; . \tag{C.20}$$

The integration is subsequently computed as a simple (left) Riemann summation using $\mathrm{d}k'_l = \Delta k'_{l,n} = k'_{l,n} - k'_{l,n-1}$, so that we may write

$$\begin{aligned} P_{xx}(f) = {} & \frac{B_0^2}{vL^{1/3}} \sum_{i=1}^{N-1} \sum_{j=-N}^{N-1} \Delta k'_{y,i}\, \Delta k'_{z,j} \\ & \cdot \left[\frac{k_y'^2}{\left[(k'_x \sin(\theta) - k'_z \cos(\theta))^2 + k_y'^2\right]^2} + \gamma \frac{k_x'^2 \left(k_x^* \cos(\theta) + k'_z \sin(\theta)\right)^2}{\left((k'_x \sin(\theta) - k'_z \cos(\theta))^2 + k_y'^2\right)^2 k'^2} \right] \\ & \cdot \exp\left(- \left[(k'_x \sin(\theta) - k'_z \cos(\theta))^2 + k_y'^2\right] \rho_e \right) \begin{cases} E'_{\mathrm{MHD}} & \text{if } k_\perp < \rho_i^{-1} \wedge k_\perp > L^{-1} \\ E'_{\mathrm{KAW}} & \text{if } \rho_i^{-1} < k_\perp < \rho_e^{-1} \\ E'_{\mathrm{ED}} & \text{if } k_\perp > \rho_e^{-1} \end{cases} \end{aligned} \tag{C.21}$$

$$\begin{aligned} P_{yy}(f) = {} & \frac{B_0^2}{vL^{1/3}} \sum_{i=1}^{N-1} \sum_{j=-N}^{N-1} \Delta k'_{y,i}\, \Delta k'_{z,j} \\ & \cdot \left[\frac{k_x'^2}{\left[(k'_x \sin(\theta) - k'_z \cos(\theta))^2 + k_y'^2\right]^2} + \gamma \frac{k_y'^2 \left(k_x^* \cos(\theta) + k'_z \sin(\theta)\right)^2}{\left[(k'_x \sin(\theta) - k'_z \cos(\theta))^2 + k_y'^2\right]^2 k'^2} \right] \\ & \cdot \exp\left(- \left[(k'_x \sin(\theta) - k'_z \cos(\theta))^2 + k_y'^2\right] \rho_e \right) \begin{cases} E'_{\mathrm{MHD}} & \text{if } k_\perp < \rho_i^{-1} \wedge k_\perp > L^{-1} \\ E'_{\mathrm{KAW}} & \text{if } \rho_i^{-1} < k_\perp < \rho_e^{-1} \\ E'_{\mathrm{ED}} & \text{if } k_\perp > \rho_e^{-1} \end{cases} \end{aligned} \tag{C.22}$$

and

$$P_{zz}(f) = \frac{B_0^2}{vL^{1/3}} \sum_{i=1}^{N-1} \sum_{j=-N}^{N-1} \Delta k'_{y,i}\, \Delta k'_{z,j} \cdot \gamma \frac{\left[(k'_x \sin(\theta) - k'_z \cos(\theta))^2 + k'^2_y\right]}{k'^2} \tag{C.23}$$
$$\cdot \exp\left(-\left[(k'_x \sin(\theta) - k'_z \cos(\theta))^2 + k'^2_y\right] \rho_e\right) \begin{cases} E'_{\mathrm{MHD}} & \text{if } k_\perp < \rho_i^{-1} \wedge k_\perp > L^{-1} \\ E'_{\mathrm{KAW}} & \text{if } \rho_i^{-1} < k_\perp < \rho_e^{-1} \\ E'_{\mathrm{ED}} & \text{if } k_\perp > \rho_e^{-1} \end{cases}$$

where

$$E'_{\mathrm{MHD}} = \left[(k'_x \sin(\theta) - k'_z \cos(\theta))^2 + k'^2_y\right]^{-5/3} \cdot \exp\left(-L^{1/3} \frac{|k'_x \cos(\theta) + k'_z \sin(\theta)|}{\left((k'_x \sin(\theta) - k'_z \cos(\theta))^2 + k'^2_y\right)^{1/3}}\right) \tag{C.24}$$

$$E'_{\mathrm{KAW}} = \rho_i^{-1/3} \left[(k'_x \sin(\theta) - k'_z \cos(\theta))^2 + k'^2_y\right]^{-11/6} \cdot \exp\left(-L^{1/3} \rho_i^{1/3} \frac{|k'_x \cos(\theta) + k'_z \sin(\theta)|}{\left((k'_x \sin(\theta) - k'_z \cos(\theta))^2 + k'^2_y\right)^{1/6}}\right) \tag{C.25}$$

$$E'_{\mathrm{ED}} = \rho_i^{-1/3} \left[(k'_x \sin(\theta) - k'_z \cos(\theta))^2 + k'^2_y\right]^{-11/6} \cdot \exp\left(-L^{1/3} \rho_i^{1/3} \rho_e^{1/3} \cdot |k'_x \cos(\theta) + k'_z \sin(\theta)|\right) \tag{C.26}$$

are the energy distributions in the rotated frame.

The results of this integration were verified by computation of the integral using the Simpson rule, which yielded only negligible higher accuracy but needed much more CPU time. To calculate a PSD in the solar wind from 10^{-3} Hz up to 1 Hz Equations (C.21)-(C.23) are evaluated for each frequency f_i. As suitable parameters we use $k_{\min} = -10$, $k_{\max} = -1$ and $N = 1000$ to get a smooth spectral shape. For plasmas with outer scales L, velocities v, and gyro radii ρ on different orders of magnitudes than those found in the solar wind, the values of these parameters will differ accordingly. The higher the resolution N, the more accurate is the numerical integration. Artefacts are usually observed as oscillations in the highest resolved frequencies.

For the sake of completeness we also provide the Matlab code, which was used to numerically calculate the reduced spectra. Here, the user has the choice between different functions to describe the critically balanced cascade. Besides the exponential function used in the derivation in this section, the user may choose a Gaussian distribution around the critical balance or a Heviside function that cuts all parallel wave vectors larger than those given by the critical balance. All these functions lead to the same scaling as is shown in Figure C.1. Here, we show the resulting PSD for field-to-flow angles $\theta = [0°, 1°, 5°, 20°, 90°]$ based on an exponential function (solid lines), a Gaussian (dot-dashed lines), and a Heaviside function (dashed lines). Besides a visible difference between the spectra for $\theta = 0°$ and $\theta = 1°$], all spectra have a similar scaling and show the

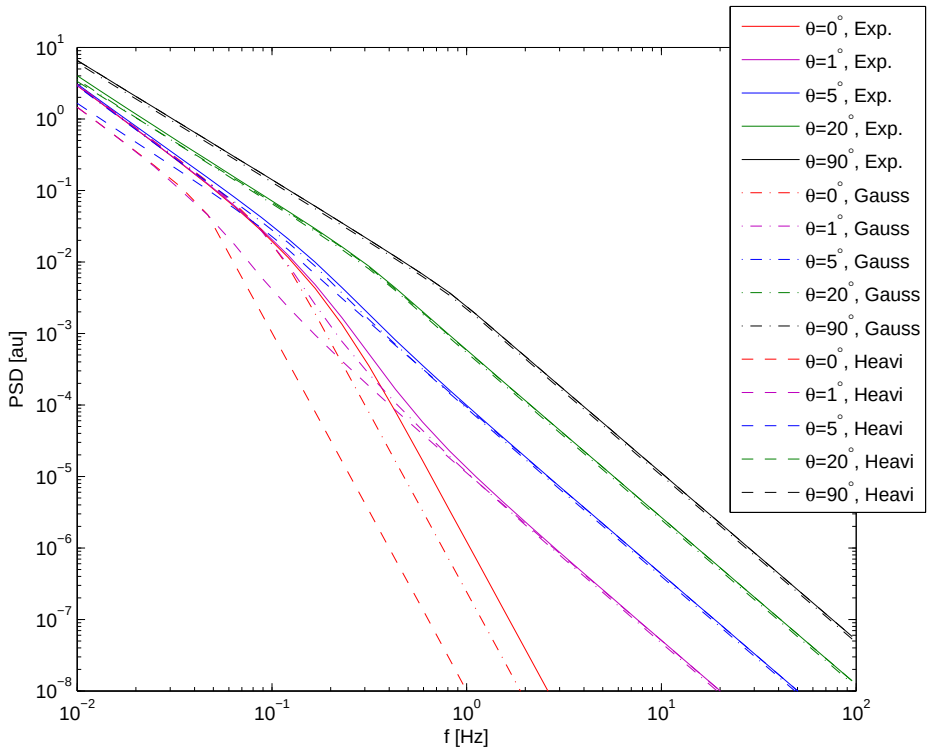

Figure C.1: *Comparison of spectra controlled by different functions containing the critical balance for several field-to-flow angles θ. Solid lines show the results for an exponential function, dot-dashed lines the results for a Gaussian and dashed lines the results for a Heaviside function.*

same characteristics discussed for the case of the exponential function.

```
1  %% Numerically integrates P_i(f,\theta)=\int dk^3 E_i(k) ...
       \▵(2\pi f - k*v) for given kx(=2pi f/v, kx is in rotated ...
       frame with kx||v) and \theta under assumption of Taylor's ...
       hypothesis. Model of P_i(k) is critically balanced with ...
       k_para¬L^(1/3)k_perp^(2/3) in inertial range and ...
       k_\para¬L^(1/3)\rho^(1/3)k_\perp^(1/3) in kinetic range. ...
       This code is introduced and discussed in detail in: von ...
       Papen, 2014, PhD thesis, Cologne, Germany. More info on the ...
       topic can be found in Cho et al., 2002 (ApJ), Forman et ...
       al., 2011 (ApJ), or Wicks et al., 2012 (ApJ)
2  %%
3  %%
4  %%  Input:
5  %%      f       Frequncy in Hz
6  %%      theta   Field-to-flow angle in degrees
7  %%      n       Number of nodes in one dimension
8  %%      fun     function to evaluate ( 1=exp, 2=expdamp, ... )
9  %%      L       Outer scale in m
10 %%      rho     Gyro radius (or else) in m
11 %%      v       Plasma bulk velocity in m/s
12 %%      va      Alfven velocity in m/s
13 %%      B       Magnetic field strength in nT
14 %%      bounds  Boundary in log10 for integration ( bounds = ...
       [kmin kmax] )
15 %%      ratioTP Ratio between toroidal T and poloidal P ...
       fluctuations
16 %%      rhoe    Electron gyro radius (or else)
17 %%      si_in   Spectral index in [MHD kinetic] range
18 %%      cb_in   Critical balance exponent in [MHD kinetic] range
19 %%
20 %%  Output:
21 %%      P       PSD in nT^2/Hz
22 %%
23 %%  Author: Michael von Papen
24 %%  Date: 04.08.2014
25 %%
26 %% Notice: Please acknowledge the use of this code in any ...
       publications:
27 %% Reference: von Papen, M., 2014: Turbulence in Saturn's ...
       Magnetosphere and Forward Modeling of Reduced Spectra from ...
       Three-Dimensional Wave Vector Space, PhD thesis, Cologne
28 %%
29 %% I would be pleased to receive a copy of such publications ...
       under:
30 %%  Michael von Papen
31 %%  Institute of Geophysics
32 %%  Pohligstr. 3
33 %%  50969 Cologne, Germany
34 %%  E-mail: vonpapen@geo.uni-koeln.de
35 %% -----------------------------------------------
36
37 function  [ P ] = cbspec ( f, theta, n, fun, L, rho, v, va, B, ...
       bounds, ratioTP, rhoe, si_in, cb_in)
38
```

```
39
40 %% Check Input
41 if nargin<14; cb_in=[2/3 1/3]; end
42 if nargin<13; si_in=[-10/3 -11/3]; end
43 if nargin<11; ratioTP=0; end
44 if nargin<10; bounds=[-10 -2]; end
45 if nargin<9; B=1; end
46 if nargin<8; va=60e3; end
47 if nargin<7; v=600e3; end
48 if nargin<6; rho=1e5; end
49 if nargin<5; L0=1e10; end
50 if nargin<4; fun=1; end
51 if nargin<3; n=500; end
52 if nargin<2; theta=[0 90]; end
53 if nargin<12; rhoe=rho/42.85; end
54
55
56 %% Wave vector in rotated coordinate system
57 kix=2*pi*f/v;
58
59 %% Basic Parameter
60 si=si_in(1); %-10/3->k^{-5/3}
61 si2=si_in(2); %-11/3->k^{-7/3}
62 cb=cb_in(1); % 2/3->alfven
63 cb2=cb_in(2); %1/3->KAW
64
65
66 %% K-space gridpoints
67 % Set boundaries a little bit wider than kmin,kmax for ...
       numerical reasons.
68 % Later everything outside [kmin,kmax] will be disregarded
69 kmin=bounds(1);
70 kmax=bounds(2);
71
72
73 ky=10.^[kmin+(0:n-1)*(kmax-kmin)/(n)];
74 dky=[ky(2:end) 2*10^kmax]-ky;
75 %nz log verteilt auf pos UND neg Achse
76 kiz=repmat([-ky(end:-1:1) ky],n,1);
77 dkiz=repmat([dky(end:-1:1) dky],n,1);
78 ky=ky(ones(1,2*n),:)'; % ≤> ky=repmat(ky',1,2*n);
79 dky=dky(ones(1,2*n),:)';
80
81 %% Ion-cyclotron frequency (wic) cut-off. All k_para ¬ ...
       w_ic/V_A are subject to ion-cyclotron damping. Thus, ...
       parallel scales cannot reach k_para >> w_ic/V_A
82 wic=1.6e-19*B/1.67e-27; %wic for protons
83
84 %% Set output variable
85 if ratioTP ≠0
86   if isopol==1
87     P=zeros(6,length(kix),length(theta));
88   else
89     P=zeros(4,length(kix),length(theta));
90   end
```

```
91  else
92      P=zeros(length(kix),length(theta));
93  end
94
95  %% Begin with loop over theta
96  for k=1:length(theta)
97
98
99    %% Begin loop over frequency
100   for i=1:length(kix)
101
102     %% Calculate PSD at z
103     if theta(k)==0
104       kx=kix(i)*sind(theta(k))-kiz.*cosd(theta(k)); %=kx in ...
              unrotated system
105       %ky=kiy in unrotated system
106       kz=kix(i)*cosd(theta(k))+kiz.*sind(theta(k)); %=kz in ...
              unrotated system
107     else
108       kx=kix(i)*sind(theta(k)) - kiz.*cosd(theta(k)) + ...
              kix(i).*cosd(theta(k))^2/sind(theta(k)); %=kx in ...
              unrotated system with kiz=0 on x-axis
109       %ky=kiy in unrotated system
110       kz=kiz.*sind(theta(k)); %=kz in unrotated system with ...
              kiz=0 on x-axis
111     end
112
113     kern=zeros(n,2*n);
114
115     kp2=ky.^2+kx.^2; % k_perp^2
116     kabs2=kp2+kz.^2; % |k|
117
118     %% Equations written in unprimed coordinates for the sake ...
          of brevity, but integration is done over primed ...
          variables, which is why dkiy and dkiz is used.
119
120     %% Single components Alfven cascade
121     i1=find(kp2 <= 1/rho^2 & kp2 > 1/L^2 & kabs2 <= ...
          10^(2*kmax)); % take out '& kp2 > 1/L^2' when checking ...
          for fmax
122     switch fun
123       case 1 %'exp'
124       kern( i1 ) = kp2(i1).^(si/2) .* exp(-L^(1-cb) .* abs( ...
              kz(i1) ) ./ kp2(i1).^(cb/2) ) .* dky(i1).*dkiz(i1);
125       case 2 %'expdamp' for Ti=Te => rho_e = sqrt(me/mi) * rho_i
126       kern( i1 ) = kp2(i1).^(si/2) .* exp( - L^(1-cb) .* abs( ...
              kz(i1) ./ kp2(i1).^(cb/2) ) - sqrt( kp2(i1) ) * rhoe ...
              - abs(kz(i1)) * va / wic ) .* dky(i1) .* dkiz(i1);
127       case 3 %'gauss'
128       kern( i1 ) = kp2(i1).^(si/2) .* exp( - (L^(1-cb) * abs( ...
              kz(i1) ) ./ kp2(i1).^(cb/2) - 1 ).^2 ) .* dky(i1) .* ...
              dkiz(i1) / sqrt(pi);
129       case 4 %'gaussdamp'
130       kern( i1 ) = kp2(i1).^(si/2) .* exp( - ( L^(1-cb) * ...
              abs(kz(i1)) ./ kp2(i1).^(cb/2) - 1 ).^2 - ...
```

```
            sqrt(kp2(i1)) * rhoe - abs(kz(i1)) * va / wic ) .* ...
            dky(i1) .* dkiz(i1) / sqrt(pi);
        case 5 %'heavi'
        i2 = find( L^(1-cb) * abs(kz(i1) ./ kp2(i1).^(cb/2) ) ≤ ...
            1 );
        kern( i1(i2) ) = kp2(i1(i2)).^(si/2) .* dky(i1(i2)) .* ...
            dkiz(i1(i2));
    end


    %% Single components KAW cascade
    i1=find(kp2 > 1/rho^2 & kp2 > 1/L^2 & kabs2 ≤ 10^(2*kmax) ...
        & kp2 ≤ 1/rhoe^2);
    switch fun
        case 1 %'exp'
        kern( i1 ) = rho^(si2-si) .* kp2(i1).^(si2/2) .* exp( ...
            -L^(1-cb) * rho^(cb-cb2) * abs(kz(i1)) ./ ...
            kp2(i1).^(cb2/2) ) .* dky(i1) .* dkiz(i1);
        case 2 %'expdamp' for Ti=Te => rho_e=sqrt(me/mi)*rho_i
        kern( i1 ) = rho^(si2-si) .* kp2(i1).^(si2/2) .* exp( ...
            -L^(1-cb) * rho^(cb-cb2) * abs(kz(i1)) ./ ...
            kp2(i1).^(cb2/2) - sqrt(kp2(i1)) * rhoe - abs(kz(i1)) ...
            * va / wic ) .* dky(i1) .* dkiz(i1);
        case 3 %'gauss'
        kern( i1 ) = rho^(si2-si) .* kp2(i1).^(si2/2) .* exp( ...
            -(L^(1-cb) * rho^(cb-cb2) * abs(kz(i1)) ./ ...
            kp2(i1).^(cb2/2) - 1 ).^2 ) .* dky(i1) .* dkiz(i1) / ...
            sqrt(pi);
        case 4 %'gaussdamp'
        kern( i1 ) = rho^(si2-si) .* kp2(i1).^(si2/2) .* exp( ...
            -(L^(1-cb) * rho^(cb-cb2) * abs(kz(i1)) ./ ...
            kp2(i1).^(cb2/2) - 1 ).^2 - sqrt(kp2(i1)) * rhoe - ...
            abs(kz(i1)) * va / wic ) .* dky(i1) .* dkiz(i1) / ...
            sqrt(pi);
        case 5 %'heavi'
        i2 = find( L^(1-cb) * rho^(cb-cb2) * abs(kz(i1)) ./ ...
            kp2(i1).^(cb2/2) ≤ 1 );
        kern( i1(i2) ) = rho^(si2-si) .* kp2(i1(i2)).^(si2/2) .* ...
            dky(i1(i2)) .* dkiz(i1(i2));
    end

    %% Single components of cascade at electron scales
    i1=find(kp2 > 1/rhoe^2 & kabs2 ≤ 10^(2*kmax));
    switch fun
        case 1 %'exp'
        kern( i1 ) = rho^(si2-si) .* kp2(i1).^(si2/2) .* exp( ...
            -L^(1-cb) * rho^(cb-cb2) * abs(kz(i1)) * rhoe^cb2 ) ...
            .* dky(i1) .* dkiz(i1);
        case 2 %'expdamp' for Ti=Te => rho_e=sqrt(me/mi)*rho_i
        kern( i1 ) = rho^(si2-si) .* kp2(i1).^(si2/2) .* exp( ...
            -L^(1-cb) * rho^(cb-cb2) * abs(kz(i1)) * rhoe^cb2 - ...
            sqrt(kp2(i1)) * rhoe - abs(kz(i1)) * va / wic) .* ...
            dky(i1) .* dkiz(i1);
        case 3 %'gauss'
        kern( i1 ) = rho^(si2-si) .* kp2(i1).^(si2/2) .* exp( ...
```

```
            -(L^(1-cb) * rho^(cb-cb2) * abs(kz(i1)) * rhoe^cb2 - ...
            1 ).^2 ) .* dky(i1) .* dkiz(i1) / sqrt(pi);
        case 4 %'gaussdamp'
        kern( i1 ) = rho^(si2-si) .* kp2(i1).^(si2/2) .* exp( ...
            -(L^(1-cb) * rho^(cb-cb2) * abs(kz(i1)) * rhoe^cb2 - ...
            1 ).^2 - sqrt(kp2(i1)) * rhoe - abs(kz(i1)) * va / ...
            wic ) .* dky(i1) .* dkiz(i1) / sqrt(pi);
        case 5 %'heavi'
        i2 = find( L^(1-cb) * rho^(cb-cb2) * abs(kz(i1)) * ...
            rhoe^cb2 ≤ 1 );
        kern( i1(i2) ) = rho^(si2-si) .* kp2(i1(i2)).^(si2/2) .* ...
            dky(i1(i2)) .* dkiz(i1(i2));
      end


      %% Full version with Toroidal and Poloidal parts
      % Sum up to get power for one ky value
      if ratioTP ≠ 0
        Tor = ratioTP / (1+ratioTP) * kern ./ kp2;

        %% Add Spectra to PSD
        P(1,i,k)=sum(sum( ky.^2.*Tor + (kx.*kz).^2 ./ kp2 .* Pol ));
        P(2,i,k)=sum(sum( kx.^2.*Tor + (ky.*kz).^2 ./ kp2 .* Pol ));
        P(3,i,k)=sum(sum( kp2 .* Pol ));
        P(4,i,k)=sum(P(1:3,i,k));
      else
        P(i,k)=sum(sum(2*kern));
      end
    end
  end

  %% Multiply with B^2/v/L^(1-cb_in(1)) for PSD in nT^2/Hz
  P=B^2/v/L^(1-cb_in(1)).*P;
```

Bibliography

Achilleos, N., C. S. Arridge, C. Bertucci, C. M. Jackman, M. K. Dougherty, K. K. Khurana, and C. T. Russell (2008), Large-scale dynamics of Saturn's magnetopause: Observations by Cassini, *Journal of Geophysical Research*, *113*(A11), 1–14. 37, 39, 40, 60, 141

Achilleos, N., P. Guio, and C. S. Arridge (2010), A model of force balance in Saturn's magnetodisc, *Monthly Notices of the Royal Astronomical Society*, *401*(4), 2349–2371. 39, 51, 52, 100

Alexandrova, O., and J. Saur (2008), Alfvén vortices in Saturn's magnetosheath: Cassini observations, *Geophysical Research Letters*, *35*, L15,102, doi:10.1029/2008GL034411. 39

Alexandrova, O., V. Carbone, P. Veltri, and L. Sorriso-Valvo (2008a), Small-scale energy cascade of the solar wind turbulence, *The Astrophysical Journal*, *674*(2), 1153–1157, doi:10.1086/524056. 12, 31, 32, 55, 68, 76, 77, 78, 80, 102, 103

Alexandrova, O., C. Lacombe, and A. Mangeney (2008b), Spectra and anisotropy of magnetic fluctuations in the Earth's magnetosheath: Cluster observations, *Annales Geophysicae*, *26*(11), 3585–3596, doi:10.5194/angeo-26-3585-2008. 55

Alexandrova, O., J. Saur, C. Lacombe, A. Mangeney, J. Mitchell, S. Schwartz, and P. Robert (2009), Universality of solar-wind turbulent spectrum from MHD to electron scales, *Physical Review Letters*, *103*(16), 14–17, doi:10.1103/PhysRevLett.103.165003. 28, 71, 75, 89

Alexandrova, O., C. Lacombe, A. Mangeney, R. Grappin, and M. Maksimovic (2012), Solar wind turbulent spectrum at plasma kinetic scales, *The Astrophysical Journal*, *760*(2), 121, doi:10.1088/0004-637X/760/2/121. 24, 28, 30, 70, 75, 91, 114, 122, 138, 139, 144, 158

Alexandrova, O., C. H. K. Chen, L. Sorriso-Valvo, T. S. Horbury, and S. D. Bale (2013), Solar wind turbulence and the role of ion instabilities, *Space Science Reviews*, *178*(2-4), 101–139, doi:10.1007/s11214-013-0004-8. 71, 141

André, N., M. K. Dougherty, C. T. Russell, J. S. Leisner, and K. K. Khurana (2005), Dynamics of the Saturnian inner magnetosphere: First inferences from the Cassini magnetometers about small-scale plasma transport in the magnetosphere, *Geophysical Research Letters*, *32*(14), 1–5, doi: 10.1029/2005GL022643. 49

André, N., et al. (2007), Magnetic signatures of plasma-depleted flux tubes in the Saturnian inner magnetosphere, *Geophysical Research Letters*, *34*, L14,108, doi:10.1029/2007GL030374. 49, 50, 64, 68, 89

Andrews, D. J., A. J. Coates, S. W. H. Cowley, M. K. Dougherty, L. Lamy, G. Provan, and P. Zarka (2010), Magnetospheric period oscillations at Saturn: Comparison of equatorial and high latitude magnetic field periods with north and south Saturn kilometric radiation periods, *Journal of Geophysical Research*, *115*(A12252), doi:10.1029/2010JA015666. 46, 47, 48, 51, 52, 61, 83, 101, 103

Andrews, D. J., S. W. H. Cowley, M. K. Dougherty, L. Lamy, G. Provan, and D. J. Southwood (2012), Planetary period oscillations in Saturn's magnetosphere: Evolution of magnetic oscillation properties from southern summer to post-equinox, *Journal of Geophysical Research*, *117*(A4), A04,224, doi: 10.1029/2011JA017444. 46, 47, 51

Argoul, F., A. Arnéodo, G. Grasseau, Y. Gagne, E. J. Hopfinger, and U. Frisch (1989), Wavelet analysis of turbulence reveals the multifractal nature of the Richardson cascade, *Nature*, *338*(2), 51 – 53, doi:10.1038/338051a0. 11

Armstrong, J. W., and B. J. Rickett (1995), Electron density power spectrum in the local interstellar medium, *The Astrophysical*, *443*, 209–221, doi:10.1086/175515. 19

Arridge, C. S., C. T. Russell, K. K. Khurana, N. Achilleos, N. André, A. M. Rymer, M. K. Dougherty, and A. J. Coates (2007), Mass of Saturn's magnetodisc: Cassini observations, *Geophysical Research Letters*, *34*(9), L09,108, doi:10.1029/2006GL028921. 50, 51

Arridge, C. S., K. K. Khurana, C. T. Russell, D. J. Southwood, N. Achilleos, M. K. Dougherty, A. J. Coates, and H. K. Leinweber (2008a), Warping of Saturn's magnetospheric and magnetotail current sheets, *Journal of Geophysical Research*, *113*, A08,217, doi:10.1029/2007JA012963. 39, 40, 41, 51, 61, 63, 85

Arridge, C. S., C. T. Russell, K. K. Khurana, N. Achilleos, S. W. H. Cowley, M. K. Dougherty, D. J. Southwood, and E. J. Bunce (2008b), Saturn's magnetodisc current sheet, *Journal of Geophysical Research*, *113*, A04,214, doi:10.1029/2007JA012538. 51, 70

Arridge, C. S., et al. (2011), Periodic motion of Saturn's nightside plasma sheet, *Journal of Geophysical Research*, *116*(A11), 1–22, doi:10.1029/2011JA016827. 48

Bagenal, F., and P. A. Delamere (2011), Flow of mass and energy in the magnetospheres of Jupiter and Saturn, *Journal of Geophysical Research*, *116*, A05,209, doi:10.1029/2010JA016294. 3, 38, 41, 43, 81, 83, 103, 131, 141

Bagenal, F., and J. D. Sullivan (1981), Direct plasma measurements in the Io torus and inner magnetosphere of Jupiter, *Journal of Geophysical Research*, *86*(A10), 8447–8466, doi:10.1029/JA086iA10p08447. 43

Batchelor, G. K., and A. A. Townsend (1949), The nature of turbulent motion at large wave-numbers, *Proceedings of the Royal Society of London A*, *199*(1057), 238–255, doi:10.1098/rspa.1949.0136. 10

Baumjohann, W., and R. A. Treumann (1997), *Basic space plasma physics*, Imperial College Press, London. 13, 14, 22, 23, 60

Bavassano Cattaneo, M. B., G. Moreno, G. Russo, and J. D. Richardson (2000), MHD turbulence in Saturn's magnetosheath downstream of a quasi-parallel bow shock, *Journal of Geophysical Research*, *105*(A10), 23,141–23,151, doi:10.1029/2000JA000093. 39

Belcher, J. W., and L. Davis (1971), Large-amplitude Alfvén waves in the Interplanetary Medium, 2, *Journal of Geophysical Research*, *76*(16), 3534, doi:10.1029/JA076i016p03534. 14, 28, 31

Bevington, P. R., and D. K. Robinson (2003), *Data reduction and error analysis for the physical sciences*, 3 ed., McGraw-Hill, New York. 96, 97

Bieber, J. W., J. Chen, W. H. Matthaeus, and C. W. Smith (1993), Long-term variations of interplanetary magnetic field spectra with implications for cosmic ray modulation, *Journal of Geophysical Research*, *98*(A3), 3585–3603, doi:10.1029/92JA02566. 54, 55

Bieber, J. W., W. Wanner, and W. H. Matthaeus (1996), Dominant two-dimensional solar wind turbulence with implications for cosmic ray transport, *Journal of Geophysical Research*, *101*(A2), 2511–2522, doi:10.1029/95JA02588. 18, 59, 110, 112, 126

Boldyrev, S., and J. C. Perez (2012), Spectrum of Kinetic-Alfvén Turbulence, *The Astrophysical Journal*, *758*(2), L44, doi:10.1088/2041-8205/758/2/L44. 26, 76, 77, 102, 135, 144

Bourouaine, S., O. Alexandrova, E. Marsch, and M. Maksimovic (2012), On spectral breaks in the power spectra of magnetic fluctuations in fast solar wind between 0.3 and 0.9 AU, *The Astrophysical Journal*, *749*(2), 102, doi:10.1088/0004-637X/749/2/102. 20, 24, 59, 75

Bruno, R., and V. Carbone (2005), The solar wind as a turbulence laboratory, *Living Reviews in Solar Physics*, *2*(4), doi:10.12942/lrsp-2005-4. 18, 56, 66

Bruno, R., V. Carbone, L. Sorriso-Valvo, and B. Bavassano (2003), Radial evolution of solar wind intermittency in the inner heliosphere, *Journal of Geophysical Research*, *108*(A3), 1130, doi:10.1029/2002JA009615. 12, 31

Bunce, E. J., S. W. H. Cowley, I. I. Alexeev, C. S. Arridge, M. K. Dougherty, J. D. Nichols, and C. T. Russell (2007), Cassini observations of the variation of Saturn's ring current parameters with system size, *Journal of Geophysical Research*, *112*(A10), 1–21, doi:10.1029/2007JA012275. 46, 57

Bunce, E. J., et al. (2014), Cassini nightside observations of the oscillatory motion of Saturn's northern auroral oval, *Journal of Geophysical Research: Space Physics*, *119*(5), 3528–3543, doi:10.1002/2013JA019527. 101

Burch, J. L., J. Goldstein, T. W. Hill, D. T. Young, F. J. Crary, A. J. Coates, N. André, W. S. Kurth, and E. C. Sittler (2005), Properties of local plasma injections in saturn's magnetosphere, *Geophys. Res. Lett*, *32*, L14S02, doi:10.1029/2005GL022611. 49

Burch, J. L., A. D. DeJong, J. Goldstein, and D. T. Young (2009), Periodicity in Saturn's magnetosphere: Plasma cam, *Geophysical Research Letters*, *36*(14), L14,203, doi:10.1029/2009GL039043. 83, 90, 101, 103, 143

Burlaga, L. F. (1992), Multifractal structure of the magnetic field and plasma in recurrent streams at 1 AU, *Journal of Geophysical Research*, *97*(A4), 4283–4293, doi:10.1029/91JA03027. 11, 31, 77

Burton, M. E., M. K. Dougherty, and C. T. Russell (2010), Saturn's internal planetary magnetic field, *Geophysical Research Letters*, *37*(24), 3–7, doi:10.1029/2010GL045148. 46, 66

Carbary, J. F. (2013), Longitude dependences of Saturn's ultraviolet aurora, *Geophysical Research Letters*, *40*(10), 1902–1906, doi:10.1002/grl.50430. 101, 103

Carbary, J. F., and D. G. Mitchell (2013), Periodicities in Saturn's magnetosphere, *Reviews of Geophysics*, *51*, 1–30, doi:10.1002/rog.20006. 44, 83, 101

Carbone, V., P. Veltri, and R. Bruno (1995), Experimental evidence for differences in the extended self-similarity scaling laws between fluid and magnetohydrodynamic turbulent flows, *Physical review letters*, *75*(17), 3110–3113, doi:10.1103/PhysRevLett.75.3110. 11

Carr, T. D., M. D. Desch, and J. K. Alexander (1983), *Phenomenology of magnetospheric radio emissions*, pp. 226–284, Cambridge University Press. 44

Cassidy, T. A., and R. E. Johnson (2010), Collisional spreading of Enceladus' neutral cloud, *Icarus*, *209*(2), 696–703, doi:10.1016/j.icarus.2010.04.010. 38, 48, 52

Chané, E., J. Saur, and S. Poedts (2013), Modeling Jupiter's magnetosphere: Influence of the internal sources, *Journal of Geophysical Research: Space Physics*, *118*(5), 2157–2172, doi:10.1002/jgra.50258. 100

Chen, C. H. K., T. S. Horbury, A. A. Schekochihin, R. T. Wicks, O. Alexandrova, and J. Mitchell (2010a), Anisotropy of solar wind turbulence between ion and electron scales, *Physical Review Letters*, *104*(25), 255,002, doi:10.1103/PhysRevLett.104.255002. 24, 27, 32, 33, 79, 102, 111, 115, 121, 125, 127, 128, 129, 138, 144

Chen, C. H. K., A. Mallet, T. A. Yousef, A. A. Schekochihin, and T. S. Horbury (2011), Anisotropy of Alfvénic turbulence in the solar wind and numerical simulations, *Monthly Notices of the Royal Astronomical Society*, *415*(4), 3219–3226, doi:10.1111/j.1365-2966.2011.18933.x. 27

Chen, C. H. K., S. Boldyrev, Q. Xia, and J. C. Perez (2013), Nature of subproton scale turbulence in the solar wind, *Physical Review Letters*, *110*(22), 225,002, doi:10.1103/PhysRevLett.110.225002. 23

Chen, F. C. (1990), Kinetic Theory, in *Plasma physics and controlled fusion*, 2 ed., chap. 7, pp. 225–285, Plenum Press, New York. 28, 29

Chen, Y., T. W. Hill, A. M. Rymer, and R. J. Wilson (2010b), Rate of radial transport of plasma in Saturn's inner magnetosphere, *Journal of Geophysical Research*, *115*(A10), 1–10, doi:10.1029/2010JA015412. 89

Chian, A. C.-L., and P. R. Muñoz (2011), Detection of current sheets and magnetic reconnections at the zurbulent leading edge of an interplanetary coronal mass ejection, *The Astrophysical Journal*, *733*(2), L34, doi:10.1088/2041-8205/733/2/L34. 29

Cho, J., and A. Lazarian (2004), The anisotropy of electron magnetohydrodynamic turbulence, *The Astrophysical Journal*, *615*(1), L41–L44, doi:10.1086/425215. 78

Cho, J., and A. Lazarian (2005), Generation of compressible modes in MHD turbulence, *Theoretical and Computational Fluid Dynamics*, *19*, 127–157, doi:10.1007/s00162-004-0157-x. 15, 110

Cho, J., and A. Lazarian (2009), Simulations of electron magnetohydrodynamic turbulence, *The Astrophysical Journal*, *701*(1), 236–252, doi:10.1088/0004-637X/701/1/236. 31

Cho, J., and E. T. Vishniac (2000), The anisotropy of magnetohydrodynamic Alfvénic turbulence, *The Astrophysical Journal*, *539*(1), 273–282, doi:10.1086/309213. 33

Cho, J., A. Lazarian, and E. T. Vishniac (2002), Simulations of magnetohydrodynamic turbulence in a strongly magnetized medium, *The Astrophysical Journal*, *1*(564), 291–301, doi:10.1086/324186. 22, 26, 33, 79, 110, 111, 143

Clarke, K. E., et al. (2006), Cassini observations of planetary-period oscillations of Saturn's magnetopause, *Geophysical Research Letters*, *33*(23), L23,104, doi:10.1029/2006GL027821. 88

Cornilleau-Wehrlin, N., et al. (2003), First results obtained by the Cluster STAFF experiment, *Annales Geophysicae*, *21*, 437–456, doi:10.5194/angeo-21-437-2003. 40

Cowley, S. W. H., S. V. Badman, E. J. Bunce, J. T. Clarke, J.-C. Gérard, D. Grodent, C. M. Jackman, S. E. Milan, and T. K. Yeoman (2005), Reconnection in a rotation-dominated magnetosphere and its relation to Saturn's auroral dynamics, *Journal of Geophysical Research*, *110*, A02,201, doi:10.1029/2004JA010796. 52

Cranmer, S. R., and A. A. van Ballegooijen (2012), Proton, electron, and ion heating in the fast solar wind from nonlinear coupling between Alfvénic and fast-mode turbulence, *The Astrophysical Journal*, *754*(92), 29pp, doi:10.1088/0004-637X/754/2/92. 28, 29, 122, 123

David, F. N. (1949), The moments of the z and F distributions, *Biometrika*, *36*(3-4), 394–403, doi:10.1093/biomet/36.3-4.394. 97

DeJong, A. D., J. L. Burch, J. Goldstein, A. J. Coates, and F. Crary (2011), Day-night asymmetries of low-energy electrons in Saturn's inner magnetosphere, *Geophysical Research Letters*, *38*(L08106), doi:10.1029/2011GL047308. 89

Delamere, P. A., and F. Bagenal (2008), Longitudinal plasma density variations at Saturn caused by hot electrons, *Geophysical Research Letters*, *35*(3), L03,107, doi:10.1029/2007GL031095. 101

Delamere, P. A., F. Bagenal, V. Dols, and L. C. Ray (2007), Saturn's neutral torus versus Jupiter's plasma torus, *Geophysical Research Letters*, *34*(9), L09,105, doi:10.1029/2007GL029437. 28

Desch, M. D., and M. L. Kaiser (1981), Voyager measurement of the rotation period of Saturn's magnetic field, *Geophysical Research Letters*, *8*(3), 253–256, doi:10.1029/GL008i003p00253. 44

Dmitruk, P., W. H. Matthaeus, and N. Seenu (2004), Test particle energization by current sheets and nonuniform fields in magnetohydrodynamic turbulence, *The Astrophysical Journal*, *617*(1), 667–679, doi:10.1086/425301. 29, 122

Dougherty, M. K., et al. (2004), The Cassini magnetic field investigation, *Space Science Reviews*, *114*(1-4), 331–383, doi:10.1007/s11214-004-1432-2. 54, 63, 147, 149, 151, 152

Dougherty, M. K., et al. (2005), Cassini magnetometer observations during Saturn orbit insertion, *Science*, *307*(5713), 1266–70, doi:10.1126/science.1106098. 46, 57, 66

Dougherty, M. K., L. W. Esposito, and S. M. Krimigis (2009), *Saturn from Cassini-Huygens*, Springer, London, doi:10.1007/978-1-4020-9217-6. 35, 37, 38

Elsässer, W. M. (1950), The hydromagnetic equations, *Physical Review Letters*, *79*, 183, doi:10.1103/PhysRev.79.183. 13

Espinosa, S. A., D. J. Southwood, and M. K. Dougherty (2003), How can Saturn impose its rotation period in a noncorotating magnetosphere?, *Journal of Geophysical Research*, *108*(A2), 1086, doi:10.1029/2001JA005084. 46, 83

Farge, M. (1992), Wavelet transforms and their applications to turbulence, *Annual Review of Fluid Mechanics*, *24*, 395–457, doi:10.1146/annurev.fl.24.010192.002143. 31, 54

Feynman, R. P., R. B. Leighton, and M. Sands (2010), The relation of physics to other sciences, in *The Feynman lectures on Physics*, edited by M. A. Gottlieb and R. Pfeiffer, new millen ed., chap. 3.7, California Institute of Technology. 1

Fleshman, B. L., P. A. Delamere, F. Bagenal, and T. Cassidy (2013), A 1-D model of physical chemistry in Saturn's inner magnetosphere, *Journal of Geophysical Research: Planets*, *118*, 1567–1581, doi:10.1002/jgre.20106. 28, 38, 48, 52

Forman, M. A., R. T. Wicks, and T. S. Horbury (2011), Detailed fit of "critical balance" theory to solar wind turbulence measurements, *The Astrophysical Journal*, *733*(2), 76, doi:10.1088/0004-637X/733/2/76. 15, 22, 32, 109, 112, 115, 116, 121, 127, 143

Forman, M. A., R. T. Wicks, T. S. Horbury, and S. Oughton (2013), Scaling anisotropy of the power in parallel and perpendicular components of the solar wind magnetic field, in *AIP Conference Proceedings*, vol. 1539, p. 167, doi:10.1063/1.4811014. 111

Fredricks, R. W., and F. V. Coroniti (1976), Ambiguities in the deduction of rest frame fluctuation spectrums from spectrums computed in moving frames, *Journal of Geophysical Research*, *81*(31), 5591–5595, doi:10.1029/JA081i031p05591. 112

Frisch, U. (1995), *Turbulence*, Cambridge University Press, Cambridge. 1, 5, 6, 7, 8, 9, 10, 31

Galopeau, P. H. M., and A. Lecacheux (2000), Variations of Saturn's radio rotation period measured at kilometer wavelengths, *Journal of Geophysical Research*, *105*(A6), 13,089–13,101, doi:10.1029/1999JA005089. 44

Galtier, S. (2006), Wave turbulence in incompressible Hall magnetohydrodynamics, *Journal of Plasma Physics*, *72*(5), 721–769, doi:10.1017/S0022377806004521. 76, 102

Galtier, S., and A. Bhattacharjee (2005), Anisotropic wave turbulence in electron MHD, *Plasma Physics and Controlled Fusion*, *47*(12B), B691–B701, doi:10.1088/0741-3335/47/12B/S51. 26

Galtier, S., S. V. Nazarenko, A. C. Newell, and A. Pouquet (2000), A weak turbulence theory for incompressible magnetohydrodynamics, *Journal of Plasma Physics*, *63*(5), 447–488. 19, 21

Galtier, S., A. Pouquet, and A. Mangeney (2005), On spectral scaling laws for incompressible anisotropic magnetohydrodynamic turbulence, *Physics of Plasmas*, *12*(9), 092,310, doi:10.1063/1.2052507. 25, 26, 76, 78, 102

Gibson, C. H., and W. H. Schwarz (1963), The universal equilibrium spectra of turbulent velocity and scalar fields, *Journal of Fluid Mechanics*, *16*(3), 365, doi:10.1017/S0022112063000835. 10

Goldreich, P., and S. Sridhar (1995), Toward a theory of interstellar turbulence. 2: Strong Alfvénic turbulence, *The Astrophysical Journal*, *438*(2), 763–775, doi:10.1086/175121. 3, 5, 19, 20, 25, 33, 78, 110, 111, 143

Goldreich, P., and S. Sridhar (1997), Magnetohydrodynamic turbulence revisited, *The Astrophysical Journal*, *485*, 680, doi:10.1086/304442. 18, 25

Gombosi, T. I., T. P. Armstrong, C. S. Arridge, K. K. Khurana, S. M. Krimigis, N. Krupp, A. M. Persoon, and M. F. Thomsen (2009), Saturn's Magnetospheric Configuration, in *Saturn from Cassini-Huygens*, edited by M. K. Dougherty, L. Esposito, and S. M. Krimigis, pp. 203–255, Springer, London, doi:10.1007/978-1-4020-9217-6. 37, 38, 68, 69

Grappin, R., and W.-C. Müller (2010), Scaling and anisotropy in magnetohydrodynamic turbulence in a strong mean magnetic field, *Physical Review E*, *82*(2), 026,406, doi:10.1103/PhysRevE.82.026406. 117, 121

Grappin, R., A. Mangeney, and E. Marsch (1990), On the origin of solar wind MHD turbulence: Helios data revisited, *Journal of Geophysical Research*, *95*(A6), 8197–8209, doi:10.1029/JA095iA06p08197. 71

Gurnett, D. A., et al. (2004), The Cassini Radio and Plasma Wave Investigation, in *The Cassini-Huygens Mission, 2*, edited by C. T. Russell, pp. 395–463, Springer, Dordrecht, doi:10.1007/978-1-4020-2774-1_6. 44

Gurnett, D. A., et al. (2005), Radio and plasma wave observations at Saturn from Cassini's approach and first orbit., *Science*, *307*(5713), 1255–9, doi:10.1126/science.1105356. 44

Gurnett, D. A., A. M. Persoon, W. S. Kurth, J. B. Groene, T. F. Averkamp, M. K. Dougherty, and D. J. Southwood (2007), The variable rotation period of the inner region of Saturn's plasma disk., *Science*, *316*(5823), 442–5, doi:10.1126/science.1138562. 46, 86, 90, 101, 103, 143

Gurnett, D. A., A. Lecacheux, W. S. Kurth, A. M. Persoon, J. B. Groene, L. Lamy, P. Zarka, and J. F. Carbary (2009), Discovery of a north-south asymmetry in Saturn's radio rotation period, *Geophysical Research Letters*, *36*(16), L16,102, doi:10.1029/2009GL039621. 45

Gurnett, D. A., J. B. Groene, T. F. Averkamp, W. S. Kurth, S.-Y. Ye, and G. Fischer (2011), An SLS4 longitude system based on a tracking filter analysis of the rotational modulation of Saturn kilometric radiation, in *Planetary Radio Emissions VII*, pp. 51–64. 43, 45, 46, 85, 86, 99, 142

Hamilton, K., C. W. Smith, B. J. Vasquez, and R. J. Leamon (2008), Anisotropies and helicities in the solar wind inertial and dissipation ranges a 1 AU, *Journal of Geophysical Research*, *113*, A01,106, doi:10.1029/2007JA012559. 110

Harland, D. M. (2007), *Cassini at Saturn: Huygens Results*, vol. 214, Springer, Berlin. 36, 37

Hasegawa, A. (1976), Particle acceleration by MHD surface wave and formation of aurora, *Journal of Geophysical Research*, *81*(28), 5083–5090. 23

He, J., C. Tu, E. Marsch, S. Bourouaine, and Z. Pei (2013), Radial evolution of the wavevector anisotropy of solar wind turbulence between 0.3 and 1 AU, *The Astrophysical Journal*, *773*(1), 72, doi:10.1088/0004-637X/773/1/72. 33

Higdon, J. C. (1984), Density fluctuations in the interstellar medium: Evidence for anisotropic magnetogasdynamic turbulence. I. Model and astrophysical sites, *The Astrophysical Journal*, (285), 109–123, doi:10.1086/162481. 19, 20

Hill, T. W., and F. C. Michel (1976), Heavy ions from the Galilean satellites and the centrifugal distortion of the Jovian magnetosphere, *Journal of Geophysical Research*, *81*(25), 4561–4565, doi:10.1029/JA081i025p04561. 42, 49

Hill, T. W., et al. (2005), Evidence for rotationally driven plasma transport in Saturn's magnetosphere, *Geophysical Research Letters*, *32*, L14S10, doi:10.1029/2005GL022620. 49, 68

Hnat, B., S. C. Chapman, and G. Rowlands (2003), Intermittency, scaling, and the Fokker-Planck approach to fluctuations of the solar wind bulk plasma parameters as seen by the WIND spacecraft, *Physical Review E*, *67*(5), 056,404, doi:10.1103/PhysRevE.67.056404. 31

Horbury, T. S., M. A. Forman, and S. Oughton (2008), Anisotropic scaling of magnetohydrodynamic turbulence, *Physical Review Letters*, *101*(17), 1–4, doi:10.1103/PhysRevLett.101.175005. 18, 26, 27, 32, 33, 55, 79, 111, 125, 126, 127, 128, 138, 144

Horbury, T. S., R. T. Wicks, and C. H. K. Chen (2011), Anisotropy in space plasma turbulence: solar wind observations, *Space Science Reviews*, *172*(1-4), 325–342, doi:10.1007/s11214-011-9821-9. 125

Hospodarsky, G. B., T. F. Averkamp, W. S. Kurth, D. A. Gurnett, J. D. Menietti, O. Santolik, and M. K. Dougherty (2008), Observations of chorus at Saturn using the Cassini Radio and Plasma Wave Science instrument, *Journal of Geophysical Research*, *113*(A12), A12,206, doi:10.1029/2008JA013237. 49

Howes, G. G. (2009), Limitations of Hall MHD as a model for turbulence in weakly collisional plasmas, *Nonlinear Processes in Geophysics*, *16*(2), 219–232, doi:10.5194/npg-16-219-2009. 122

Howes, G. G., and K. D. Nielson (2013), Alfvén wave collisions, the fundamental building block of plasma turbulence I: asymptotic solution, *Physics of Plasmas*, *20*(7). 16, 17

Howes, G. G., S. C. Cowley, W. Dorland, G. W. Hammett, E. Quataert, and A. A. Schekochihin (2006), Astrophysical gyrokinetics: basic equations and linear theory, *The Astrophysical Journal*, *651*(1), 590–614, doi:10.1086/506172. 15, 23, 28, 29, 75, 76, 81, 103, 142

Howes, G. G., S. C. Cowley, W. Dorland, G. W. Hammett, E. Quataert, and A. A. Schekochihin (2008), A model of turbulence in magnetized plasmas: Implications for the dissipation range in the solar wind, *Journal of Geophysical Research*, *113*(A5), A05,103, doi:10.1029/2007JA012665. 22, 23, 24, 28, 29, 111, 113, 114, 122, 123, 143

Howes, G. G., J. M. TenBarge, and W. Dorland (2011a), A weakened cascade model for turbulence in astrophysical plasmas, *Physics of Plasmas*, *18*(10), 102,305, doi:10.1063/1.3646400. 24, 76, 102

Howes, G. G., J. M. TenBarge, W. Dorland, E. Quataert, A. A. Schekochihin, R. Numata, and T. Tatsuno (2011b), Gyrokinetic simulations of solar wind turbulence from ion to electron scales, *Physical Review Letters*, *107*(3), 035,004, doi:10.1103/PhysRevLett.107.035004. 122

Howes, G. G., S. D. Bale, K. G. Klein, C. H. K. Chen, C. S. Salem, and J. M. TenBarge (2012), The slow-mode nature of compressible wave power in solar wind turbulence, *The Astrophysical Journal*, *753*(L19), doi:10.1088/2041-8205/753/1/L19. 15

Howes, G. G., K. G. Klein, and J. M. TenBarge (2014a), Validity of the Taylor hypothesis for linear kinetic waves in the weakly collisional solar wind, *The Astrophysical Journal*, *789*(2), 106, doi:10.1088/0004-637X/789/2/106. 20, 22, 23, 59, 60

Howes, G. G., K. G. Klein, and J. M. TenBarge (2014b), The quasilinear premise for the modeling of plasma turbulence, *arXiv preprint*. 28

Iroshnikov, P. S. (1964), Turbulence of a conducting fluid in a strong magnetic field, *Soviet Astronomy*, *7*(4), 566–571. 16

Jackman, C. M., N. Achilleos, E. J. Bunce, S. W. H. Cowley, M. K. Dougherty, G. H. Jones, S. E. Milan, and E. J. Smith (2004), Interplanetary magnetic field at ∼9 AU during the declining phase of the solar cycle and its implications for Saturn's magnetospheric dynamics, *Journal of Geophysical Research*, *109*, A11,203, doi:10.1029/2004JA010614. 52

Jackman, C. M., et al. (2008), A multi-instrument view of tail reconnection at Saturn, *Journal of Geophysical Research*, *113*(A11), 1–9, doi:10.1029/2008JA013592. 52, 100

Jacobsen, S., F. M. Neubauer, J. Saur, and N. Schilling (2007), Io's nonlinear MHD-wave field in the heterogeneous Jovian magnetosphere, *Geophysical Research Letters*, *34*, L10,202, doi:10.1029/2006GL029187. 53

Jia, X., K. C. Hansen, T. I. Gombosi, M. G. Kivelson, G. Tóth, D. L. DeZeeuw, and A. J. Ridley (2012a), Magnetospheric configuration and dynamics of Saturn's magnetosphere: A global MHD simulation, *Journal of Geophysical Research*, *117*, A05,225, doi:10.1029/2012JA017575. 51, 52, 100

Jia, X., M. G. Kivelson, and T. I. Gombosi (2012b), Driving Saturn's magnetospheric periodicities from the upper atmosphere/ionosphere, *Journal of Geophysical Research*, *117*(A4), A04,215, doi:10.1029/2011JA017367. 51, 88

Kellett, S., E. J. Bunce, A. J. Coates, and S. W. H. Cowley (2009), Thickness of Saturn's ring current determined from north-south Cassini passes through the current layer, *Journal of Geophysical Research*, *114*(A4), 1–16, doi:10.1029/2008JA013942. 50

Kellett, S., C. S. Arridge, E. J. Bunce, A. J. Coates, S. W. H. Cowley, M. K. Dougherty, A. M. Persoon, N. Sergis, and R. J. Wilson (2010), Nature of the ring current in Saturn's dayside magnetosphere, *Journal of Geophysical Research*, *115*(A8), 1–10, doi:10.1029/2009JA015146. 50

Kennelly, T. J., J. S. Leisner, G. B. Hospodarsky, and D. A. Gurnett (2013), Ordering of injection events within Saturnian SLS longitude and local time, *Journal of Geophysical Research: Space Physics*, *118*(2), 832–838, doi:10.1002/jgra.50152. 83, 89

Kimura, T., et al. (2013), Long-term modulations of Saturn's auroral radio emissions by the solar wind and seasonal variations controlled by the solar ultraviolet flux, *Journal of Geophysical Research: Space Physics*, doi: 10.1002/2013JA018833. 52

Kiyani, K. H., S. C. Chapman, Y. V. Khotyaintsev, M. W. Dunlop, and F. Sahraoui (2009), Global scale-invariant dissipation in collisionless plasma turbulence, *Physical Review Letters*, *103*(7), 075,006, doi:10.1103/PhysRevLett.103.075006. 11, 31, 77, 121, 143

Kiyani, K. H., S. C. Chapman, F. Sahraoui, B. Hnat, O. Fauvarque, and Y. V. Khotyaintsev (2013), Enhanced magnetic compressibility and isotropic scale invariance at sub-ion Larmor scales in solar wind turbulence, *The Astrophysical Journal*, *763*(1), 10, doi:10.1088/0004-637X/763/1/10. 11, 31, 68

Klein, K. G., G. G. Howes, J. M. TenBarge, S. D. Bale, C. H. K. Chen, and C. S. Salem (2012), Using synthetic spacecraft data to interpret compressible fluctuations in solar wind turbulence, *The Astrophysical Journal*, *755*(2), 159, doi:10.1088/0004-637X/755/2/159. 15, 23

Kolmogorov, A. N. (1941a), The local structure of turbulence in incompressible viscous fluid for very large Reynolds numbers, *Doklady Akademiia Nauk SSSR*, *30*, 299–303, doi:10.1098/rspa.1991.0075. 8, 10

Kolmogorov, A. N. (1941b), On the degeneration of isotropic turbulence in an incompressible viscous liquid, *Doklady Akademiia Nauk SSSR*, *31*(6), 538–541. 8

Kolmogorov, A. N. (1941c), Dissipation of energy in the locally isotropic turbulence, *Doklady Akademiia Nauk SSSR*, *32*(1), 16–18. 8

Kolmogorov, A. N. (1941d), On the logarithmically normal law of distribution of the size of particles under pulverisation, *Doklady Akademiia Nauk SSSR*, *31*, 99–101. 8

Kraichnan, R. H. (1965), Inertial-range spectrum of hydromagnetic turbulence, *Physics of Fluids*, *8*(7), 1385, doi:10.1063/1.1761412. 16

Krimigis, S. M., D. G. Mitchell, D. C. Hamilton, S. Livi, J. Dandouras, and S. Jaskulek (2004), Magnetosphere imaging instrument (MIMI) on the Cassini mission to Saturn/Titan, *Space Science Reviews*, *114*(1-4), 233–329, doi:10.1007/s11214-004-1410-8. 49, 68, 130

Krimigis, S. M., et al. (2005), Dynamics of Saturn's magnetosphere from MIMI during Cassini's orbital insertion, *Science*, *307*, 1270–1273, doi:10.1126/science.1105978. 40, 83

Krimigis, S. M., N. Sergis, D. G. Mitchell, D. C. Hamilton, and N. Krupp (2007), A dynamic, rotating ring current around Saturn., *Nature*, *450*(7172), 1050–3, doi:10.1038/nature06425. 50

Krupp, N., et al. (2009), Energetic particles in Saturn's magnetosphere during the Cassini nominal mission (July 2004–July 2008), *Planetary and Space Science*, *57*(14-15), 1754–1768, doi:10.1016/j.pss.2009.06.010. 50

Kurth, W. S., A. Lecacheux, T. F. Averkamp, J. B. Groene, and D. A. Gurnett (2007), A Saturnian longitude system based on a variable kilometric radiation period, *Geophysical Research Letters*, *34*(2), L02,201, doi:10.1029/2006GL028336. 44, 61, 86

Kurth, W. S., T. F. Averkamp, D. A. Gurnett, J. B. Groene, and A. Lecacheux (2008), An update to a Saturnian longitude system based on kilometric radio emissions, *Journal of Geophysical Research*, *113*(A5), 222, doi:10.1029/2007JA012861. 44, 45, 86, 99

Lamy, L. (2011), Variability of southern and northern SKR periodicities, in *Planetary Radio Emissions VII*, pp. 38–50. 45, 85, 86, 99, 142

Lamy, L., B. Cecconi, R. Prangé, P. Zarka, J. D. Nichols, and J. T. Clarke (2009), An auroral oval at the footprint of Saturn's kilometric radio sources, colocated with the UV aurorae, *Journal of Geophysical Research*, *114*(A10), A10,212, doi:10.1029/2009JA014401. 101

Lamy, L., R. Prangé, W. Pryor, J. Gustin, S. V. Badman, H. Melin, T. Stallard, D. G. Mitchell, and P. C. Brandt (2013), Multispectral simultaneous diagnosis of Saturn's aurorae throughout a planetary rotation, *Journal of Geophysical Research: Space Physics*, *118*(8), 4817–4843, doi:10.1002/jgra.50404. 101

Leamon, R. J., C. W. Smith, N. F. Ness, W. H. Matthaeus, and H. K. Wong (1998), Observational constraints on the dynamics of the interplanetary magnetic field dissipation range, *Journal of Geophysical Research*, *103*(A3), 4775–4787, doi:10.1029/97JA03394. 79, 102

Leamon, R. J., C. W. Smith, N. F. Ness, and H. K. Wong (1999), Dissipation range dynamics: kinetic Alfven waves and the importance of β_e, *J. Geophys. Res*, *104*(A10), 22,331–22,344, doi:10.1029/1999JA900158. 24, 29, 81, 82, 83, 93, 122, 142

Leamon, R. J., W. H. Matthaeus, C. W. Smith, G. P. Zank, D. J. Mullan, and S. Oughton (2000), MHD-driven kinetic dissipation in the solar wind and corona, *The Astrophysical Journal*, pp. 1054–1062, doi:10.1086/309059. 29

Leisner, J. S., and C. T. Russell (2005), Warm flux tubes in the E-ring plasma torus: Initial Cassini magnetometer observations, *Geophysical Research Letters*, *32*, L14S08, doi:10.1029/2005GL022652. 49, 52

Leisner, J. S., C. T. Russell, M. K. Dougherty, X. Blanco-Cano, R. J. Strangeway, and C. Bertucci (2006), Ion cyclotron waves in Saturn's E ring: Initial Cassini observations, *Geophysical Research Letters*, *33*, L11,101, doi: 10.1029/2005GL024875. 48, 69, 70, 141

Leisner, J. S., C. T. Russell, H. Y. Wei, and M. K. Dougherty (2011), Probing Saturn's ion cyclotron waves on high-inclination orbits: Lessons for wave generation, *Journal of Geophysical Research*, *116*(A9), A09,235, doi: 10.1029/2011JA016555. 48

Lithwick, Y., and P. Goldreich (2001), Compressible magnetohydrodynamic turbulence in interstellar plasmas, *The Astrophysical Journal*, *562*(1), 279–296, doi:10.1086/323470. 15, 110, 143

Liu, X., T. W. Hill, R. A. Wolf, S. Sazykin, R. W. Spiro, and H. Wu (2010), Numerical simulation of plasma transport in Saturn's inner magnetosphere using the Rice Convection Model, *Journal of Geophysical Research*, *115*(A12), A12,254, doi:10.1029/2010JA015859. 49, 50

Lysak, R. L., and W. Lotko (1996), On the kinetic dispersion relation for shear Alfvén waves, *Journal of Geophysical Research*, *101*(95), 5085–5094, doi:10. 1029/95JA03712. 22

Mangeney, A. (2012), Intermittency and regularity in the Alfvenic range of solar wind turbulence, *AIP Conference Proceedings*, *26*(1), doi:10.1063/1.3701349. 11, 12, 77, 103

Mangeney, A., C. Lacombe, M. Maksimovic, A. A. Samsonov, N. Cornilleau-Wehrlin, C. C. Harvey, J.-M. Bosqued, and P. Travnicek (2006), Cluster observations in the magnetosheath – Part 1 : Anisotropies of the wave vector distribution of the turbulence at electron scales, *Annales Geophysicae*, *24*(12), 3507–3521, doi:10.5194/angeo-24-3507-2006. 20, 59

Markovskii, S. A., B. J. Vasquez, and C. W. Smith (2008), Statistical analysis of the high-frequency spectral break of the solar wind turbulence at 1 AU, *The Astrophysical Journal*, *675*(2), 1576–1583, doi:10.1086/527431. 24

Maron, J., and P. Goldreich (2001), Simulations of incompressible magnetohydrodynamic turbulence, *The Astrophysical Journal*, *554*(2), 1175–1196, doi: 10.1086/321413. 33

Matthaeus, W. H., and M. L. Goldstein (1982), Measurement of the rugged invariants of magnetohydrodynamic turbulence in the solar wind, *Journal of Geophysical Research*, *87*(A8), 6011–6028, doi:10.1029/JA087iA08p06011. 15, 30

Matthaeus, W. H., and C. W. Smith (1981), Structure of correlation tensors in homogeneous anisotropic turbulence, *Physical Review A*, *24*(4), 2135–2144. 106, 107

Matthaeus, W. H., M. L. Goldstein, and D. A. Roberts (1990), Evidence for the presence of quasi-two-dimensional nearly incompressible fluctuations in the solar wind, *Journal of Geophysical Research*, *95*(A12), 673–684, doi:10.1029/JA095iA12p20673. 18, 26, 28, 59, 122

Mauk, B. H., et al. (2005), Energetic particle injections in Saturns magnetosphere, *Geophysical Research Letters*, *32*, L14S05, doi:10.1029/2005GL022485. 49, 52, 68, 89

McComas, D. J., et al. (2000), Solar wind observations over Ulysses' first full polar orbit, *Journal of Geophysical Research*, *105*(A5), 10,419, doi:10.1029/1999JA000383. 125

Meneveau, C., and K. R. Sreenivasan (1991), The multifractal nature of turbulent energy dissipation, *Journal of Fluid Mechanics*, *224*, 429, doi:10.1017/S0022112091001830. 11

Menietti, J. D., O. Santolik, A. M. Rymer, G. B. Hospodarsky, A. M. Persoon, D. A. Gurnett, A. J. Coates, and D. T. Young (2008), Analysis of plasma waves observed within local plasma injections seen in Saturn's magnetosphere, *Journal of Geophysical Research*, *113*(A5), A05,213, doi:10.1029/2007JA012856. 49

Mitchell, D. G., et al. (2005), Energetic ion acceleration in Saturn's magnetotail: Substorms at Saturn?, *Geophysical Research Letters*, *32*, L20S01, doi:10.1029/2005GL022647. 100

Mitchell, D. G., et al. (2009), Recurrent energization of plasma in the midnight-to-dawn quadrant of Saturn's magnetosphere, and its relationship to auroral UV and radio emissions, *Planetary and Space Science*, *57*(14-15), 1732–1742, doi:10.1016/j.pss.2009.04.002. 50, 88

Montgomery, D., and L. Turner (1981), Anisotropic magnetohydrodynamic turbulence in a strong external magnetic field, *Physics of Fluids*, *24*(5), 825, doi:10.1063/1.863455. 16, 18, 26, 108

Müller, A. L., J. Saur, N. Krupp, E. Roussos, B. H. Mauk, a. M. Rymer, D. G. Mitchell, and S. M. Krimigis (2010), Azimuthal plasma flow in the Kronian magnetosphere, *Journal of Geophysical Research*, *115*, A08,203, doi:10.1029/2009JA015122. 49, 83, 89

Muzy, J. F., E. Bacry, and A. Arnéodo (1993), Multifractal formalism for fractal signals: The structure-function approach versus the wavelet-transform modulus-maxima method, *Physical review E*, *47*(2), 875, doi:10.1103/PhysRevE.47.875. 11

Narita, Y., and S. P. Gary (2010), Inertial-range spectrum of whistler turbulence, *Annales Geophysicae*, *28*(2), 597–601, doi:10.5194/angeo-28-597-2010. 26, 76, 102

Narita, Y., S. P. Gary, S. Saito, K.-H. Glassmeier, and U. Motschmann (2011), Dispersion relation analysis of solar wind turbulence, *Geophysical Research Letters*, *38*(5), doi:10.1029/2010GL046588. 25

NASA (2014), Planetary Fact Sheet, `http://nssdc.gsfc.nasa.gov`. 36, 37, 38

Nazarenko, S. (2011), *Wave turbulence, Lecture Notes in Physics 825*, Springer. 14

Ng, C. S., and A. Bhattacharjee (1997), Scaling of anisotropic spectra due to the weak interaction of shear-Alfvén wave packets, *Physics of Plasmas*, *4*(3), 605, doi:10.1063/1.872158. 18, 25

Nichols, J. D., B. Cecconi, J. T. Clarke, S. W. H. Cowley, J.-C. Gérard, A. Grocott, D. Grodent, L. Lamy, and P. Zarka (2010), Variation of Saturn's UV aurora with SKR phase, *Geophysical Research Letters*, *37*(15), doi:10.1029/2010GL044057. 101

Nielson, K. D., G. G. Howes, and W. Dorland (2013), Alfvén wave collisions, The fundamental building block of plasma turbulence II: Numerical solution, *Physics of Plasmas*, *20*(7). 16

Osman, K. T., and T. S. Horbury (2009), Multi-spacecraft measurement of anisotropic power levels and scaling in solar wind turbulence, *Annales Geophysicae*, *27*, 3019–3025, doi:10.5194/angeo-27-3019-2009. 27, 31, 32

Oughton, S., K.-H. Rädler, and W. H. Matthaeus (1997), General second-rank correlation tensors for homogeneous magnetohydrodynamic turbulence, *Physical Review E*, *56*(3), 2875–2888, doi:10.1103/PhysRevE.56.2875. 106, 109

Oughton, S., P. Dmitruk, and W. H. Matthaeus (2004), Reduced magnetohydrodynamics and parallel spectral transfer, *Physics of Plasmas*, *11*(5), 2214, doi:10.1063/1.1705652. 20

Perri, S., M. L. Goldstein, J. C. Dorelli, and F. Sahraoui (2012), Detection of small-scale structures in the dissipation regime of solar-wind turbulence, *Physical Review Letters*, *109*(19), 191,101, doi:10.1103/PhysRevLett.109.191101. 29, 31, 77

Perschke, C., Y. Narita, S. P. Gary, U. Motschmann, and K.-H. Glassmeier (2013), Dispersion relation analysis of turbulent magnetic field fluctuations in fast solar wind, *Annales Geophysicae*, *31*(11), 1949–1955, doi:10.5194/angeo-31-1949-2013. 25

Podesta, J. J. (2009), Dependence of solar-wind power spectra on the direction of the local mean magnetic field, *The Astrophysical Journal*, *698*(2), 986–999, doi:10.1088/0004-637X/698/2/986. 18, 27, 32, 111, 125

Podesta, J. J. (2013), Evidence of kinetic Alfvén waves in the solar wind at 1 AU, *Solar Physics*, *286*(2), 529–548, doi:10.1007/s11207-013-0258-z. 23

Podesta, J. J., and J. M. TenBarge (2012), Scale dependence of the variance anisotropy near the proton gyroradius scale: Additional evidence for kinetic Alfvén waves in the solar wind at 1 AU, *Journal of Geophysical Research*, *117*, A10,106, doi:10.1029/2012JA017724. 23, 80, 102, 111

Podesta, J. J., D. A. Roberts, and M. L. Goldstein (2006), Power spectrum of small-scale turbulent velocity fluctuations in the solar wind, *Journal of Geophysical Research*, *111*(A10109), doi:10.1029/2006JA011834. 64, 133

Podesta, J. J., J. E. Borovsky, and S. P. Gary (2010), A kinetic Alfvén wave cascade subject to collisionless damping cannot reach electron scales in the solar wind at 1 AU, *The Astrophysical Journal*, *712*(1), 685–691, doi:10.1088/0004-637X/712/1/685. 28

Provan, G., S. W. H. Cowley, J. Sandhu, D. J. Andrews, and M. K. Dougherty (2013), Planetary period magnetic field oscillations in Saturn's magnetosphere: Postequinox abrupt nonmonotonic transitions to northern system dominance, *Journal of Geophysical Research: Space Physics*, *118*(6), 3243–3264, doi:10.1002/jgra.50186. 46, 51

Roberts, O. W., X. Li, and B. Li (2013), Kinetic plasma turbulence in the fast solar wind measured by Cluster, *The Astrophysical Journal*, *769*(1), 58, doi:10.1088/0004-637X/769/1/58. 25

Robertson, H. P. (1940), The invariant theory of isotropic turbulence, *Mathematical Proceedings of the Cambridge Philosophical Society*, *36*(02), 209–223, doi:10.1017/S0305004100017199. 106

Russell, C. T. (1972), Comments on the measurement of power spectra of the interplanetary magnetic field, in *Solar Wind, NASA SP-308*, pp. 365–374. 64, 134, 151

Russell, C. T. (2003), *The Cassini-Huygens Mission. Overview, Objectives and Huygens Instrumentarium*, Springer. 147

Russell, C. T. (2004a), *The Cassini-Huygens Mission. Orbiter In Situ Investigations*, Springer. 147

Russell, C. T. (2004b), *The Cassini-Huygens Mission. Orbiter Remote Sensing Investigations*, Springer. 147

Russell, C. T., J. S. Leisner, C. S. Arridge, M. K. Dougherty, and X. Blanco-Cano (2006), Nature of magnetic fluctuations in Saturn's middle magnetosphere, *Journal of Geophysical Research*, *111*, A12,205, doi:10.1029/2006JA011921. 48, 52, 64, 69

Sahraoui, F., M. L. Goldstein, G. Belmont, P. Canu, and L. Rezeau (2010), Three dimensional anisotropic k spectra of turbulence at subproton scales in the solar wind, *Physical Review Letters*, *105*(13), 131,101, doi:10.1103/PhysRevLett.105.131101. 23, 25, 28, 30, 31, 59, 75, 121, 122, 143

Sahraoui, F., G. Belmont, and M. L. Goldstein (2012), New insight into short-wavelength solar wind fluctuations from Vlasov theory, *The Astrophysical Journal*, *748*(2), 100, doi:10.1088/0004-637X/748/2/100. 22, 23

Salem, C. S., A. Mangeney, S. D. Bale, and P. Veltri (2009), Solar wind magnetohydrodynamics turbulence: Anomalous scaling and role of intermittency, *The Astrophysical Journal*, *702*(1), 537–553, doi:10.1088/0004-637X/702/1/537. 11, 31, 77, 103

Salem, C. S., G. G. Howes, D. Sundkvist, S. D. Bale, C. C. Chaston, C. H. K. Chen, and F. S. Mozer (2012), Identification of kinetic Alfvén wave turbulence in the solar wind, *The Astrophysical Journal*, *745*(1), L9, doi:10.1088/2041-8205/745/1/L9. 80, 102

Saur, J. (2004), Turbulent heating of Jupiters middle magnetosphere, *The Astrophysical Journal Letters*, *602*(2), 137–140, doi:10.1086/382588. 80, 81, 82, 83, 93, 132, 142, 144

Saur, J., H. Politano, A. Pouquet, and W. H. Matthaeus (2002), Evidence for weak MHD turbulence in the middle magnetosphere of Jupiter, *Astronomy & Astrophysics*, *386*, 699–708, doi:10.1051/0004-6361. 2, 19, 71, 102

Saur, J., A. Pouquet, and W. H. Matthaeus (2003), An acceleration mechanism for the generation of the main auroral oval on Jupiter, *Geophysical Research Letters*, *30*(5), 1260, doi:10.1029/2002GL015761. 71

Saur, J., et al. (2006), Anti-planetward auroral electron beams at Saturn., *Nature*, *439*(7077), 699–702, doi:10.1038/nature04401. 75

Saur, J., N. Schilling, F. M. Neubauer, D. F. Strobel, S. Simon, M. K. Dougherty, C. T. Russell, and R. T. Pappalardo (2008), Evidence for temporal variability of Enceladus' gas jets: Modeling of Cassini observations, *Geophysical Research Letters*, *35*(20), L20,105, doi:10.1029/2008GL035811. 38

Schekochihin, A. A., S. C. Cowley, W. Dorland, G. W. Hammett, G. G. Howes, G. G. Plunk, E. Quataert, and T. Tatsuno (2008), Gyrokinetic turbulence: a nonlinear route to dissipation through phase space, *Plasma Physics and Controlled Fusion*, *50*(12), 124,024, doi:10.1088/0741-3335/50/12/124024. 78, 104

Schekochihin, A. A., S. C. Cowley, W. Dorland, G. W. Hammett, G. G. Howes, E. Quataert, and T. Tatsuno (2009), Astrophysical gyrokinetics:

Kinetic and fluid turbulent cascades in magnetized weakly collisional plasmas, *The Astrophysical Journal Supplement Series*, *182*(1), 310–377, doi:10.1088/0067-0049/182/1/310. 15, 20, 23, 24, 29, 75, 77, 78, 81, 101, 110, 111, 115, 122, 123, 126, 142, 143, 144

Schippers, P., et al. (2008), Multi-instrument analysis of electron populations in Saturn's magnetosphere, *Journal of Geophysical Research*, *113*, A07,208, doi:10.1029/2008JA013098. 41, 43, 75, 130, 131, 132, 135

Schippers, P., N. André, D. A. Gurnett, G. R. Lewis, A. M. Persoon, and A. J. Coates (2012), Identification of electron field-aligned current systems in Saturn's magnetosphere, *Journal of Geophysical Research*, *117*, A05,204, doi:10.1029/2011JA017352. 75

Seal, D. (2005), Cassini Mission Plan, *Revision O, Change 1*, *August*(JPL D-5564). 147, 148, 149, 150

Sergis, N., S. M. Krimigis, D. G. Mitchell, D. C. Hamilton, N. Krupp, B. H. Mauk, E. C. Roelof, and M. K. Dougherty (2009), Energetic particle pressure in Saturn's magnetosphere measured with the Magnetospheric Imaging Instrument on Cassini, *Journal of Geophysical Research*, *114*(A2), A02,214, doi:10.1029/2008JA013774. 43

Sergis, N., et al. (2010), Particle pressure, inertial force, and ring current density profiles in the magnetosphere of Saturn, based on Cassini measurements, *Geophysical Research Letters*, *37*, L02,102, doi:10.1029/2009GL041920. 41, 50

Sittler, E. C., et al. (2008), Ion and neutral sources and sinks within Saturn's inner magnetosphere: Cassini results, *Planetary and Space Science*, *56*(1), 3–18, doi:10.1016/j.pss.2007.06.006. 38, 41, 43

Smith, C. W., K. Hamilton, and B. J. Vasquez (2006), Dependence of the dissipation range spectrum of interplanetary magnetic fluctuationson the rate of energy cascade, *The Astrophysical Journal*, *645*(1), 85–88, doi:10.1086/506151. 24

Smith, C. W., B. J. Vasquez, and J. V. Hollweg (2012), Observational constraints on the role of cyclotron damping and kinetic Alfvén waves in the solar wind, *The Astrophysical Journal*, *745*(1), 8, doi:10.1088/0004-637X/745/1/8. 31, 69, 121

Sorriso-Valvo, L., V. Carbone, and P. Veltri (1999), Intermittency in the solar wind turbulence through probability distribution functions of fluctuations, *Geophysical Research Letters*, *26*(13), 1801–1804, doi:10.1029/1999GL900270. 31

Sorriso-Valvo, L., V. Carbone, P. Giuliani, P. Veltri, R. Bruno, V. Antoni, and E. Martines (2001), Intermittency in plasma turbulence, *Planetary and Space Science*, *49*(12), 1193–1200, doi:10.1016/S0032-0633(01)00060-5. 11, 31, 77

Southwood, D. J., and S. W. H. Cowley (2014), The origin of Saturn's magnetic periodicities: Northern and southern current systems, *Journal of Geophysical Research: Space Physics*, *196*(3), doi:10.1002/2013JA019632. 46, 47, 51

Southwood, D. J., and M. G. Kivelson (2009), The source of Saturn's periodic radio emission, *Journal of Geophysical Research*, *114*(A9), A09,201, doi:10.1029/2008JA013800. 88, 101

Sridhar, S. (2011), Magnetohydrodynamics turbulence: An astronomical perspective, *Pramana*, *77*(1), 185–198. 15

Sridhar, S., and P. Goldreich (1994), Toward a theory of interstellar turbulence. 1: Weak Alfvenic turbulence, *The Astrophysical Journal*, *432*, 612–621. 16, 18, 19, 114

Stawicki, O., S. P. Gary, and H. Li (2001), Solar wind magnetic fluctuation spectra: Dispersion versus damping, *Journal of Geophysical Research*, *106*, 8273–8281. 23, 28

Taylor, G. I. (1938), The spectrum of turbulence, *Proceedings of the Royal Society of London. Series A*, *164*(919), 476–490. 59

TenBarge, J. M., and G. G. Howes (2012), Evidence of critical balance in kinetic Alfvén wave turbulence simulations, *Physics of Plasmas*, *19*, 1–8, doi:10.1063/1.3693974. 33

TenBarge, J. M., J. J. Podesta, K. G. Klein, and G. G. Howes (2012), Interpreting magnetic variance anisotropy measurements in the solar wind, *The Astrophysical Journal*, *753*(2), 107, doi:10.1088/0004-637X/753/2/107. 15, 23, 31, 79, 110

TenBarge, J. M., G. G. Howes, and W. Dorland (2013), Collisionless damping at electron scales in solar wind turbulence, *The Astrophysical Journal*, *774*(2), 139, doi:10.1088/0004-637X/774/2/139. 23, 111, 114, 122, 143

Tessein, J. A., C. W. Smith, B. T. MacBride, W. H. Matthaeus, M. A. Forman, and J. E. Borovsky (2009), Spectral indices for multi-dimensional interplanetary turbulence at 1 AU, *The Astrophysical Journal*, *692*(1), 684–693, doi:10.1088/0004-637X/692/1/684. 27, 32, 79

Thomsen, M. F., D. B. Reisenfeld, D. M. Delapp, R. L. Tokar, D. T. Young, F. J. Crary, E. C. Sittler, M. A. McGraw, and J. D. Williams (2010), Survey of ion plasma parameters in Saturn's magnetosphere, *Journal of Geophysical Research*, *115*, A10,220, doi:10.1029/2010JA015267. 41, 42, 43, 49, 52, 53, 54, 56, 60, 81, 100, 130, 132, 135, 142

Thomsen, M. F., R. J. Wilson, R. L. Tokar, D. B. Reisenfeld, and C. M. Jackman (2013), Cassini/CAPS observations of duskside tail dynamics at Saturn,

Journal of Geophysical Research: Space Physics, (1), doi:10.1002/jgra.50552. 50

Thomsen, M. F., C. M. Jackman, R. L. Tokar, and R. J. Wilson (2014), Plasma flows in Saturn's nightside magnetosphere, *Journal of Geophysical Research: Space Physics*, *119*, doi:10.1002/2014JA019912. 41, 43

Thomson, W. (1887), XLV. On the propagation of laminar motion through a turbulently moving inviscid liquid, *Philosophical Magazine Series 5*, *24*(149), 342–353, doi:10.1080/14786448708628110. 6

Torrence, C., and G. P. Compo (1998), A practical guide to wavelet analysis, *Bulletin of the American Meteorological Society*, *79*, 61–78, doi:10.1175/1520-0477(1998)079<0061:APGTWA>2.0.CO;2. 54

Tu, C. Y., Z. Y. Pu, and F. S. Wei (1984), The power spectrum of interplanetary Alfvénic fluctuations: Derivation of the governing equation and its solution, *Journal of Geophysical Research*, *89*(A11), 9695–9702, doi:10.1029/JA089iA11p09695. 15, 30

Turner, A. J., G. Gogoberidze, S. C. Chapman, B. Hnat, and W.-C. Müller (2011), Nonaxisymmetric anisotropy of solar wind turbulence, *Physical Review Letters*, *107*(9), 095,002, doi:10.1103/PhysRevLett.107.095002. 18

Turner, A. J., G. Gogoberidze, and S. C. Chapman (2012), Nonaxisymmetric anisotropy of solar wind turbulence as a direct test for models of magnetohydrodynamic turbulence, *Physical Review Letters*, *108*(8), 085,001, doi:10.1103/PhysRevLett.108.085001. 109, 112, 116

Vasyliunas, V. M. (1983), Plasma Distribution and Flow, in *Physics of the Jovian Magnetosphere*, edited by A. J. Dessler, chap. 11.4, pp. 395–453, Cambridge University Press, New York. 48, 51

Voitenko, Y., and J. De Keyser (2011), Turbulent spectra and spectral kinks in the transition range from MHD to kinetic Alfvén turbulence, *Nonlinear Processes in Geophysics*, *18*(5), 587–597, doi:10.5194/npg-18-587-2011. 69, 121

von Papen, M., J. Saur, and O. Alexandrova (2014), Turbulent magnetic field fluctuations in Saturn's magnetosphere, *Journal of Geophysical Research*, *119*, 2797–2818, doi:10.1002/2013JA019542. 3, 35

Vörös, Z., D. Jankovičová, and P. Kovács (2002), Scaling and singularity characteristics of solar wind and magnetospheric fluctuations, *Nonlinear Processes in Geophysics*, *9*(2), 149–162, doi:10.5194/npg-9-149-2002. 12

Wan, M., S. Oughton, S. Servidio, and W. H. Matthaeus (2009), Generation of non-Gaussian statistics and coherent structures in ideal magnetohydrodynamics, *Physics of Plasmas*, *16*(8), 080,703, doi:10.1063/1.3206949. 31

Wan, M., S. Oughton, S. Servidio, and W. H. Matthaeus (2012), von Kármán self-preservation hypothesis for magnetohydrodynamic turbulence and its consequences for universality, *Journal of Fluid Mechanics*, *697*, 296–315, doi:10.1017/jfm.2012.61. 10

Warwick, J. W., et al. (1981), Planetary radio astronomy observations from Voyager 1 near Saturn, *Science*, *212*(4491), 239–243, doi:10.1126/science.212.4491.239. 44

Wicks, R. T., T. S. Horbury, C. H. K. Chen, and A. A. Schekochihin (2010), Power and spectral index anisotropy of the entire inertial range of turbulence in the fast solar wind, *Monthly Notices of the Royal Astronomical Society: Letters*, *407*(1), L31–L35, doi:10.1111/j.1745-3933.2010.00898.x. 27, 31, 32, 109, 126

Wicks, R. T., M. A. Forman, T. S. Horbury, and S. Oughton (2012), Power anisotropy in the magnetic field power spectral tensor of solar wind turbulence, *The Astrophysical Journal*, *746*(1), 103, doi:10.1088/0004-637X/746/1/103. 15, 18, 26, 107, 110

Wilson, R. J., R. L. Tokar, M. G. Henderson, T. W. Hill, M. F. Thomsen, and D. H. Pontius (2008), Cassini plasma spectrometer thermal ion measurements in Saturn's inner magnetosphere, *Journal of Geophysical Research*, *113*, A12,218, doi:10.1029/2008JA013486. 100

Wilson, R. J., R. L. Tokar, and M. G. Henderson (2009), Thermal ion flow in Saturn's inner magnetosphere measured by the Cassini plasma spectrometer: A signature of the Enceladus torus?, *Geophysical Research Letters*, *36*(23), L23,104, doi:10.1029/2009GL040225. 27

Wishart, J. (1947), The cumulants of the z and of the logarithmic χ^2 and t distributions, *Biometrika*, *34*(1-2), 170–178, doi:10.1093/biomet/34.1-2.170. 97

Wright, A. N. (1987), The interaction of Io's Alfvén waves with the Jovian magnetosphere, *Journal of Geophysical Research*, *92*(A9), 9963–9970, doi:10.1029/JA092iA09p09963. 53

Young, D. T., et al. (2004), Cassini plasma spectrometer investigation, *Space Science Reviews*, *114*(1-4), 1–112, doi:10.1007/s11214-004-1406-4. 41, 130

Zimbardo, G., A. Greco, L. Sorriso-Valvo, S. Perri, Z. Vörös, G. Aburjania, K. Chargazia, and O. Alexandrova (2010), Magnetic turbulence in the geospace environment, *Space Science Reviews*, *156*(1-4), 89–134, doi:10.1007/s11214-010-9692-5. 31

Versicherung

Ich versichere, dass ich die von mir vorgelegte Dissertation selbständig angefertigt, die benutzten Quellen und Hilfsmittel vollständig angegeben und die Stellen der Arbeit - einschließlich Tabellen, Karten und Abbildungen -, die anderen Werken im Wortlaut oder dem Sinn nach entnommen sind, in jedem Einzelfall als Entlehnung kenntlich gemacht habe; dass diese Dissertation noch keiner anderen Fakultät oder Universität zur Prüfung vorgelegen hat; dass sie - abgesehen von unten angegebenen Teilpublikationen - noch nicht veröffentlicht worden ist, sowie, dass ich eine solche Veröffentlichung vor Abschluss des Promotionsverfahrens nicht vornehmen werde. Die Bestimmungen der Promotionsordnung sind mir bekannt. Die von mir vorgelegte Dissertation ist von Professor Joachim Saur betreut worden.

Teilpublikation

von Papen, M., J. Saur, O. Alexandrova (2014), Turbulent magnetic field fluctuations in Saturn's magnetosphere, *Journal of Geophysical Research: Space Physics, 119*, 2797-2818.

Danksagung

Diese Dissertation wäre ohne die Unterstützung und Hilfe vieler meiner Kollegen und Freunde nicht denkbar gewesen. Die Inspiration aber auch die Ablenkung, die ich durch sie während der dreieinhalb Jahre dauernden Arbeit erfahren habe, waren unersetzlich. Ihnen soll an dieser Stelle mein Dank ausgesprochen werden.

Besonderer Dank gilt dem Betreuer meiner Arbeit, Joachim Saur, der mich durch seine offenherzige Art und mit seinem klaren Verstand sicher durch manche Untiefe gelotst hat. Er hat mir die wissenschaftliche Arbeit beigebracht und mir die Möglichkeit gegeben sie auf etlichen Konferenzen zu präsentieren. Seine Motivation für die Turbulenz und die Wissenschaft im Allgemeinen war immer ein wesentlicher Antrieb für mich. Ebenfalls möchte ich Sven Simon danken, der mir in vielen Diskussionen Saturn's Magnetosphäre und seine Plasmaphysik näher bringen konnte und die vielen Publikationen zum Thema für mich in einen sinnvollen Zusammenhang brachte. Es war mir eine besondere Freude das ehrliche Interesse zu spüren, welches beide an den Resultaten meiner Arbeit hatten.

Ein ebenfalls großer Dank gilt allen meinen Arbeitskollegen am Institut für Geophysik, insbesondere Pritam Yogeshwar, Anne Schreiner, Fabrizio Musacchio, Oliver Hartkorn und Moritz Feyerabend, die durch Korrekturlesen und Latexhilfe wesentlich zur Verbesserung dieser Arbeit beigetragen haben. Des Weiteren möchte ich Klaus Lippert, Amir Haroon, Juliane Adrian und Hannah Großbach für die lustige gemeinsame Zeit, Kaffeepausen und Mittagessen danken.

A special thanks goes to Olga Alexandrova, who substantially helped to shape the published paper and who never stopped to ask questions that led to significant insights.

Diese Arbeit hätte nicht ohne die beständige Liebe meiner Frau Lena entstehen können. Dir gehört nicht nur mein Dank, sondern mein ganzes Herz.